

# **Novel daylighting system based on advanced embedded optical microstructures for various facade orientation and climates**

**Thèse N° 9390**

**Présentée le 2 mai 2019**

**à la Faculté de l'environnement naturel, architectural et construit  
Laboratoire d'énergie solaire et physique du bâtiment  
Programme doctoral en energie**

**pour l'obtention du grade de Docteur ès Sciences**

**par**

**Jing GONG**

**Acceptée sur proposition du jury**

**Dr S.-R. Cherkaoui, président du jury  
Prof. J.-L. Scartezzini, Dr A. Schueler, directeurs de thèse  
Prof. P. Hoffmann, rapporteur  
Dr A. Hafner, rapporteur  
Dr Y. Leterrier, rapporteur**

**2019**



# Acknowledgement

I would like to thank Dr. Andreas Schüler for accepting me in this exciting PhD thesis. His inspiring advices and cheerful personality, gave me confidence and determination to tackle the problems during my PhD study. His profound insight in physics and strong experimental intuition are just like a light in darkness, ensuring me on the right track to my destination. His passion about scientific research, strong spirit of creativity, and good work-life balance are a model for me. I feel very lucky to be able to work with him.

I would like to thank Prof. Jean-louis Scartezzini for welcoming me in the Laboratory of Solar Energy and Building Physics (LESO-PB) of EPFL. He gathers all the wonderful people together who always make me smile and happy at LESO. He helps guarantee a lively and loving atmosphere in the Lab. Moreover, I am very thankful for his great advice concerning the daylighting performance of a complex fenestration system. He also helped me improve a lot the language of my thesis.

Concerning the financial support for my PhD thesis, I would like to thank the Swiss Competence Center for Energy Research SCCER FEEB&D of the Swiss Innovation Agency Innosuisse.

I am grateful to Dr. Cherkaoui Sidi-Rachid, Dr. Yves Letterier, Prof. Patrik Hoffmann and Dr. Andreas Hafner, for being the jury members for my PhD exam and taking time to assess my work.

For this highly interdisciplinary PhD thesis, without the help of numerous people I would not be able to accomplish my work. I would like to show my great gratitude to Prof. Patrik Hoffmann at the Laboratory for Advanced Materials Processing at EMPA, for his generosity in giving me the access to the laser equipment for master mold fabrication, and devices for sample characterization; he was very dedicated in helping me to understand the principles of laser ablation, and helped me analyze the data. I appreciate his strong critical thinking, and set this as a good model for me. I would also like to show my appreciation to Georgios Violakis, Daniel Infante and Christoph Amsler for their assistance concerning the master mold fabrication. I would like to thank Dr. Yves Letterier at Laboratory for Processing of Advanced Composites (LPAC) at EPFL, for granting me access to their lab and sharing his profound experience in UV-imprinting. He also helped me a lot in data analysis. Moreover, I would like to thank Luca Mueller at LPAC for assisting me with UV-imprinting roll-to-roll process. I would like to show my great gratitude to Daniel Laub for her very professional experience in the preparation of samples for characterization with electron microscopy. I would like to show my great gratitude to Dr. André Kostro, for his guidance in the simulation for complex fenestration systems and the experimental work, as well as his time for

active discussion. I also would like to thank Dr. Andreas Hafner at BASF for his confidence in this project, and great support in industrial upscaling.

I would like to thank Pierre Loesch and Luc Burnier for building up the new experimental setups. Their great work is very helpful for the development of mechanical engraving method on soft substrates and exciting results from this method. I would like to thank my students who did their master semester projects with me: Kejia Cui, Frank Meyer, and Julien Chiappinelli for their hard work and inspiring results to the development of the thesis.

I also would like to thank Marlène Muff, Barbara Smith, and Cécile Taverney for their patience and nice work, ensuring all kinds of things go well during my PhD study.

I would like to show my great gratitude to my lovely colleagues: Bouvard Olivia, Anna Karmmer, Pietro Florio, Dan Assoulin, Dasaraden Mauree, Dasun Perera, Marta Benedetti, Jérémy Fleury, Alina Walch, Yujie Wu, Ali Motamed, Silvia Coccolo, Roberto Castello, Govinda Upadhyay, Lenka Maierova, Sara Vanzo. Thanks to them bringing me so much joy, inspiration and encouragement, I enjoy very much my PhD study.

Finally, I would like to thank my families. I would like to show my appreciation to my husband Stephen Loh. He is my great friend and soul mate. He has been very supportive, always trying his best to help me with my work and whatever I wanted to do. He is the one who can bring out the best in me. I would like to thank my little baby who arrived at my tummy when I was crazily busy with thesis writing; thank you for being so strong during that tough period, and accompanying me to accomplish my PhD journey. I would like to show my great gratitude to my parents who have been tremendously understanding and supportive, making me feel warm and secure. They shared their experiences, which inspired me to be confident, persistent, problem solving oriented and pursue my dreams. They guided and encouraged me in times of difficulties. I am also very thankful to my extended families: grandparents, uncles, aunties, etc; they have been being so supportive and brought me a lot of warm.

Overall, I feel so fortunate and grateful with what I have experienced in the last several years in EPFL.

Jing Gong

January 15, 2019



# Abstract

The design of highly glazed building has become a worldwide trend in modern architecture. However, glazing may induce large thermal loss in winter while increasing cooling load in summer, and it may also cause glare.

In order to solve the problems, a novel multifunctional glazing with embedded optical microstructures is proposed for seasonal thermal control, daylighting, glare protection and clear view. The glazing consists of a polymer layer with embedded optical microstructures, and the polymer layer is laminated with a glass pane of glazing. The proposed glazing is based on the combination of microstructured geometry and optical coating. According to the geometry, two types of embedded optical microstructures were originally suggested and developed in the present thesis: i) “L”-shape retro-reflective optical microstructure, and ii) micro compound parabolic concentrators (symmetric and asymmetric). The suggested optical microstructures are applicable for different tilted angle of glazing (with respect to the horizon), different orientation of facades, various locations and diverse climates.

The work for the present thesis was sorted into three categories: simulation to estimate the potential benefits of the proposed glazing, fabrication of samples, and experimental characterization.

Prior to the fabrication, ray-tracing simulation was used to optimize the geometrical parameters of the microstructures. Computer models were built for simulation, and the experimental validation was conducted for the computer models. The angular-dependent transmittance for glazing with various optical microstructures was calculated from ray-tracing simulation. The sensitivity of angular-dependent transmittance to the change of the height of microstructures was analyzed. Dynamic solar gains and the direct transmittance as function of working hours were calculated to evaluate the potential benefits. In order to fully explore the potential advantages in daylighting and glare protection, metrics based on illuminance, uniformity, glare and directivity were used for a south-facing façade equipped with the optical microstructures in Lausanne (46°30' N and longitude 6°37' E), Switzerland.

In order to redirect daylight as desired, high aspect ratio microstructures and microstructures with overhang were needed. However, the fabrication of such microstructures was challenging with the existing technique. At the lab scale, the procedures for the fabrication of embedded micro optics were sorted into five steps. First, master molds with various microstructures were fabricated by laser ablation. Alternatively, a novel mechanical engraving on soft materials (wax mixture in the present thesis) was developed for master mold fabrication. Secondly, one or two times replication using polydimethyl-siloxane (PDMS), with the induction of a hydroxypropyl-methyl

cellulose (HPMC) interlayer, were conducted to obtain the microstructures of either an identical or a contradictory shape to the master mold. At the third step, the PDMS mold was used as stamp for UV imprinting with a UV-curable polyester-acrylated hyperbranched polymer (HBP) on a glass substrate. Following that, the HBP microstructure on the glass substrate was used for thermal evaporation deposition, and the functional coating deposited on the selected surface. At the end, the grooves of microstructure with functional coating were filled with identical HBP again for UV-imprinting, and therefore, the embedded micro optics were achieved. The present thesis focuses on the feasibility for the fabrication of the mentioned microstructures above, development of novel processing methods and the shape fidelity of each fabrication step.

Structural characterization was conducted during the fabrication steps using conventional optical microscopy, confocal microscopy, and scanning electron microscopy (SEM). Concerning optical characterization, goniophotometer was used to evaluate the angular-dependent transmittance and the light-redirectability of the fabricated samples. Spectrometers were also used to obtain the reflectance and transmittance spectrum of the deposited thin films.

**Key words:** Multifunctional glazing, Optical microstructures, Functional coating, Seasonal thermal dynamics, Daylighting potential, Laser ablation, Mechanical scanning engraving, UV-imprinting.

# Résumé

L'utilisation des bâtiments vitrés est une tendance mondiale de l'architecture moderne. Cependant, le vitrage peut induire une grande perte thermique en hiver et augmenter la consommation d'électricité pour la climatisation en été. Les rayons solaires peuvent également provoquer un éblouissement.

Afin de résoudre ces problèmes, un nouveau vitrage multifonctionnel avec des microstructures optiques encapsulées dans une couche de polymère est proposé ; le but est d'améliorer le contrôle thermique saisonnier, l'éclairage naturel, la protection contre l'éblouissement et la visibilité. Cette couche de polymère est ensuite laminée sur une vitre. Le vitrage proposé repose sur la combinaison de la géométrie des microstructures et les couches optiques.

Selon la géométrie des microstructures, deux types de microstructures optiques sont suggérés et développés : i) microstructure optique rétro-réfléchissante en forme de «L», et ii) concentrateurs paraboliques de grandeur micrométrique. Les microstructures optiques suggérées sont applicables pour différents angles d'incidence par rapport à l'horizon, différentes orientations de façades, aux localisations variées et divers climats.

Les travaux de la présente thèse sont divisés en trois parties: simulation afin d'estimer les avantages potentiels du vitrage proposé, fabrication d'échantillons et caractérisation expérimentale.

Avant la fabrication, la simulation par tracée de rayons est utilisée pour optimiser les paramètres géométriques des microstructures. Des modèles de calcul sont développés pour la simulation et une validation expérimentale est effectuée. La transmittance dépendante de l'angle pour les microstructures optiques est calculé utilisant la simulation de « ray-tracing ». La sensibilité de la transmittance dépendante de l'angle par rapport à la hauteur des microstructures est analysée. Les gains solaires dynamiques et la transmittance directe en fonction des heures de la journée sont calculés afin d'évaluer les avantages thermiques potentiels. Afin d'explorer pleinement les avantages potentiels de l'éclairage naturel et la protection contre l'éblouissement, les indices sur l'éclairement lumineux, l'uniformité, l'éblouissement et directivité sont utilisés pour évaluer la performance d'une façade orientée au sud à Lausanne, Suisse, et équipée avec les microstructures

Pour rediriger la lumière de la manière désirée, des microstructures avec rapport hauteur/largeur élevé et des microstructures avec surplombs sont nécessaires. Malheureusement, la fabrication de telles microstructures reste difficile en utilisant les technologies existantes. En laboratoire, les procédures de fabrication des microstructures optiques encapsulées sont classées en cinq étapes. Tout d'abord, un moule avec les microstructures est fabriqué par ablation laser. Alternativement, une méthode de gravure à balayage mécanique sur matériaux

mous est développée. Ensuite, la forme du moule est répliquée une fois (négatif de la forme) ou deux fois (forme identique) afin d'obtenir les microstructures désirées. Cette réplication est effectuée en utilisant du polydiméthyl-siloxane (PDMS), avec l'introduction d'une intercouche d'hypermellose (HPMC). Pour la troisième étape, le moule de PDMS est utilisé comme tampon pour l'impression UV avec un polyester acrylate polymère hyper-ramifié (HBP) sur un substrat de verre. Après cela, les couches métalliques sont déposées par évaporation thermique sur les surfaces sélectionnées de la microstructure HBP. Pour finir, le même matériau (HBP) est utilisé pour remplir les rainures des microstructures avec les couches optiques pour l'impression UV, et par conséquent, les microstructures optiques enclavées sont obtenues. Cette thèse démontre la faisabilité de la fabrication des microstructures, développe les nouveaux procédés de traitement, et analyse la fidélité de forme de chaque étape de fabrication.

La caractérisation structurale est réalisée pendant les étapes de fabrication à l'aide de microscopie optique traditionnelle, microscopie confocale, et microscopie électronique à balayage (SEM). Concernant la caractérisation optique, un goniophotomètre est utilisé pour évaluer la transmittance dépendante de l'angle et la redirection de la lumière des échantillons fabriqués. Différents spectromètres sont utilisés pour obtenir le spectre de réflectance et de transmittance des couches déposés.

**Mots-clés:** Vitrages multifonctionnels, Microstructures optiques, Couches minces fonctionnelles, Dynamique thermique saisonnière, L'éclairage naturel, Ablation laser, Gravure à balayage mécanique, L'impression UV.

# Table of contents

Cover page .....	i
Acknowledgement .....	ii
Abstract .....	iv
Résumé .....	vi
Table of contents .....	viii
List of figures .....	xiv
List of tables.....	xxiv
List of acronyms .....	xxv
List of symbols .....	xxvi
<b>Chapter 1 Introduction.....</b>	<b>1</b>
1.1 Motivation.....	1
1.2 Approach.....	2
1.3 Thesis outline .....	2
<b>Chapter 2 State of the art .....</b>	<b>3</b>
2.1 Glazing with daylighting devices .....	3
2.1.1 Anidolic system .....	3
2.1.2 Mini-optical light shelf daylighting system .....	4
2.1.3 Laser cut panels .....	5
2.1.4 Blinds/Louvres.....	5
2.1.5 Aerogel.....	6
2.2 Glazing with controlled solar heat gain.....	7
2.2.1 Chromogenic glazing .....	7
2.2.1.1 Liquid crystal.....	7
2.2.1.2 Suspended particle devices .....	8
2.2.1.3 Electrochromic devices.....	8
2.2.1.4 Thermalchromic glazing.....	10
2.2.2 Fluid window .....	11
2.3 Microstructured glazing for combined solutions .....	12
2.3.1 Switchable prismatic glazing .....	12
2.3.2 Microstructured glazing with optically functional coatings.....	13
2.3.3 First generation of glazing with embedded micro mirrors.....	14
<b>Chapter 3 Glazing with novel embedded optical microstructures .....</b>	<b>16</b>
3.1 Research questions .....	16

3.2	Novel optical microstructures .....	17
3.2.1	Glazing with “L”-shape retro-reflective optical microstructure .....	17
3.2.2	Glazing with embedded micro compound parabolic concentrators .....	19
<b>Chapter 4</b>	<b>Methods of computer modeling and simulations .....</b>	<b>21</b>
4.1	Advanced optical ray tracing software CFSpro .....	21
4.1.1	Basic principles .....	21
4.1.2	Graphical User Interface .....	22
4.2	Computer modeling of glazing with embedded micro-mirrors for ray-racing simulation .....	23
4.2.1	Glazing with light-redirecting and retro-reflective micro mirrors .....	23
4.2.2	Glazing with embedded micro compound parabolic concentrators .....	26
4.2.2.1	Principle and assumption .....	26
4.2.2.2	Experimental validation of the computer modeling methodology .....	27
4.2.2.3	Investigated configurations .....	28
4.2.2.4	Sensitivity analysis .....	29
4.3	Angular-dependent transmittance .....	29
4.4	Specification of reference rooms .....	29
4.5	Simulation of seasonal thermal dynamics .....	30
4.5.1	Dynamic solar gains .....	30
4.5.2	Calculation of direct transmittance for Switzerland and Greece .....	30
4.6	Simulation of daylighting performance and visual comfort .....	31
4.6.1	Principles of RADIANCE software for daylighting simulation .....	31
4.6.2	Glazing configuration .....	31
4.6.3	Data collection and metrics .....	32
4.6.3.1	Steady and dynamic illuminance .....	32
4.6.3.2	Luminance ratio .....	33
4.6.3.3	Daylight Glare Index (DGI) .....	34
4.6.3.4	Vector-to-scalar illuminance ratio ( $E_v/E_s$ ) .....	35
<b>Chapter 5</b>	<b>Methods of sample fabrication and principles .....</b>	<b>37</b>
5.1	Laser ablation .....	37
5.1.1	KrF excimer laser .....	38
5.1.2	Machining mechanism .....	39
5.1.3	Ablation products and their kinetics during ablation .....	39
5.1.3.1	Ablation products: plume and debris .....	39
5.1.3.2	Impact of ramp angle on the distribution of debris .....	40
5.1.4	Ablation rate .....	41
5.1.4.1	Dependence on photon energy and fluence .....	41
5.1.4.2	Dependence on pulse number .....	42
5.1.4.3	Dependence on ambient atmosphere .....	42
5.1.5	Machine .....	43
5.1.6	Scanning mask projection laser ablation .....	45

5.1.6.1	Static projected ablation .....	45
5.1.6.2	Scanning ablation .....	45
5.1.7	Mask .....	46
5.1.8	Substrate.....	47
<b>5.2</b>	<b>Scanning mechanical engraving.....</b>	<b>48</b>
5.2.1	Engraving on flat substrates.....	48
5.2.2	Engraving on rolls.....	50
5.2.3	Design and fabrication of the blades.....	52
5.2.4	Materials .....	53
<b>5.3</b>	<b>Replication of microstructures.....</b>	<b>55</b>
5.3.1	Principles .....	56
5.3.1.1	Surface wetting physics .....	56
5.3.1.2	Under-liquid wetting dynamics for microstructured surface .....	57
5.3.1.3	Ultrasound-assisted wetting.....	58
5.3.2	Materials and Experiments .....	58
5.3.2.1	Materials and property.....	58
	PDMS .....	58
	Paraffin .....	59
	Beeswax .....	59
	HPMC .....	59
5.3.2.2	Replication procedures .....	59
	PDMS-PDMS .....	60
	PDMS-Wax.....	61
<b>5.4</b>	<b>Shape fidelity analysis during UV-printing .....</b>	<b>62</b>
5.4.1	Basics of Acrylated polyesters HBP .....	63
5.4.1.1	Polymerization reaction and kinetics.....	63
5.4.1.2	Viscosity .....	64
5.4.1.3	Shrinkage.....	64
5.4.2	Mechanics of materials .....	65
5.4.3	Parameters and experiments .....	65
5.4.3.1	Concentration of photoinitiator .....	65
5.4.3.2	Accelerated aging test.....	66
5.4.4	Equipment.....	67
5.4.5	Shape fidelity analysis .....	68
<b>5.5</b>	<b>Thin film deposition .....</b>	<b>69</b>
5.5.1	Principles and experimental setup .....	69
5.5.2	Facet-selective coating based on self-shadowing effects.....	70
5.5.3	Coating with post-polishing.....	71
5.5.4	Coating Materials.....	71
	Al .....	71
	Ag .....	71
	Indium tin oxide.....	71

<b>5.6</b>	<b>Roll-to-roll extrusion for upscaling .....</b>	<b>73</b>
<b>5.7</b>	<b>Characterization and measurements.....</b>	<b>74</b>
5.7.1	Structural characterization techniques .....	74
5.7.1.1	Optical microscope .....	74
5.7.1.2	Confocal microscope .....	74
5.7.1.3	Scanning electron microscope .....	74
5.7.2	Optical characterization .....	75
5.7.2.1	Spectrometers .....	75
5.7.2.2	Mini-goniophotometer .....	76
<b>Chapter 6</b>	<b>Simulation results and discussion.....</b>	<b>79</b>
<b>6.1</b>	<b>Angular-dependent transmittance from ray-tracing simulation .....</b>	<b>79</b>
6.1.1	Experimental validation of the computer model for ray-tracing simulation.....	79
6.1.2	Angular-dependent transmittance .....	80
6.1.2.1	Glazing with “L”-shape retro-reflective optical microstructure .....	80
6.1.2.2	Glazing with micro compound parabolic concentrators (CPCs) .....	81
6.1.3	Sensitivity analysis .....	84
6.1.3.1	Glazing with “L”-shape retro-reflective optical microstructure .....	84
6.1.3.2	Glazing with micro compound parabolic concentrators (CPCs) .....	85
<b>6.2</b>	<b>Seasonal thermal dynamics .....</b>	<b>88</b>
6.2.1	Dynamic solar gains.....	89
6.2.2	Direct transmittance during working hours .....	91
6.2.2.1	First case study .....	91
6.2.2.2	Second case study.....	92
<b>6.3</b>	<b>Simulation of daylighting performance and visual comfort.....</b>	<b>93</b>
6.3.1	Steady and dynamic illuminance .....	93
6.3.2	Luminance ratio .....	98
6.3.3	Daylight Glare Index .....	99
6.3.4	Vector-to-scalar illuminance ratio ( $E_v/E_s$ ) .....	102
6.3.5	Discussion.....	104
<b>Chapter 7</b>	<b>Experimental results and discussion .....</b>	<b>107</b>
<b>7.1</b>	<b>Laser ablation .....</b>	<b>107</b>
7.1.1	Curve sidewall grooves for micro CPCs.....	107
7.1.1.1	Curve side wall grooves at different scales for CPC(30, 30).....	107
	Static ablation .....	107
	Scanning ablation.....	109
	Quality analysis of the observed cross-sections.....	110
7.1.1.2	Curve sidewall grooves for CPC(40, 40).....	111
7.1.2	Sharp edges for micro CPCs .....	113
7.1.2.1	Dependence on repetition rate .....	113
7.1.2.2	Quality analysis of the observed cross-sections .....	116
7.1.3	High aspect-ratio triangular grooves for the retro-reflective microstructure .....	117



7.1.3.1	Static ablation with various ablation rates .....	117
7.1.3.2	Scanning laser ablation under various repetition rate .....	118
7.1.4	Feasibility of laser ablation .....	119
<b>7.2</b>	<b>Scanning mechanical engraving.....</b>	<b>121</b>
7.2.1	High aspect-ratio rectangle-like microstructure with parabolic side wall .....	121
7.2.2	Microstructures with overhang .....	124
7.2.2.1	Roughness .....	125
7.2.3	Engraving on wax cylinder roll.....	127
7.2.4	Summary of the engraving results .....	128
7.2.5	Comparison between laser ablation and mechanical engraving .....	128
<b>7.3</b>	<b>Replication of PDMS.....</b>	<b>131</b>
7.3.1	PDMS replicated from PDMS .....	131
7.3.2	PDMS replicated from wax .....	133
7.3.2.1	Flat wax substrates .....	133
7.3.2.2	Wax substrates with asymmetric CPCs .....	134
7.3.2.3	Wax substrates with retro-reflective microstructures .....	135
<b>7.4</b>	<b>Shape fidelity analysis during UV-imprinting.....</b>	<b>138</b>
7.4.1	Light-redirecting HBP microstructures with sharp edges.....	138
7.4.1.1	Impact of photoinitiator concentration .....	138
7.4.1.2	Impact of thermal aging.....	139
7.4.1.3	Impact on the redirection of daylight.....	140
7.4.2	Trapezoid-like HBP microstructures .....	142
7.4.3	Discussion.....	143
<b>7.5</b>	<b>Thin film deposition and optical properties.....</b>	<b>144</b>
7.5.1	Facet-selective coating based on self-shadowing effect .....	144
7.5.1.1	Results .....	144
7.5.1.2	Discussion .....	145
7.5.2	Feasibility of polishing after coating .....	146
7.5.2.1	Results .....	146
7.5.2.2	Discussion .....	147
7.5.3	Symmetric micro CPCs with various optical coatings.....	147
7.5.3.1	Aluminum coating .....	148
	Spectral direct transmittance of Al thin film.....	148
	Diffraction.....	149
	Angular-dependent transmittance .....	152
	Light redirection ability .....	153
7.5.3.2	Silver coating.....	155
	Spectral properties of Ag thin films .....	155
	Appearance and diffraction of encapsulated samples .....	156
	Angular-dependent transmittance of encapsulated samples.....	159
	Discussion.....	160
7.5.3.3	Indium tin oxide coating.....	160
<b>7.6</b>	<b>Roll-to-roll extrusion for upscaling .....</b>	<b>162</b>

<b>Chapter 8</b>	<b>Conclusions and outlook .....</b>	<b>164</b>
<b>8.1</b>	<b>Summary of the key achievements .....</b>	<b>164</b>
<b>8.2</b>	<b>Conclusions .....</b>	<b>165</b>
8.2.1	Simulation .....	165
8.2.2	Fabrications .....	166
8.2.2.1	Laser ablation .....	167
8.2.2.2	Engraving .....	167
8.2.2.3	Replications .....	167
8.2.2.4	UV-imprinting .....	167
8.2.3	Optical characterization .....	168
<b>8.3</b>	<b>Research outlook .....</b>	<b>168</b>
<b>Appendix A:</b>	<b>Mask openings for laser ablation .....</b>	<b>169</b>
<b>Appendix B:</b>	<b>Blades with micro asymmetric CPCs for engraving .....</b>	<b>172</b>
<b>Bibliography</b>	<b>.....</b>	<b>174</b>
<b>Curriculum Vitae</b>	<b>.....</b>	<b>185</b>

# List of figures

Figure 2-1. First design of an anidolic daylighting system: (a) dimensions of the zenithal collector; (b) ray tracing of diffuse daylight component through the system (Scartezzini and Courret, 2002). .....	4
Figure 2-2. Sketch of a light shelf installed over a double glazing view window and the related dimensions(Ochoa and Capeluto, 2006). .....	4
Figure 2-3. The Sketch (left) (Labib, 2013) of the cross-section of laser cuts and the view (right)(SOLARTRAN, 2018) seen through a laser cut panel prototype. ....	5
Figure 2-4. Ray tracing through louvers for varying incoming elevation angles(Thuot and Andersen, 2013). .....	6
Figure 2-5. Cross-sectional diagrams of a glazing unit with the louvre: (a) side view and (b) top view (Thuot and Andersen, 2011). .....	6
Figure 2-6. (a) The view seen through a aerogel prototype (b) and the application of erogel in skylights (Buratti and Moretti, 2012). .....	7
Figure 2-7. A SPD glazing at its on (a) and off (b) state(Ghosh, Norton and Duffy, 2016b). .....	8
Figure 2-8. Schematic of the layer structure of an electrochromic window (not to scale). The schematic is assumed for a cathodic material, e.g., tungsten oxide (Lampert, 2004). .....	9
Figure 2-9. Electrochromic windows controlled at different states (Jerod, 2018). .....	10
Figure 2-10. Thermochromic material below (a) and above (b) the transition temperature (Costanzo, Evola and Marletta, 2016). .....	11
Figure 2-11. Sketch of water flow circuits of the laboratory set-up (Chow and Li, 2013). .....	11
Figure 2-12. Systems with micro-prismatic arrays on both surfaces may significantly change their performance due to small profile variances, e.g., by vertical shifts $\Delta$ (Klammt, Neyer and Müller, 2012). .....	12
Figure 2-13. Cross sections of PDMS prototypes with structure dimensions of 250 $\mu\text{m}$ (Klammt, Neyer and Müller, 2012). .....	13
Figure 2-14. (a) SEM image of the prism array in polystyrene (PS). For indicating the self-shading effect for facet-selective coating,the red arrows show the incident angle of the direction of the vapor in the PVD process. (b) CPCs in PMMA. The “exit aperture” is coated with highly reflective thin film (Walze et al., 2005) .....	13

Figure 2-15. A computer model of the polymer layer with embedded micro-mirrors for ray-tracing simulation with the incident direct rays at the angle of 25° and 65° .....	15
Figure 3-1. A computer model of the polymer layer with embedded retro-reflective micro-mirrors for ray-tracing simulation with the incident direct rays at the angle of 30° (winter) and 70° (summer). .....	18
Figure 3-2. The examples and the design principle of compound parabolic concentrators: (a) symmetric compound parabolic concentrator, and (b) asymmetric compound parabolic concentrator.....	19
Figure 3-3. 2-D computer modeling and cross section of a double glazing with the embedded micro CPCs in a polymer layer. The incident angle of the incoming light are 25° and 65° respectively. ....	20
Figure 4-1. The graphical user interface of CFSpro. ....	23
Figure 4-2(a) Model of embedded micro-mirrors in a polymer layer for ray-tracing simulation in the present work; (b) simulated angular-dependent transmittance. The arrow is used to indicate the effective reduction of direct transmittance by the secondary mirrors at an incident angle of approximately 60° . ....	25
Figure 4-3. Coordinate systems for computer modelling of a compound parabolic concentrator unit. ....	27
Figure 4-4. The polystyrene foam support fabricated by hot wire cutting for parabolic reflectors .....	28
Figure 4-5. A typical example of the fish-eye view image for the calculation of luminance ratio on April 7th at 12:00 (GMT+2), where a large contrast of daylight distribution appears on the table for the room with the conventional low-e double glazing. ....	34
Figure 5-1. Impact of ramp angle on the distribution of debris on the ablated channel floor. ....	41
Figure 5-2. Ablation rate (ablation depth per shot) with the variation of fluence (Pedder and Holmes, 2006) . The measurement was conducted using KrF excimer laser on polycarbonate (PC). Solid lines are cubic polynomial fits to extended data sets; dashed lines are best-fit “Beer’s law” ablation curves. ....	42
Figure 5-3. The two KrF excimer laser systems and the movement directions indicated by the red arrows.....	44
Figure 5-4. . Left: The sketch of the configuration of the scanning excimer laser ablation and the resulting micro structure. From top to bottom: Excimer laser beam, projection mask, objective lens, polycarbonate substrate. Right: Top, side and front view of a single and multiple shot	

exposure of the mask pattern on the substrate. As long as the motion step, $s$ , of the substrate is shorter than that of the structure length, $L$ , the total dose on the longer part will be higher resulting in deeper structures (more ablated material).....	46
Figure 5-5. The sketch of the example computer design for the contours on a mask, and the resulting cross-sections with actual aspect ratio of the three types of micro structures. ....	47
Figure 5-6. Sketch of the process flow from scanning engraving to HBP microstructures on glass substrate. ....	49
Figure 5-7. (a) A schematic design of the head which is installed on a CNC machine with the blade. (b) The fabricated head based on the design .....	49
Figure 5-8. Engraving on wax cylinder. ....	51
Figure 5-9. The metal cylinder coated with wax. ....	51
Figure 5-10. Typical UV-LIGA process (Joye et al., 2010). ....	52
Figure 5-11. An example of a two-level photoplastic SU-8 microstructure after UV exposure. The microstructure is used for electroplating (Despont, 1997).....	52
Figure 5-12. The sketch of the cross-sections of the four microstructures on the blades.....	53
Figure 5-13. The hydrophilic and hydrophobic situations.....	57
Figure 5-14. Sketch of the possible wetting states on structured surface under water: (a) superhydrophobic state (Cassie & Baxter state), (b) superhydrophilicity state (Wenzel state), and (c) depinned metastable state. ....	57
Figure 5-15. The three investigated microstructures for the replication of PDMS from PDMS..	61
Figure 5-16. The monomer structure of the acrylated polyester hyperbranched polymer (Gonzales Lazo, 2015). ....	62
Figure 5-17. The sketch of UV curing process (Brilliant Universal Limited, 2012).....	63
Figure 5-18. Typical shapes of kinetic curves for the polymerization of a monomethacrylate monomer (Andrzejewska, 2001): a) polymerization rate as a function of irradiation time; b) conversion of double bonds as a function of time; and c) polymerization rate as a function of double bond conversion. ....	64
Figure 5-19. Conversion versus exposure time for polymerization of diacrylate monomer with different photoinitiator concentration, in the presence of 3 % (w/w) tertiary amine (triethyl amine) as synergist additive at 30°C (Macarie and Ilia, 2005). ....	66

Figure 5-20. Photograph of the UV light source for UV imprinting: (a) the UV LEDs with a light diffuser and (b) the controller to vary and UV intensity and the exposure time. ....	68
Figure 5-21. The configurations of the thermal evaporation chamber. ....	70
Figure 5-22. The self-shadowing effect of a microstructure for facet-selective coating. ....	70
Figure 5-23. The sketch of the extrusion procedures (Murthy et al., 2016). ....	73
Figure 5-24. Integrated sphere with the first and second opening. ....	75
Figure 5-25. The set-up for the measurement of direct spectral transmittance. ....	76
Figure 5-26. The set-up of the mini-goniophotometer. ....	77
Figure 5-27. The top view sketch (with respect to Figure 5-26 of the measurement principle for transmittance distribution and the total transmittance. ....	77
Figure 6-1. (a) The prototype of the milimetric CPC arrays placed between two glass panes, and (b) the measured and simulated angular-dependent transmittance at the azimuth angle of $0^\circ$ . ....	79
Figure 6-2. The simulated angular-dependent transmittance for conventional double glazing, low-e double glazing, and conventional double glazing with “L”-shape retro-reflective micro-mirrors (“RF” for this type of glazing) at the azimuth angle of $0^\circ$ . “ $T_{up}$ ” means transmittance due to upward redirected-redredirected light. The sketch of “L” shape microstructure embedded in the polymer layer is shown on the upper right of the figure. ....	80
Figure 6-3. The simulated angular-dependent transmittance for conventional double glazing, low-e double glazing, and conventional double glazing with symmetric CPCs at the azimuth angle of $0^\circ$ . The numbers in the brackets are the half acceptance angles of left and right parabolas. The sketch of micro CPCs embedded in the polymer layer is shown on the upper right of the figure. ....	82
Figure 6-4. The simulated angular-dependent transmittance for conventional double glazing, low-e double glazing, and conventional double glazing with asymmetric CPCs at the azimuth angle of $0^\circ$ . The sketch of asymmetric micro CPCs embedded in the polymer layer is shown on the upper right of the figure. ....	83
Figure 6-5. The profiles of angular-dependent transmittance as function of the height for glazing with with “L”-shape retro-reflective micro-mirrors. ....	84
Figure 6-6. The behavior of the incoming rays after interacting with the “L”-shape micro-mirrors of different heights. ....	85

Figure 6-7. The profiles of angular-dependent transmittance as function of the height for CPC(30, 30). .....	85
Figure 6-8. The profiles of angular-dependent transmittance as function of the height for CPC(80, 0). .....	86
Figure 6-9. An example of self-shadowed zone to the direct incoming light which is enclosed by the parabolic curve and the dash line. ....	87
Figure 6-10. (a) Annual heating demand weather and (b) annual cooling demand for weather files based on present (shaded) annual (dashed), monthly (solid) and hourly (dotted) changes (Cox, Rimante A., et al, 2015.). ....	89
Figure 6-11. Ratio of (a) transmitted-direct solar radiation, and (b) transmitted-diffuse solar radiation between glazing with the “L”-shape retro-reflective micro-mirrors (RF) and conventional double glazing (DG) in Lausanne. ....	89
Figure 6-12. Ratio of (a) transmitted-direct solar radiation, and (b) transmitted-diffuse solar radiation between glazing with the “L”-shape retro-reflective micro-mirrors (RF) and conventional double glazing (DG) in Athens. ....	90
Figure 6-13. The calculation of the direct transmittance during working hours (considered as 8:00 – 17:00) for the winter solstice, the spring equinox and the summer solstice, respectively, for the first case study.....	91
Figure 6-14. The calculation of the direct transmittance during working hours (considered as 8:00 – 17:00) for the winter solstice, the spring equinox and the summer solstice, respectively, for the second case study. ....	92
Figure 6-15. Fish-eye views seen from a working position with the distance of 8 m from the window show the illuminance of the office on the winter solstice at 12:00 (Greenwich Mean Time (GMT) + 2) in Lausanne: (a) reference room with the conventional low-e double glazing, (b) case of embedded micro-mirrors in the upper third of a low-e double glazing, (c) case of embedded micro-mirrors in the upper two-thirds of a low-e double glazing and (d) case of embedded micro-mirrors in the whole low-e double glazing. ....	94
Figure 6-16. Illuminance on the working plane for (a) standard CIE overcast sky, (c) standard CIE intermediate sky and (e) standard CIE clear sky with Sun at spring equinox solstice noon. (b), (d) and (f) show the corresponding illuminance for the region from 4 m deep to 8 m deep.96	
Figure 6-17. Annual average illuminance for working hours (8:00 – 18:00) for the center of the working plane along the depth of room. ....	97

Figure 6-18. The illuminance maps on April 7th at 12:00 (GMT+2) in Lausanne: (a) the case with conventional low-e double glazing, (b) the case of micro-mirrors in the upper third of the glazing, (c) the case of micro-mirrors in the case of micro-mirrors in the upper two-thirds of the glazing and (d) the case of micro-mirrors in the whole glazing. ....	98
Figure 6-19. Daylight Glare Index sorted in three ranges: acceptable, unacceptable and intolerable. ....	100
Figure 6-20. The plots of hourly Daylight Glare Index (DGI) values: a) on the spring equinox, and b) on the winter solstice at the employee's position. ....	101
Figure 6-21. The plots of hourly Daylight Glare Index (DGI) values: a) on the spring equinox, and b) on the winter solstice at the guest's position. ....	101
Figure 6-22. The vector-to-scalar illuminance ratios ( $E_v/E_s$ ) along the depth of the room for different working hours on the spring equinox in Lausanne. ....	103
Figure 6-23. Percentage of the vector-to-scalar illuminance ratios ( $E_v/E_s$ ) falls in the preferred range, acceptable or harsh range for different time on the spring equinox in Lausanne. ...	103
Figure 7-1. The top-view microscope images of the three elongated triangular mask openings for the CPCs on a PC substrate.....	108
Figure 7-2. The cross-sections of the CPCs for A, B, and C on PC substrates. ....	109
Figure 7-3. The profiles of the fabricated grooves extracted from the microscope images and the theoretical design. ....	110
Figure 7-4. Computer model with extracted profile of the theoretical design for ray-tracing simulation; (b) calculated angular-dependent transmittance at the azimuth angle of $0^\circ$ . ....	111
Figure 7-5. (a) the top-view microscope images of the elongated triangular-like mask openings for the CPC(40, 40) on a PC substrate, coupling with the profile (upper part of Figure 6-5 (a)) of the ablated depth along the length of the projected mask opening, under static ablation; (b) the cross-section of CPC(40, 40) under scanning ablation. ....	112
Figure 7-6. The comparison of the extracted contours of theoretical design and the obtained microstructures on the PC substrate.....	113
Figure 7-7. The elongated mask opening (the darker part) projected on the PC substrate under static ablation for 2 pulses. ....	114
Figure 7-8. The PDMS microstructures replicated from the microstructure on PC substrate under 50 Hz repetition rate, and the cross-sections of the UV-cured polymer microstructures imprinted by the PDMS microstructures at two different regions. ....	114



Figure 7-9. (a) The PDMS mold replicated from the microstructure on PC substrate, and (b) the cross-section on PC substrate under the scanning ablation with 20 Hz repetition rate. ....	115
Figure 7-10. The profiles of the fabricated grooves extracted from the microscope images for the case of 20 Hz and 50 Hz, and the theoretical design. ....	116
Figure 7-11. The sketch of the two scanning direction: the present (false) direction and the preferred (correct) direction. The dash contours represent the projected mask opening from next pulse. ....	117
Figure 7-12. The top-view microscope images of the elongated triangular mask openings for the “L”-shape microstructure on a PC substrate. ....	118
Figure 7-13. The cross-sections of the resulted microstructure on the PC substrates under scanning laser ablation with the two repetition rates: (a) 50 Hz, and (b) 200 Hz. ....	119
Figure 7-14. A sample with microstructures of aspect ratio of 3.8 on the paraffin-based substrate. The sample is observed lower than (a) 25° and higher than (b) 60° with respect to the normal to the surface. ....	121
Figure 7-15. The cross-sections of the microstructures on the blade A and B and their corresponding HBP microstructures. ....	122
Figure 7-16. The simulated angular-dependent transmittance for blade A and B and their corresponding HBP microstructures. ....	124
Figure 7-17. An UV-cured polymer microstructure with overhang replicated from the engraved wax substrate. ....	124
Figure 7-18. The cross-sections of the the microstructure on blade C and D and the corresponding HBP microstructure D. ....	125
Figure 7-19. Roughness profile of the bottom platform (as marked in Figure 7-18) of the HBP microstructure D replicated from wax substrate with 5% beeswax and 20% beeswax. For each case, the upper graph shows the top view of the bottom channel, and the lower graph shows the roughens profile along the scan. The roughness profile is taken using a confocal microscope. ....	126
Figure 7-20. The swarf from the peel-off surface of the wax substrate with 5% beeswax .....	127
Figure 7-21. A sample engraved with blade A on wax cylinder roll with 5% beeswax. ....	127
Figure 7-22. A sample engraved with blade A on wax cylinder roll with 20% beeswax. ....	128

Figure 7-23. The three status of the PDMS mold: (a) before immerse liquid with the sketch of the cross-section, (b) during the pouring of 0.5% HPMC solution, (c) 30 S after being immersed under the 0.5% HMPC solution. ....	131
Figure 7-24. The appearance of the 1 <sup>st</sup> CPC(30, 30) PDMS microstructures coated with HPMC of the three concentrations, and the resulted 2 <sup>nd</sup> PMDS. ....	132
Figure 7-25. The appearance of the 1 <sup>st</sup> CPC(40, 40) PDMS microstructures coated with HPMC of the three concentrations, and the resulted 2 <sup>nd</sup> PMDS. ....	133
Figure 7-26. The top view of the macroscopic appearance of the PDMS mold and the zoom-in image from the optical microscope. ....	135
Figure 7-27. The HBP microstructures replicated from the PDMS mold with and without wax residual. The cross-sectional images are taken using the confocal microscope. ....	135
Figure 7-28. The top view of the macroscopic appearance of the PDMS mold. ....	136
Figure 7-29. The cross-sectional morphology of (a) microstructures in the region where straight and regular lines appear when observed from the top; and (b) microstructures in the region where the wave-like appearance is observed. ....	137
Figure 7-30. An example of the light-redirecting HBP microstructures with sharp edges and the measured parameters. ....	138
Figure 7-31. Dimensional changes with the variation of the concentration of the photoinitiator. ....	139
Figure 7-32. Dimensional changes as functions of exposure time under accelerated aging at 80°C. ....	140
Figure 7-33. (a) extracted micro-mirrors profiles (points) and corresponding quadratic fits; (b) ray-tracing analysis of model parabolic micro-mirrors embedded in a polymer layer with refractive index of 1.495 showing direct-transmitted rays and reflected rays; (c) total transmittance ( $T_{tot}$ ) and transmittance of redirection ( $T_{up}$ ) as a function of incident angle at normal incidence; (d) derivatives of the polynomial fits as functions of the height of parabolic surfaces. ....	141
Figure 7-34. Trapezoid-like HBP Microstructures of two different aspect-ratio: CPC (30, 30) and CPC (40, 40). The photonitiator is 6 wt%. ....	143
Figure 7-35. An example of a polymer layer with embedded parabolic micro-mirrors observed by scanning electron microscope. ....	144

Figure 7-36. Sketch of the key components and dimensions for the facet-selective coating based on self-shadowing effect in the thermal evaporation chamber. ....	145
Figure 7-37. Optical microscope image of the cross-section of the HBP microstructure which was used for the polishing test. ....	146
Figure 7-38. Optical microscope images (top view) for the evolution of the microstructures and the coated surface at the beginning, the mid and the finishing status of the polishing.....	147
Figure 7-39. Spectral characteristics of direct transmittance of Aluminum thin films with various thicknesses. ....	149
Figure 7-40. Diffraction phenomenon when the edge of a computer screen is seen through sample 52-36. The numbers “52” and “36” stand for the nominal thin film thickness of the two side walls for a micro CPC.....	149
Figure 7-41. Diffraction effect identified by a red laser beam. The numbers “52” and “36” stand for the nominal thin film thickness of the two side walls for a micro CPC.....	151
Figure 7-42. Side fringes due to the interference of the redirected light by parabolic reflective surface with (a) 50-nm Aluminum thin film and (b) 11-nm Al thin film. ....	151
Figure 7-43. Views seen through the samples with various thicknesses of the Aluminum thin films. The numbers in the name of a sample, stand for the thickness of the nominal thin film thickness of the two side walls for a micro CPC. ....	151
Figure 7-44. Angular-dependent total transmittance with respect to various incident angles for samples with aluminum coating. The measurement is conducted by minigonio-photometer, and the measuring procedure is described in the section 5.7.2.2. ....	152
Figure 7-45. Normalized intensity distribution of the transmitted light for the three samples with Al thin films encapsulated. The incident angle is at the normal incidence.....	153
Figure 7-46. Distribution of the transmitted light at the incident angle of 55° for the sample CPC (50, 11). ....	154
Figure 7-47. Example paths along which the light goes through the polymer layer with embedded CPC for (a) the case where the incident light is first redirected by the 11-nm thick Al coating (represented by the red curves), and (b) by the 50-nm Al coating (represented by the purple curves). The example paths are indicated by blue dash lines. ....	154
Figure 7-48. Spectral characteristics of Silver thin films with various thicknesses measured by spectrometer with integrated sphere. ....	156
Figure 7-49. The appearance of the encapsulated samples. ....	157

Figure 7-50. The sketch of the light path (indicated by gray arrows) coming to observer's eyes for a) incoming light at normal incidence, and b) incoming light at high incident angle. ....	157
Figure 7-51. The blue appearance of the sample 10-10 when it is viewed at higher incident angle. .....	158
Figure 7-52. View see through the samples. In the reference case, the view is directly seen through a conventional double glazing without a sample. ....	158
Figure 7-53. Angular dependent transmittance with respect to various incident angles for samples with silver coating). The measurement is conducted using the mini-goniophotometer. ....	159
Figure 7-54. The as-deposited ITO thin film on a glass substrate and ITO thin film after annealing at 490°C for 1h. ....	161
Figure 7-55. Direct transmittance as function of wavelength for the as-deposited and annealed ITO thin film on glass substrates. ....	161
Figure 7-56. The cross-sectional optical microscope images of the two microstructures fabricated by roll-to-roll extrusion. The embedded small images are the cross-sections of the microstructures on the master molds fabricated by laser ablation. ....	162
Figure 8-1. Fabrication flow of samples in the lab. ....	166
Figure A-1. The mask opening of the rectangle-like microstructures for “L”-shape optical microstructures at different aspect ratio. The periodicity for such mask openings are 35 $\mu\text{m}$ , 50 $\mu\text{m}$ and 75 $\mu\text{m}$ . Unit for the numbers in the graph: $\mu\text{m}$ . ....	169
Figure A-2. The mask opening of the sharp edges for micro CPC(30, 30). On the mask there are also mask opening of the same shape with the periodicity of 50. Mask opening for sharp edges for micro CPC(40, 40) is aslo on the mask, and the critical geometrical parameter is presented in Table 4-2. Unit for the numbers in the graph: $\mu\text{m}$ . ....	170
Figure A-3. Mask openings for curve-sidewall grooves for micro CPC(30, 30). On the mask there are also mask opening of the same shape with the periodicity of 50. Mask opening for curve- sidewall grooves for CPC(40, 40) is aslo on the mask, and the critical geometrical parameter is presented in Table 4-2. ....	171
Figure B-1. Blade with micro asymmetric CPC(50, 0). ....	172
Figure B-2. Blade with micro asymmetric CPC(65, 0). ....	173

# List of tables

Table 3-1. Configurations of coating materials for the “L” – shape optical microstructures and the resulting functions.....	18
Table 4-1. Parameters of embedded micro-mirrors for simulation.....	25
Table 4-2. Summaries of the parameters to define a CPC unit.....	28
Table 4-3. Radiance parameters used for the calculation of view (V) matrix and daylight (D) matrix. ....	33
Table 4-4. Criteria of Daylight Glare Index.....	35
Table 5-1. The characteristics of polycarbonate .....	47
Table 5-2. Mechanical properties of wax. ....	54
Table 6-1. The seasonal percentage of the diffuse and direct radiation for both horizontal and vertical south-oriented façade in Lausanne (46.5° N) .....	88
Table 6-2. The seasonal percentage of the diffuse and direct radiation for both horizontal and vertical south-oriented façade in Athens (38° N) .....	88
Table 7-1. Average ablation rate as function of repetition rate under static ablation with 20 pulses. ....	118
Table 7-2. The feasibility and the key impact factors of the fabrication for the three types of microstructures using laser ablation.....	120
Table 7-3. The ease of demolding and curing level for the replication of PDMS from wax substrates with different beeswax concentration but no engraved microstructures, for various HPMC concentrations. ....	134
Table 7-4. Operating parameters for Aluminum coating with different thickness by physical vapor deposition. The values of the thickness are read from the monitor, i.e., nominal thickness. ....	148
Table 7-5. Operating parameters for six silver thin films of different thickness for three samples with embedded CPC arrays. The values of the thickness are read from the monitor. ....	155
Table 8-1. The suggested applications and the corresponding configurations of the proposed glazing.....	164
Table 8-2. The advantages and disadvantages of the proposed glazing .....	164

# List of acronyms

Ag	silver
Al	aluminum
AR	aspect-ratio
BTDF	bidirectional transmission distribution function
CPCs	compound parabolic concentrators
CNC	computer numeric control
DGI	daylight glare index
EDM	electrical discharge machining
EV/ES	Vector-to-scalar ratio
GUI	graphical user interface
H	height
HPMC	hydroxypropylmethylcellulose
HBP	hyperbranched polymer
ITO	indium tin oxide
LCP	laser cut panel
MS <sub>1/3</sub>	micro-mirrors in the upper third of the glazing
MS <sub>2/3</sub>	micro-mirrors in the upper two-thirds of the glazing
MS <sub>full</sub>	micro-mirrors in the whole glazing
P	period
PI	photoinitiator
PDMS	polydimethylsiloxane
PDLC	polymer dispersed liquid crystal
RP	rate polymerization
RF	conventional double glazing with "L"-shape retro-reflective microstructure
SHGC	solar heat gain coefficient
SG	conventional low-e double glazing
SPD	suspended particle device
UV	ultraviolet
UV-LIGA	ultraviolet-lithographie, galvanoförmung und abförmung
UDI	useful daylight illuminance
W	width
W <sub>1/2</sub>	width at mid height

# List of symbols

$\alpha$	half acceptance angle for the right parabola of a compound parabolic concentrator
$\beta$	half acceptance angle for the left parabola of a compound parabolic concentrator
$k$	sky patch index
$L_{ed,k,t}$	diffuse radiance for a given patch
$E_{eb,t}$	direct solar irradiance for a given time step
$\nu_{d,k}$	transmittance coefficient
$Q_t$	dynamic solar gains through a glazing at time step t
$\tau_{b,t}$	energy transmittance for the direction corresponding to the sun position at a given time step
$t$	time step t
V	view matrix
T	transmission matrix
T	Transmittance
D	daylight matrix
S	sky matrix
$L_{s,i}$	luminance of a glare source ( $i$ ) in the field of view
$\Omega_{s,i}$	solid angle subtended by the source
$L_b$	luminance of the visual field excluding the glare sources
$\omega_{s,i}$	solid angle subtended by the glare source.
$d$	ablation rate
$\alpha_{\text{eff}}$	effective absorption coefficient
$F$	fluence
$F_{th}$	threshold fluence
$\vartheta$	ramp angle
$d_{tot}$	total ablated depth

$L$	length of the irradiated spot
$\alpha_p$	absorption coefficient of the vapor plume
$f$	repetition rate
$\gamma$	interfacial tension
$\theta$	contact angle
$\lambda$	wavelength



# Chapter 1 Introduction

## 1.1 Motivation

A field study reported that the cooling systems alone of UAE buildings consumed about 60% – 75% of the total building electricity consumption (Radhi, 2009). The energy consumptions for heating and cooling accounts for 48% of total energy consumption in a residential building in US (EIA-U.S. Energy Information Administration, 2018). For highly glazed buildings, glazing accounts for large amount of solar heat gain. Large solar gain can provide free heat in winter. However, it can also cause overheating in summer, resulting in increased cooling load. For glazing with steady solar heat gain coefficient (SHGC), a careful optimization must be conducted to balance the solar heat gain and overheating. Glazing with (seasonal) dynamic solar heat gain coefficients, i.e, high SHGC in winter and low SHGC in summer, is desired and can be effective to reduce considerable energy consumption by buildings.

It was reported that, in a commercial building in Switzerland in 2015, the average consumption of electricity in lighting is 24% (Bundesamt für Energie Bern, 2016). Daylighting is considered as good alternative to artificial lighting, and it is defined as the use of controlled daylight admitted into a building to reduce electricity consumption in lighting. It was reported that daylighting provides more pleasant and attractive indoor environment, improving student performance and health in schools (Chang and Chen, 2005; Shin, 2007; Demir and Necdet Konan, 2013). Simulation analysis as well as field-monitoring studies show that daylighting controls can result in significant lighting energy savings ranging from 30% to 77% (Hee *et al.*, 2015).

However, more daylight permitted to enter into a room may raise the concern about glare and visual discomfort due to non-homogenous distribution of daylight. In order to avoid glare, people usually pull the window blinds down. However, the blinds significantly reduce the illuminance level of daylight (Huang, Niu and Chung, 2014). What is worse is that, people often leave the blinds down for days, months or even years (Rea, 1984). Therefore, advanced glazing systems are desired; they will provide daylighting as well as glare protection, improve visual comfort and eliminate inappropriate use of blinds (and or other shading devices).

A glazing is expected to have at least 30-years lifetime (Citherlet, Di Guglielmo and Gay, 2000). The device integrated with a glazing should also cover similar life span and be at low maintenance during this period. The advantage of glazing allows the visual connection between indoor and outdoor environment. Therefore, it is preferred that the device offers a clear view through glazing.

In the past years, various advanced glazing systems have been developed, and these systems will be present in more details in chapter 2. However, the systems, which meet all the expectations mentioned above, are currently very limited.

## **1.2 Approach**

A novel multifunctional glazing with embedded optical microstructures is proposed. The glazing consists of a polymer layer with embedded optical microstructures, the polymer layer being laminated with a glass pane. The proposed system is based on the combination of optimized microstructures and optical coating. According to the geometry of the microstructures, two types of embedded optical microstructures are originally suggested and developed: i) “L”-shape retro-reflective optical microstructure, and ii) micro compound parabolic concentrators (symmetric and asymmetric). Generally speaking, the microstructures consist of a light-redirecting part and a light-blocking part. In winter, where the solar elevation angles are low, the incident light going through the proposed glazing will be redirected by the light-redirecting microstructures and then transmitted in to an interior space. In contrast, in summer where the solar elevation angles are high, the incident light is blocked by the blocking microstructures and then reflected back to the exterior space. Thanks to the selected geometries, glazing with embedded optical microstructures can have seasonal dynamics of solar heat gain coefficient, and provide daylighting, resulting in the reduction of CO<sub>2</sub> emission. The proposed glazing can also provide glare protection. Moreover, because of the micrometric size of the optical structure and the flat surface of the polymer film, a clear view is remained from the conventional glazing. The combination of various microstructures with different optically functional coatings enable the proposed glazing system to adapt to diverse facade orientations, tilted glazing angles with respect to the horizon, locations, and climates.

## **1.3 Thesis outline**

Chapter 2 reviews the previous state-of-the-art glazing systems, analyzing the working principles, advantages and well as the drawbacks. In chapter 3, a multifunctional glazing with embedded optical microstructures is proposed. Two types of novel microstructured geometries are suggested. For the suggested microstructure geometries, simulation was conducted to estimate the potential benefit. The samples were fabricated, and structural as well as optical characterization were carried out. In chapter 4, the simulation methods are presented, while both the experimental methods and characterization methods are introduced in chapter 5. In chapter 6, the corresponding simulation results are shown and discussed. The results of fabrication and characterization are presented and discussed in chapter 7. At the end, the main achievements and the outlook of future work are summarized in chapter 8.

# Chapter 2 State of the art

In this chapter, the state of the art of the existing techniques for advanced glazing will be reviewed. Based on the major functions of the techniques, they are sorted into three group: a) glazing with daylighting devices, b) glazing with controlled solar heat gain and c) microstructured glazing for combined solutions (daylighting, seasonal thermal control and clear view). The working principles of the existing techniques, the advantages as well as the drawbacks up to today will be analyzed.

## 2.1 Glazing with daylighting devices

It is shown that, proper usage of daylighting in offices can reduce the total electricity consumption in conventional office buildings by as much as 25–30%, leading to the reduction of CO<sub>2</sub> emission (Gago *et al.*, 2015). Moreover, daylight may bring benefits on both the physical and psychological health of humans (Demir and Necdet Konan, 2013). Various daylighting devices integrated with glazing have been developed over the last several decades and will be presented in this section.

### 2.1.1 Anidolic system

Non-imaging optics, which is commonly used for solar concentrators, can also be used for novel daylighting systems to efficiently collect and redistribute the diffused daylight. These devices are called anidolic systems. A well-studied anidolic system (Scartezzini and Courret, 2002) had been developed at Solar Energy and Building Physics Laboratory (LESO-PB), Swiss Federal Institute of Technology in Lausanne (EPFL). The sketch of the anidolic system with the dimension of the zenithal collector is shown in Figure 2-1. The zenithal anidolic collector is made of two different compound parabolic concentrators (CPCs). One serves as external zenithal collector, and the other one is used as internal daylight projector. Therefore, the anidolic system can angularly select the admitted light rays and diffuse daylight are collected with the minimal number of reflections (Scartezzini and Courret, 2002). It has been experimentally demonstrated that the anidolic daylighting system was able to increase the illuminance level at the rear part of a room while reducing the illuminance level near windows, reducing energy consumption in lighting, improving the visual comfort in an indoor environment (Wittkopf, Yuniarti and Soon, 2006; Wittkopf, 2007). However, the installation of an external anidolic collector which varies in size from 0.5 to 1 m long can be an architectural challenge.

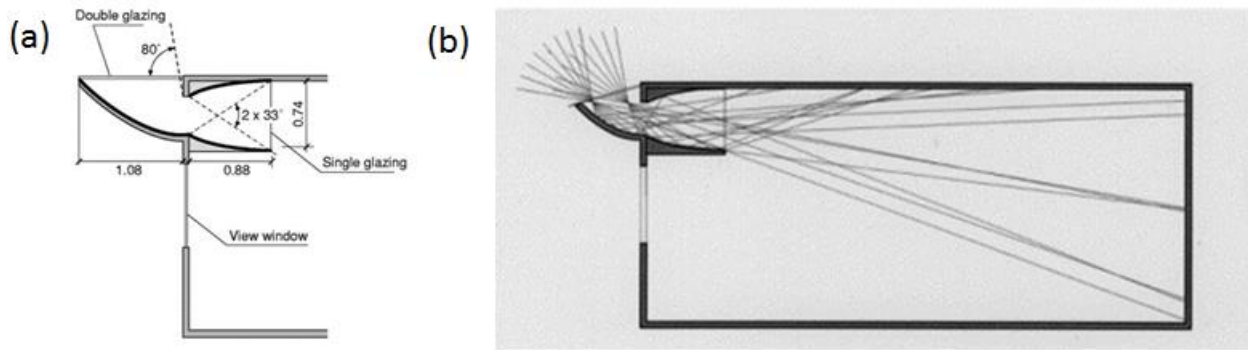


Figure 2-1. First design of an anidolic daylighting system: (a) dimensions of the zenithal collector; (b) ray tracing of diffuse daylight component through the system (Scartezzini and Courret, 2002).

## 2.1.2 Mini-optical light shelf daylighting system

The lightshelf (Freewan, 2010) is a horizontal or an inclined plane projected over a view window. Fig. shows a typical lightshelf and its dimensions (Ochoa and Capeluto, 2006). A light shelf is used as shading device to prevent direct sun light from entering a room, thus reducing glare and heat gain. It is also used as a daylighting system to improve uniformity and reflect light deep into the interior of a room. The direct sun light will be received by light shelf, and is reflected to the ceiling and from there to the back of the room. Therefore, location, the dimensions and reflectance of a light shelf, surface reflectance of a room and ceiling geometry have important impact on the performance of the light shelf.

However, similar to the anidolic system, the installation of an external lightshelf which varies in size going from 0.5 to 1 m long can be an architectural challenge. Moreover, it was reported that in order to make the redirected daylight reach the deep into room (e.g., distance greater than 4-m from the window), a curved ceiling was preferred (Freewan, Shao and Riffat, 2008; Freewan, 2010).

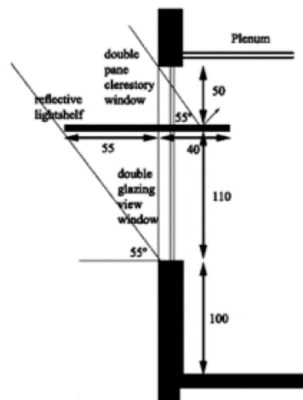


Figure 2-2. Sketch of a light shelf installed over a double glazing view window and the related dimensions (Ochoa and Capeluto, 2006).

### 2.1.3 Laser cut panels

A laser cut panel (LCP) is a thin transparent acrylic panel having parallel cuts made by laser cutting machine (Labib, 2013). The acrylic panel normally has the thickness of 2 - 20 mm. Usually, the laser-cut panel is placed between two glass panes of a double glazed window. Because of the refraction of light, the surface of each laser cut works as an internal mirror that deflects light passing through the panel. LCP is cost-effective, and it is relatively easy to fabricate and install, requiring low maintenance. However, the cuts will obstruct the view through a LCP. Moreover, in order to more effectively redirect the sunlight to the deep part of an interior, it is preferred to install a LCP at a tilted position with respect to vertical window.

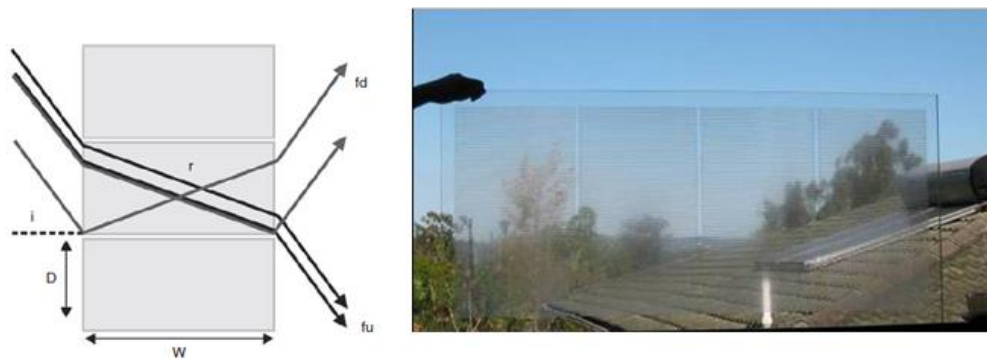


Figure 2-3. The Sketch (left) (Labib, 2013) of the cross-section of laser cuts and the view (right)(SOLARTRAN, 2018) seen through a laser cut panel prototype.

### 2.1.4 Blinds/Louvres

A new passive Louver-Based Daylighting System (Thuot and Andersen, 2013) was developed and patented in 2013. As shown in Figure 2-4, the system includes three parts: (i) a leading edge defined by a parabolic concentrator surface and a flat surface; and (ii) a trailing edge consisting of a lower compound parabolic concentrator profile, and an upper compound parabolic concentrator profile (iii) refractive rods used to diffuse light in the azimuth direction. Figure 2-5 shows the cross-sectional diagrams of the glazing with the louvre from side view and top view (Thuot and Andersen, 2011). Light enters the louvre array through a skyward tilted compound parabolic concentrator, and is guided there through to the deeper part of a room for daylighting. Moreover, it can prevent direct sun from coming to the interior of a room. However, similar to other louvres, the system is vulnerable to mechanical damage due to the plurality of movable slats, leading to difficulty in maintenance, especially for the louvre system installed in a double glazing. The view through the system is also obstructed.

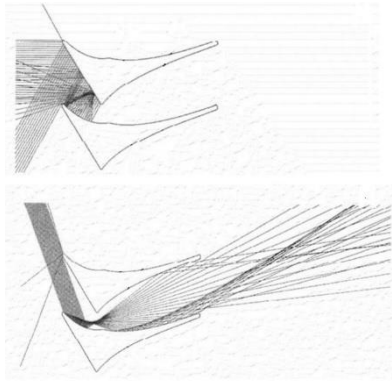


Figure 2-4. Ray tracing through louvers for varying incoming elevation angles(Thuot and Andersen, 2013).

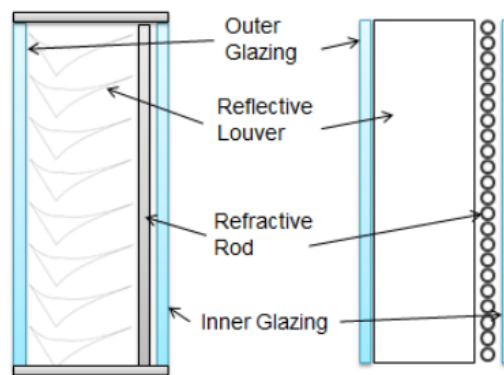


Figure 2-5. Cross-sectional diagrams of a glazing unit with the louver: (a) side view and (b) top view (Thuot and Andersen, 2011).

### 2.1.5 Aerogel

Silica-based aerogels have low thermal conductivity. For example, monolithic aerogel glazings can achieve U-values lower than  $0.5 \text{ W m}^{-2} \text{ K}^{-1}$  (Buratti and Moretti, 2012). By comparison, a typical low-e double glazing has a thermal conductivity of 1.0. Aerogels are light-weight and can be sandwiched between sheets of glass or plastic to provide good insulation. This glazing can be used in existing and new residential and commercial buildings. Usually, aerogel glazing can be used as skylight or roofing materials to enlarge the sector for daylight transmission, thus improving the daylighting illuminance level while keep good insulation in a room. However, aerogel panes showed the scattering of the light, which decreases the optical quality of vision through the material.

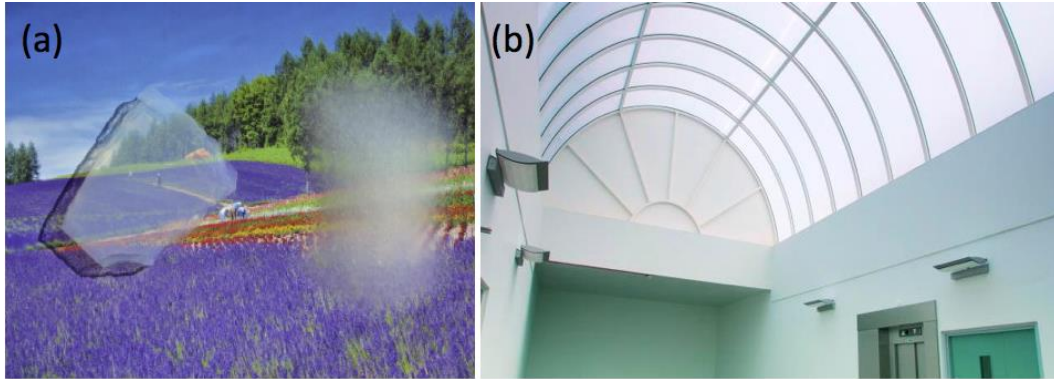


Figure 2-6. (a) The view seen through a aerogel prototype (b) and the application of aerogel in skylights (Buratti and Moretti, 2012).

## 2.2 Glazing with controlled solar heat gain

It was reported that around 30–40% of the world primary energy consumption by buildings for heating, cooling, and ventilation to maintain indoor thermal comfort (Waqas and Ud Din, 2013; Ghosh, Norton and Duffy, 2016a; Lei, Yang and Yang, 2016). A way to improve the thermal efficiency of building and reduce the CO<sub>2</sub> emission is to control admitted solar radiation through building envelopes. Glazing with dynamic solar heat gain coefficient (called dynamic g-value) can contribute to controlled admitted solar radiation. In the following sections, two types of glazing technologies with dynamic g value, namely chromogenic glazing and fluid glazing, are introduced.

### 2.2.1 Chromogenic glazing

#### 2.2.1.1 Liquid crystal

Polymer dispersed liquid crystal (PDLC) films (Park and Hong, 2009) have academic and industrial interest in the past decades. A PDLC film composes of liquid crystal microdroplets dispersed in a polymer matrix. It is considered as electro-optical system. Its transparent state can be switched on by applying an electric field from a scattering OFF state. In the off state, the device appears translucent white which can cause haziness, as the microdroplets scatter light rather than absorb light. When an electric field is applied, the microdroplets align with the field and the device becomes transparent. Usually, these devices operate between 24 and 100 V of alternative current and the power consumption is less than 5 W/m<sup>2</sup> (Lampert, 2003). However, they require continuous power to maintain the transparent state. In general, compared to electrochromic glazing which will be introduced in the following section, the power consumption for liquid crystals is higher due to the need of continuous power in the transparent state. The typical integrated hemispherical visible transmission values for a PDLC device are off–on = 50–80% (Lampert, 2003). The visible transmittance of the translucent state is in the order of 50%, which is enough in

some situations to reduce the cooling load. Moreover, a PDLC glazing is either transparent or opaque with no in-between, and this two-state characteristic constrains its application.

### 2.2.1.2 Suspended particle devices

A suspended particle device (Ghosh, Norton and Duffy, 2016b; Ghosh and Norton, 2017) composes of suspended particles which are induced dipoles when an electric field is applied. A suspended particle device (SPD) glazing is shown in Figure 2-7. The active layer has particles of dihydrocinchonidine bisulfite polyiodide suspended in an organic fluid or gel laminated or filled between two electrical conductors (Barrios Ricardo; Sanchez-Pena, Jose M.; Granqvist, Claes G.; Niklasson, Gunnar A., 2013; Ghosh, Norton and Duffy, 2016b). In a SPD glazing, the SPD material is sandwiched between two glass panes. Without applied voltage, particles are suspended randomly and absorb light. In the presence of alternative supply, particles are aligned perpendicularly to the charged plates. It was reported that the transmission of SPD window ranges from 5% to 55% and the typical switching speeds were 100–200 ms.

A SPD glazing also has some advantages over LC glazing. First, since the suspended particles absorbs the light instead of scattering the light, in “transparent” state, there is no haze like LC. Secondly, it has intermediate states between “opaque” and “transparent”. However, similar to LC glazing, the suspended particles devices require continuous power to maintain the transparent state and needs more energy than the electrochromic glazing.

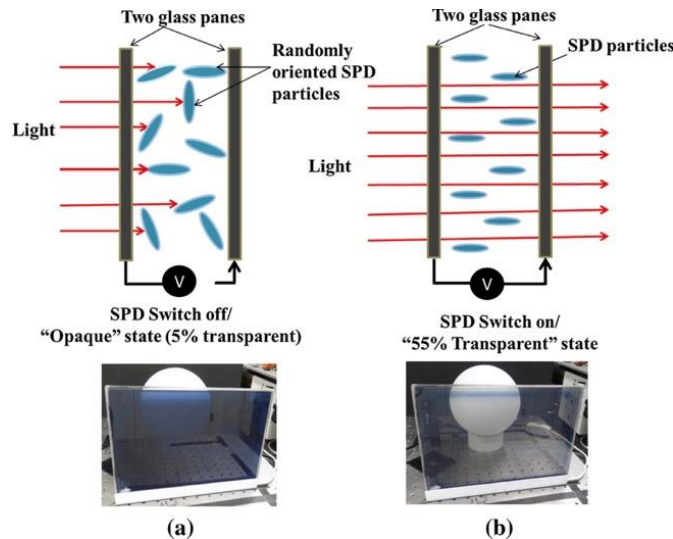


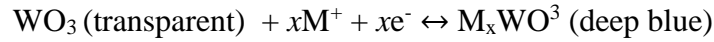
Figure 2-7. A SPD glazing at its on (a) and off (b) state (Ghosh, Norton and Duffy, 2016b).

### 2.2.1.3 Electrochromic devices

Electrochromism is the property of a device to change its optical properties reversibly if an external potential is applied, associated with ion insertion and extraction processes (Baetens, Jelle and Gustavsen, 2010). In tungsten oxide  $WO_3$  thin films, the electrochromic phenomenon of



materials was originally discovered. By far, it is still most used electrochromic material in electrochromic devices. Despite of its complexity, the electrochromism of tungsten oxide may be represented by the simple reaction:



Other interesting electrochromic binary inorganic oxides are NiO, IrOx, V<sub>2</sub>O<sub>5</sub>, and MoO<sub>3</sub>. Besides the metal oxide films there are also polymer films with electrochromic property. However, most of them show UV degradation which limit their applications in exterior smart glazing for energy saving.

The structure of an electrochromic glazing, in brief, can be represented as multilayers which consist of two transparent conductor oxides, an ion conductor or an electrolyte, an ion storage layer, and an electrochromic layer, as shown in Figure 2-8.

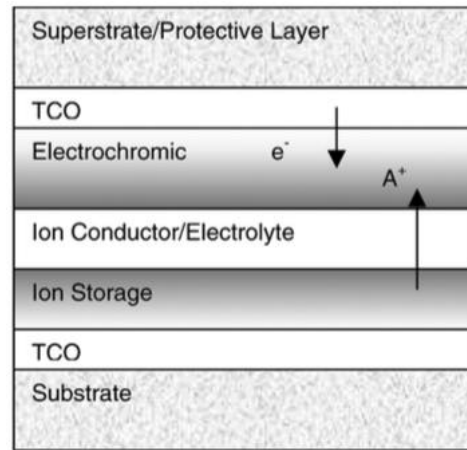


Figure 2-8. Schematic of the layer structure of an electrochromic window (not to scale). The schematic is assumed for a cathodic material, e.g., tungsten oxide (Lampert, 2004).

Typical electrochromic devices have visible transmission of  $T_v = 70\text{-}50\%$  at transparent state and fully colored transmission of  $T_v = 25\text{-}10\%$  (Lampert, 2004). The visible transmittance of less than 1% is also possible. The applied DC voltage to darken the electrochromic window is very small and typically ranges from 1-5 V. After removing the voltage, the gel returns to its natural and transparent state. In contrast to LC or SPD devices, no energy is consumed in the transparent state, and has a low power consumption of 0.5Wh/m<sup>2</sup> or lower in the darkened state. The voltage can be precisely controlled and adjusted in small increments to induce the intermediate states of light transmittance, as shown in Figure 2 9.

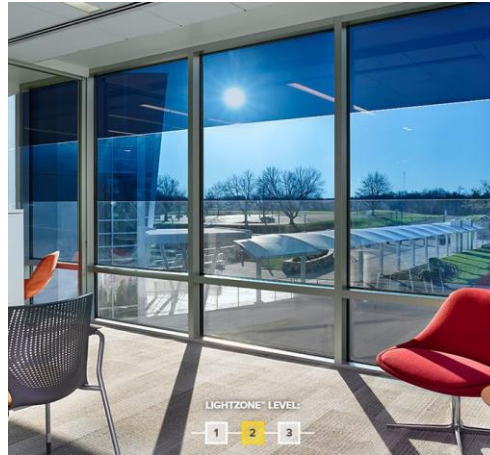


Figure 2-9. Electrochromic windows controlled at different states (Jerod, 2018).

EC glazings have several issues to solve in order to increase the market share for adaptive facade. First of all, compared with LC device and SPD device, the switching time of EC glazing is relatively slow. Sky illuminance can change from 20 to 40 klux within 1– 2 s. However, the available commercial EC glazing changes its state between 1 and 30 min, depending on the area of EC glazing unit. Second, despite a lifetime of 105 cycles and 30 years, durability can be an issue with EC glazing due to the leakage of electrolyte. Third, the electrochromic material rejects heat by absorption instead of reflection, and therefore, it can get quite hot when it is heavily irradiated. For some electrochromic devices, switching cannot work effectively if the maximum design temperature of the device is too high (above 60°C).

#### 2.2.1.4 Thermalchromic glazing

Thermochromic materials (Costanzo, Evola and Marletta, 2016) can change their optical properties in response to their temperature. Typically, at low temperatures a thermalchromic material is semiconducting and rather transparent to both visible and infrared radiation, while above a certain temperature (defined as transition temperature), thermochromic material transits into a metallic state, and becomes relatively opaque, as shown in Figure 2-10 (b). It is reported that thermochromic material has large potential in energy saving for buildings (Allen and Wu, 2015). However, unlike electrochromic glazing, one cannot control the outdoor weather conditions to gain the intermediate state. When the appearance of the thermochromic glazing becomes opaque, there is no longer the view through the glazing.

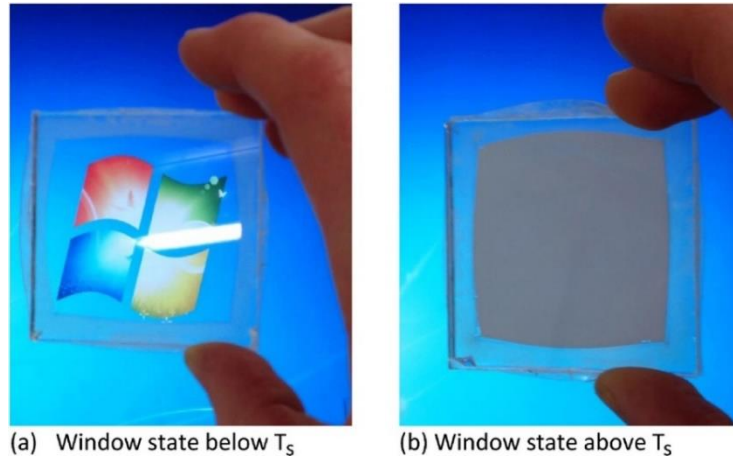


Figure 2-10. Thermochromic material below (a) and above (b) the transition temperature (Costanzo, Evola and Marletta, 2016).

### 2.2.2 Fluid window

Water-flow double-pane window design (Chow, Li and Lin, 2011; Chow and Li, 2013; Gil-Lopez and Gimenez-Molina, 2013) is a concept that involves a controlled flow of water within the cavity between the two glass panes. Much more heat can be extracted by flowing water than by ventilating air. Therefore, the fluid glass has the potential to reduce the room heat gain, and meanwhile, the window can serve as a water pre-heating device. However, the cooling tank, circulation pump, pipes for water flow and other components of the system make the installation very complex. Moreover, the maintenance can be quite high to deal with the possible water leaks. Furthermore, electricity consumed for pumping offset the reduced cooling load due to the decrease in solar heat gain.

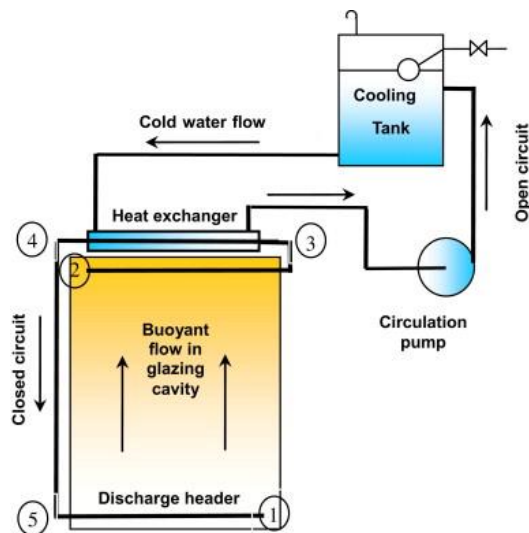


Figure 2-11. Sketch of water flow circuits of the laboratory set-up (Chow and Li, 2013).

## 2.3 Microstructured glazing for combined solutions

### 2.3.1 Switchable prismatic glazing

Based on the configurations of the lenses, two types of switchable prismatic glazing are developed (Klammt, Neyer and Müller, 2012), as shown in Figure 2-12 and Figure 2-13, respectively. The first type is the pure prism systems, as shown in Figure 2-12. In the first type, all direct sunlight will penetrate the panel with the same outgoing angle through the first prismatic array due to the prisms' simple geometry. Light within very narrow angular range will be redirected by the second prismatic array towards ceiling. However, the alignment of the two arrays of prisms has to be very accurate. Slight misalignment due to variation of fabrication will lead to most of the light will transmitted not being redirected

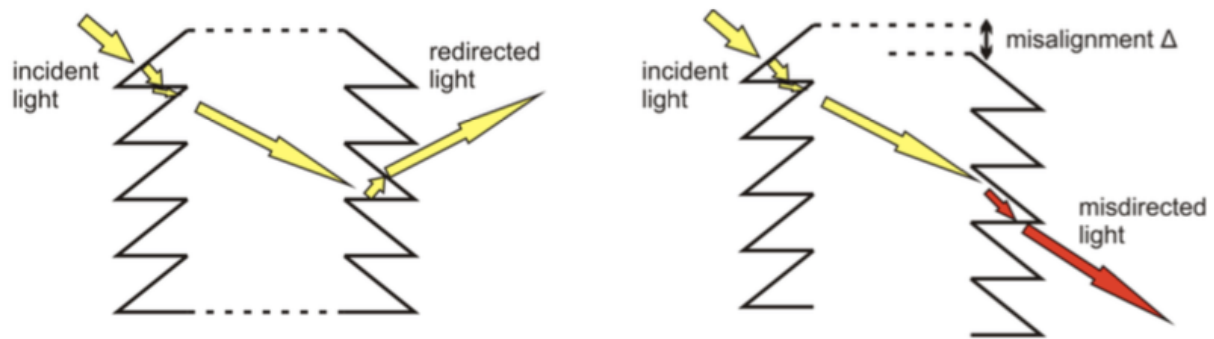


Figure 2-12. Systems with micro-prismatic arrays on both surfaces may significantly change their performance due to small profile variances, e.g., by vertical shifts  $\Delta$  (Klammt, Neyer and Müller, 2012).

In the second type of the prismatic glazing, the prism geometry on sun-facing side replaced by the prism-like geometries with curve lenses. It is shown that the direct incident sunlight is focused by the curve lenses and diffusely distributed over the prismatic side. The focal length of the lenses is shorter than the panel thickness. Ray-tracing simulations showed that the lens-like microstructures resulted in acceptable angular redirection efficiencies. Furthermore, color effects were avoided which were inherently present in pure prismatic systems, due to lens induced angular scattering. However, the non flat surface of the two prismatic glazing systems will create haze and the view through the glazing will be obstructed.

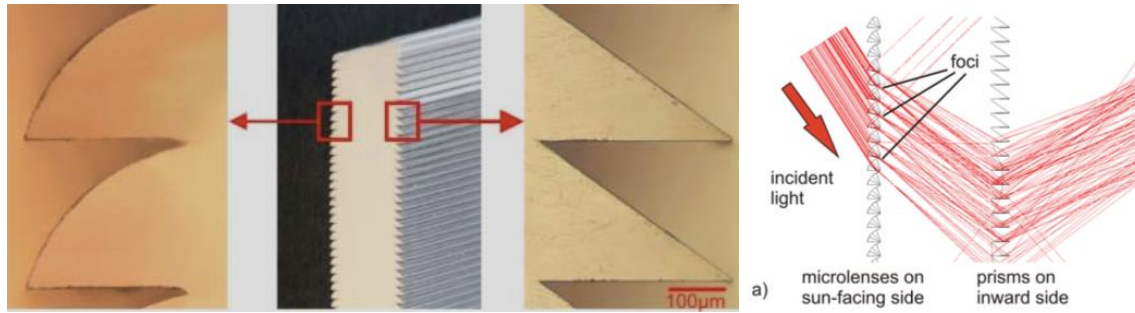


Figure 2-13. Cross sections of PDMS prototypes with structure dimensions of  $250\ \mu\text{m}$  (Klammt, Neyer and Müller, 2012).

### 2.3.2 Microstructured glazing with optically functional coatings

Two types of microstructures with facet-selective coating by physical vapor deposition for light-guiding and sun-shading systems had been developed (Walze *et al.*, 2005). The large scale microstructures were fabricated by interference lithography (Gombert *et al.*, 2003). The first type is a prismatic array where prisms and parallel planar substrate areas alternate, as shown in Figure 2-14 (a). The red lines indicate the direction of the vapors and the surface of the prism are coated. Due to the total internal reflection at the lower face and the shelf-shading effect, the micro prism array with facet-selective Aluminum coating (reflectance of about 90%), can reduce the transmittance from 0.8 to 0.2 for incident angle beyond  $40^\circ$ . The critical angles of total reflection depend on the geometry of the prism arrays, the periodicity of the prism with the planar substrate areas, and the refraction index. The parameters mentioned above can be optimized to achieve a minimum of transmittance of the direct summer sunlight on a vertical south facade.

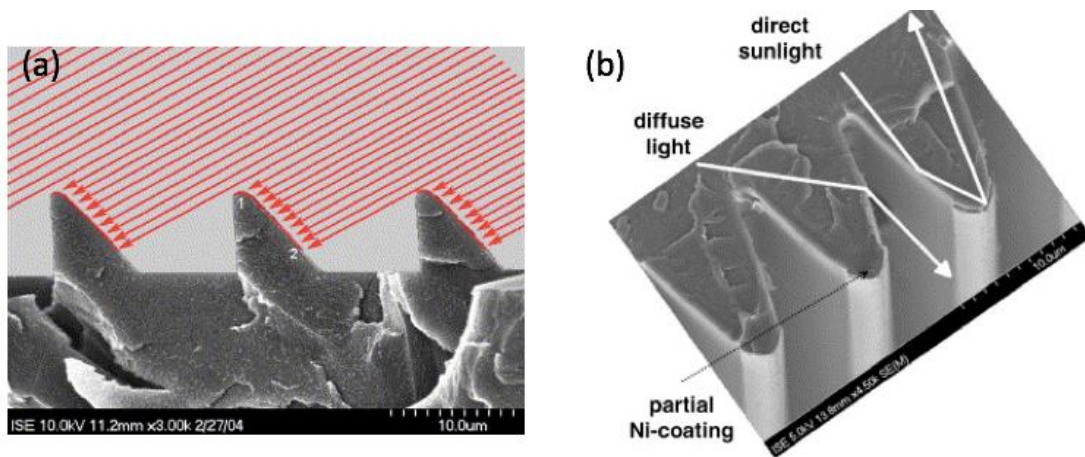
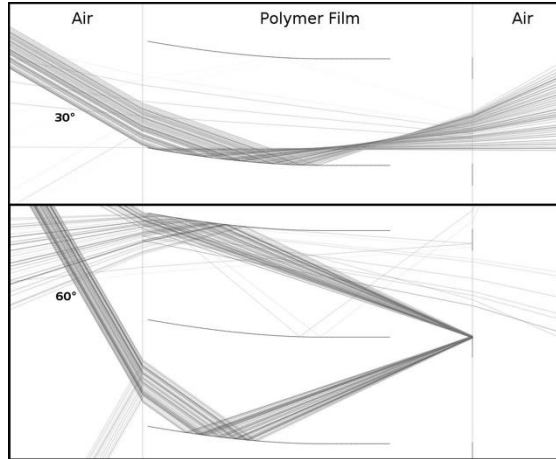


Figure 2-14. (a) SEM image of the prism array in polystyrene (PS). For indicating the self-shading effect for facet-selective coating, the red arrows show the incident angle of the direction of the vapor in the PVD process. (b) CPCs in PMMA. The “exit aperture” is coated with highly reflective thin film (Walze *et al.*, 2005).

The second concept is based on 2-D extruded compound parabolic concentrators (CPCs) (Rabl, 1976). Incident light of certain angles through the incoming exit will be focused onto the lower exit of the structure. When the exit aperture is covered by a reflective mirror, all light with the incident angles between the aperture angles will be reflected back to the incoming side, as shown in Figure 2-14 (b). Incident light with angles greater than the critical aperture angles will transmit and be redirected. Due to the rejected angles of CPCs are in the vicinity of the normal incidence of the structured panel, they are more appropriate for tilted façade, e.g., skylight (Walze *et al.*, 2005).

### **2.3.3 First generation of glazing with embedded micro mirrors**

Glazing with embedded micro-mirrors for seasonal thermal control, daylighting and clear view had been proposed by (Kostro and Schüler, 2017). The first generation design consists of two separated arrays of mirrors, i.e., an array of parabolic mirrors and an array of blocking mirrors. The mirrors are embedded in a polymer layer which can be laminated to the glass pane of a glazing. The parabolic mirrors are used to redirect light for daylighting and to focus light with a certain range of incident angles onto the blocking mirrors. The blocking mirrors block light from the selected range back through the system. The combination of the two components enables both daylighting and seasonal thermal control. Figure 2-15 shows a computer model of the polymer layer with embedded micro-mirrors for ray-tracing simulation with the incident direct rays at the angle of  $25^\circ$  and  $65^\circ$ , respectively. At a low sun elevation angle, the direct solar light splits into redirected part and direct-transmitted part. At a high elevation angle, the majority of direct solar light is redirected. The redirected solar light at high elevation angle will be reflected outside and therefore seasonal regulation of solar gains can be achieved. The redirected solar light may result in the improvement of daylight quality and quantity in an interior space. Depending on the latitude, the geometrical parameters of two array of reflective surfaces can be optimized and adapt to various latitudes and climates. Thanks to the micrometric size of the embedded reflective surface and the flat surface of the polymer, a clear view seen through the proposed glazing can be achieved.



*Figure 2-15. A computer model of the polymer layer with embedded micro-mirrors for ray-tracing simulation with the incident direct rays at the angle of 25° and 65°.*

For the first generation design, the specialized ray-tracing software for the optimization of the geometries has been developed. The proof-of-concept of the embedded micro-mirrors has been conducted. However, precise alignment between the two arrays is required. Moreover, accurate control of the distance between the parabolic reflective surface and the back reflective surface is also necessary. So far, the samples with only one array of embedded parabolic reflective surface has been achieved. Because of the absence of the blocking mirrors, the samples cannot perform the capacity of seasonal thermal control.

# Chapter 3 Glazing with novel embedded optical microstructures

## 3.1 Research questions

Based on the review of the state of the art in the previous chapter, the following research questions are envisaged for the present thesis:

- For south oriented façade, can glazing with a novel geometry of embedded optical microstructure simplify processing?
- For the same orientation, can a microstructure be found which avoids the extra-reflected radiation which causes the heat island effect and or glare on the street?
- Can we find an optical microstructure, which is applicable for diverse façade orientation, tilted glazing angle with respect to the horizon, locations, and climates?
- Can we quantify the potential energy saving in heating and cooling due to the use of the embedded optical microstructures?
- Can we quantify the advantages in daylighting and visual comfort?
- Can we prepare the samples in the lab?
- Can we fabricate the optical microstructures with coatings of various materials and what are the benefits?
- How can we adapt the lab fabrication process to the industrial upscaling?

In the following section of 3.2, two novel geometries of optical microstructures which can answer the first three research questions are presented. In chapter 4 and chapter 5, the methodologies are introduced for solving the other research questions. In chapter 6 and 7 the corresponding results are presented.



## 3.2 Novel optical microstructures

In order to simplify the fabrication procedure, and finally achieve the glazing with seasonal thermal dynamics, glazing with two new geometries of embedded microstructures are originally proposed. Moreover, various optical coatings, for example highly reflective and spectrally selective coatings, were applied and developed in the present thesis. The combination of the optimized geometry and optical coatings enables the novel optical properties to satisfy the applications for different locations and climates.

### 3.2.1 Glazing with “L”-shape retro-reflective optical microstructure

A novel “L”-shape retro-reflective optical microstructure is proposed. Similar to the first generation design mentioned in 2.3.3, there is an array of parabolic optical surface and a secondary optical surface. However, in the “L”-shape geometry, the two arrays of the optical surface are connected to each and made from one microstructure. Therefore, with the “L”-shape microstructure, no alignment is needed between the two arrays of the optical surface. Thanks to that, the processing procedures can be simplified. Very interestingly, by careful optimization of geometrical parameters, the “L”-shape optical microstructures can have retro-reflective property, which means, in summer when the solar elevation angle is high, the unwanted solar radiation is reflected outside of building along the direction of the incoming path, as shown in Figure 3-1. Therefore, it contributes to reduce the indoor solar gains in warm summer, providing daylighting, but avoid the heat island effect in the outdoor environment from the reflection of glazing. In summary, for the “L”-shape optical microstructures, there are two distinguished advantages from the first generation microstructures: the mandatory procedure is simplified and extra heat in the outdoor environment is reduced.

Thin film coatings with various materials can be applied based on the need for different locations. Coating for the parabolic materials and the back mirror are not necessarily identical. Table 3-1 summarizes the configurations of coating materials for the “L”-shape optical microstructures and the resulting functions. In summer, solar radiation is redirected and then focused onto the secondary optical surface. If the optical surface is coated with highly reflective materials, the solar radiation will be reflected toward an outer space; if it is coated with low-emissivity materials, ultraviolet and infrared light will be reflected back to outside; if it is coated with electrochromic materials, only the selected spectrum of solar radiation can be transmitted into an interior space at the colored state of coating.

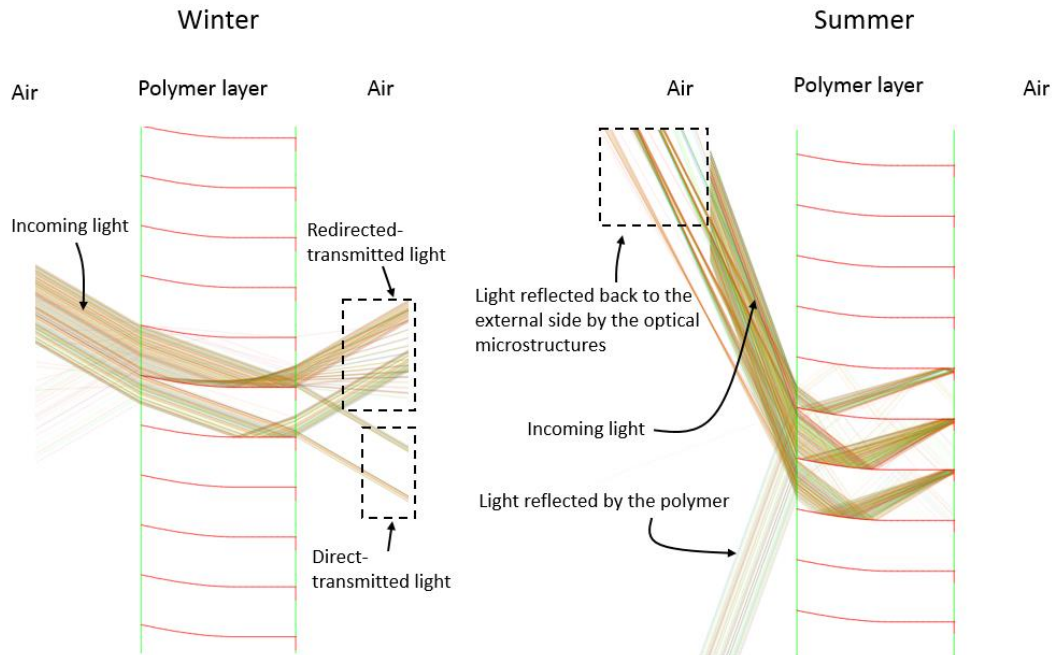


Figure 3-1. A computer model of the polymer layer with embedded retro-reflective micro-mirrors for ray-tracing simulation with the incident direct rays at the angle of 30° (winter) and 70° (summer).

Table 3-1. Configurations of coating materials for the “L” – shape optical microstructures and the resulting functions.

Configuration of coating materials	Functions
(opaque reflective coatings, opaque reflective coating)	Daylighting, seasonal thermal control
(opaque reflective coating, spectral-selective coating)	Daylighting, seasonal thermal control of NIR radiation
(opaque reflective coating, switchable coating)	Daylighting, dynamic thermal control by users
(spectral selective coating, spectral selective coating)	Seasonal thermal control of NIR radiation

### 3.2.2 Glazing with embedded micro compound parabolic concentrators

Daylighting systems based on micro compound parabolic concentrators (CPCs) is also proposed and developed in the present thesis. The CPC (Welford and Winston, 1978) is commonly used as a solar concentrator, and generally consist of two symmetric parabolas (named parabola L and parabola R respectively in our case), as shown in Figure 3-2 (a). The focal point for parabola L ( $F_L$ ) lies on parabola R, likewise the focal point of parabola (Welford and Winston, 1978) R ( $F_R$ ) lies on parabola L. According to the definition, the axis of parabola L passes through the focal point of parabola L and likewise the axis of parabola R passes through the focal point of parabola R. The angle that the axes of the parabola L and R make with axis of the CPC defines the acceptance angle of the CPC (Stine and Geyer, 2018). Incident rays within the acceptance angle are concentrated and leave the concentrator via the lower exit of the structure, while the incoming rays out of acceptance angle will be reflected back out through the input aperture.

The focal and end points of the two parabolas of an asymmetric compound parabolic concentrator (ACPC) lead to different acceptance angles on the two sides (Rabl, 1976; Sarmah, Richards and Mallick, 2011), as shown in Figure 3-2 (b). In order to make one-dimensional periodic array of ACPC, truncation is necessary. In the example of Figure 3-2 (b), the left side of the ACPC is terminated at the point  $(\bar{x}, \bar{y})$  instead of the end point  $(x_L, y_L)$  of the full ACPC. The right side of the ACPC can be truncated in an analogous manner. After truncation, the effective acceptance angle is  $\theta_e = \theta_L + \theta_R$  while the opening angle is  $\theta_f$ . Compared with symmetric CPC (SCPC), ACPC can be aligned in a direction so that it can have the desired profile of angular-dependent transmittance for different latitudes. ACPC may also reduce the quantity of reflector materials and system weight to reach the expected geometrical concentration.

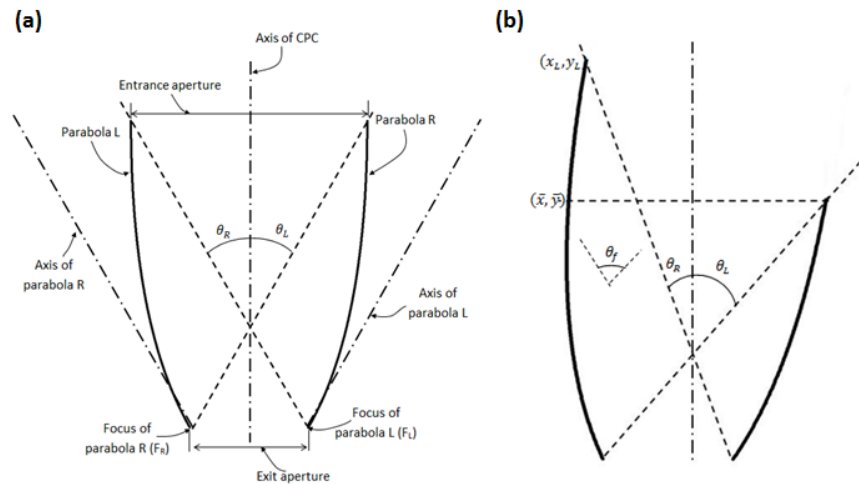


Figure 3-2. The examples and the design principle of compound parabolic concentrators: (a) symmetric compound parabolic concentrator, and (b) asymmetric compound parabolic concentrator.

Figure 3-3 shows a 2-D computer modeling and the cross section of a double glazing with the embedded micro CPCs in a polymer layer, which is attached to the inner side of the outer glass pane. The refractive indexes of glass and the selected UV polymer are identical (refractive index  $n = 1.5$ ). The reflectance of a reflective parabolic surface is set as 0.9. The thickness of the glass panes and the thickness of the polymer layer for modelling are larger by factors of 10-100 than that of reality, for the convenience of viewing. In winter where solar elevation angles are low, the solar radiation is partially redirected by the reflective parabolic surface and then enters in the interior space. In contrast, in summer where the elevation angle is high, the direct solar radiation is reflected outside after two or more reflections.

It should be noted that, for high elevation angles, most of the light reflected back to the exterior by micro-CPCs is up-warded, i.e., the reflection is near retro-reflection. Therefore, compared with the first-generation embedded microstructure, there will be less heat going to streets in summer.

Similar to the “L”-shape microstructures, the two arrays of the parabolic surface can be made from one microstructure: therefore, no alignment is required. Moreover, coatings with various materials can be applied to the micro CPCs, in order to adapt to different locations and climates.

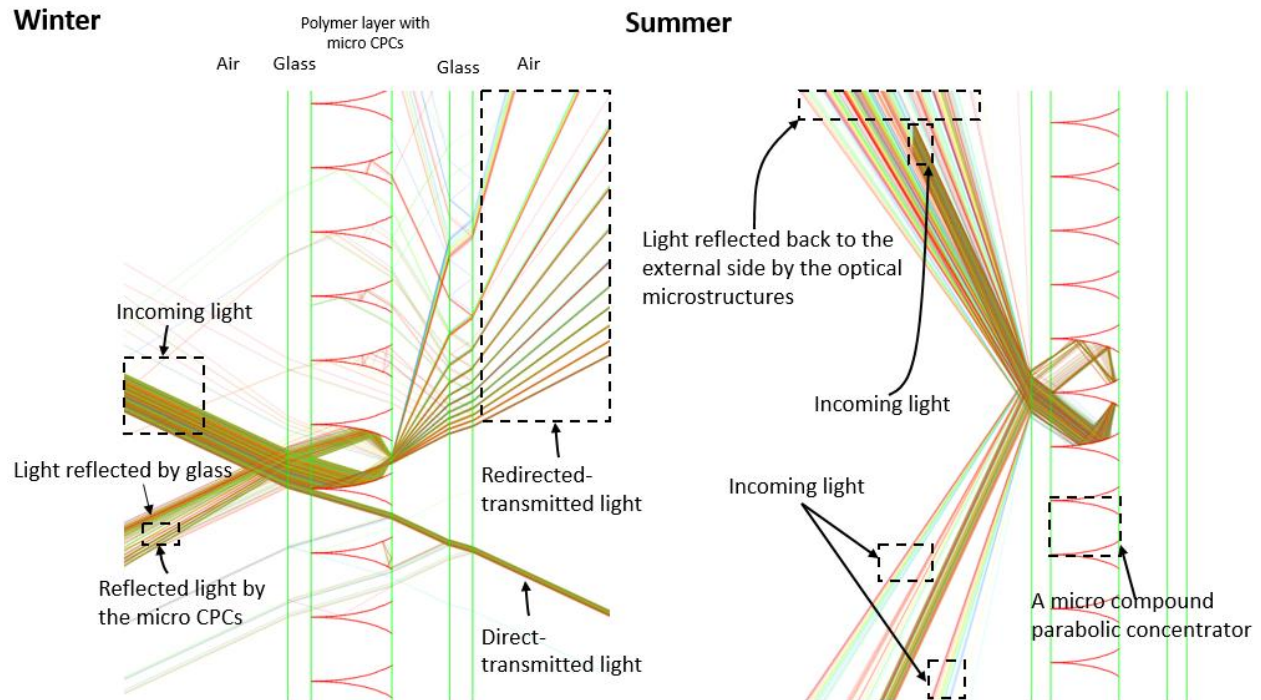


Figure 3-3. 2-D computer modeling and cross section of a double glazing with the embedded micro CPCs in a polymer layer. The incident angle of the incoming light are  $25^\circ$  and  $65^\circ$  respectively.

# Chapter 4 Methods of computer modeling and simulations

Prior to the fabrication, optimization of the geometrical parameters of the micro mirrors was conducted and the potential benefits were evaluated by backwards ray-tracing simulation. In the present chapter, the advanced optical ray tracing software CFSpro and the methodology for computer modeling of glazing with embedded optical microstructures are presented. Parameters used for the calculation of angular-dependent transmittance are introduced. Dynamic annual solar gains, and direct transmittance for various façades and different climates, were used to estimate the potential of seasonal thermal control. The potential advantages in daylighting were studied and the used criteria concerning daylight illuminance, glare, uniformity and directivity is presented.

## 4.1 Advanced optical ray tracing software CFSpro

### 4.1.1 Basic principles

An efficient simulation software named CFSpro by André Kostro (Kostro *et al.*, 2016) has been developed at the Solar Energy and Building Physics Laboratory of EPFL for the study of complex fenestration systems. The development of CFSpro was based on ray tracing technique, Monte Carlo algorithms and mixed dimensionality approach. Ray tracing (Glassner, 1989; Kostro *et al.*, 2016) is a technique used to model the path taken by light rays in an environment by following rays of light. It is often used for the design of lenses in microscopes, reflectors and other optical devices. CFSpro takes into account thin films, geometry, material properties and interfaces between materials to determine the path of light rays and accurately simulate reflection, refraction and absorption.

Monte Carlo algorithms are of stochastic nature and are used in cases where analytical or numerical solutions do not exist or are too difficult to implement. In a typical Monte Carlo algorithm, random draws define a chain of local occasions characterizing the global event and leading to a final state: each draw follows a given distribution of the corresponding event. By repeating this succession of random events numerous times, a probability distribution of the final states is obtained (Kostro *et al.*, 2016). The accuracy of this result depends on how well the problem is described and on the number of random draws. In CFSpro, every physical phenomenon (reflection, refraction, absorption) occurs randomly according to the probability distribution given by the corresponding physical laws.

A mix of 2D and 3D approaches (mixed dimensionality) is used (Kostro *et al.*, 2016). In a pure 2D ray tracing of such a profile, it is limited to in-plane characterization. For out-of-the plane

problem, the errors can be considerable after multiple reflections and refractions. This is not acceptable for evaluation of annual energy transmittance and daylighting performances, which require a 3D bidirectional transmission and reflection distribution functions (BTDF and BRDF) (Andersen, 2002; Ward, Mistrick, Ph, *et al.*, 2011). In the mixed dimensionality approach, the Monte Carlo algorithm separates the computation for intersection and interaction. Intersection is defined as event where the path of a ray crosses with an interface. Interaction events are refraction, reflection and absorption. The system is defined as a 2D extruded profile and the intersection can be considered in a 2-D plane; however, the corresponding z coordinate can then be retrieved by a 3-D vectorial calculus (Kostro *et al.*, 2016) if necessary. It is very fast to find intersections in dimensions using a binary space partitioning (BSP) tree (Ize, Wald and Parker, 2008). Interactions are computed in 3D using vector calculus. Therefore, compared with a plain 3-D approach, the mixed dimensionality approach experiences smaller computational load while providing accurate enough results.

#### **4.1.2 Graphical User Interface**

Figure 4-1 shows the graphical user interface (GUI) of the software CFSpro. The interface mainly contains four sections. Section 1 is the virtual realization, which shows the cross-section of the computer model of a complex fenestration system, and the paths of the rays after interacting with the system. The incident angle of the direct incoming rays can be modified and one can instantly visualize the transmitted and reflected light rays. Section 2 shows the structure tree of simulation for four different aspects which comply to complex requirements. Clicking the “Ray Tracer”, we can go to the interface where one can change the angle of the incoming rays and instantly visualize the interaction between incoming rays and the optical system. On the interface of Performance for the analysis of angular behavior, we can calculate the angular-dependent transmittance, get the matrix of bidirectional transmittance distribution and obtain the annual energy transmittance. Section 3 is the place where one can input the script, which describes the geometry and the properties of the materials for building a complex fenestration system. In addition to the JavaScript language for making the script, functions specific to ray tracing are implemented to draw interfaces between two points and to define materials and light sources. Thanks to a flexible description, almost any 2D extruded structure can be defined in a script and then visualized and modified in the GUI (Kostro *et al.*, 2016). Section 4 is the place where the geometrical parameters can be modified in the GUI with instantaneous display of resulting ray paths.

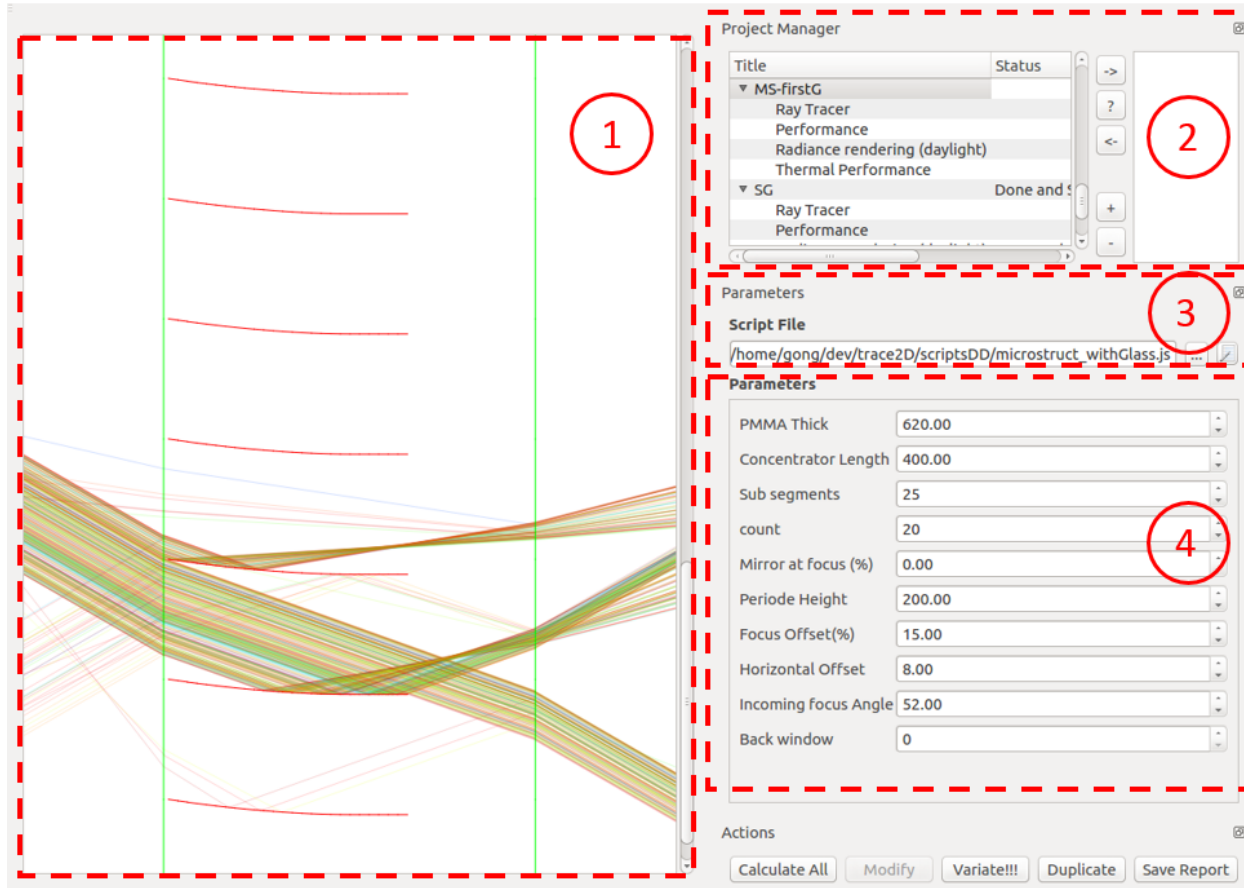


Figure 4-1. The graphical user interface of CFSpro.

## 4.2 Computer modeling of glazing with embedded micro-mirrors for ray-racing simulation

### 4.2.1 Glazing with light-redirecting and retro-reflective micro mirrors

For both light-redirecting (first-generation) and “L”-shape retro-reflective microstructures, the principle for computer modeling is based on a vector method. If the parabolic optical surface is coated with highly reflective materials, it is called micro-mirror; in the following section (i.e., the explanation for computer modeling), the highly reflective coating is adopted. First, the thickness of the polymer layer, the length of the parabolic micro-mirrors, and the starting point as well as the end point of the parabolic micro-mirrors, are defined. Second, the coordinates of the focus point for the parabolic micro-mirror, the length of the back mirror through the focus point and the highest sun elevation angle are specified. It is assumed that a parabolic micro mirror is evenly divided to, e.g., 25 segments, the normal to each segments point to the focus position at the highest sun elevation angle. Finally, a parabolic micro-mirrors and a back micro mirrors are defined. If the periodicity is given, we will have two arrays of periodic micro mirrors. Compared with the light

redirecting micro-mirrors (or first generation micro mirrors), two essential difference for computer modelling the retro-reflective micro mirrors are: i) the presence of the blocking mirror; ii) the parabolic mirrors connecting to the blocking mirrors.

Figure 4-2 (a) shows the resulting model for a double glazing with light-redirecting micro-mirrors for simulation and the corresponding visible transmittance with the variation of incident angles at the azimuth of  $0^\circ$ . Since the redirectibility is essential for light-redirecting systems, the average visible transmittance of redirected light is presented in Figure 4-2 (b). In the configuration shown in Figure 4-2, the integrated hemispherical transmittances at  $0^\circ$  azimuth are around 0.52 and 0.5 for the glazing with micro-mirrors and low-e double glazing, respectively. In the present study, the polymer layer with micro-mirrors is assumed to be attached to the second surface (inner side of outer pane). The polymer layer may also be attached to other surfaces, depending on specific location, climate condition and personal preference. At certain angular ranges (e.g., from  $35^\circ$  to  $55^\circ$  and from  $70^\circ$  to  $90^\circ$ ) the transmittance of glazing with micro-mirrors was higher than that of low-e double glazing. The reason may be that the micro-mirrors decreased the incoming angles at the interface 2 (marked in Figure 4-2 (a)), 3 and 4. The refractive indexes of the glass and the polymer are identical (refractive index  $n = 1.5$ ), and therefore, the glass pane where the polymer layer was attached, was not modeled in the simulation for the convenience of viewing. Parameters used to define the geometry of the micro-mirrors are summarized in Table 1, and the tilted angle of the end of the parabolic surface with respect to the horizon was approximately  $14^\circ$ . In reality, the total thickness of glass panes for a conventional double glazing is typically 4 mm, and a polymer layer with embedded micro-mirrors ranges from 0.15 mm to 0.2 mm. Experimental measurement of transmittance of glass pane with such a polymer layer has been conducted; it is shown that the average relative reduction of transmittance in the visible radiation is only around 1.8% with respect to a clean glass pane. Therefore, the absorption of the visible solar radiation by inducing a polymer layer is neglected for daylighting simulation. Since only the numbers and the types of interfaces affected the transmittance of solar radiation, the thickness of the polymer layer for simulation is not necessarily identical as that in the reality, for the better observation in ray-tracing simulation. It should be noted that, the current geometrical parameters of micro-mirrors are not necessary the best but representative.



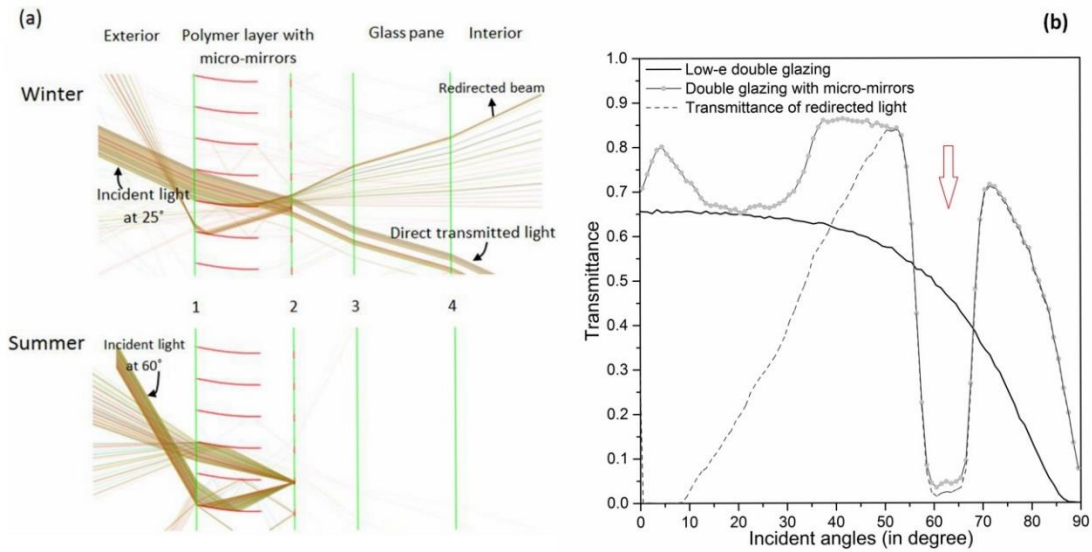


Figure 4-2(a) Model of embedded micro-mirrors in a polymer layer for ray-tracing simulation in the present work; (b) simulated angular-dependent transmittance. The arrow is used to indicate the effective reduction of direct transmittance by the secondary mirrors at an incident angle of approximately 60°.

Table 4-1. Parameters of embedded micro-mirrors for simulation.

Parameter	Value
Thickness of the polymer layer ( $\mu\text{m}$ )	620
Refractive index of the polymer	1.50
Length of the parabolic mirrors ( $\mu\text{m}$ )	400
Height of the secondary mirrors ( $\mu\text{m}$ )	40
Periodicity ( $\mu\text{m}$ )	200
Target solar elevation angle at which the incoming rays are focused on the secondary reflective surface ( $^{\circ}$ )	67
Reflectance of mirrors (-)	0.9

## 4.2.2 Glazing with embedded micro compound parabolic concentrators

### 4.2.2.1 Principle and assumption

The design of a compound parabolic concentrator (CPC) is based on the method developed by Rabl [16]. The methodology for programming and modelling can be summarized into 4 steps: (i) input the necessary parameters; (ii) define the parabolas at their own system. (iii) convert the coordinates for the parabola to the coordinate system for the compound parabolic concentrators; and (iv) calculate the periodicity and make a periodic array of the compound parabolic concentrators.

As mentioned before, a CPC unit is defined by the opening width of the outgoing aperture, and the half acceptance angle. The height of the CPC unit  $h$  and other parameters will be set once the opening width of the outgoing aperture and the half acceptance angle are given.

As shown in Figure 4-3, the right branch of the asymmetric CPC (named parabola R in the present work) lies in the coordinate system  $x_R-y_R$ . For a parabola through the coordinate origins (0,0) of a coordinate and satisfies equation  $y = ax^2$ , the coordinate of the focus point is (0,  $1/4a$ ). Since the focus point for the right branch sits at the coordinate (0,0), then we can get the equation for the right branch as

$$y = ax^2 - \frac{1}{4a} \quad (4-1)$$

where  $a$  is an unknown constant. We know that the focus  $F_L$  for the left branch lies on the parabola R. Therefore, based on the trigonometric functions, the coordinate of  $F_L$  is  $(s \cdot \cos\alpha, -s \cdot \sin\alpha)$ ; knowing  $F_L$  with the combination of  $y$ , we can get the value of  $a$ .

Accounting for the expression, the coordinates will then be transferred to the coordinate system (X, Y) for a unit of a parabolic concentrator by applying rotation and if necessary, translation, based on the following formula:

$$X = x \cdot \cos\alpha - y \cdot \sin\alpha \quad (4-2)$$

$$Y = x \cdot \sin\alpha + y \cdot \cos\alpha \quad (4-3)$$

$F_L$  is obviously the starting point of the parabola R. The terminating point will be at the height  $h$ , i.e.,  $Y = h$ . Correspondingly,  $X$  can be calculated using formula (4-1), (4-2) and (4-3). Till this step, the parabola R at the coordinate system X-Y is fully defined. Likewise, the parabola L will be defined using the same methodology.

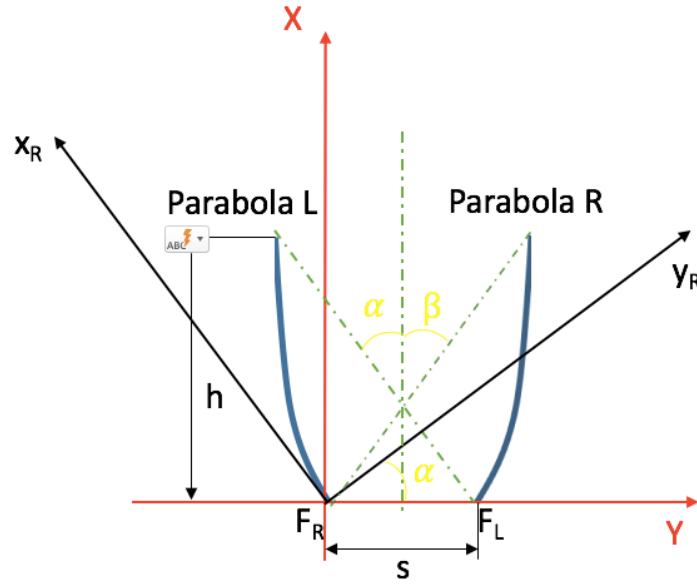


Figure 4-3. Coordinate systems for computer modelling of a compound parabolic concentrator unit.

For the computer models of glazing with CPC, five assumptions are made to simplify the analysis:

A-1: the CPC is ideal and free of fabrication error.

A-2: the physical and optical properties of materials are independent of temperature.

A-3: the absorption coefficient of materials is set as 0, and only the number as well as the type of interface affects the transmittance (therefore the real spacing distance is not adopted between the polymer layer and the glass panel for the convenience of viewing).

A-4: the reflectance of parabolic surface is 0.9.

A-5: the reflection is specular.

#### 4.2.2.2 Experimental validation of the computer modeling methodology

To validate the methodology for computer modeling, prototypes of double glazing with milimetric CPCs were prepared. Hot wire cutting on light-weight polystyrene foam is used to fabricate the supports for parabolic reflectors: the resulting structure is shown in Figure 4-4. The curve sidewalls of the supports were glued with aluminum foils. The reflectance of aluminum foils for visible light was about 0.9. The periodic milimetric CPCs were placed between two glass panes of a double glazing, instead of being embedded in a polymer layer laminated with a glass pane. The corresponding computer model was built. The angular-dependent transmittance was measured with an integrated sphere. The experimental measurement was compared with the simulation results.

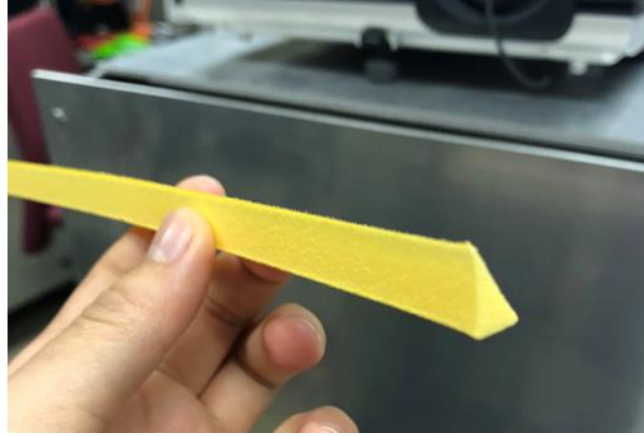


Figure 4-4. The polystyrene foam support fabricated by hot wire cutting for parabolic reflectors

#### 4.2.2.3 Investigated configurations

The two half-acceptance angles, the spacing and the height of various CPC units investigated in the present work are summarized in Table 4-2. It must be noted that, in order to obtain periodic ACPC structure, the higher parabola is truncated for the configuration of which a half acceptance angle  $\leq 65^\circ$ . For the configuration of which a half acceptance angle is  $\geq 75^\circ$ , both the left parabola and the right parabola are truncated.

Table 4-2. Summaries of the parameters to define a CPC unit

Configuration	Alpha	Beta	Height of a CPC unit ( $\mu\text{m}$ )	Opening width of exit aperture ( $\mu\text{m}$ )
(30, 30)	$30^\circ$	$30^\circ$	140	55.5
(40, 40)	$40^\circ$	$40^\circ$	140	100
(45, 45)	$45^\circ$	$45^\circ$	140	117
(50, 0)	$50^\circ$	$50^\circ$	140	80.3
(65, 0)	$65^\circ$	$0^\circ$	140	76.5
(75, 0)	$75^\circ$	$0^\circ$	140	85
(80, 0)	$80^\circ$	$0^\circ$	140	100
(85, 0)	$85^\circ$	$0^\circ$	140	127

#### 4.2.2.4 Sensitivity analysis

Due to the resolution of the fabrication methods, which will be introduced in details in chapter 5, and due to the possible loss of shape fidelity, the fabricated micro CPCs may differ from the theoretical design. Therefore, the sensitivity analysis of the optical properties to the geometrical parameters is needed. In the present work, the height is varied for selected micro CPCs. The curvature of the micro CPC varies corresponding to the change of the opening width of entrance aperture. The corresponding angular dependent transmittance to the variation mentioned above will be calculated and compared.

### 4.3 Angular-dependent transmittance

In order to optimize structures with potential seasonal thermal dynamics, the transmittance as function of the incoming elevation angle was calculated. It was assumed that the window was vertically installed in a room; in order estimate the daylighting potential, the transmittance could be considered with two groups, based on the direction of the transmitted rays with respect to the norm of a window: the direct-transmitted light rays through a window with a downward direction to a floor (named  $T_{\text{down}}$ ) and the transmittance due to the the redirected-transmitted light rays towards the upper upper side of the norm (named  $T_{\text{up}}$ ).  $T_{\text{up}}$  is expected to contribute more daylight to the depth of the room than that by  $T_{\text{down}}$ .

The simulation of angular-dependent transmittance of a double glazing with refractive index 1.5 was carried on as control group. The angular-dependent transmittance was calculated for the incident angles from  $-90^\circ$  to  $+90^\circ$  (i.e. from  $0^\circ$  to  $180^\circ$ ) in the plane with  $0^\circ$  azimuth angle. The interval of incident angles was  $1^\circ$ . The transmittance with a variation of the time of a specific day was also investigated. The total transmittance and the transmittance due to upward-transmitted rays are presented.

### 4.4 Specification of reference rooms

The reference office was designed based on Reinhart's definition (Reinhart, Jakubiec and Ibarra, 2013): it is referred to as standard Reinhart-defined room for the evaluation of dynamic facades and lighting technologies. It represents a south-facing office located in Lausanne, Switzerland, as its base climate. The office is not obstructed by neighboring buildings; its interior room dimensions are 3.6 m (width) x 8.2 m (depth) x 2.8 m (height). The large room depth of 8.2 m (corresponding to nearly 3.5 times the floor to ceiling height) is deliberately chosen to be rather large so that the effect of the complex fenestration system on daylighting remained visible for all variants. The office had a 2.9 m (width) x 1.6 m (height) window; the window-to-wall ratio for the south-facing façade was 48%. The bottom of the window was at 1 m from the ground. The reflectance of the ceiling, the walls and the floor were 0.8, 0.5 and 0.2, respectively.

## 4.5 Simulation of seasonal thermal dynamics

### 4.5.1 Dynamic solar gains

To assess seasonal thermal control, the dynamics of solar gains were examined. For each square meter of window, a portion of the incoming radiation was transmitted and heated up the space behind the window. To estimate this value, diffuse and direct transmittance factors were calculated separately using CFSPPro; then the two factors were combined with radiometric data derived from the Perez model introduced previously, based on climatic data from the Meteonorm model. The following formula was used at CFSPPro for the calculation of dynamic solar gains through a glazing:

$$Q_t = \sum_{k=1}^{k=p_s} (L_{ed,k,t} \cdot v_{d,k}) + E_{eb,t} \cdot \tau_{b,t} \quad (4-4)$$

where  $k$  is the sky patch index,  $p_s$  patches cover the hemisphere centered around the normal to the glazing excluding the sun position.  $L_{ed,k,t}$  is the diffuse radiance for a given patch while  $E_{eb,t}$  is the direct solar irradiance for time step  $t$ .  $v_{d,k}$  is the transmittance coefficient of the CFS for the set of incoming directions corresponding to the  $k_{th}$  patch (including the solid angle for conversion to resulting irradiance), while  $\tau_{b,t}$  is the energy transmittance for the direction corresponding to the sun position at this time step  $t$ . All values are time dependent except  $v_{d,k}$  which is constant for each patch of a given CFS. The formula does not take into account the radiative heat gains due to heat absorption in the window.

The dynamic solar gains were calculated for the south-oriented facades with vertical glazing in Lausanne and Athens, respectively.

### 4.5.2 Calculation of direct transmittance for Switzerland and Greece

Based on its angular-dependent transmittance, micro CPCs are appropriate for tilted glazing (or horizontal skylight). However, the dynamics solar gains can only be calculated for vertical glazing. Therefore, the potential benefit of seasonal thermal dynamics for glazing with micro CPCs is estimated by the calculation of direct transmittance as function of working hours, and two glazing configurations in Athens are used. In the first configuration, the glazing is set with symmetric CPC(45, 45) applied to the conventional double glazing of 65° degree tilted from the horizons. In the second configuration, embedded CPC(80,0) is applied to a horizontal skylight.

## **4.6 Simulation of daylighting performance and visual comfort**

### **4.6.1 Principles of RADIANCE software for daylighting simulation**

In the software of RADIANCE, almost all calculation procedures can be specifically controlled by the users through appropriate parameters. Therefore, it is a popular ray tracing software for lighting and daylighting simulations (Compagnon, 2001; Larson and Shakespeare, 2003; Ward, Mistrick, Ph, *et al.*, 2011). RADIANCE is based on the backward ray tracing technique, meaning that light rays are traced from the eye to the light sources (Compagnon, 2001). It takes into account all physical interactions with the object surfaces but consideration of polarization of light rays is excluded.

RADIANCE uses a geometrical description of a "scene" based on the external surfaces of objects (Compagnon, 2001); these surfaces define empty enclosed volumes. A normal vector is attached to each surface to define surface orientation. Cartesian coordinate system (X, Y, Z) is used to describe the scenes. In the default setting, the X axis is pointed towards the East, the Y axis towards the North and the Z axis towards the zenith. It is suggested to align the principal planes (e.g. the walls of a cubic room) along the X,Y,Z axis, while for the description of sky, it is rotated around the Z axis in order to correctly orient the scene (Compagnon, 2001). Coordinates can be given in any unit of length; however, for a simulation, the unit must be consistent for the multiple scenes. Each single ray "carries" a certain amount of radiance expressed in  $[W/m^2sr]$ . The radiance is divided into three channels, corresponding to the red, green and blue primary colors. The total radiance is a weighted sum of the radiances of the three channels (Compagnon, 2001).

### **4.6.2 Glazing configuration**

Three configurations according to the position of the embedded micro-mirrors in the glazing were tested: (i) micro-mirrors in the upper third (daylighting section (Tzempelikos and Athienitis, 2003; Tzempelikos, 2005)) of the conventional double glazing and the lower two-thirds (view section) consisting of low-e double glazing, (ii) micro-mirrors in the upper two-thirds of the double glazing and the lower third comprising of low-e double glazing, and (iii) micro-mirrors in the whole double glazing. The three configurations are referred to as  $MS_{1/3}$ ,  $MS_{2/3}$  and  $MS_{full}$ . A reference room with a low-e double glazing were used (marked as SG, standard glazing). The conventional low-e double glazing was simulated by the way of the Window function of the Radiance program (Compagnon, 2001), while the glazing with micro-mirrors was characterized by bidirectional transmittance distribution function (BTDF) (Andersen, 2002).

### 4.6.3 Data collection and metrics

Simulations were performed for each configuration in four aspects: (i) the impacts of micro-mirrors on the steady and dynamic illuminance in an interior space were studied; (ii) assessment of the uniformity of daylight was performed using the luminance ratio, (iii) the evaluation glare was conducted by Daylight Glare Index (DGI); and (iv) directivity of daylight through vector-to-scalar illuminance ratios was investigated.

#### 4.6.3.1 Steady and dynamic illuminance

The study of illuminance was divided into 3 steps. For the first aspect, the calculation of illuminance maps with contours spaced linearly on the winter solstice at 12:00 (GMT+2) under the standard CIE clear sky with sun was performed. The coordinate of the view point was {1.8, 8, 1.25} corresponding to {width, length, height} respectively. For the second aspect, calculation of illuminance on the working plane (1 m high) was conducted for CIE overcast sky, intermediate sky and clear sky on the spring equinox solstice at noon, where around 90% of incident light was redirected.

An annual hourly and climate-based estimation of daylight performance was carried out using the Useful Daylight Illuminance (UDI) for the third aspect. The calculation of UDIs was conducted for the working hours of a day (8:00 – 18:00) for the rear of the room (depth from 4 m to 8 m in the present model), where with conventional glazing the space is generally dark but with micro-mirrors an improvement of illuminance to UDI-autonomous level should be seen. Useful Daylight Illuminance (UDI) is defined as the annual fraction of time when the indoor horizontal daylight illuminance at a given point falls in a given range (Nabil and Mardaljevic, 2006; Carlucci *et al.*, 2015). From an energy saving point of view, the useful illuminances are defined in the range of 300 lux to 3000 lux, where additional artificial lighting will most likely not be needed (Mardaljevic, J., Andersen, 2012). Illuminances lower than 300 lux are defined as falling short of the useful range, while illuminances larger than 3000 lux exceed the useful range. The calculation of UDIs was conducted with the three-phase method (McNeil, 2014), as it has been theoretically and experimentally validated (Ward, Mistrick, Ph, *et al.*, 2011; McNeil and Lee, 2012). The three phase method separates the light transport between the sky patches and the illuminance sensor points into three phases: exterior transport, fenestration transmission and interior transport (Ward, Mistrick, Ph, *et al.*, 2011; McNeil, 2014). This process is described by the following equation (McNeil, 2014):

$$I = VTDS \quad (4-5)$$

where I is a matrix containing time series of illuminance or luminance result; V is a view matrix relating outgoing directions on window to desired results at interior; T is a transmission matrix,



relating incident window directions to exiting directions (BTDF); D is a daylight matrix relating sky patches to incident directions on window; and S is a sky matrix of a collection of sky vector. The sky matrix is based on the annual weather data obtained from Meteonorm, which is the software contains a database with climate data (irradiation, temperature, etc.) from 8,300 stations around the world. For the calculation of the V matrix, D matrix and S matrix in Radiance, the parameters summarized in Table 4-3 are used and may generate reliably accurate results (Ward, Mistrick, Lee, *et al.*, 2011). The mesh of sensors is 10 (along the width of the room)  $\times$  23 (along the depth of the room) on the working plane, i.e., every interval of two sensor was 0.356 m.

Table 4-3. Radiance parameters used for the calculation of view (V) matrix and daylight (D) matrix.

Radiance simulation parameters	V matrix	D matrix	S matrix
<b>Ambient bounces (-ab)</b>	12	2	-
<b>Ambient divisions (-ad)</b>	65536	1024	-
<b>Limit weight (-lw)</b>	1.52e-5	-	-
<b>Sample rays per Klems division (-c)</b>	-	1000	-
<b>Type of sky divisions (-m)</b>	-	4	4

#### 4.6.3.2 Luminance ratio

For a sound uniformity, in the so-called ergorama area (a cone of 60° with respect to the focal point), the luminance with respect to the line of sight should not exceed three times or be less than one-third of the luminance of the main visual task. The luminance in the panorama (a cone of 120°) should not exceed ten times or be less than one-tenth of the luminance of the main visual task.

The distribution of daylight was assessed by luminance ratios. The luminance was calculated for an occupant sitting for paper task on April 7<sup>th</sup> at 12:00 (Greenwich Mean Time + 2) under the standard CIE clear sky with sun. All the directed solar rays (elevation angle of 50° in Lausanne) through the micro-mirrors were redirected. The situation was deliberately chosen to have a harsh contrast in the field of view for conventional glazing. The glazing with embedded micro-mirrors was expected to enhance the uniformity of daylight distribution in this field of view. Figure 4-5 shows the example of the fish-eye view image for the calculation of luminance ratio, and the definition of ergorama and panorama. For people achieving a common paper reading, the direction of view was towards the desk surface. The viewing vector pointing downwards (45° from the horizontal) from the eye towards the desk is chosen. The direct sunlight in the case of the reference room covered half of the area of the desk, which is considered as an uncomfortable working situation. It is assumed that the paper reading consisted of a perfectly diffuse, white sheet of paper

with a reflectance of 0.8. The command *pvalue* (Larson and Shakespeare, 2003) in Radiance was used to obtain the values of luminance for each pixel. The luminance ratio was calculated for every pixel in the ergorama and panorama with respect to the pixels of the stared point.

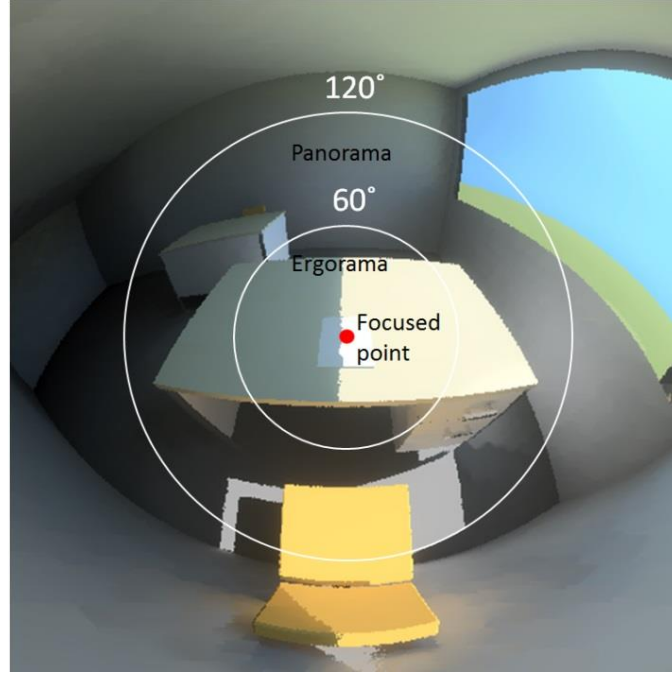


Figure 4-5. A typical example of the fish-eye view image for the calculation of luminance ratio on April 7th at 12:00 (GMT+2), where a large contrast of daylight distribution appears on the table for the room with the conventional low-e double glazing.

#### 4.6.3.3 Daylight Glare Index (DGI)

The aim of the Daylight Glare Index (DGI) is to assess the glare from large sources (Carlucci *et al.*, 2015). It is defined as follows:

$$DGI = 10 \log 0.478 \sum_{i=1}^n \frac{L_{s,i}^{1.6} \cdot \Omega_{s,i}^{0.8}}{L_b + 0.07 \omega_{s,i}^{0.5} L_{s,i}} \quad (4-6)$$

where  $L_{s,i}$  (cd/m<sup>2</sup>) is the luminance of a glare source ( $i$ ) in the field of view,  $\Omega_{s,i}$  (sr) is the solid angle subtended by the source, modified for the effect of the position of the observer in relation to the source,  $L_b$  (cd/m<sup>2</sup>) is the average luminance of the visual field excluding the glare sources, and  $\omega_{s,i}$  (sr) is the solid angle subtended by the glare source.

The criteria of glare using DGI are summarized in Table 4-4 (Carlucci *et al.*, 2015). In the present paper, two viewpoints were chosen in the standard Reinhart-defined room. One was set at 1 m distance from the window, with a height of 1.25 m and the line of sight pointed towards the wall, in order to consider a working position in a realistic state, referred to as employee position.

This viewpoint was in the area where direct sunlight was generally received during most of the year with a conventional glazing, and was considered as an uncomfortable position. The other viewpoint was set at 3 m away from the window at a height of 1.25 m, with the view line towards and perpendicular to the window, referred to as guest position. These two viewpoints reflected the worst cases with conventional glazing, and the risk of glare is expected to reduce by using glazing with micro-mirrors.

*Table 4-4. Criteria of Daylight Glare Index.*

<b>Glare criterion</b>	<b>Daylight Glare Index (DGI)</b>
<b>Intolerable</b>	30
<b>Just intolerable</b>	28
<b>Uncomfortable</b>	26
<b>Just uncomfortable</b>	24
<b>Unacceptable</b>	22
<b>Just acceptable</b>	20
<b>Perceptible</b>	18
<b>Just perceptible</b>	16
<b>Imperceptible</b>	14

#### **4.6.3.4 Vector-to-scalar illuminance ratio ( $E_v/E_s$ )**

The vector-to-scalar illuminance ratio ( $E_v/E_s$ ) (Cantin and Dubois, 2011), i.e., the ratio of the magnitude of the illumination vector  $|\vec{E}|$  and the mean spherical illuminance  $E_{sr}$ , was used to evaluate the directivity of daylight environment in the standard Reinhart-defined room. Strong directivity suggests strong contrast, which may induce glare. Directivity may also be useful in museum and art galleries to study the effect of alternative daylight design on various object appearance (Inanici, 2007). In terms of the appearance of 3D objects, 1.2-1.8 is the preferred range on a scale from 0 to 4; 1.8-2.5 or 0.5-1.2 is acceptable, larger than 2.5 will be too harsh.  $E_v/E_s = 4$  may occur on a sphere illuminated by collimated beam of light in a totally black room.  $E_v/E_s = 0$  takes place when the source vector distribution on a sphere is totally symmetric.

Following the methodology described by Cuttle (Cuttle, 1997, 2014), for the calculation of the vector-to-scalar ratio, cubic illuminance meters along the depth of the room were used. The height of the center of the cubic illuminance is 1.2 m, which was around the height of the head of a sitting

occupant. The axis of the cubic illumination meter was tilted by  $35^\circ$ , so that the long corner-to-corner diagonal of the cube is vertical, and three facets of the cube faces upwards and three downwards (Cuttle, 1997, 2014).

# Chapter 5 Methods of sample fabrication and principles

At the lab scale, the procedure for the fabrication of embedded optical microstructures can be sorted into five steps. First, master molds with the well-optimized microstructures are fabricated; in the present work, laser ablation and mechanical engraving on soft materials are used. Second, in order to avoid contamination and preserve the master mold, a replica with the microstructures of either an identical or a negative shape to the master mold is necessary. In the present work, replica made of an elastomer polymer named polydimethyl-siloxane (PDMS, Sylgard 184) is used. Then at the third step, the PDMS mold is used as stamp for UV imprinting with a UV-curable polyester-acrylated hyperbranched polymer (HBP, CN2305 Sartomer) on a glass substrate. In the fourth step, the HBP microstructure on the glass substrate is used for thermal evaporation deposition, and the optically functional coating will be deposited on the selected surface, based on the self-shadowing effect of a microstructure. In the last step, the grooves of microstructure with functional coating will be filled with identical HBP again for UV-imprinting, and therefore, the embedded micro optics are achieved.

At the industrial scale, the idea of roll-to-roll process is proposed for large-area micro structured fabrication. For this thesis, in order to find out the appropriate process for various microstructures, the preliminary feasibility study of roll-to-roll extrusion process was conducted.

In this chapter, the experimental procedures and the parameters to solve the challenges in the master mold fabrication, replications, shape fidelity analysis of UV imprinting, thin film deposition and roll-to-roll process will be presented. The principles of the fabrication and processing techniques will also be introduced.

## 5.1 Laser ablation

For the proposed geometries of the embedded micro optics, curve sidewall microstructures are needed. Electrical discharge machining (EDM) makes use of electrical energy and turns it into thermal energy through a series of discrete electrical discharges occurring between the electrode and workpiece immersed in a dielectric fluid (Ho and Newman, 2003). Two common types of EDM are sinker EDM and wire-cut EDM. A sinker EDM consists of an electrode and workpiece submerged in an insulating liquid and the two components are connected to proper power supply. Sinker EDM is a kind of method which transcribe the shape of the electrode to the workpiece (KD Solution.Co., 2018). Therefore, the shape of the cross-section of the machined structure and the resolution are limited by the geometrical parameters of the electrode. For window-size microstructured area with thousands of micro-channels (grooves), the efficiency of sinker EDM

with the electrode scanning along only a single channel can be very low. A wire-cut EDM uses a slim wire to move in a carefully controlled pattern, feeding through the workpiece. Therefore, it is inappropriate for the in-plane optical microstructures for glazing. Moreover, it is reported that the resolution of wire-cut EDM is about 5  $\mu\text{m}$  (Ho and Newman, 2003), whereas the roughness of the optical surface required for glazing needs to be sub-micron. Lift-off lithography refers to the process of exposing a pattern into photoresist, depositing a thin film over the entire area, and then washing away the photoresist to leave behind the film only in the patterned area. However, lift-off lithography is difficult to fabricate curve sidewalls with controlled optical surface (Bratton *et al.*, 2006). Grey-scale direct laser writing uses masks with changing opacity makes it possible to fabricate curved side wall microstructures (Tien *et al.*, 2003). However, the technique requires high-end equipment and the procedure is delicate. Moreover, the microstructured area is constrained by the size of the mask.

In the present work, the feasibility of UV excimer laser ablation for various high aspect ratio microstructures with curve sidewalls is investigated. The shape fidelity will be analyzed. Excimer lasers are gas-type lasers of the ultraviolet (UV) or deep UV region with short pulse durations (normally 20 ns). The short wavelengths enables high-energy intensity and high resolution for the effective removal of material (Tseng *et al.*, 2007). As a result, excimer lasers can directly machine the substrate material without photoresists for pattern transfer. Moreover, clean-room facilities are not required as that for conventional semiconductor fabrication. Since several decades ago, excimer lasers have been widely used in various areas, such as fabrication of microgears (Ghantasala *et al.*, 2001), diffraction grating (Zhang, Sugioka and Midorikawa, 1998), microlenses (Kopitkovas *et al.*, 2004), microfluidics (Kim and Xu, 2003), and optical waveguides (Van Steenberge *et al.*, 2006).

### **5.1.1 KrF excimer laser**

The word “excimer” is an abbreviation of the term “excited dimer”. Excimer is a dimeric or heterodimeric molecule formed from two species, at least one of which the valence shell has been completely filled with electrons (e.g., noble gases). The excimer, before emission of light, is in an electronically excited state. For excimer lasers, the active medium is a mixture of a noble gas like argon, xenon, and krypton, and a halogen gas such as chlorine, bromine and fluorine, and a buffer gas, usually neon. Gas mixture normally consists of 2–9% of a noble gas, 0.2% of a halogen gas, and 90–98% of a buffer gas which serves as a medium to transport energy (Abramczyk, 2005). In the present work, the mixture is confined in a pressure vessel at a pressure of about 3500 millibars. The gas mixture is usually excited by fast electric discharge lasting a few tens of nanoseconds. Since each of these binary mixtures has a characteristic emission wavelength, the excimer laser is normally named after the mixture. Consequently, the wavelength of an excimer laser can be varied by changing the gas mixture.

In the present work, KrF excimer laser is chosen due to its combination of overall average power, lasting efficiency, operational cost, and good absorption characteristics in plastics for ablation of polymers (e.g., polycarbonate).

### 5.1.2 Machining mechanism

In a simplified picture, the most important processes involved in pulse laser ablation include the optical excitation and energy dissipation, as well as the decomposition and removal of the material itself. The light is absorbed in the polymer substrate, resulting in electronic excitation of the polymers molecules. Part of the electronic excitation relaxes, and the emitted energy is converted into heat. The heat induces phase changes, and bond breaking, evaporation and desorption of the resulting small molecules or atoms (“thermal” mechanism). The other part of the electronic excitation directly may lead to bond breaking without the generation of heat (“photonic” mechanism). The relative importance of the two possible decomposition pathway has been discussed controversially. Nonetheless, for sure the relative importance of the two decomposition mechanisms differs for different materials and wavelengths.

The ablation rate  $d(F)$ , the effective absorption coefficient  $\alpha_{eff}$  and the ablation threshold fluence  $F_{th}$  are the main characteristics which describe polymer ablation. The ablation threshold fluence is defined as the minimum fluence where significant ablation starts to be observed. The ablation process is often described by the equation (5-1) (Bäuerle, 2011):

$$d(F) = \frac{1}{\alpha_{eff}} \ln\left(\frac{F}{F_{th}}\right) \quad (5-1)$$

### 5.1.3 Ablation products and their kinetics during ablation

It was pointed out that, ablation products can take away up to 80% of the energy of a laser pulse (Dallies, Berger and Huge, 1995). Therefore, understanding the nature of the ablation products, and the distribution, is important for high-quality fabrication of the microstructures.

#### 5.1.3.1 Ablation products: plume and debris

**Plume:** After the impact of the laser energy, substrate material is transformed into gases, eventually liquids or even solid particles that are leaving the substrate. The high temperature in this volume results in visible light emission and a rapid expansion of the gaseous material containing atoms, ions, electrons, clusters, droplets, and solid particles depending on the material and the impinging light properties. This expanding material is often called the ablation plume. The ablation plume is cooling off and its expansion speed is a strong function of the environment especially the gas pressure. The higher the pressure, the faster the plume decelerates and the smaller it becomes. Time of Flight Mass spectroscopy has been conducted to investigate the

velocity profiles of species ejected in ultraviolet laser ablation of several polymers (Hansen, 1989). In Hansen's work, it was concluded that the velocity ranges from  $1 \times 10^3$  cm/s to  $1 \times 10^4$  cm/s for all molecule groups.

**Debris:** Cooling of gases and liquids result in particle condensation from gases and formation of particulate products are formed if the ablation is carried out in ambient atmosphere. The re-deposited products on an ablated substrate is called debris. It mainly consists of amorphous and graphitic carbon (Lippert *et al.*, 1999), and the composition depends on the atmosphere for ablation. Due to its good adherence, debris can be regarded as a surface modification, and therefore, it is unwanted for some circumstance, e.g. laser ablation of high aspect-ratio microstructures with controlled shape.

#### 5.1.3.2 *Impact of ramp angle on the distribution of debris*

A ramp forms under the beam due to the scanning is schematically presented in Figure 5-1 for the central line of a triangular mask or a cross section through the ramp of a rectangular mask. The ramp angle  $\vartheta$  between the ramp and the original substrate surface is decided by the total depth  $d_{tot}$  of the groove and the length of the irradiated spot  $L$  along the scanning direction and the relation is expressed as:

$$\vartheta = \text{atan}(d_{tot} / L) \quad (5-2)$$

During the scanning ablation, the distribution of debris is affected by ramp angle, as shown in Figure 5-1. With higher ramp angle, more solid angle (region below the horizontal dash blue lines) of the ablation products is covered by the channel floor, and therefore, more debris deposits directly on the fabricated structures.



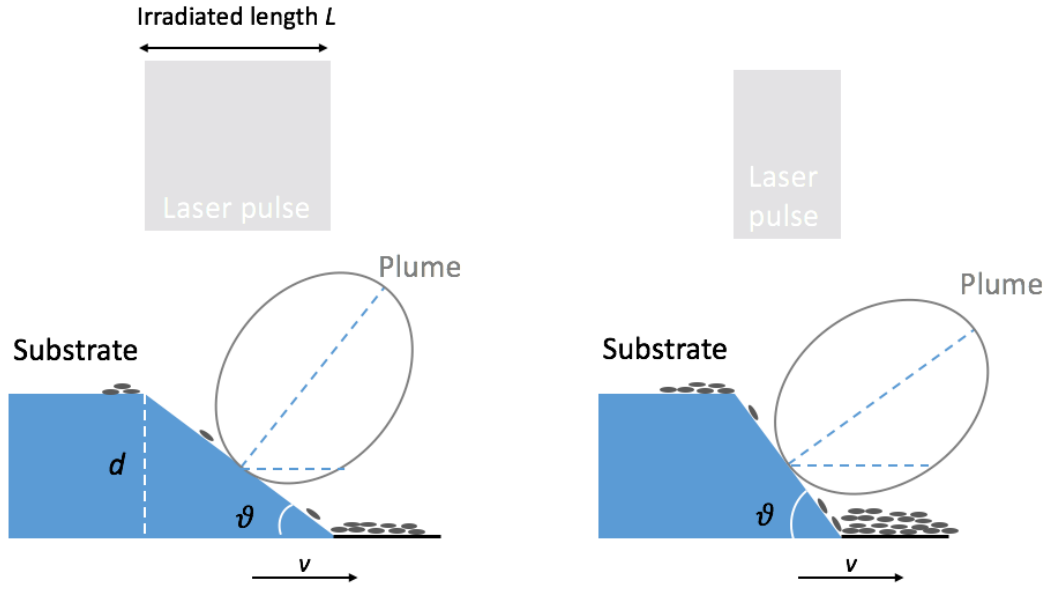


Figure 5-1. Impact of ramp angle on the distribution of debris on the ablated channel floor.

## 5.1.4 Ablation rate

Ablation rate is the parameter which directly relates to the ablated depth, the shape and the quality of the ablated microstructures. In the following sections, the influencing factors on ablation rate will be introduced.

### 5.1.4.1 Dependence on photon energy and fluence

The ablation rate with the variation of fluence for polycarbonate has been conducted by Pedder (Pedder and Holmes, 2006) using KrF excimer laser, as shown in Figure 5-2. It is found that, for high fluences (from 100 mJ/m<sup>2</sup> to 1000 mJ/m<sup>2</sup>), the increase of the ablation rate shows the logarithmic behavior, which can be described by the following equation (Bäuerle, 2011)

$$\Delta h = \frac{1}{\alpha_p} \ln[1 + \alpha_p B(F - F_{th})] \quad (5-3)$$

Where  $\alpha_p$  is the absorption coefficient of the vapor plume recalculated to the density of the condensed phase, i.e.,  $\alpha_p = \alpha\sigma_v/\sigma_s$ . Here,  $\sigma_v$  and  $\sigma_s$  are the absorption cross sections of species in the vapor and the condensed phases, respectively.

In the present work, the ablation rate for static ablation of less than 20 pulses is set to 0.25  $\mu\text{m}/\text{pulse}$ , the corresponding fluence can be 500 mJ/cm<sup>2</sup> based on the literature (Pedder and Holmes, 2006). The precise reproducible static ablation rate for 20 pulses is adjusted by fixing constant energy/pulse mode of the laser and an automatically fluence correcting attenuator.

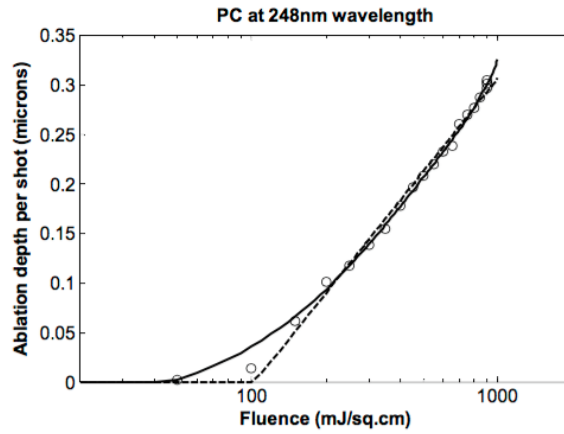


Figure 5-2. Ablation rate (ablation depth per shot) with the variation of fluence (Pedder and Holmes, 2006) . The measurement was conducted using KrF excimer laser on polycarbonate (PC). Solid lines are cubic polynomial fits to extended data sets; dashed lines are best-fit “Beer’s law” ablation curves.

#### 5.1.4.2 Dependence on pulse number

For strongly absorbing materials, the total ablated depth increases initially linearly with the number of laser pulses and the slope depends on the fluence, i.e., the ablation rate is independent of pulse number. However, for deep holes or grooves, the ablation rate can strongly decrease as pulse number increase. With increasing depth, the transport of ablated species becomes less efficient and favors material recondensation/redeposition within the hole/groove. The velocity of the slow species ejected out of the hole is  $10^3$ – $10^4$  m/s (Bäuerle, 2011). During a laser pulse of 20 ns, these species will travel about 20–200  $\mu\text{m}$ . As a result, for deep holes/grooves the attenuation of the incident light due to scattering and secondary excitation of ablation products is important and becomes more evident with increasing ablation depth.

In the present work, the pulse number will be varied in order to achieve the desired depth of the different microstructures. The theoretical pulse number will be calculated and compared with the experimental pulse number.

#### 5.1.4.3 Dependence on ambient atmosphere

Compared with ablation in vacuum, where the visible excimer laser ablation plume expands fast and up to several centimeters away from the substrate, in air at atmospheric pressure, the laser ablation plume remains closer and favors the formation of debris and clusters. Due to collisions with gas-phase molecules, the transport of ablated species away from the irradiated surface area is hindered, and therefore, laser intensity is attenuated. The confinement of the vapor plume contributes to the attenuation of the incident laser light and reduces the effective laser fluence reaching the substrate during each pulse. All of these effects become more significant with increasing gas pressure. Consequently, the (net) ablation rate decreases. The expansion of the

plume depends also on the size and geometry of the irradiated surface and therefore the ablation rate depends on several parameters and varies from case to case and varies also during ablation with increasing depth.

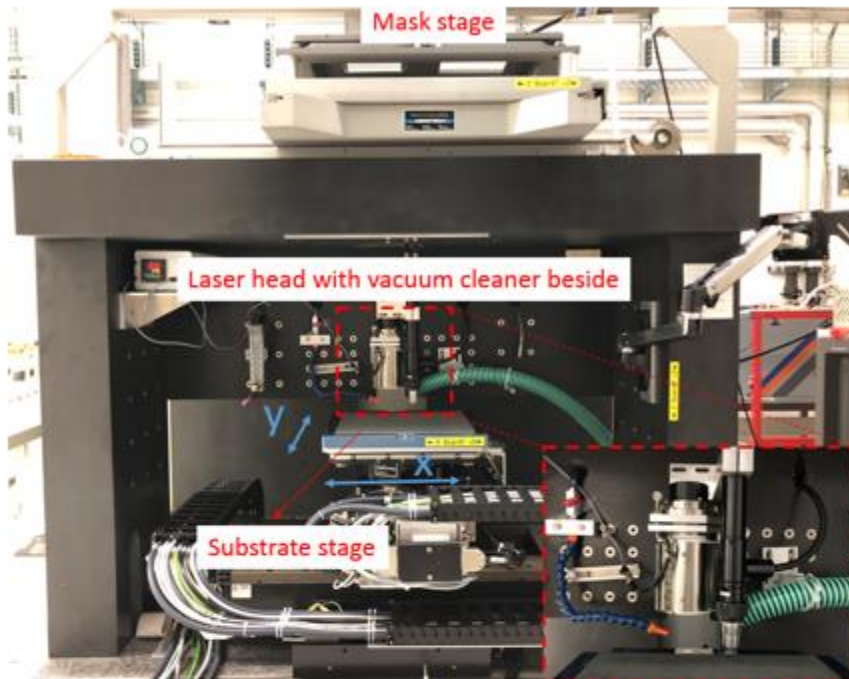
In vacuum, the formation of the shock wave is avoided. H<sub>2</sub> or He also manages to reduce the shockwave (Küper and Brannon, 1991), thanks to the low mass and the high speed of sound in these gasses. Ablation in appropriate reactive atmospheres also help avoids debris (Singleton, Paraskevopoulos and Irwin, 1989).

In the present work, laser ablation is conducted in air.

### **5.1.5 Machine**

Two KrF excimer laser systems (Lambda Physik LPX 200 Pro) were used for the fabrication of the microstructures. Based on the machinable size, the machines were named as XL and XXL, respectively. The scanning mask projection method was applied in the study. For the XL machine, cylindrical field lenses correct for the Excimer laser beam divergence and two 10 mm × 10 mm lens arrays homogenize the laser beam that illuminates a classical DUV black and white photomask (100 nm chromium on 4mm fused silica) containing the structures, commercially produced by laser or e-beam lithography, to be transferred on the substrate. The mask was imaged by a 5 times reduction through a high-resolution projection objective onto the substrate. The maximum laser processable area was about 0.5 m × 0.3 m. For the XXL machine, two 75 mm × 15 mm cylindrical lens array homogenizers were used together with several cylindrical lenses. The mask was also imaged by a 5 times reduction factor high quality objective lens system. The machinable area can be up to 1.5 m × 2 m. The two machines and the movement directions indicated by the x and y arrows are shown in Figure 5-3. The vacuum direction for removing the ablated materials is perpendicular to the scanning direction.

## XL machine



## XXL machine

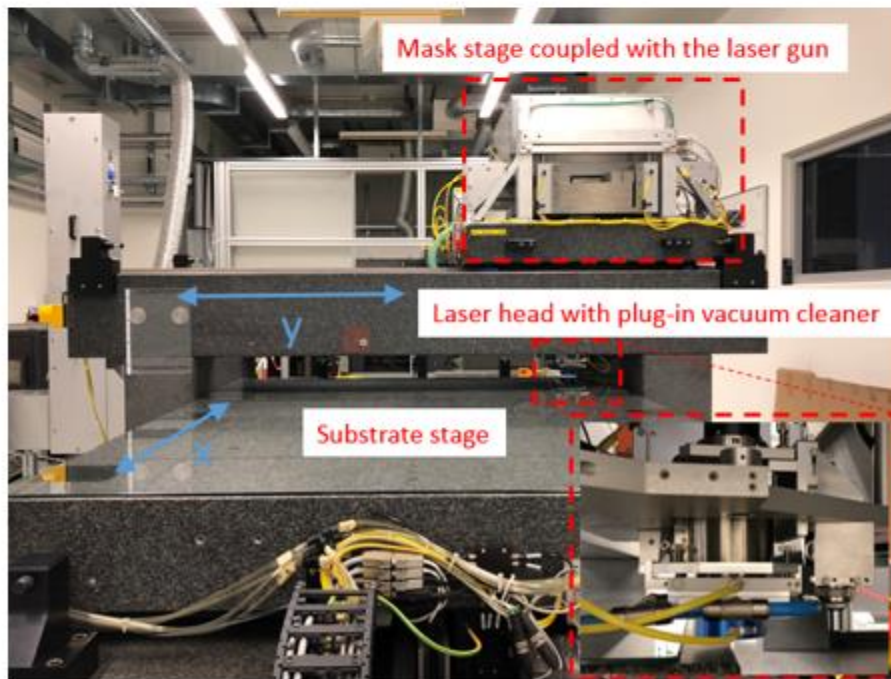


Figure 5-3. The two KrF excimer laser systems and the movement directions indicated by the red arrows.

### 5.1.6 Scanning mask projection laser ablation

Scanning mask projection laser ablation is the process in which the mask projection laser ablation is conducted with the relative movement of the mask and the substrates. The desired 3D microstructures can be manufactured with appropriate mask design, precise motion of the stage and control of the laser operating parameters. In the present system, the mask stage keeps stationary while the workpiece is moving at a constant speed. The directions of the relative movement for the two machines mentioned above are shown in Figure 5-3.

The scanning projection laser ablation fabrication process can be sorted into two steps: static mask project ablation and scanning ablation.

#### 5.1.6.1 Static projected ablation

Prior to the scanning ablation, static projected ablation, where there is no relative movement between laser beam, mask, and the substrate, is conducted to obtain the static ablation rate to calculate the theoretical pulses number needed for the scanning ablation. Moreover, the following information can also be extrapolated from the static ablation: homogeneity of the intensity of the laser beam, the translation from the mask to the contour on the substrate, the smallest feature of the projected contour which may lead to diffraction effect of the laser beam.

In the present work, the static ablation was conducted with 20 laser pulses. The static ablation rate is then the total ablated depth over the 20 pulses. Important is the control of perfect image plane focusing, that is the z-axis adjustment as slight defocusing results in strong differences in the edge quality and ablation rate per pulse.

#### 5.1.6.2 Scanning ablation

For the scanning ablation, the cross-section of the groove is determined by the shape of the mask as the ablation depth of the groove is inversely proportional to the ratio of the substrate step,  $s$ , between two consequent pulses, over the length of the structure  $L$ . The smaller the step,  $s$ , the deeper the structure will be, as the total dose on each spot of the substrate will be higher.

The speed is optimized by the numerical model to estimate the ablated depth  $D$ :

$$D = \frac{L}{V} \times f \times d_{static} \quad (5-4)$$

where  $V$  is the scanning speed,  $f$  corresponding to the laser pulse repetition rate, and  $d_{static}$  is the ablation rate/per pulse determined under static ablation for 20 pulses.

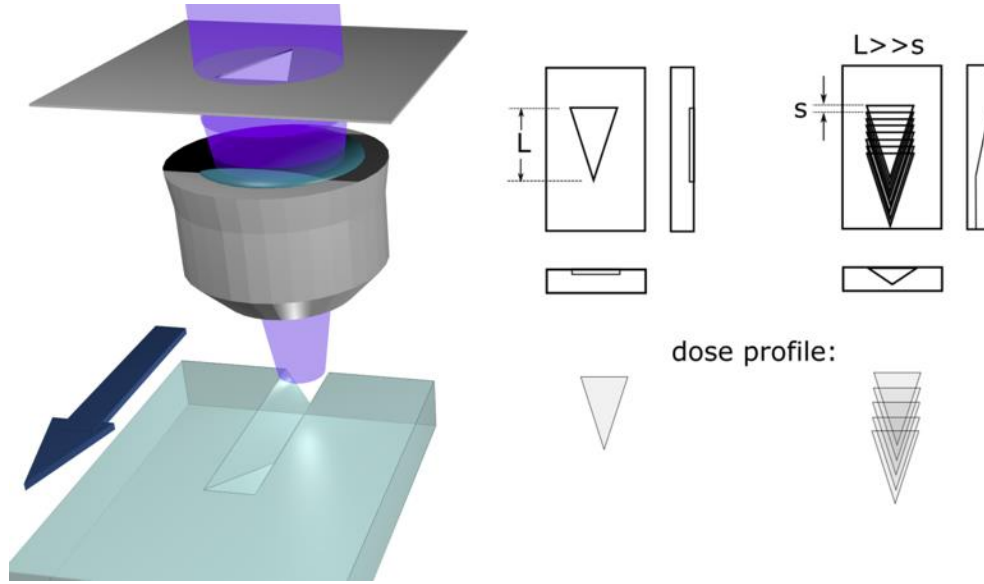


Figure 5-4. . Left: The sketch of the configuration of the scanning excimer laser ablation and the resulting micro structure. From top to bottom: Excimer laser beam, projection mask, objective lens, polycarbonate substrate. Right: Top, side and front view of a single and multiple shot exposure of the mask pattern on the substrate. As long as the motion step,  $s$ , of the substrate is shorter than that of the structure length,  $L$ , the total dose on the longer part will be higher resulting in deeper structures (more ablated material).

### 5.1.7 Mask

Periodic arrays of contours are imaged and directly ablated on the substrate. Three types of the contours are designed. They are retro-reflective microstructures, symmetric micro CPC positive and symmetric micro CPC negative microstructures. The sketch of the example computer design for the contours on a mask, and the resulting cross-sections with actual aspect ratios for the three types of microstructures after ablation are shown in Figure 5-5. The gray part represents the resulted microstructures on the polycarbonate molds after laser ablation, whereas the original computer design of the mask opening is the white confined area, more details about the geometrical parameters can be found in Appendix A: Mask openings for laser ablation. The mask was fabricated by Compugraphics International Limited, UK. It should be noted that, the length (marked with  $L$  as shown in Figure 5-5) of the masking opening was prolonged after being transferred from the original computer design to the patterns on a mask. The elongation was taken as offset for the increased attenuation of fluence by plume and debris as the ablated depth increases. The widest contour width  $W$  remains unchanged. The precision and roughness of the cuts were in the range of some microns.

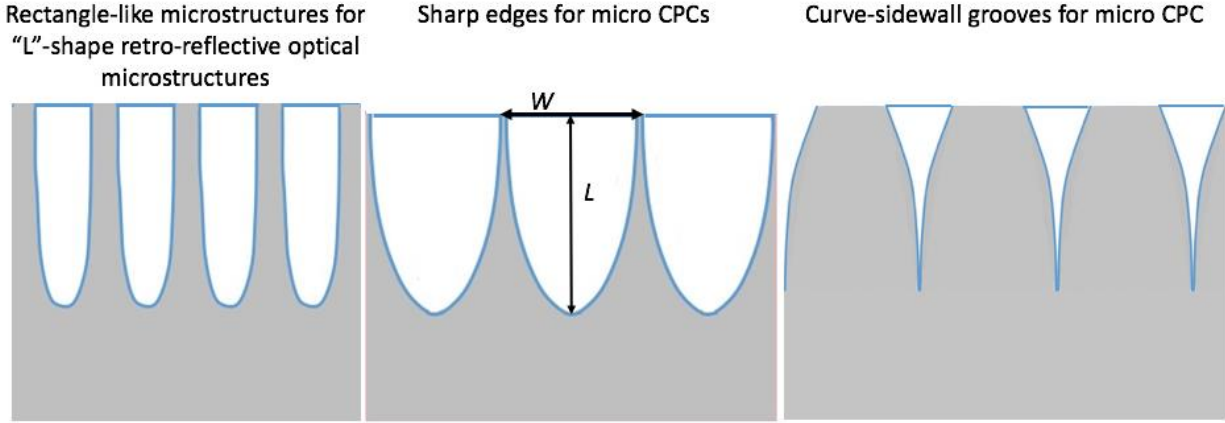


Figure 5-5. The sketch of the example computer design for the contours on a mask, and the resulting cross-sections with actual aspect ratio of the three types of micro structures.

### 5.1.8 Substrate

Polycarbonate substrates from SABIC, Netherlands, are used as material for the scanning laser ablation because of its excellent absorption and ablation characteristics at the wavelength of 248 nm. The polycarbonate substrates were stored in the controlled atmosphere (relative humidity:  $30 \pm 5\%$  and temperature:  $25 \pm 0.5^\circ\text{C}$ ) of the Laser center at EMPA Thun in Switzerland. The characteristics are listed in Table 5-1.

Table 5-1. The characteristics of polycarbonate

Parameter	Value
Refractive index at 632.8 nm	1.581
Compressive strength	> 80 MPa
Tensile strength	55 - 70 MPa
Thermal expansivity at 23°C	$66 - 70 \times 10^{-6} \text{ K}^{-1}$
Thermal conductivity at 23°C	$0.19 - 0.22 \text{ Wm}^{-1}\text{K}^{-1}$
Heat deflection temperature	140°C at 0.45 MPa
Thickness	$0.5 \pm 0.05\text{mm}$

## 5.2 Scanning mechanical engraving

For the retro-reflective micro optics, the rectangle-like microstructures with the aspect ratio larger than 3 and curve sidewall should be fabricated. However, due to the complex physical and or chemical interaction between debris and laser in large-volume laser ablation, for the microstructures mentioned above, it will be very difficult to have controlled shapes. Moreover, for glazing with asymmetric CPCs, microstructures with overhang is necessary. With the conventional methods mentioned in the previous section, the fabrication for large-area microstructures with overhang is very challenging.

In order to fabricate the retro-reflective microstructures and asymmetric micro CPC structures, a novel mechanical multi-line scanning method for large area fabrication of linear microstructures was developed. The following procedures of micro UV-imprinting from the master mold steps were also introduced. The potential procedures and device for upscaling were also investigated.

Even though the method was initially developed for the glazing with embedded optical microstructures, it can potentially be applied to rapid prototyping of micro lense arrays (e.g. micro V grooves) for grating (Ohmori *et al.*, 2001) and light-guiding (Priyadarshi *et al.*, 2006). Moreover, it can be also used for the fast fabrication of artificial superhydrophobic surfaces with patterned microstructures (Varnik *et al.*, 2011; Kong *et al.*, 2013). Additionally, it has good potential for the realization of microfluidic channels for cell biology research (Kim, Lee and Suh, 2008) and protein crystallization (Chayen and Saridakis, 2008).

### 5.2.1 Engraving on flat substrates

The fabrication process for the optical microstructures is divided into five steps: substrate preparation, engraving, UV imprinting, mold removing and cleaning. Figure 5-6 shows the sketch of the process flow from scanning engraving to HBP microstructures on glass substrate. The details of the five steps are described as follows: (1) Paraffin substrates mixed with bee wax are prepared. (2) The micro-toothed blade is installed on a special designed head attached to a CNC machine, and the substrate is fixed on a stage. Then the blade is dragged through the soft material in a direction perpendicular to the profile with enough pressure. The aim consisted in obtaining a negative of the blade profile in the soft material. (3) The obtained mold is then printed onto a UV-curable liquid acrylated hyper-branched polymer (HBP) and exposed to UV light. (4) Once the polymer is cured by the UV light, the master mold is molten on a heat plane with a temperature of about 60°C. (5) Finally the obtained HBP microstructures with the opposite pattern with respect to the paraffin-based master mold are immersed in universal solvent (DISSOLV. CELLUL. 201, Brenntag) and cleaned in ultra-sonic bath for 10 - 30 minutes.



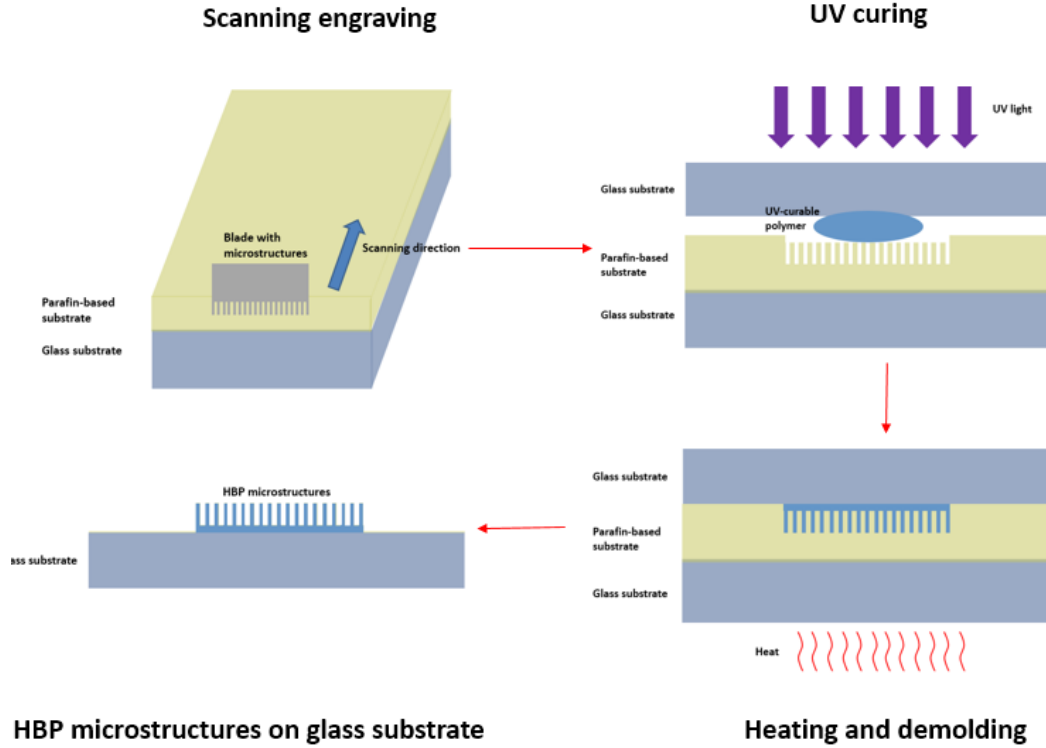


Figure 5-6. Sketch of the process flow from scanning engraving to HBP microstructures on glass substrate.

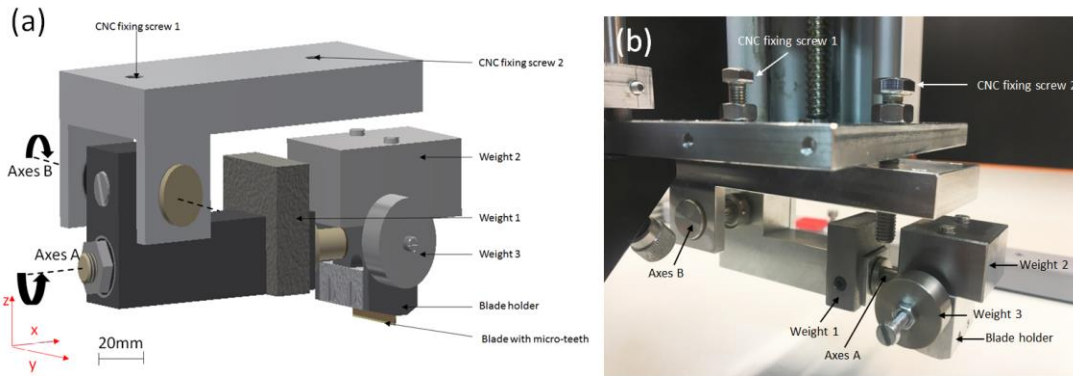


Figure 5-7. (a) A schematic design of the head which is installed on a CNC machine with the blade. (b) The fabricated head based on the design.

A head on which the blade is fixed and attached was designed and installed on a Computer Numeric Control (CNC) machine with a positioning resolution of  $10\mu\text{m}$ . The design of the head and the defined coordinates are shown in Figure 5-7. Screw 1 and screw 2 were used to install the head to a CNC machine. Two axes were used in the present work. Axes A allows the rotation around X axis and ensure the placement of the blade is parallel to the substrate. Axes B enables the rotation around the Y axis and allows the linear movement of the sample holder along the y direction. Screw 1 will fix the sample holder at the certain position but the rotation around y axis is possible. During engraving, the force applied on the blade A was equivalent to about 7.8 N and

the force on the blade B was approximately 9.8 N. The scanning engraving was conducted at room temperature in ambient atmosphere.

After engraving, the mold was placed on a flat plane. Then liquid crylated HBP was dropped and a glass substrate was put on the mold. After the liquid HBP fully filled the microstructured area, an exposure to UV light at an intensity of around 8 mW/cm<sup>2</sup> with the emitted wavelength of 375 nm for 180 seconds was conducted. The UV curing was carried out at room temperature in ambient atmosphere. After that, the sample was flipped and exposed to the same intensity for another 180 seconds, in order to ensure homogeneous photo-conversion of the  $300 \pm 20 \mu\text{m}$  thick sample. Once the polymer was cured by the UV light, the mold was melted on a heat plate (brand name) with a temperature of about 60 °C in ambient atmosphere. Finally, the obtained HBP microstructures with the opposite pattern with respect to the paraffin-based master mold were immersed in universal solvent (DISSOLV. CELLUL. 201, Brenntag) and cleaned in an ultra-sonic bath for about 10 minutes. Then the HBP sample was further immersed in ethanol in the ultrasonic bath for approximately 5-15 minutes, and naturally dried in air.

### **5.2.2 Engraving on rolls**

In order to further improve the efficiency of fabrication, reduce the accumulation of fragments, engraving on candle rolls was conducted. A wax cylinder with the diameter of about 18 mm was prepared in the lab. Then the wax cylinder was installed on a lathe machine, as shown in Figure 5-8. Lathe is a tool that rotates the workpiece about an axis of rotation to perform various operations such as cutting, sanding, knurling, drilling and etc., with tools that are applied to the workpiece to create an object with symmetry about that axis. The surface of the wax cylinder was peeled off and polished by a soft paper during the rotation of the wax cylinder. A blade was clamped and placed beside the cylinder. For engraving, the sample holder can be adjusted and therefore control the penetrated depth. The rotating speed of the wax cylinder was 40 r/min. The rotating direction was clockwise to reduce the accumulation removal materials on the blade.



*Figure 5-8. Engraving on wax cylinder.*

After proving the feasibility of engraving on the wax cylinder, a metal cylinder coated with wax was developed to further upscale the engraving area, as shown in Figure 5-9.

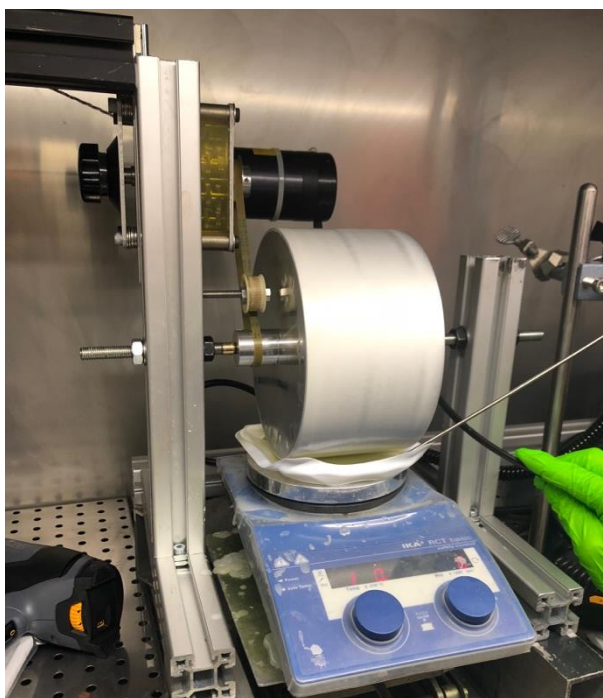


*Figure 5-9. The metal cylinder coated with wax.*

### 5.2.3 Design and fabrication of the blades

The blades used for engraving were fabricated by Mimotech based on the UV-LIGA (German Acronym for “Lithographie, Galvanoformung und Abformung” corresponding to “lithography, electroforming, and molding”) process. Deep UV-lithography demonstrated the fabrication of highly 2.5-dimensional structure and has been widely used especially in watch-making industry (Genolet and Lorenz, 2014). The procedure can be divided into two main parts: (1) UV lithography patterning on a relatively thick photoresist and (2) electroplating a structural material into the resulting resist pattern from step (1). Figure 5-10 shows the typical process flow of UV-LIGA (Joye *et al.*, 2010). The features of a final microstructure can be down to a few microns or even less (Qu *et al.*, 1998).

In the present work, the material of the blades was nickel. Blades with four microstructures were fabricated. The sketch of the cross-sections of the four microstructures on the blades are shown in Figure 5-12: two are the retro-reflective microstructures of different aspect ratio (AR) (Figure 5-12 (a) and (b)), while the other two belong to asymmetric microstructures (Figure 5-12 (c) and (d)) with overhangs. The thickness of the blades with retro-reflective microstructures is about 150  $\mu\text{m}$ , while the thickness of the blades with asymmetric CPCs is 400  $\mu\text{m}$ . The material of the blades is nickel.

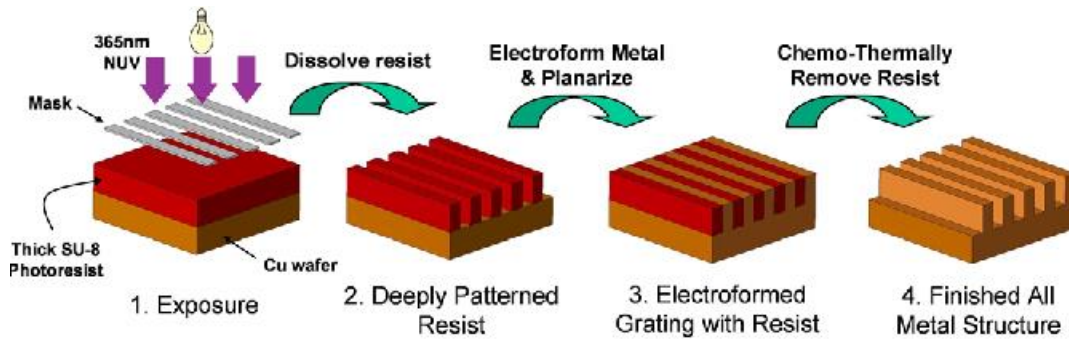


Figure 5-10. Typical UV-LIGA process (Joye *et al.*, 2010).

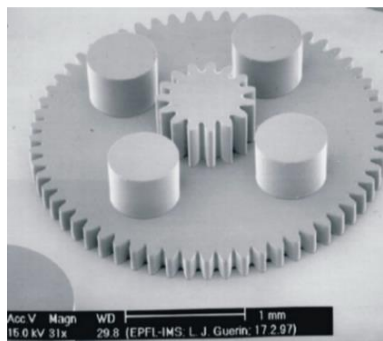


Figure 5-11. An example of a two-level photoplastic SU-8 microstructure after UV exposure. The microstructure is used for electroplating (Despont, 1997).

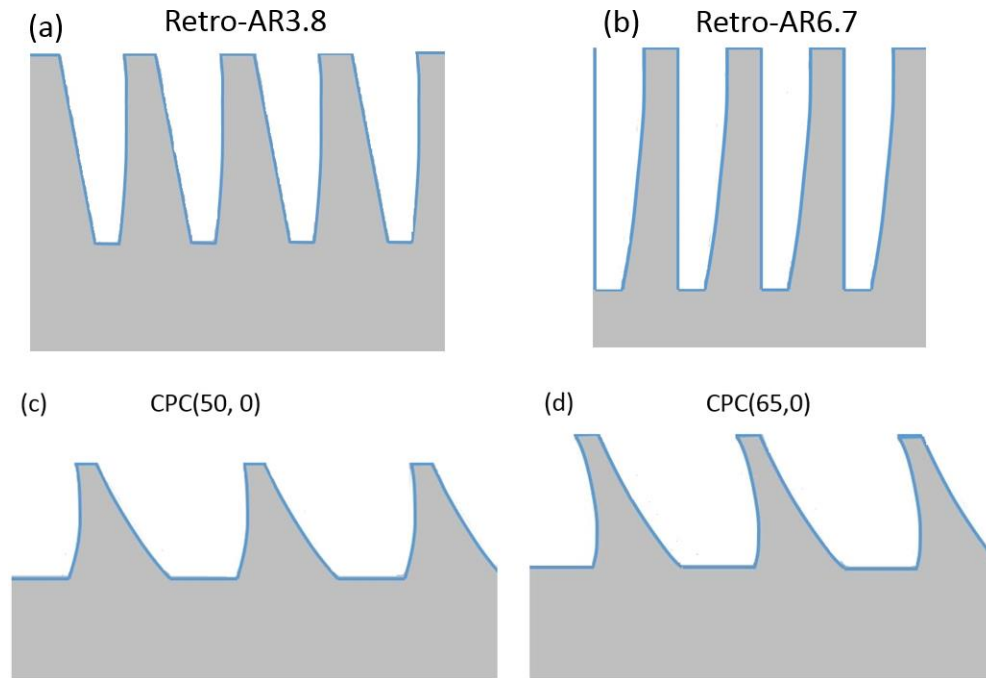


Figure 5-12. The sketch of the cross-sections of the four microstructures on the blades.

## 5.2.4 Materials

The method is based on engraving a soft material using a blade with patterned micro-teeth. Paraffin-based substrates with beeswax of various weight percentage were used in the present study.

Paraffin wax (Hossain *et al.*, 2009) is a tasteless and odorless white translucent solid. The source of paraffin wax (see Figure 1) is petroleum as indicated in Figure 2 presenting its pathway. It is produced following petroleum refining by dewaxing light lubricating oil stocks. It consists of a mixture of solid aliphatic hydrocarbons of high molecular weight such as  $C_{36}H_{74}$ . Its molecular formula is  $C_nH_{2n+2}$  (Lewis, 2002).

Beeswax is a type of wax from the honeycomb of the honeybees. It is yellow, brown, or white bleached solid. Beeswax is a complex mixture (more than 300 components) of hydrocarbons, free fatty acids, esters of fatty acids and fatty alcohol, diesters and exogenous substances (Fratini *et al.*, 2016).

The mechanical properties of wax are the important factors to consider for engraving. Table 5-2 shows mechanical properties obtained from uniaxial compression test conducted by Hossain. The fracture of paraffin shows brittle property while beeswax fail in a ductile manner (Hossain, 2015; Kozowyk, Langejans and Poulis, 2016). Typical brittle fracture exhibit little plastic deformation and low energy absorption before fracture, i.e., the crack propagates rapidly without increase in

applied stress. In contradictory, typical ductile fracture shows extensive plastic deformation and energy absorption (defined as toughness) before fracture.

Adding beeswax in paraffin can decrease the compressive strength and elasticity, and therefore favor the forward movement of the comb and the stability of the processing. However, the presence of beeswax can increase the ductility, which results in higher roughness of the engraved surface (Lange and Jennings, 1992). In the present work, substrates with different ratio of beeswax in the wax mixture were used and appropriate ratios were optimized. The used paraffin has a density of 0.9 g/cm<sup>3</sup> and the melting point of 42 - 72 °C, while for beeswax , its density is 0.95 g/cm<sup>3</sup> and its melting point is 62 °C - 65 °C (Hossain *et al.*, 2009).

*Table 5-2. Mechanical properties of wax.*

<b>Wax type</b>	<b>Density (g/cm<sup>3</sup>)</b>	<b>Compressive strength (kPa)</b>	<b>Modulus of elasticity (MPa)</b>
Paraffin	0.7855	658.4	55.7
Beeswax	0.854961	526.7	39.0

### 5.3 Replication of microstructures

In order to avoid the contamination or not damage the master molds, it is preferred that the master molds obtained through laser ablation and engraving are not directly used for the UV imprinting. Therefore, replication of polydimethylsiloxane (PDMS) between the master molds and UV imprinting is usually used.

Based on the strengths and the limitations of the master mold fabrication methods, the microstructures of the master molds can be either positive (high aspect-ratio edges in the present work) or negative (i.e., micro curve sidewall grooves). For facet-selective coating, the positive structures are desired. For the master mold with the micro curve sidewall grooves, two PDMS replications are needed. However, casting (2<sup>nd</sup>) PDMS over (1<sup>st</sup>) PDMS is challenging as both PDMS layers significantly adhere to each other. In the past, a process to cast PDMS from a PDMS-master just by wetting the surface of the mould using a phosphate buffer solution with hydrophilic polymer hydroxypropylmethylcellulose (HPMC) had been developed by (Gitlin, Schulze and Belder, 2009). The master was microfluidic channel on a Silicon (Si) substrate. The height of the micro channel on the Si master was 20  $\mu\text{m}$  and the width of the channel was about 50  $\mu\text{m}$ . For the 2<sup>nd</sup> PDMS copy, the channel height was 18 -19  $\mu\text{m}$ , showing good shape fidelity. Submicron structures were proven to be well reproduced.

Certain materials, chemicals, curing agents, and plasticizers can inhibit the cure of Sylgard 184 Silicone Elastomer. Most notable of these include:

- Organotin and other organometallic compounds
- Silicone rubber containing organotin catalyst
- Sulfur, polysulfides, polysulfones, or other sulfur-containing materials
- Amines, urethanes, or amine- containing materials
- Unsaturated hydrocarbon plasticizers
- Some solder flux residues

Since the wax used for engraving can contain unsaturated fatty acids and alcohols (Tulloch, 1970; Patel, Nelson and Gibbs, 2001) which inhibit the curing of PDMS, the interlayer for the PDMS casting from the wax substrate is desired.

In the present work, we developed a method for PDMS casting from PDMS and the problem of PDMS casting from a wax mold by inducing solutions with HPMC diluted in water. The research will try to answer the following questions:

- Can HPMC diluted in water generate an effective interlayer between PDMS and PDMS, as well as PDMS and wax, for the replication of high-aspect ratio microstructures
- What are the appropriate HPMC concentrations?

- What are the geometrical parameters of the microstructures, which favor the wetting of HPMC solution and the formation of an effective interlayer?
- What is the good composition of a wax substrate for the formation of an effective HPMC interlayer?

### 5.3.1 Principles

Understanding the wetting dynamics for microstructured surface immersed in HPMC solution is essential for the PDMS casting from PDMS, and PDMS casting from wax substrate, with the induction of a HPMC interlayer. Therefore, in the section of 5.3.1, the basics of surface wetting physics, under-liquid wetting dynamics for microstructured surface, and ultrasound-assisted wetting are introduced, subsequently.

#### 5.3.1.1 Surface wetting physics

In a pure liquid, each molecule in the bulk is pulled equally in every direction by neighboring liquid molecules, resulting in a net force of zero; however, the molecules exposed at the surface do not have neighboring molecules in all directions to provide a balanced net force. Therefore, a molecule at a surface tends to be drawn into the bulk of the liquid, i.e., work must be done in order to move a molecule within a liquid to its surface. The potential energy is lower as the surface area decreases. A liquid droplet tends to be spherical, because a sphere has the smallest ratio of surface area to volume among the geometric shapes. Surface tension is defined as the amount of work that must be done in order to create unit area of surface. As the drops get bigger, their weight deforms them into the typical tear shape.

When a molecule of a liquid is in contact with another phase, its behavior depends on the relative attractive strengths of its neighbors on the two sides of the phase boundary. As first described by Thomas Young in 1805, the contact angle of a liquid drop on an ideal solid surface is defined by the mechanical equilibrium of the drop under the action of three interfacial tensions, as summarized in the following equation:

$$\gamma^{lv} \cos \theta = \gamma^{sv} - \gamma^{sl} \quad (5-5)$$

where  $\gamma^{lv}$ ,  $\gamma^{sv}$ , and  $\gamma^{sl}$  represent the liquid-vapor, solid-vapor, and solid-liquid interfacial tensions, respectively, and  $\theta$  is the contact angle. If  $\theta < 90^\circ$ , the liquid is considered wetting the surface and is called "hydrophilic". With  $\theta > 90^\circ$  it is considered "hydrophobic". Figure 5-13 shows the two situations.



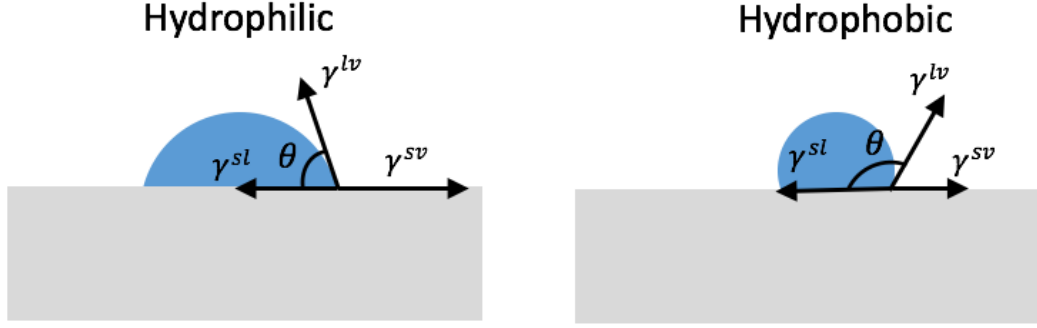


Figure 5-13. The hydrophilic and hydrophobic situations.

### 5.3.1.2 Under-liquid wetting dynamics for microstructured surface

When it comes to micro-structured surfaces, the physics of wetting can lead to various unexpected behaviors which depends on the micro-pattern shape. The sketch of the possible wetting states on structured surface under water As shown in Figure 5-14 (a) (Lafuma and Quéré, 2003). Under an optimized combination of surface roughness and the hydrophobicity of material, superhydrophobicity status is formed and called Cassie & Baxter state. However, it is pointed out that such status is instable and affected by various physical phenomenon, such as pressure, impact, air diffusion and fluid flow, etc (Xue *et al.*, 2016). As a consequence, the superhydrophobicity is destroyed under the perturbation by the various factors mentioned above, and a superhydrophilicity state, which is called Wenzel state may appear, as shown in Figure 5-14 (b). Depending on the triggering effect, the wetting transition from Cassie & Baxter status to Wenzel status may not occur immediately but gradually on a various timescale (Xue *et al.*, 2016).

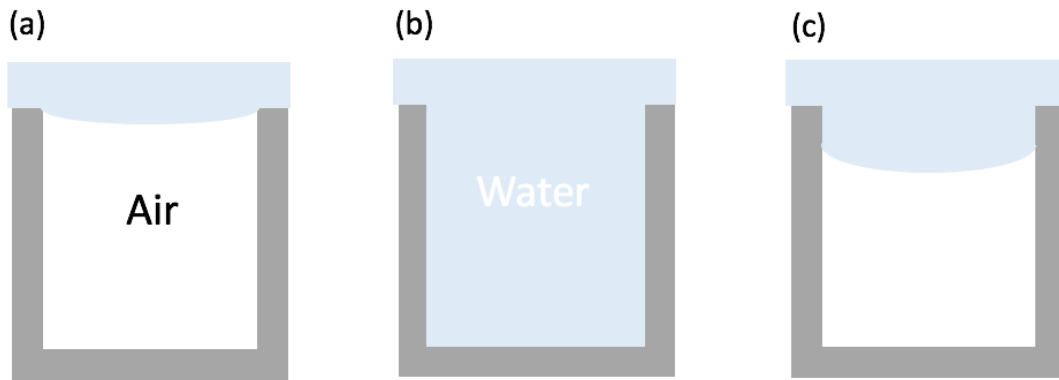


Figure 5-14. Sketch of the possible wetting states on structured surface under water: (a) superhydrophobic state (Cassie & Baxter state), (b) superhydrophilicity state (Wenzel state), and (c) depinned metastable state.

For open cavities, wetting transition happens immediately after the liquid pressure exceed a critical value. Taken cylindrically shaped pores as an example, the balance of the meniscus shown in Figure 5-14 (c) is described by

$$P_L - P_A = - \frac{2\sigma \cos \theta}{R} \quad (5-6)$$

where  $P_L$  and  $P_A$  represent liquid and air pressures, respectively.  $P_A$  equals to the ambient pressure for open cavity.  $\sigma$  is the surface tension and  $\theta$  is the contact angle.  $R$  is pore radius. From the equation (5-6) we can see that, if the pore radius increases or the contact angle decreases, the transition to Wenzel status is facilitated.

When a microstructure is immersed in liquid, which is the case for the present work, the entrapped air cavities are isolated from the ambient; a depinned metastable state is formed, as shown in Figure 5-14 (c). The balance is established when both mechanical and chemical equilibriums are achieved. The mechanical equilibriums can also be described by equation (5-6). However, the air pressure depends on the compressibility of air. For the chemical equilibrium, the main contributing factor is the chemical potential gradient of the air across the liquid-air interface. Therefore, the wetting transition is affected by air diffusion under different pressure. The transition time span is from several minutes to days.

### 5.3.1.3 *Ultrasound-assisted wetting*

Ultrasonic waves are sonic vibrations with a frequency above 17 kHz - beyond the audible range of a human being. Ultrasound is used in a wide range of physical, chemical and biological processes. Homogenizing, emulsifying, and dispersing are examples for physical processes. Most of the applications of high intensity ultrasound are based on cavitation effects (Hielscher, 2005). When sonicating liquids at high intensities, the sound waves that propagate into the liquid media result in alternating high-pressure (compression) and low pressure (rarefaction) cycles, with rates depending on the frequency. During the low-pressure cycle, high-intensity ultrasonic waves create small vacuum bubbles or voids in the liquid. When the bubbles attain a volume at which they can no longer absorb energy, they collapse violently during a high pressure cycle. This phenomenon is termed cavitation. Ultrasound can reduce the contact angle by changing the balance of interfacial energies between the solution, microstructure and the air bubble in the microstructures.

## 5.3.2 **Materials and Experiments**

### 5.3.2.1 *Materials and property*

#### **PDMS**

Polydimethyl-siloxane (PDMS) is an elastomer polymer composed of covalently bonded alternating Silicon and Oxygen atoms forming the siloxane. Water stable end groups are the Trimethylsilyl groups resulting in the formula:  $\text{H}_3\text{C}-((\text{CH}_3)_2\text{Si}-\text{O})_n-\text{Si}(\text{CH}_3)_3$ . Two Methyl-groups attached to each Silicon atom completes the structure of this polymer. The methyl-group is

after the  $-CF_3$  –group one of the lowest surface energy groups of organic groups. This chemical composition of PDMS offers a good internal mobility and flexibility of its molecules and a free volume. This allows the molecules to align efficiently at interface with other materials. Depending on the chain length (suffix n) and the cross linking level, PDMS can be found under liquid, resin or elastomer form. It has a good thermal stability, resistance to UV, excellent release properties, highly permeable to gases while being hydrophobic. Its surface tension is around 40 [mN/m] depending on the viscosity (C.M.Kuo, 1999).

The present PDMS (Sylgard 184) kit is from Dow Corning Corporation. The kit contains two chemicals: Base (part A) and Curing Agent (part B), which are mixed in 10:1 mass ratio. Both the chemicals are transparent and quite viscous in nature.

### ***Paraffin***

Paraffin wax is a derivative from the oil industry. It is mainly composed of alkanes - hydrogen saturated carbon chains. Paraffin melting point ranges from 50°C to 70°C depending on the chain length distribution of the alkanes. The viscosity increases with the melting point increase. Paraffin is a stable and non-reactive material with most of the chemicals, though it is affected by UV-light and temperature. Values for surface tension are ranging from 22 to 35 [mN/m] (Jańczuk and Białopiotrowicz, 1990). Shorter alkanes have even lower surface tension, but are not called wax any more.

### ***Beeswax***

Beeswax is produced by the honey bees. It has a melting point around 62°C and is used as a glazing agent in cosmetic or food industry to retain water, so it acts as a hydrophobic material. It can be used a sealing wax or lubricant as well. It is softer than paraffin wax.

### ***HPMC***

HPMC is also called hypromellos. It is a water-soluble polymer derived from cellulose. It used extensively in medical area for oral drug release because of its properties of water-retention agent and ability to form a gel-layer acting as lubricant. HPMC can dissolve in ethanol and propanol as well. Dissolution does not depend on pH. Solution of HPMC is highly transparent. Amongst its properties, HPMC is inert material, viscoelastic polymer, lubricant, can form films and is used as emulsifier. Its surface tension ranges from 42 to 56 [mN/m] while water is 72 [mN/m] at 20°C. A typical surfactant has a surface tension of 30 mN/m.(Phadtare, Phadtare and Asawat, 2014).

#### ***5.3.2.2 Replication procedures***

Two types of replication experiments were investigated. The first one studied the replication of a second PDMS from a first PDMS mold. The second replication was focused on the replication

of PDMS from wax microstructures. The replication quality Results were investigated by qualitative observations concerning the ease of de-molding and the appearance of the replica. The UV-cured polymer microstructures from the replicas were characterized using optical microscope.

### ***PDMS-PDMS***

Master mold M0 contains the positive shape of the micro-structure. The first step is the replication of this master mold with PDMS resin. It gives the contrary shape of the master mold labelled M1-a. The PDMS was prepared with Sylgard 184 resin and curing agent. The ratio resin/agent was 10:1. After the homogenous mixture was poured onto the master mold M0, it was placed under vacuum for degassing for 30 minutes. Degassing step allows a good fill of the master grooves and removes air bubbles induced by the mixing. To cure the resin, the preparation was put in oven for 2h30mins at 80°C. After these steps M1-a was ready and could be released from M0.

The second step consisted of the replication of M1-a to another PDMS layer with positive micro- structure pattern. This second PDMS replica (M2) was prepared with the same recipe as M1-a. Because the same resin was used, it needed an anti-adhesive interlayer to avoid self-polymerisation between M1-a and M2. This interlayer was a solution of tap water and HPMC. In the experiment, concentration of 0.1 wt%, 0.3 wt% and 0.5 wt% of HPMC were tested. The interlayer solution was poured onto M1-a becoming the coated mold M1-b. In order to have a good structure wetting, M1-b went in ultrasonic bath for 30 minutes. When the bath was done, excess solution was carefully removed with help of compress nitrogen. The gas below was perpendicular to the cross-section, i.e., along the extruded direction of the microstructures. The gas blowing promoted wetting and spreading of the HPMC solutions on PDMS microstructures. After drying, the second PDMS mixture (M2) was poured over M1-b layer. The curing step was similar to M1-a curing (2h30 in oven at 80°C). M2 was then peeled off from M1-b.

Three microstructures were investigated for the replication of PMDS from PDMS. The sketch of the cross-sections for the three microstructures on the master molds M0 are shown in the Figure 5-15. For the light-redirecting microstructures, the resulted pattern on the master mold was with sharp edges consisting two asymmetric parabolas; the periodicity was 50  $\mu\text{m}$  and the height of the edges was about 90  $\mu\text{m}$ . For the used master mold with CPC 30-30 and CPC 40-40 micro grooves, the exit apertures were approximately 50  $\mu\text{m}$ ; however, the width of the base was different, as indicated in Figure 5-15.

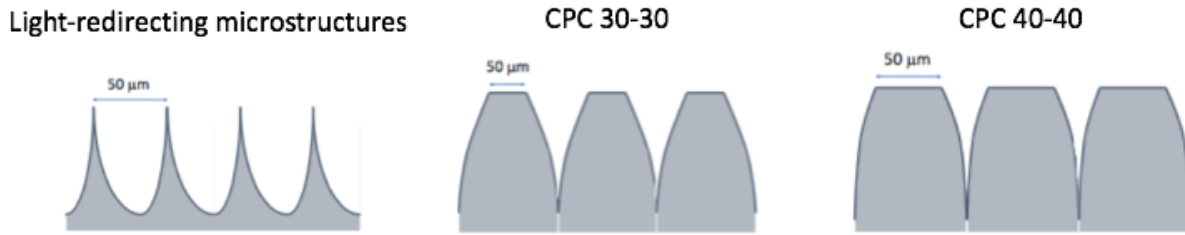


Figure 5-15. The three investigated microstructures for the replication of PDMS from PDMS.

### ***PDMS-Wax***

The other set of replication was PDMS casting from wax substrates. The preliminary feasibility study was conducted on the wax substrates containing 5 wt%, 10 wt%, 20 wt% beeswax and the rest of paraffin. Beeswax softens the mixture when it solidifies which is practical to pattern the micro-structure on it. The substrates mentioned above with no microstructures were immersed in the solutions with HPMC of different concentrations ((0.1 wt%, 0.3 wt% or 0.5 wt%) for 24 hours. It should be noted that, the wax substrates in the HPMC solutions were not placed in the ultrasonic bath. After the HPMC coating, the substrates were left for natural drying for about 24 hours. The PDMS liquid was poured on the substrates and cured at room temperature for more than 48 hours.

The beeswax concentration was optimized based on the replication on the non-texturized substrates. After that, four microstructures with the combs shown in Figure 5-12 were engraved on the wax substrates with the optimized beeswax concentrations. The optimized wax mixtures for the retro-reflective microstructure was 10 wt% while for the micro CPCs it is 5 wt%. PDMS replication from texturized substrate with 0.5 wt % HPMC layer was conducted.

## 5.4 Shape fidelity analysis during UV-printing

UV-curing resins are materials that are polymerized and cured in a short time by the energy radiated from ultraviolet irradiation devices. A UV curing formulation contains two main components [63]: a photoinitiator that effectively absorbs the incident light and generates initiating radicals, and a monomer and/or an oligomer with at least two unsaturation ( $C=C$ ) that will generate the polymer network. Compared with thermosetting polymer, the UV-curable resins have the following advantages:

- The curing speed is very fast and can be within a few seconds for a film of several  $\mu m$ .
- There are fewer restriction and the process is more controllable during UV coating or imprinting, because the polymer stop curing without UV irradiation
- They can cure at room temperature.

Acrylated polyesters hyper branched polymer (Gao and Yan, 2004) is one of the most commercialized UV-curable polymers, due to their relative low cost and the large number of esters available which allows for a wide variation of properties. They are produced in a wide range of viscosities and are mainly used in printing inks, wood and paper coatings. In the present work, the acrylated polyesters HBP (CN2305 Sartomer) with the functionality of 16 is chosen. Its glass transition temperature is about  $165^{\circ}C$ . The structure of the monomer is shown in Figure 5-16 (Gonzales Lazo, 2015).

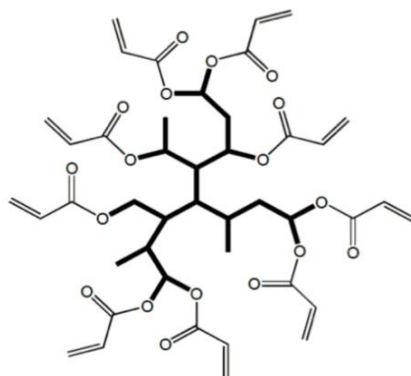


Figure 5-16. The monomer structure of the acrylated polyester hyperbranched polymer (Gonzales Lazo, 2015).

The present section focuses on i) analyzing the dimensional changes of various UV-printed microstructures related to polymerization, internal stress and thermal aging; and ii) identifying the impact of these changes on the optical properties with respect to redirection of the system. The study will try to answer the following research question

- How does the photoinitiator concentration affect the dimensional change of the microstructures?

- How does the microstructure evolve under thermal aging?
- What are the differences of the dimensional changes for microstructures with different geometrical parameters (shape and scale)?

## 5.4.1 Basics of Acrylated polyesters HBP

### 5.4.1.1 Polymerization reaction and kinetics

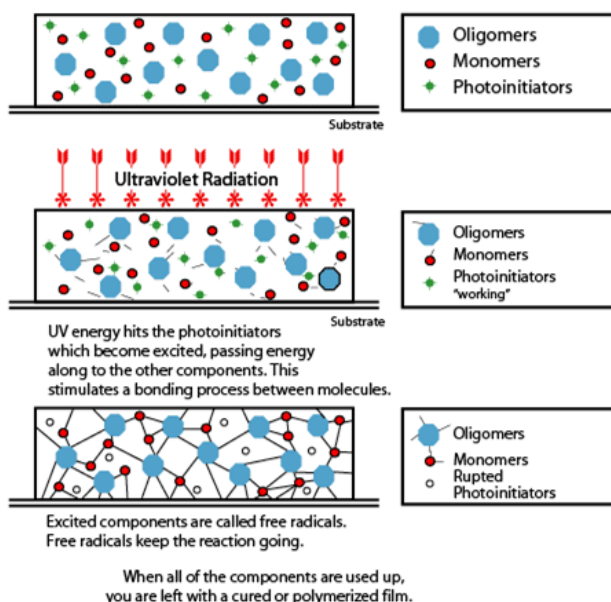


Figure 5-17. The sketch of UV curing process (Brilliant Universal Limited, 2012).

As shown in Figure 5-17, acrylates photopolymerization can be summarized into the following steps: formation of initiator radicals, chain propagation, and termination. There are numerous studies, investigating the underlying kinetics of crosslinking highly functional acrylates (Andrzejewska, 2001). The complexity of the crosslinking reaction stems from the diffusion-controlled chemistry, including effects such as gelation and vitrification. Kurdikar and Peppas (Kurdikar and Peppas, 1994) developed a model for diffusion-controlled crosslinking photopolymerization and verified it for diacrylate monomers.

Figure 5-18 shows typical kinetic curves for a monometh- acrylate (Andrzejewska, 2001): polymerization rate ( $R_p$ ) as a function of time ( $t$ ), degree of double bond conversion ( $p$ ) as a function of time and  $R_p = (f_p)$ . At the beginning of the reaction, a sharp increase in the rate of polymerization is observed, which corresponded to gelation or autoacceleration. As conversion gets higher, the gel effect appears to stop and the polymerization rate reaches maximum value,  $R_p^{max}$ . After the maximum rate, the polymerization rate  $R_p$  decrease due to the significantly decreased amount of monomers and vitrification. The key element which leads to the termination is limited diffusion, both translational and segmental. Each of diffusion are affected differently by

the level of conversion. Translational diffusion is the diffusion of the mass center of a polymer coil; it is chain-dependent, and decreases as polymerization proceeds due to an increasing viscosity of the system. Segmental diffusion is defined as the reorientation of two macroradicals, leading to two radicals' ends are sufficiently closed to each other for chemical reaction to form a radical  $\pm$  radical encounter pair (Andrzejewska, 2001). It is independent of chain length; however, it increases as the decrease of the size of polymer coils.

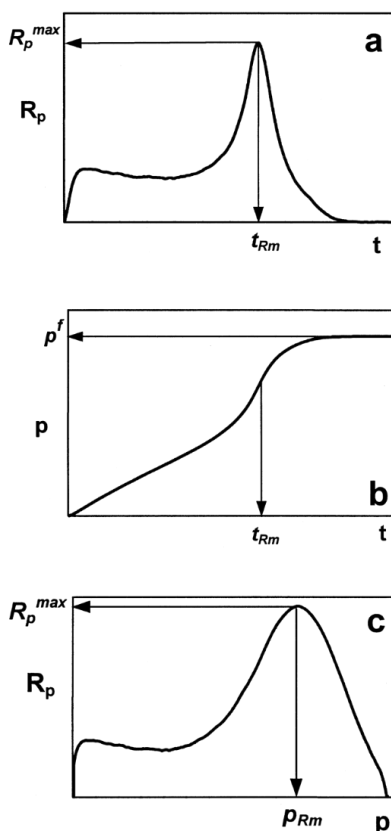


Figure 5-18. Typical shapes of kinetic curves for the polymerization of a monomethacrylate monomer (Andrzejewska, 2001): a) polymerization rate as a function of irradiation time; b) conversion of double bonds as a function of time; and c) polymerization rate as a function of double bond conversion.

#### 5.4.1.2 Viscosity

The viscosity of hyperbranched polymer is lower than that of their linear counterparts (Boogh, Pettersson and Månson, 1999) and they behave more like a Newtonian fluid, due to the absence of entanglements (Luciani *et al.*, 2004); the relatively low viscosity enables the synthesis of comparatively high molecular weight photo-curable polymers.

#### 5.4.1.3 Shrinkage

The origin of polymerization shrinkage is because of a change in interatomic spacing between molecules. Before polymerization, monomer molecules are about 4 Å apart (Van der Waals length



scale). During polymerization, the interatomic spacing is replaced by single covalent bonds of about 1.5 Å length. Hence, shrinkage occurs during polymerization and is related to conversion.

### **5.4.2 Mechanics of materials**

Poisson effect is the phenomenon in which a material has the tendency to expand in directions perpendicular to the direction where the compressive force is applied. Assuming that the material is stretched or compressed along the axial direction, the resulting Poisson's ratio is the ratio between the change of the transverse strain and the change of axial strain. Normally for a stable and isotropic polymer the Poisson's ratio is about 0.4

### **5.4.3 Parameters and experiments**

The kinetics of bulk photopolymerizations is a largely diffusion-controlled process (Schmidt, L. E., Leterrier, Y., Schmäh, D., Månson, J. A. E., James, 2007). Parameters influencing the curing behavior include temperature, UV intensity, photoinitiator concentration, and the nature of the monomer. In the present work, we focus on the stability analysis with respect to. Based on the related results, we can optimize the parameter, the scale and improve the processing procedure.

#### **5.4.3.1 Concentration of photoinitiator**

Conversely, if the concentration of photoinitiators were kept too low, photocurable composite materials could be under-cured (Alonso *et al.*, 2014). If inadequate levels of conversion were achieved in the polymerization, mechanical properties and wear performance could be compromised (Ferracane *et al.*, 1997), amount of leachable residual monomer increase and color stability might decline (Imazato *et al.*, 1995; Nomura *et al.*, 2006; Brandt *et al.*, 2010). However, if conversion were maximized to reduce these difficulties, then problems inherent polymerization shrinkage of the composite become more critical (Ferracane *et al.*, 1997). Figure 5-19 (Macarie and Ilia, 2005) shows conversion versus exposure time for polymerization of diacrylate monomer with different photoinitiator concentration, in the presence of 3 wt% tertiary amine (triethyl amine) as synergist additive at 30°C. Generally speaking, higher conversion occurs with higher concentration of photo initiator for a UV-curable polymer.

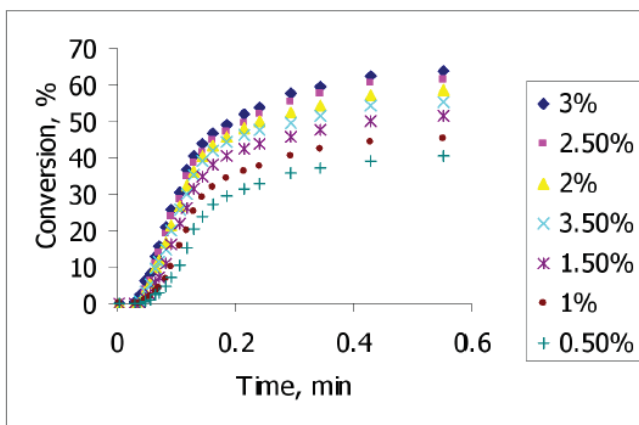


Figure 5-19. Conversion versus exposure time for polymerization of diacrylate monomer with different photoinitiator concentration, in the presence of 3 % (w/w) tertiary amine (triethyl amine) as synergist additive at 30°C (Macarie and Ilia, 2005).

One more issue related to photoinitiator concentration, is oxygen inhibition. The polymerization of hyper-branched polymer is called free radical polymerization, in which highly reactive free radicals drive a chain-growth reaction. However, early chain termination can occur when radical molecules react with oxygen in the atmosphere, resulting in an incomplete cure at air exposed surfaces. This phenomenon is called as oxygen inhibition. Oxygen inhibited surfaces are normally tacky or sticky, which could present issues for sealants, encapsulants, and coatings. Molecular oxygen easily reacts with any free radical, including the initiator molecules. This quenching results in the initiator losing its radical and reactive state, which subsequently lowers the number of free radicals produced by the initiator, less initiated polymer chains, and of course a fewer number of final polymer chains produced.

In the present work, the dimensional stability in terms of shrinkage will be investigated for the HBP with the three photoinitiator concentrations: 1.5%, 3% and 6%, at room temperature (20°C). The feasible concentration will be optimized based on the dimensional stability, color stability and surface quality.

#### 5.4.3.2 Accelerated aging test

Polymers are out of thermodynamic equilibrium (Bystritskaya, Pomerantsev and Rodionova, 1999). Their structure and their properties are changing in the course of time even in the absence of external influence. The physical–chemical process of change in polymer properties in the course of time is called “aging” of polymer materials. The prediction of such aging is the problem to be solved. A common approach to evaluate the aging property of polymer is based on the following equation (Hukins, Mahomed and Kukureka, 2008):

$$f = 2^{\Delta T/10} \quad (5-7)$$

Where  $f$  is the factor by which rate of aging is increased.  $\Delta T$  is the temperature difference between the elevated temperature at which the effects of aging are accelerated and the reference temperature. Equation (5-7) comes from the Arrhenius equation (Hemmerich, 1998; Bystritskaya, Pomerantsev and Rodionova, 1999) which relates the chemical reaction rate, temperature and activation energy. The Arrhenius equation shows an exponential increase of the reaction rate with the increase of temperature.

In the present work, the elevated temperature is at 80°C while the reference temperature is assumed to be at room temperature, which is at 20°C. It should be noted that this relation should be valid only when the temperature is far from the glass transition temperature of the polymer. Based on equation (5-7), we know that the aging rate is 64 times than that at the room temperature. Geometrical parameters (scale & shape) of the microstructure. The HBP microstructures A with sharp edges was placed in the oven at 80°C for up to two weeks.

#### 5.4.4 Equipment

Three UV light-emitting diodes (LEDs) (as shown in Figure 5-20 (a) ) with a spectrum peak at 375nm. The LEDs are of Seoul Semiconductors (P8D2 275) and have a full width at half maximum (FWHM) of 11nm. An etched Fällander glass is place below the light source to diffuse the light and increase the uniformity of the light distribution. A power controller is connected to the light source. The controller controls the output power and thus the UV intensity reaching a sample.

During UV imprinting with a PDMS stamper, drops of liquid HBP with the selected photo concentration were placed on a well-cleaned glass substrate. Then the PDMS stamper is print on the HBP drops. The liquid HBP will spread throughout the PDMS stamper under its pressure and the capillary force due to the microstructure on the stamper. After that, the sample was exposed to UV light at an intensity of around 8 mW/cm<sup>2</sup> for 180 s, and then was flipped to the side where the HBP microstructure received the UV light first for 90 s; by this step, the liquid HBP is solidified on a glass substrate and the PDMS stamper was detached from the HBP microstructure

During UV imprinting with a wax stamper, the wax stamper was placed first; liquid HBP was dropped on the wax stamper and then a well-cleaned glass substrate was placed on the wax stamper. Then the sample was exposed to UV light at an intensity of around 8 mW/cm<sup>2</sup> for 180 s, and following that the sample was flipped to the side where the wax stamper received the UV light first for 90 s; after that, the rest steps are identical for the UV curing with a PDMS stamper.

More experimental details concerning UV imprinting can be found in the publication of (Kostro, A., et. al., 2015)

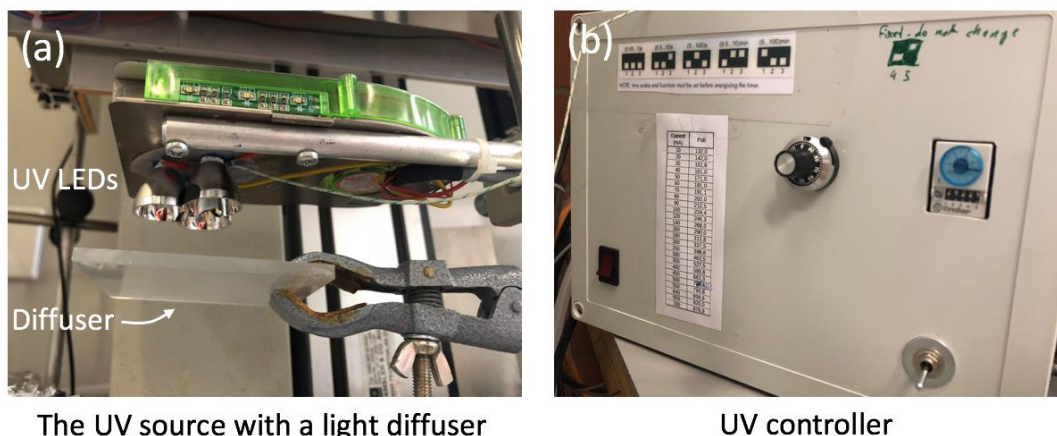


Figure 5-20. Photograph of the UV light source for UV imprinting: (a) the UV LEDs with a light diffuser and (b) the controller to vary and UV intensity and the exposure time.

### 5.4.5 Shape fidelity analysis

The dimensional changes for two different UV-imprinted microstructures were studied: a) light-redirecting HBP microstructures with sharp edges, and b) trapezoid-like HBP microstructures for which the master molds are the CPC micro grooves fabricated by laser ablation. The impact related to the concentration of photoinitiator, internal stress, thermal aging, and the shape of the UV-imprinted microstructure on the dimensional changes were identified.

Cross-sectional contours of HBP microstructure for each experimental case was selected and their contours were extracted using the software WebPlotDigitizer with step size around  $2.5\ \mu\text{m}$ . The contour of the negative PDMS microstructure was also determined as reference. The parabolic edge was fitted with second order polynomial functions. The relative dimension changes of HBP microstructures with respect to the PDMS reference were calculated. The extracted parabolic edges were used for ray-tracing simulation with CFSpro and their angular dependent transmittances at normal incidence were calculated, in order to analyze the impacts of the dimensional changes on the optical properties.

## 5.5 Thin film deposition

Due to its good directionality and compatibility with polymer material, thermal evaporation deposition is utilized for the thin-film deposition in the present work. In the following section, the principles and experimental setup, the coating procedures and the used materials will be introduced. The goal is to achieve the appropriate optical properties for various applications by varying the thin film thickness and the deposition materials.

### 5.5.1 Principles and experimental setup

One of the Physical Vapor Deposition (PVD) method is thermal evaporation. During the thermal evaporation, the material from a thermal vaporization source reaches the substrate with little collision with gas molecules. The thickness of the coatings (thin films) usually ranges from nanometers to microns. The deposition materials can be metals, oxides and nitrides. The substrates can be any of a wide variety of things such as silicon wafers, solar cells, optical components, etc.

The heating device in the deposition is a simple electrical resistive heating element, i.e., filament. The heating element is called boat which is a thin sheet of high temperature metal (e.g., tungsten) with an indentation or a trough in which the deposition material is placed. Low voltage but high current (usually several hundred Amps) goes through the boat to generate enough heat. Several rotatable sample holders of 80-mm long  $\times$  28-mm wide were fabricated and installed in the evaporation chamber. With the rotatable sample holders, desired deposition angles between the evaporated particle beam and the norm of the sample can be achieved to obtain coating on certain surface of a microstructure. The surface-selective coating will be further introduced in section 5.5.2 The deposition rate and the thickness of a thin film is measured by quartz crystal microbalance (QCM), and the values are read from the monitor (FTM-2400 from Kurt J. Lesker Company). The distance from the thermal vaporization source to both the quartz and to the was about 32 cm. Therefore, in the present thesis, the thickness read from monitor (i.e., nominal thickness) was used to represent the thickness on a sample. The configurations of the PVD chamber (Balzers BA 510) are shown in Figure 5-21.

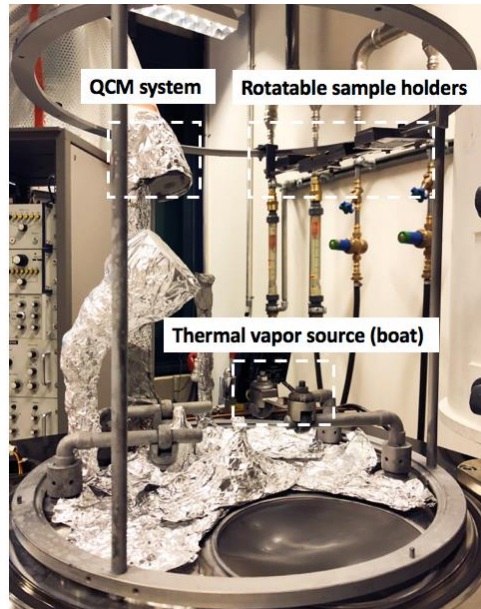


Figure 5-21. The configurations of the thermal evaporation chamber.

### 5.5.2 Facet-selective coating based on self-shadowing effects

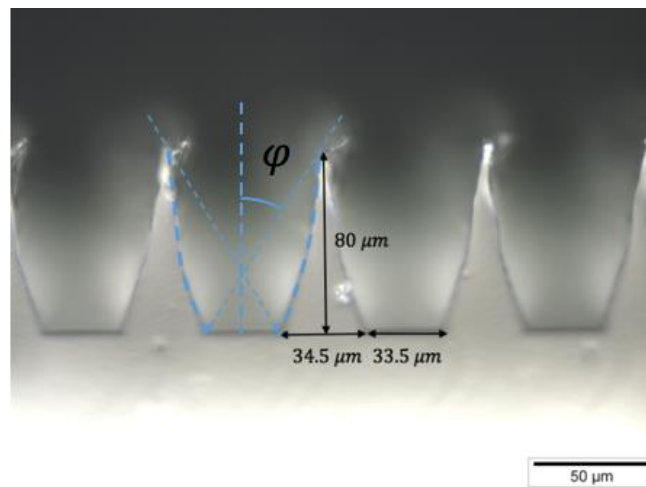


Figure 5-22. The self-shadowing effect of a microstructure for facet-selective coating.

The principle of facet-selective coating based on the self-shadowing effects of the structure. In PVD coating, the coating particles or vapor travels in a specific direction. The free parameter that determines where the structure should be coated is the angle between the particle beam (or the vapor) and the norm of the sample, and the angle is named as deposition angle. Whether the geometrical effect of shadowing will work for small feature sizes has been investigated for different types of coatings (Walze *et al.*, 2005). Figure 5-22 presents the self-shadowing effect of a microstructure for facet-selective coating. The dashed lines with arrows represent the incident angle of the particle beams for partial facet-selective physical vapor deposition. The dashed curves

show the surfaces where the highly reflective materials are deposited, and therefore,  $\varphi$  is the deposition angle. After thin film coating and encapsulation, a clear view seen through a sample with embedded micro-mirrors can be achieved.

### **5.5.3 Coating with post-polishing**

One of the alternatives to get the coating only on the desired surface is post polishing after coating. In the present work, the post-polishing was applied on the micro CPC30-30 with ultra-fine Silicon Carbide grinding paper (Struers, FEPA P4000, and the diameter of the grain size 5  $\mu\text{m}$ ) using a polishing machine (Struers Tegramin 25).

### **5.5.4 Coating Materials**

#### ***Al***

Mirrors are obtained when reflective metals with appropriate thickness deposit on the microstructures. Due to its low cost, high reflectance (generally over 0.9 for the wavelength from 248 nm to 10  $\mu\text{m}$ ) and low roughness, aluminum is chosen for mirroring the sample. Samples with various thickness of Aluminum coating were prepared.

#### ***Ag***

Silver films have been of considerable interest for years due to their better performance relative to other metal films in optical applications: the highest reflectivity and the lowest polarization for the full IR region and down to a wavelength of 400 nm. Particularly, its semi-transparency with spectral selectivity can help achieve the angular-dependent transmittance while maintain relatively good transparency.

#### ***Indium tin oxide***

Indium tin oxide (ITO) is one of the transparent conductive oxides and widely used in optoelectronic devices, mainly due to its unique combination of high transparency to visible light and rather good conductance. The two properties mentioned depends on the deposition techniques of ITO. For buildings, ITO is used for low-emissivity glazing due to its high reflectance in the infrared range. The ratio of weight percentage between Indium Oxide and Tin Oxide is 90% to 10%. The common methods for preparing ITO thin films are magnetron sputtering, electron beam evaporation, pulsed laser deposition, etc. Thermal evaporation is possible, but it will be difficult for ITO. In thermal evaporation, controlling the stoichiometry very challenging because the indium oxide and tin oxide will evaporate based on their individual melting point.

The facet-selective coating based on microstructures' self-shadowing effect requires directional coating methods. Therefore, despite of the difficulty above, in the present work, a preliminary

study concerning the feasibility of ITO coating using thermal evaporation is conducted. ITO thin films deposited on glass substrates and Si (Miller indices: 100, SE-Mat) substrates are prepared in the thermal evaporation chamber. During deposition, no oxygen is induced in the chamber. The deposition is naturally stopped until the the ITO pellet on the boat for evaporation is almost used up. After deposition, some of the samples are annealed at 490° in oven in atmosphere ambient for 1 hour, and then slow cooled down in oven to room temperature. Spectrum characterization is conducted on the samples. Structural and compositional characterization are conducted with SEM.



## 5.6 Roll-to-roll extrusion for upscaling

Roll-to-Roll (R2R) production is widely used for thin film based electronic devices (e.g. solar cells, active matrix TFT backplanes and touch screens, etc.). It is cost-effective, generates lightweight and flexible substrates and give high throughput production. R2R ultraviolet (UV) imprinting lithography stands out as one of the most promising R2R technologies to fabricate optical films due to its high resolution and environmental friendliness. Alternatively, R2E hot extrusion is considered. In the present work, the preliminary feasibility study has been conducted on R2R extrusion.

The extrusion coating process is done for various microstructures at a pilot production line at Danapak Flexibles A/S. During the extrusion coating process, the melted polymer (Polypropylene (PP)) is extruded through a flat nozzle directly onto the carrier foil made from Polyethylene terephthalate (PET) (Okulova *et al.*, 2017). The melted PP is then pressed against the cooling roll, where it solidifies and sticks to the surface of the carrier foil. The sketch of the extrusion procedures is shown in Figure 5-23 made by (Murthy *et al.*, 2016). The main factors which impact the replication fidelity are the crystallinity of the extruded polymer, the output, the temperature of the cooling roll and the pressure on the cooling roll, and the line speed.

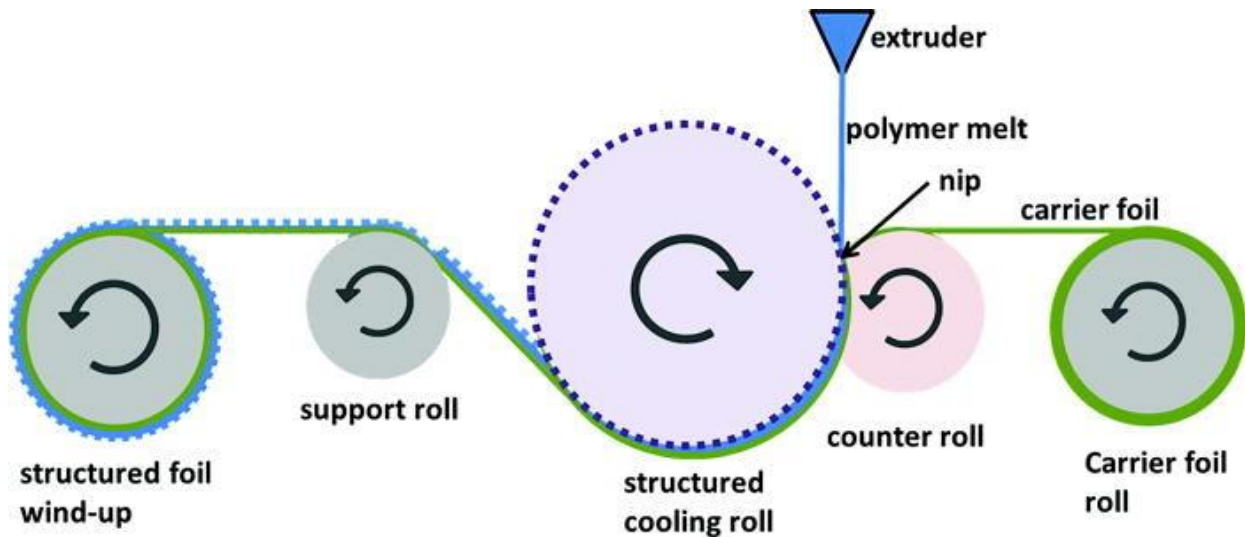


Figure 5-23. The sketch of the extrusion procedures (Murthy *et al.*, 2016).

## **5.7 Characterization and measurements**

### **5.7.1 Structural characterization techniques**

#### **5.7.1.1 *Optical microscope***

A conventional optical microscope (Olympus BX60), which is often referred to as a light microscope, is used for 2-D profile analysis. The optical microscope consists of five objectives with the magnification factor of 5, 10, 20, 50 and 100, respectively, and an adjustable halogen light source of 100 W.

#### **5.7.1.2 *Confocal microscope***

A confocal laser scanning microscope (Keyence VK-8700) is used for high-resolution images and 3D surface analysis. Unlike conventional microscope, the confocal incorporate two light sources: a white light and a laser source of 658nm. The white light source is used for collecting the color of the surface, whereas the laser is used for scanning the object surface collecting detailed height information. The laser is scanned in the XYZ directions to collect data throughout the entirety of specified range. The lateral resolution in the X-Y plane is determined by the diffraction limit of the focused spot. Vertical resolution along Z direction depends on the piezo devices and is down to several nanometers. As a result, accurate microstructured profiles and surface topography can be obtained using confocal microscope.

#### **5.7.1.3 *Scanning electron microscope***

In the present work, the thickness of the deposited thin films was from 10 nm to 100 nm. Therefore, structural characterization technique which gave the resolution down to the order of several nanometers was required for the deposited thin films. Scanning electron microscope (brand name FEI XLF30) was chosen for the present study.

Instead of using light, scanning electron microscope (SEM) uses electrons to interact with sample materials (Khursheed, 2011). The electron is emitted from the electron gun due to an electrostatic field in SEM. The emitted electrons, focussed and accelerated to the optimized energy level by magnetic fields, then arriving on the surface of a sample. Back scattered electrons are the incident electrons which change directions due to high angle diffusion by nucleus, without significant change in their kinetic energy. Larger atoms are much stronger scatters of electrons than light atoms, and therefore produce a higher signal. The number of the backscattered electrons reaching the detector is proportional to their Z number. After the interaction of the incident electrons and the materials, electrons at the transition valence or conduction band of the composition of the materials are ejected. Such ejected electrons are called secondary electrons. Secondary electrons are mainly generated near the surface. The intensity and the special

distribution of secondary electrons are sensitive to the surface topology. Therefore, secondary electrons are useful for the inspection of the surface topology. The relaxation of excited atoms can result in fluorescence X-ray which is a characteristic of the transition and thus of the element. If the transition energy is low and the emitted wavelength is in the range of visible light, one can see fluorescence light. The relaxation of excited atoms can also generate the so-called Auger electrons. When a vacancy is created due to the ejection of a core electron, an electron from a higher energy level may fall into the vacancy, leading to a release of energy. The released energy can be absorbed by another electron, and this electron run away from the atom with a characteristic energy.

## 5.7.2 Optical characterization

### 5.7.2.1 Spectrometers

In the present work, a spectrometer (Oriel, model 77400, MultiSpec 125TM, type 1/8m) with integrated sphere (LOT, RT-060-SF) was used to measure the total (diffuse + specular) transmittance and or reflectance. The spectrometric set-up consists of a halogen light source (Osram 64642 HLX, 150 W, 24 V, Xenophota), and a sensor with silicon photodiode arrays (composed by 1024 photodiodes, model 77090, Intaspec II TM detector head). With the spectrometric mentioned above, a spectrum from 400 nm to 800 nm was first measured. Then, a monochromator (Optronic Laboratories, OL 730-PbS) was used in order to obtain the spectrum from 800 nm to 2500 nm. The resolution was set at 10 nm. Therefore, the wavelength range for the spectrum could be extended from 375 nm to 2500 nm. The sample was placed at the first opening of the integrated sphere to measure the signal of all the transmitted rays (called total transmittance), and the second entrance was covered with a white board. The incident light rays arriving on a sample were at normal incidence and near normal. For a measurement of the signal of all the reflected rays (called total reflectance), the sample was placed on the second opening, as shown in Figure 5-24. The estimated error bar for a measurement was  $\pm 0.02$  in terms of transmittance (reflectance) (Paone, 2012).

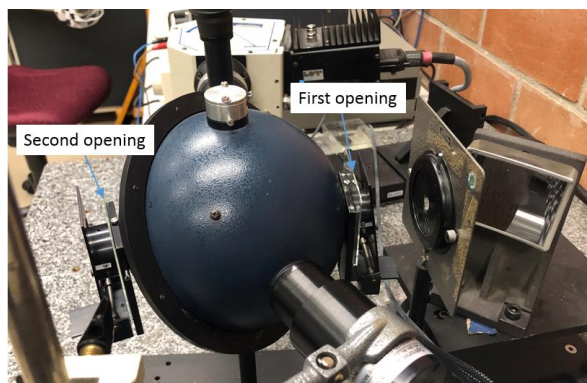


Figure 5-24. Integrated sphere with the first and second opening.

Direct transmittance in the wavelength range from 350 nm to 1800 nm (UV-Vis-NIR) was also measured with the set-up shown in Figure 5-25. This experimental set-up was composed of a light source with near UV, visible and near-infrared light, a receiver collimator with a aperture with 28-mm diameter and a Zeiss diode array spectrometer. For direct transmittance, the collimator was placed in line with the light source. When the wavelength was smaller than 500 nm, the wavelength accuracy was 0.5 nm, otherwise it was 1 nm.



Figure 5-25. The set-up for the measurement of direct spectral transmittance.

#### 5.7.2.2 Mini-goniophotometer

In order to estimate the angular-dependent optical properties of the samples, a mini-goniophotometer was developed by (Kostro, 2015). The mini-goniophotometer consists of a collimated halogen light source with a rectangle beam shape of 22 mm × 2.4 mm, an angular-selective detector based on silicone photodiode, several motors with a computer driven which controls the incoming angle of the beam and the scanning angular range of the detector, as shown in Figure 5-26. The transmittance was accurately measured until 83° of incidence (Kostro, 2015). The angular resolution of the detector was 0.1°. The top view sketch (with respect to Figure 5-26) of the measurement principle for transmittance distribution and the total transmittance is shown in Figure 5-27. The sample could be rotated with a motor in order to change the incident angle. Then the sample was fixed, and the detector was scanned around the norm of the sample. In the present work, the scanning range was ± 80°. The scan of the sensor was in-plane movement along the dash line. The scanning step is 0.2°, corresponding to the arc length of 0.5 mm.

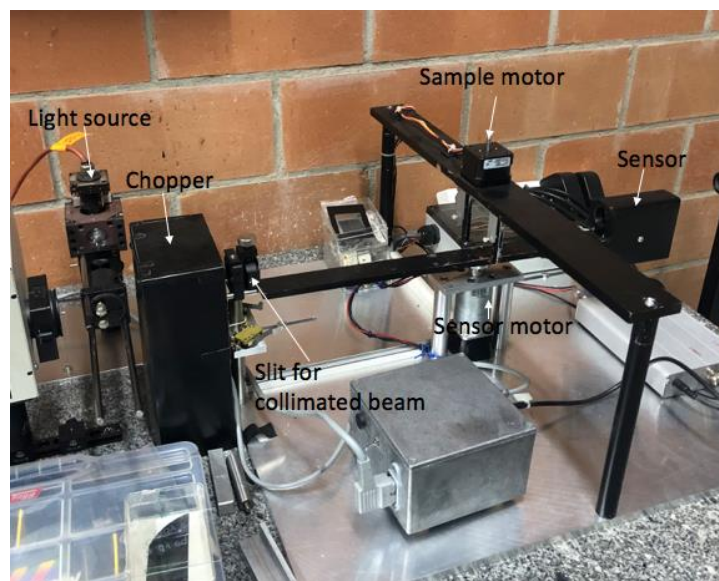


Figure 5-26. The set-up of the mini-goniophotometer.

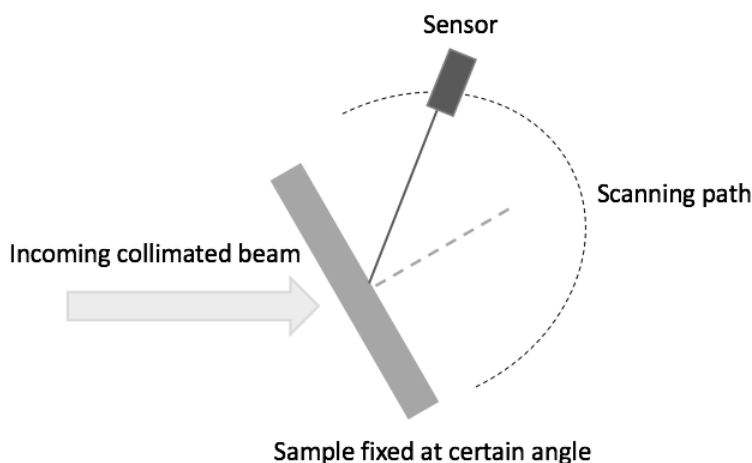


Figure 5-27. The top view sketch (with respect to Figure 5-26 of the measurement principle for transmittance distribution and the total transmittance.

The measurement of a sample with embedded CPCs was carried out between the measurements for a clear glass substrate as references. Assuming that at normal incidence the average transmittance of a clear glass was 0.92 in the visible light range, by comparing with the counts of the measurements for the samples, the first angular transmittance of the sample was calculated. The transmittance of a sample and a clear glass at normal incidence was also measured with the integrating sphere (introduced in 5.7.2.1), and then the results from the two device were compared. It was found that, at normal incidence, for the samples with opaque reflective coating, the first transmittance obtained from the mini-goniophotometer was 0.08 – 0.15 lower than the results from the integrating sphere; for the samples with semi-transparent coating, the discrepancy was 0.05 – 0.1. Based on the results of comparison, the angular-dependent transmittance of the sample was

considered as the sum of the first transmittance and the discrepancy value. The discrepancy was mainly due to the fact that, the mini-goniophotometer only carried out the measurement in 2-dimensions; however, the scattering of light by a sample was in 3-dimensions. The error bar of the angular-dependent transmittance, estimated for samples with opaque reflective coating was  $\pm 0.12$ , whereas for samples with semi-transparent coating it was  $\pm 0.08$ .



# Chapter 6 Simulation results and discussion

In the present section, the experimental validation on the computer modeling for glazing with micro CPCs is presented. The angular-dependent transmittance for glazing with various optical microstructures were calculated with ray-tracing simulations. Sensitivity analysis of angular-dependent transmittance in reaction to the variation of the microstructured height was conducted. In order to evaluate the potential seasonal thermal dynamics, annual dynamic solar gains, and the calculation of direct transmittance as function of working hours, are presented. In order to fully explore the potential advantages of the daylighting system with embedded micro-mirrors, three configurations were investigated: (i) micro-mirrors in the upper third of a double glazing, (ii) micro-mirrors in the upper two-thirds of a double glazing and (iii) micro-mirrors in the whole glazing. Metrics based on illuminance, uniformity, glare and directivity were used to assess daylighting performance for a south-facing façade in Lausanne (latitude  $46^{\circ}30'$  N, longitude  $6^{\circ}37'$  E), Switzerland.

The adaptability to diverse façade orientation, tilted angle of the glazing with respect to the horizon, locations, and climates for the proposed glazing is also presented throughout the evaluation of the potential advantages mentioned above.

## 6.1 Angular-dependent transmittance from ray-tracing simulation

### 6.1.1 Experimental validation of the computer model for ray-tracing simulation

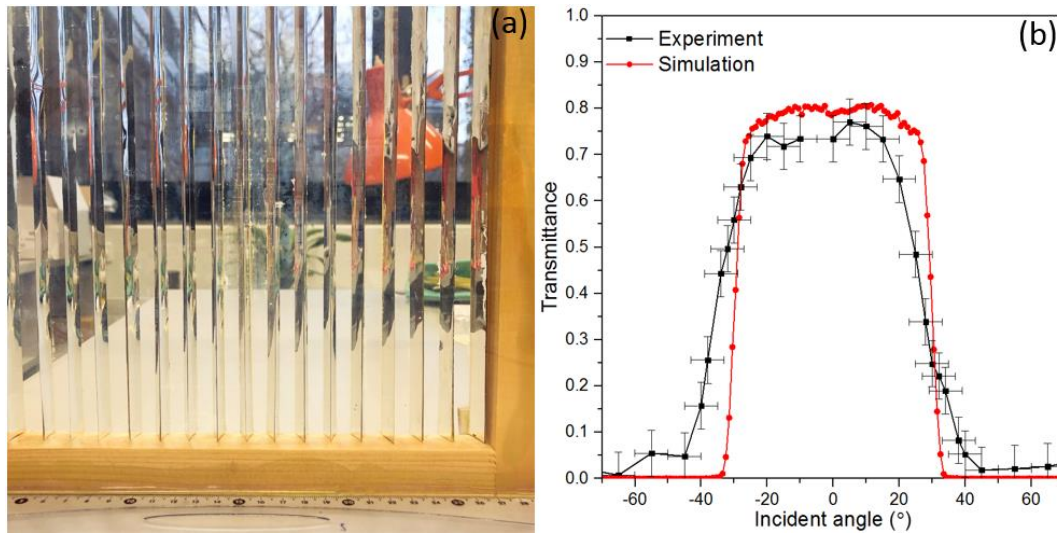


Figure 6-1. (a) The prototype of the milimetric CPC arrays placed between two glass panes, and (b) the measured and simulated angular-dependent transmittance at the azimuth angle of  $0^{\circ}$ .

A prototype based on millimetric CPCs with the half acceptance angle of  $30^\circ$  was fabricated in order to validate the computer model for ray-tracing simulation. The macroscopic CPC arrays was fabricated and placed between two glass panes. The prototype is shown in Figure 6-1 (a). The angular-dependent transmittance (diffuse + specular) at  $0^\circ$  azimuth angle had been measured using an integrating sphere (LOT, RT-060-SF) equipped with an monochromator (LOT, Omni 300) and a halogen light source. The measurement result was compared with the simulation results from the ideal CPCs, i.e., CPCs with the correct ratio of the height and the exit aperture, and smooth surface without light scattering. It is shown in Figure 6-1 (b) that, the simulation result agreed very well with the experimental data. The transmittance of the prototype was only about 0.05 less than that of the simulation, for the incident angle between  $-20^\circ$  and  $20^\circ$ . The transmittance dropped dramatically around  $\pm 30^\circ$  for both cases. Instead of the vertical drop at  $\pm 30^\circ$ , there was a slight slope for the drop of the transmittance between  $\pm 30^\circ$  and  $\pm 40^\circ$ . The minor deviation was due to the manufacturing errors which caused the change of the actual dimensions from the design, assembly imperfection which resulted in the imperfect periodicity, and the scattering of light due to the not perfectly smooth surface.

## 6.1.2 Angular-dependent transmittance

### 6.1.2.1 Glazing with “L”-shape retro-reflective optical microstructure

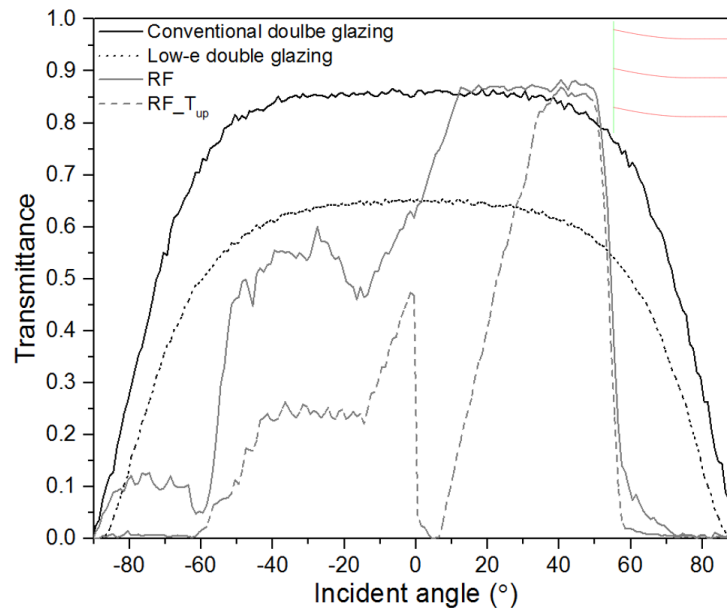


Figure 6-2. The simulated angular-dependent transmittance for conventional double glazing, low-e double glazing, and conventional double glazing with “L”-shape retro-reflective micro-mirrors (“RF” for this type of glazing) at the azimuth angle of  $0^\circ$ . “ $T_{up}$ ” means transmittance due to upward redirected-redredirected light. The sketch of “L” shape microstructure embedded in the polymer layer is shown on the upper right of the figure.



Figure 6-2 shows the simulated angular-dependent transmittance for a conventional double glazing, a low-e double glazing, and conventional double glazing with “L”-shape retro-reflective micro-mirrors at 0° azimuth angle. The application of glazing with “L”-shape retro-reflective micro-mirrors was aiming at vertical or slightly tilted façade. For the aiming application, attention was paid on angular-dependent transmittance in the angular range of 0° to 90°, which corresponded to the solar elevation angle. For the incident angle from 0° to 10°, the transmittance increased linearly from 0.7 to 0.85. For the incident angle from 10° to 50° which corresponded to the solar elevation angle during the working hour in winter and most time of spring in the latitude above 35°, the transmittance is 0.85, which was slightly higher than the conventional double glazing, due to the decrease of incoming angle for the following interface after the light was redirected by the microstructure. While beyond 50°, the transmittance dropped dramatically to about 0.1 at 60°. The transmittance was almost 0 at the incident angle beyond 70°. The big contrast of the transmittance between the low incident angle and high incident angle suggests a sound potential of seasonal thermal dynamics with “L”-shape retro-reflective micro-mirrors.

Another interesting property of glazing with “L”-shape retro-reflective micro-mirrors is its strong light-redirectability. In Figure 6-2, the transmittance due to upward redirected-transmitted light which contributes to daylighting and glare protection, is represented by the dash line. At the incident angle ranging from 0° to 5°, the upward redirected transmittance was low, because the light at this incident angular range was mainly direct-transmitted through the glazing. As the incident angle was higher, more light was redirected upward, therefore, the transmittance of upward redirected-transmitted light increased linearly from 0 to 0.8 from 5° to 30°. Then the transmittance stayed constant at 0.84 in the angular range from 35° to 55°. Thanks to the light-redirectability, glazing with optical microstructures have the potential benefits in daylighting and glare protection, which will be further presented in 6.3

#### **6.1.2.2 Glazing with micro compound parabolic concentrators (CPCs)**

Figure 6-3 shows the simulated angular-dependent transmittance for a conventional double glazing, a low-e double glazing, and a conventional double glazing with symmetric CPCs. The conventional double glazing was made of two glass panes, on which there was no metallic coating or any other type of coating. Low-e double glazing, namely low-emissivity double glazing, was made of two glass panes on which the selected surfaces were coated with low-emissivity coating. The heat conductance of low-e double glazing normally ranges from 0.28 to 0.37 W/(m²K), and the solar heat gain coefficient ranges normally between 0.27-0.66 (Glass education center, 2018). Symmetric CPC of a half acceptance angle of 30° was labelled as CPC(30, 30); likewise, with a half acceptance angle of 40° it was labelled as CPC(40, 40). Due to the refractive index of 1.5 of the polymer, the incident angles corresponding to the half acceptance angles for the CPCs

embedded in the polymer layer were  $48.6^\circ$  (CPC(30, 30)) and  $74.6^\circ$  (CPC(40, 40)). For CPC (45, 45), the half acceptance angle will be larger than  $90^\circ$ .

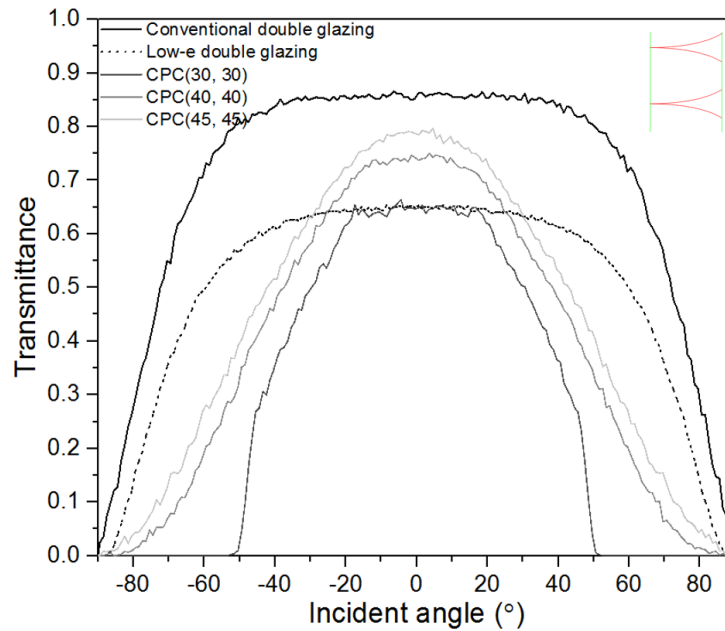


Figure 6-3. The simulated angular-dependent transmittance for conventional double glazing, low-e double glazing, and conventional double glazing with symmetric CPCs at the azimuth angle of  $0^\circ$ . The numbers in the brackets are the half acceptance angles of left and right parabolas. The sketch of micro CPCs embedded in the polymer layer is shown on the upper right of the figure.

For CPC(30, 30), the transmittance was about 0.64 which happened to be similar to that of the low-e double glazing in the angular range between  $0^\circ$  and  $25^\circ$ . Beyond  $25^\circ$ , a fraction incident light flux was redirected by two or more times and then left the system through the input aperture. Therefore, the transmittance significantly reduced beyond  $25^\circ$  and reached 0 at about  $50^\circ$ . Likewise, for CPC(40, 40), the transmittance stayed at 0.72 in the angular range between  $0^\circ$  and  $12^\circ$ . After  $12^\circ$  the transmittance gradually reduced, and this trend was unlike that of CPC30°, as the curvature of the parabolic mirrors was smoother than that of CPC(30, 30). The transmittance stayed at 0 beyond  $80^\circ$ . The trend of the angular-dependent transmittance for CPC(45, 45) was very similar to that for CPC(40, 40), due to the similar geometrical parameters.

Compared with the conventional double glazing and the low-e double glazing, glazing with symmetric CPCs showed a drastic reduction at high incident angles (incident angles greater than  $50^\circ$ ) which corresponded to the solar elevation angles in summer during the working hours. In contrast, at the low incident angles (incident angles below  $50^\circ$ ) which could correspond to the solar elevation angle in winter and/or spring, the transmittance at a relatively high value. Therefore, with such profile of angular-dependent transmittance, glazing with symmetric CPCs has a potential for season thermal control. In the present case, the polymer layer with embedded CPCs was laminated

with a conventional double glazing, and the high transmittance of such configuration lied between the transmittance of the conventional double glazing and the low-e double glazing. It should be noted that, the polymer layer could be laminated with other type of glazing, and the order of the transmittance could therefore be tuned based on the chosen glazing, in order to satisfy the requirement for a specific location and orientation of the façade.

Figure 6-4 shows examples of angular-dependent transmittance of the conventional double glazing with asymmetric CPCs. The listed asymmetric micro CPCs have common half acceptance angle of  $0^\circ$ . Due to the asymmetric geometry, the angular-dependent transmittance profile was asymmetric. No sharp drop of the transmittance around the acceptance angle, due to the truncation of the parabolic side wall. An interesting property for glazing with CPC(75, 0) and CPC(80, 0) was that the within a large angular range the direct transmittance was higher than that of the conventional double glazing. For example, for micro (80, 0), the increase of the transmittance was up to 38% in average in the angular range from  $-90^\circ$  to  $-55^\circ$ .

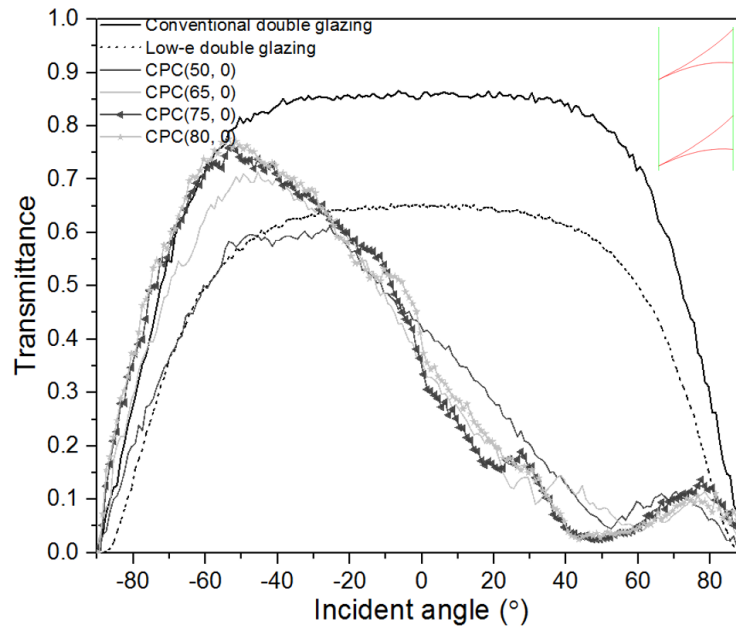


Figure 6-4. The simulated angular-dependent transmittance for conventional double glazing, low-e double glazing, and conventional double glazing with asymmetric CPCs at the azimuth angle of  $0^\circ$ . The sketch of asymmetric micro CPCs embedded in the polymer layer is shown on the upper right of the figure.

In summary, the angular-dependent transmittance showed that micro CPCs were appropriate for tilted glazing (or horizontal skylight). Micro CPCs could also be applied to façade of various orientations by optimizing the appropriate half-acceptance angles. More detail concerning the application and potential benefits in terms of seasonal thermal dynamics will be presented in the section of 6.2.2.

### 6.1.3 Sensitivity analysis

Due to the limitations of the fabrication techniques, the geometrical parameters of the resulting microstructures might deviate from the theoretical design. Among the possible dimensional variations, the reduction of the height of the microstructures is a common one. In the present sections, the sensitivity of the optical properties to the dimensional change in the height of the microstructures was investigated by analysis of the angular-dependent transmittance calculated from ray-tracing simulation.

#### 6.1.3.1 Glazing with “L”-shape retro-reflective optical microstructure

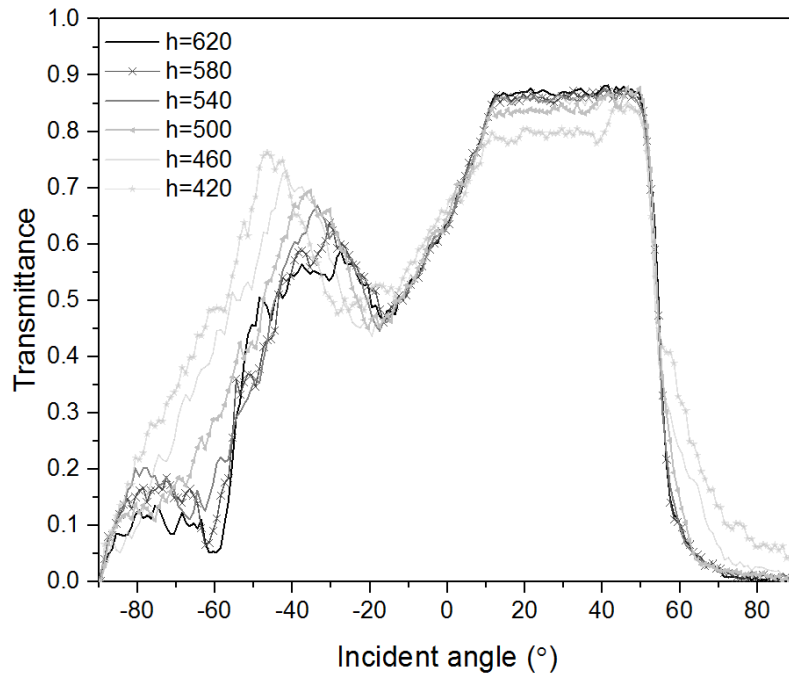


Figure 6-5. The profiles of angular-dependent transmittance as function of the height for glazing with with “L”-shape retro-reflective micro-mirrors.

Figure 6-5 shows the profiles of the angular-dependent transmittance as function of the height for glazing with “L”-shape retro-reflective micro-mirrors. The reference height was set as 640  $\mu\text{m}$  and the periodicity was 214  $\mu\text{m}$ . There was a very little change of the angular-dependent transmittance, even when the height was reduced from 620  $\mu\text{m}$  to 500  $\mu\text{m}$ , (i.e., by 19.3%). When the height was reduced from 500  $\mu\text{m}$  to 420  $\mu\text{m}$ , the variation of the angular-dependent transmittance was perceptible. Nonetheless, beyond 50°, the transmittance still dropped drastically and showed a strong potential of seasonal thermal dynamics.

Attention should also be paid to the change of retro-reflective property due to dimensional change. Figure 6-6 shows the behavior of the incoming rays after interacting with the “L”-shape micro-mirrors of different heights. The reflected-back upward rays became more scattered as the

height was reduced. The scattering of the reflected-back upward rays remained similar for the height of 460  $\mu\text{m}$  to the reference case. However, when the height was reduced to 420  $\mu\text{m}$ , the reflected-back upward rays were very scattered.

In summary, considering both angular-dependent transmittance related to seasonal thermal dynamics and retro-reflective properties, the tolerance of the height reduction was about 26%.

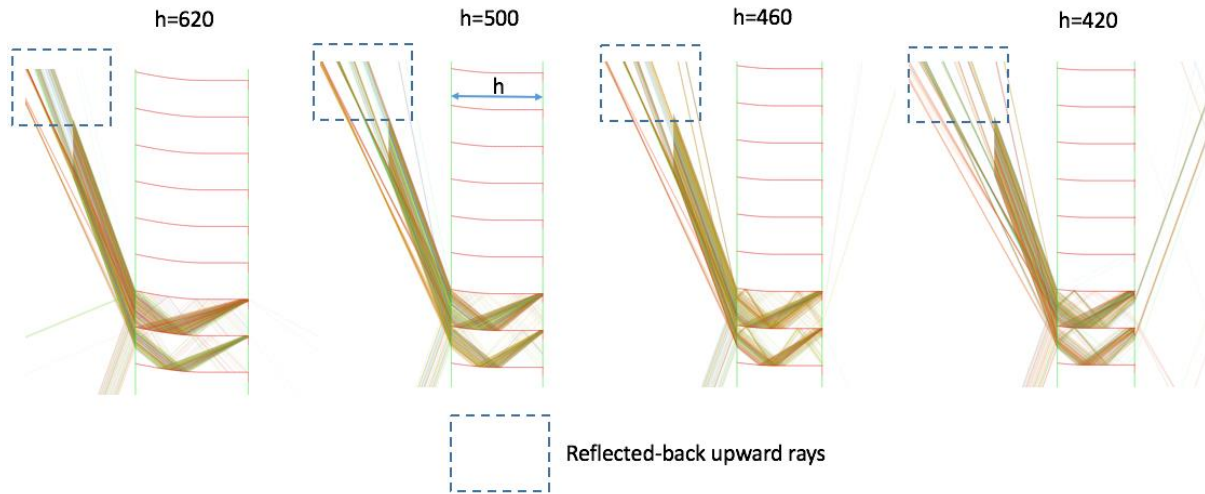


Figure 6-6. The behavior of the incoming rays after interacting with the “L”-shape micro-mirrors of different heights.

### 6.1.3.2 Glazing with micro compound parabolic concentrators (CPCs)

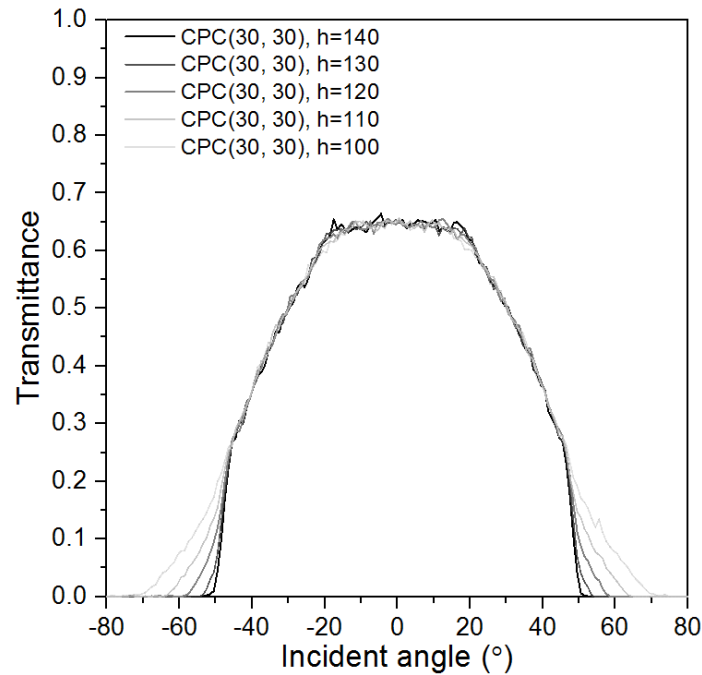


Figure 6-7. The profiles of angular-dependent transmittance as function of the height for CPC(30, 30).

Figure 6-7 Figure 6-7 shows the profiles of the angular-dependent transmittance as a function of the height for CPC(30, 30). The original height was set at 140  $\mu\text{m}$  and the width of the exit aperture at 55.5  $\mu\text{m}$ ; the deviation was observed beyond the original acceptance angle ( $48.6^\circ$ ). Instead of a sharp drop as that of CPCs with original height, the truncated CPCs showed the increase of the acceptance angle. Taking the transmittance of 0.04 as reference, for a truncated height greater than 120  $\mu\text{m}$ , the acceptance angle was expanded by  $2^\circ$  per 10- $\mu\text{m}$  reduction. For the truncated height between 120  $\mu\text{m}$  and 100  $\mu\text{m}$ , the acceptance angle was about  $5.5^\circ$  per 10- $\mu\text{m}$  reduction. For the CPCs with the height of 100  $\mu\text{m}$ , a slope hereby was decided by the transmittance of 0.25 at the original acceptance angle and the transmittance of 0.04 at the corresponding angle for each truncated CPC. In any case, the transmittance on the slope would be lower than 0.25. Therefore, the slope did not have an essential impact on the angular-dependent transmittance for seasonal thermal dynamics. In fact, the higher direct transmittance because of the truncated CPCs may be more favorable for some places under certain conditions. The truncated CPC provide an alternative for the actual application in different locations with various climates.

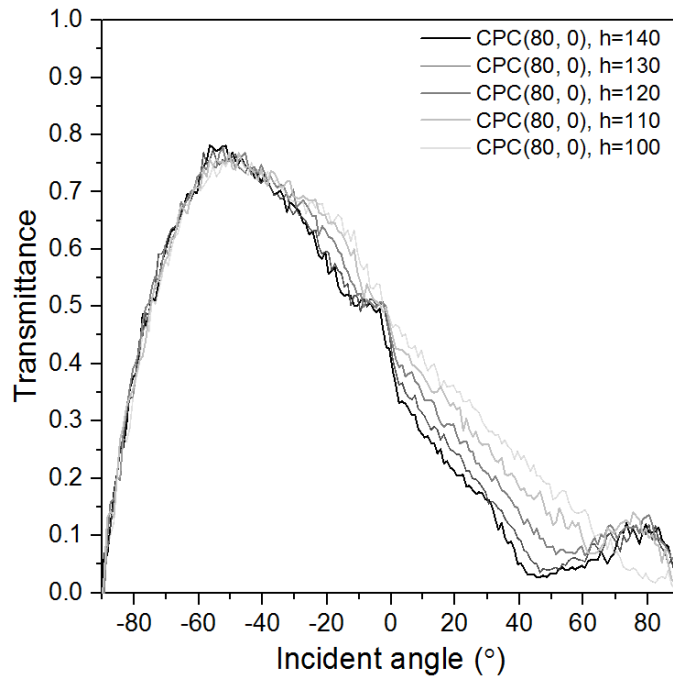
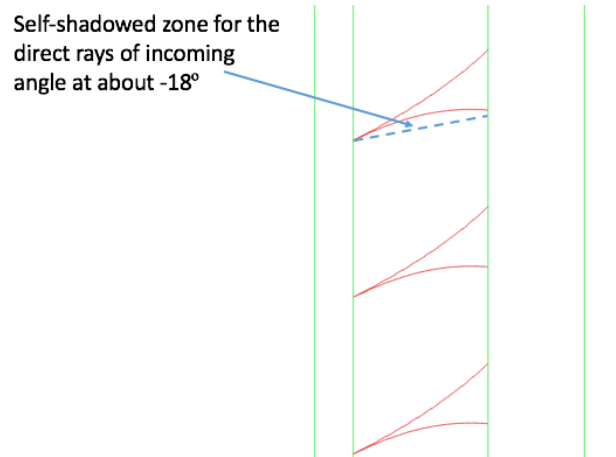


Figure 6-8. The profiles of angular-dependent transmittance as function of the height for CPC(80, 0).

Figure 6-8 shows the profiles of angular-dependent transmittance as a function of the height for CPC(80, 0). The variation of the transmittance was above  $-55^\circ$ , where the peak transmittance could be observed. The change of the transmittance was mainly due to the reduction of the self-shadowed zone for direct incoming light rays. The self-shadowed zone was created by the geometry of the microstructure; an example of a blind zone is shown in Figure 6-9. The truncation reduced the area of the self-shadowed zone, and therefore, more light rays could transmit at the same angle. When

the height was reduced from 140  $\mu\text{m}$  to 130  $\mu\text{m}$ , there was very little change of the transmittance. Taking the transmittance of 0.2 as reference, from 130  $\mu\text{m}$  to 100  $\mu\text{m}$ , the acceptance angle was about  $6.6^\circ$  per 10- $\mu\text{m}$  reduction.



*Figure 6-9. An example of self-shadowed zone to the direct incoming light which is enclosed by the parabolic curve and the dash line.*

## 6.2 Seasonal thermal dynamics

The simulation to estimate the potential seasonal thermal dynamics was conducted for both Lausanne and Athens. The weather files were exported from Meteonorm (Meteonorm, 2018). The percentage of the diffuse and direct radiation for both horizontal and vertical south-oriented façade for the two cities are summarized in Table 6-1 and Table 6-2, respectively. It is straightforward to assume that, for both horizontal and vertical façade in Lausanne, the microstructure can play rather effective role all the year round, because the percentage of the direct diffusion is always more than 40%. Whereas for vertical façade in summer for Athens, it is not so straightforward to tell the performance, which will be analyzed in the following sections.

*Table 6-1. The seasonal percentage of the diffuse and direct radiation for both horizontal and vertical south-oriented façade in Lausanne (46.5° N)*

	<b>Horizontal</b>		<b>Vertical</b>	
	<b>Diffuse</b>	<b>Direct</b>	<b>Diffuse</b>	<b>Direct</b>
<b>Winter</b>	58%	42%	37%	63%
<b>Spring</b>	50%	50%	56%	44%
<b>Summer</b>	40%	60%	60%	40%
<b>Annual</b>	47%	53%	49%	51%

*Table 6-2. The seasonal percentage of the diffuse and direct radiation for both horizontal and vertical south-oriented façade in Athens (38° N)*

	<b>Horizontal</b>		<b>Vertical</b>	
	<b>Diffuse</b>	<b>Direct</b>	<b>Diffuse</b>	<b>Direct</b>
<b>Winter</b>	43%	57%	36%	64%
<b>Spring</b>	39%	61%	58%	42%
<b>Summer</b>	43%	57%	77%	23%
<b>Annual</b>	40%	60%	50%	50%

In order to give the idea about the annual cooling demand, an example (Cox, Rimante A., et al, 2015.) from Copenhagen is cited, as shown in Figure 6-10. In that case, glazing with low-e coating and U-value of 0.8 W/m<sup>2</sup>K was used. Compared with Copenhagen, Lausanne is at lower latitude



and the climate is generally warmer. Therefore, the considerable cooling road may rise earlier and drop later in Lausanne; the percentage of the cooling demand with respect to the total thermal load may also be higher for the same type of building.

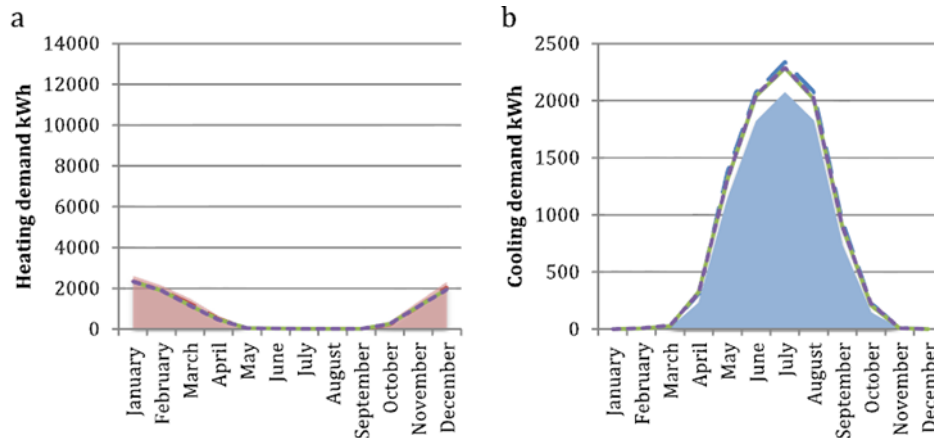


Figure 6-10. (a) Annual heating demand weather and (b) annual cooling demand for weather files based on present (shaded) annual (dashed), monthly (solid) and hourly (dotted) changes (Cox, Rimante A., et al, 2015.).

### 6.2.1 Dynamic solar gains

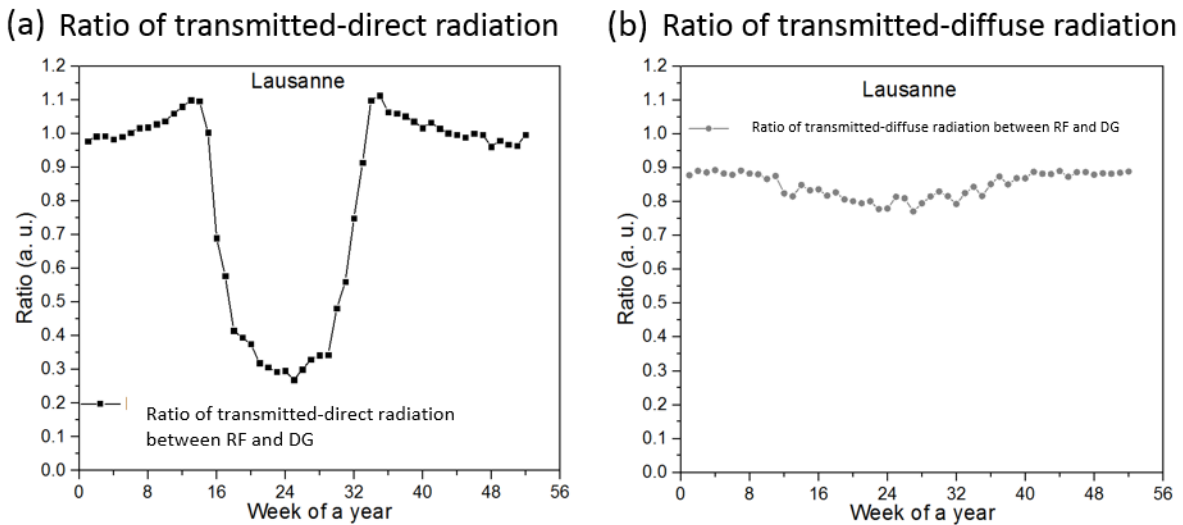


Figure 6-11. Ratio of (a) transmitted-direct solar radiation, and (b) transmitted-diffuse solar radiation between glazing with the “L”-shape retro-reflective micro-mirrors (RF) and conventional double glazing (DG) in Lausanne.

Figure 6-11 shows ratio of (a) transmitted-direct solar radiation, and (b) transmitted-diffuse solar radiation between glazing with the “L”-shape retro-reflective micro-mirrors (RF) and conventional double glazing (DG) in Lausanne. This city has a cold winter and rather warm summer during daytime. The solar radiation is from the average statistics over the years 1991 to 2010 (Meteonorm, 2018). Each data point in Figure 6-11 represents the weekly transmitted-direct radiation. It was found that there was significant average reduction of the transmitted-directed

radiation by 60% over mid April to mid September, while for the rest of the year when it was cool, the transmitted-direct solar radiation remained almost the same for the two types of glazing. For the transmitted diffuse radiation, the evident average reduction by 20% could also be observed from mid April to mid September; overall, the total reduction in the summer time was about 30%. Therefore, substantial seasonal dynamics in terms of solar gains using glazing with “L”-shape retro-reflective micro-mirrors could be achieved for Lausanne.

Figure 6-12 shows the ratio of (a) transmitted-direct solar radiation, and (b) transmitted-diffuse solar radiation between glazing with the “L”-shape retro-reflective micro-mirrors (RF) and conventional double glazing (DG) in Athens.. The climate of Athens is mild winter, warm in spring (and autumn) and very hot in summer. The configurations of the two glazing were identical to those of Lausanne. From March to mid April, the average transmitted-direct radiation was reduced by 48%. A significant reduction of 76% for transmitted-direct radiation could be observed from mid April to mid September. The reduction of the global radiation from March to mid April, and from mid April to mid September were, 28.5% and 35% respectively.

Based on the results of Lausanne and Athens, the “L”-shape retro-reflective micro-mirrors can cover a least a latitude range of 8.5° for seasonal thermal dynamics.

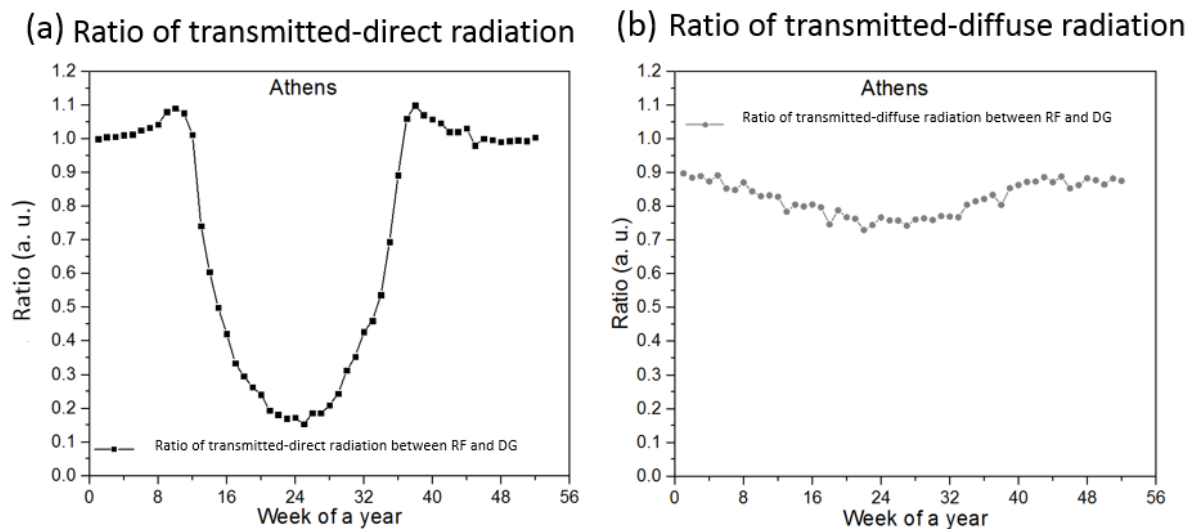


Figure 6-12. Ratio of (a) transmitted-direct solar radiation, and (b) transmitted-diffuse solar radiation between glazing with the “L”-shape retro-reflective micro-mirrors (RF) and conventional double glazing (DG) in Athens.

## 6.2.2 Direct transmittance during working hours

Based on its angular-dependent transmittance, micro CPCs are appropriate for tilted glazing (or horizontal skylight). The potential benefit of glazing with micro CPCs in terms of seasonal thermal control was estimated by the evaluation of the direct transmittance during working hours; two cases in Athens were considered.

### 6.2.2.1 First case study

In the first case, the configuration of glazing was symmetric CPC(45, 45) applied to the conventional double glazing with a  $65^\circ$  tilting above the horizon. Figure 6-13 shows the calculation of the direct transmittance during working hours (considered as 8:00 – 17:00) for the winter solstice, the spring equinox and the summer solstice, respectively. It was shown that, on winter solstice, there was about 10% average relative reduction of direct transmittance over the working hours. Nevertheless, the thermal comfort might not be degraded, as the climate in winter was mild in Athens. On spring equinox which was warm in Athens, the average relative reduction of the direct transmittance over the working hours was 18%. In summer solstice, which was very hot in Athens, the transmittance was reduced by 37% in average and 44% at noon.

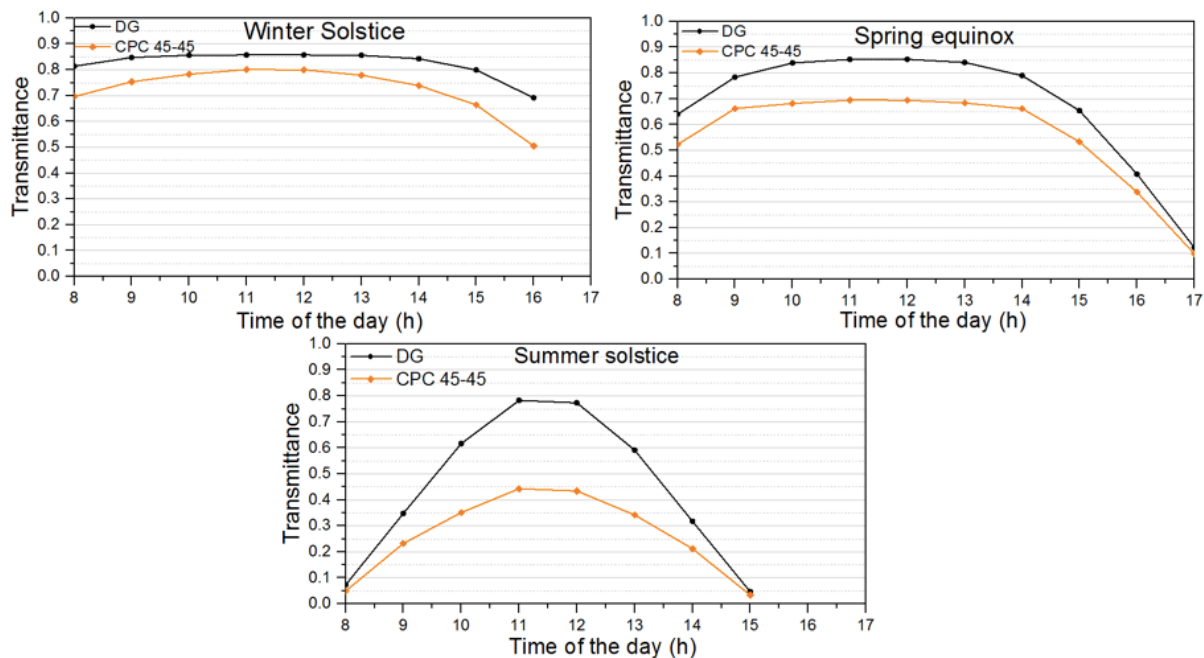


Figure 6-13. The calculation of the direct transmittance during working hours (considered as 8:00 – 17:00) for the winter solstice, the spring equinox and the summer solstice, respectively, for the first case study.

### 6.2.2.2 Second case study

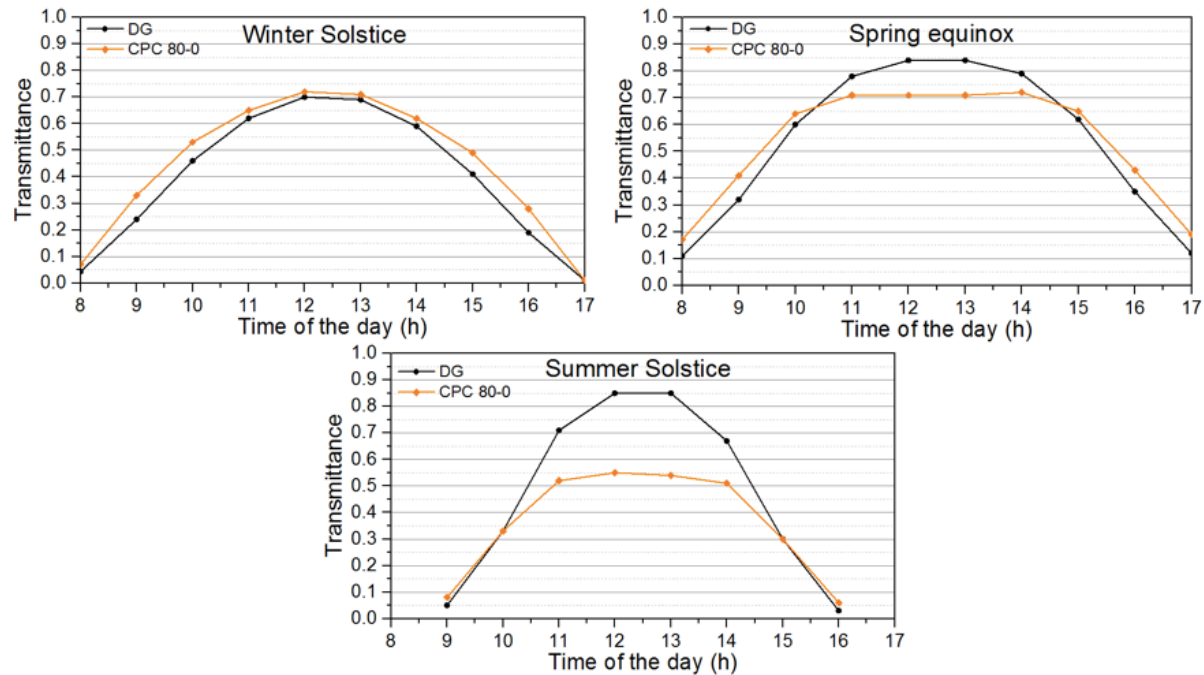


Figure 6-14. The calculation of the direct transmittance during working hours (considered as 8:00 – 17:00) for the winter solstice, the spring equinox and the summer solstice, respectively, for the second case study.

In the second case, embedded CPC(80, 0) was applied to a horizontal skylight for the location at the latitude of 38°N (e.g. in Athens). Figure 6-14 shows the calculation of the direct transmittance during working hours (considered as 8:00 – 17:00) for the winter solstice, the spring equinox and the summer solstice, respectively. One could notice that, on winter solstices, the transmittance of this configuration was higher than that of a corresponding double-glazing over the working hours; especially in the early morning and in the late afternoon, the relative increase of transmittance was more than 50%. For example, at 4 pm, the relative increase of transmittance was 67%. At spring equinox, in the early morning and the late afternoon, the time span where the temperature was low and people needed more heat gain, the direct transmittance increased, while from 10 am to 2 pm, the time span that corresponded to a warm spring noon, the relative direct transmittance is 20% at 12 am. At summer solstice, the direct transmittance was reduced considerably from 10 am to 1 pm, with a maximum relative decrease of 42%. Considering that the diffuse transmittance is reduced by approximately 50% due to the profile of the angular-dependent transmittance of CPC(80, 0), as well as that the percentage of the diffuse radiation for horizontal façade is 43%, the overall relative reduction of the transmittance at summer noon is about 46%. This significant reduction contributes to avoid overheat and improve thermal comfort in summer.

## 6.3 Simulation of daylighting performance and visual comfort

*The text and images in this section are reproduced from: Gong, J., Kostro, A., Motamed, A., & Schueler, A. (2016). Potential advantages of a multifunctional complex fenestration system with embedded micro-mirrors in daylighting. Solar Energy, 139, 412-425.*

### 6.3.1 Steady and dynamic illuminance

Figure 6-15 shows illuminance maps with contours spaced linearly on the winter solstice at 12:00 (GMT+2) under the standard CIE clear sky with sun. The coordinate of the view point was {1.8 m, 8 m, 1.25 m} corresponding to {width, length, height} respectively, in order to have an overview of the distribution of the illuminance in the reference room. With the integration of embedded micro-mirrors, the incident solar radiation was split into two parts: direct radiation and redirected radiation. Around 20% of the directed solar rays (elevation angle of  $20^\circ$ ) which passed through the glazing with micro-mirrors would be redirected. It could be observed that the redirected radiation on the ceiling was characterized by an increased level of illuminance identified by the contours.

Glazing with embedded micro-mirrors effectively redirected light rays towards the ceiling, distributing daylight more deeply into the rear of an interior space. The higher ratio of micro-mirrors in the glazing, the more daylight would be induced towards the rear of a room, i.e., beyond 4 m away from glazing. For the case where the embedded micro-mirrors were in the upper third of the glazing, the increased illuminance on the ceiling lies within the region of less than 3 m from the glazing. For the case of embedded micro-mirrors in the upper two thirds of glazing, the illuminance on the ceiling in the rear of the room increased significantly (to approximately 1125 lux). Likewise, for the case of the embedded micro-mirrors in the whole window, the illuminance of the ceiling was up to around 1500 lux in the rear of the room, suggesting more daylight would be present on the working plane due to the reflection from the ceiling.

For the case of embedded micro-mirrors in the upper two-thirds glazing, bright spots could be seen on the window. The solar altitude was  $20^\circ$ , and the direct light rays would not be able to reach the chosen view point (coordinates {1.8, 8, 1.25} corresponding to {width, length, height} respectively). The bright spots were therefore due to the defined regular output resolution of the cosine-weighted solid angle when BTDF data of the window was used, i.e., approximately every  $10^\circ$  in altitude and coarser in azimuth, and the corresponding interval of  $\theta \pm 5^\circ$  (Andersen, 2002; Ward, Mistrick, Ph, *et al.*, 2011). For the case with embedded micro-mirrors in the whole glazing, the bright spots were mainly due to the redirected solar radiation received by the view point. The impact of redirected solar radiation on visual comfort would be assessed by the simulation of Daylight Glare Index.

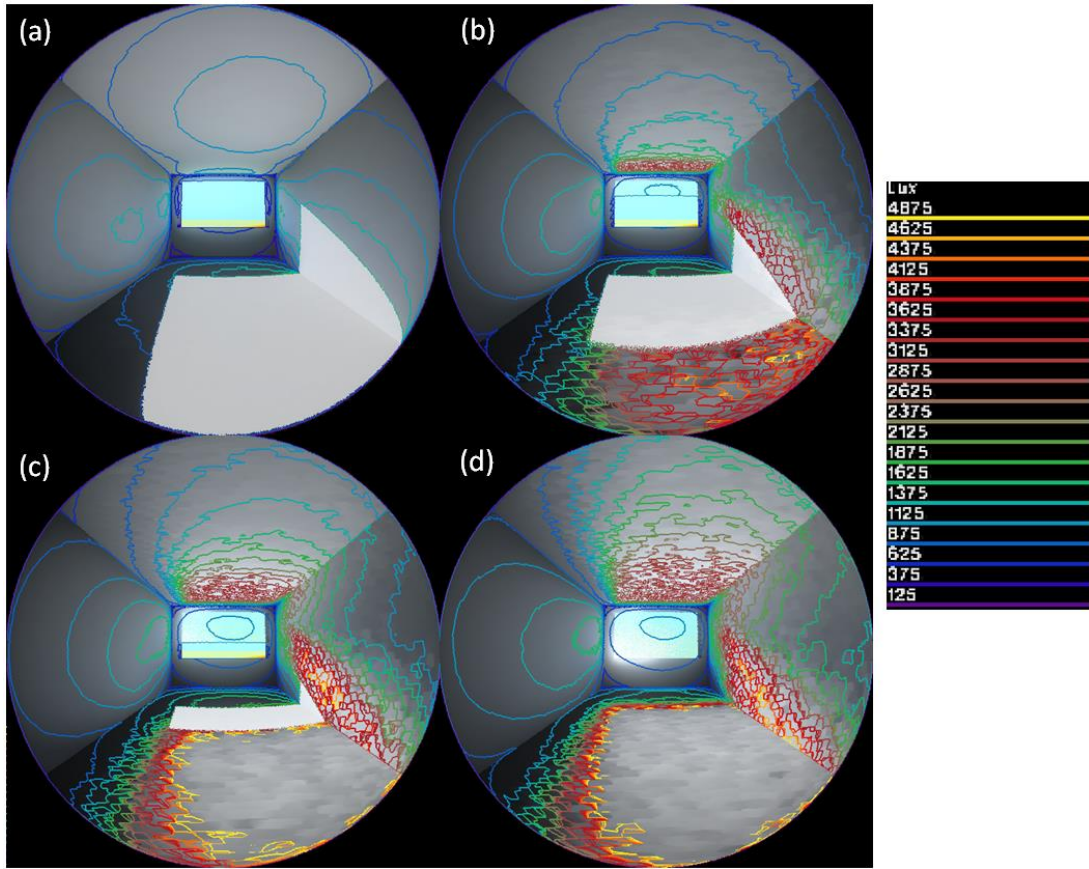


Figure 6-15. Fish-eye views seen from a working position with the distance of 8 m from the window show the illuminance of the office on the winter solstice at 12:00 (Greenwich Mean Time (GMT) + 2) in Lausanne: (a) reference room with the conventional low-e double glazing, (b) case of embedded micro-mirrors in the upper third of a low-e double glazing, (c) case of embedded micro-mirrors in the upper two-thirds of a low-e double glazing and (d) case of embedded micro-mirrors in the whole low-e double glazing.

Calculation of illuminance on working plane (1-m height) was conducted for a CIE overcast sky, an intermediate sky and clear sky at spring equinox solstice noon, where around 90% of incident light rays were redirected; the corresponding results are presented in Figure 6-16. Under the overcast sky, micro-mirrors in the whole glazing reduced the illuminance for the region within 1.7 m deep, the relative reduction being up to 43% with respect to the case with low-e glazing. For the case with micro-mirrors in the upper one-third and the upper two-thirds glazing, the work-plane illuminance at around 0.18 m deep was almost identical to the case of low-e double glazing. Beyond the depth of 0.5 m, the work-plane illuminance of the case with micro-mirrors in the upper two-thirds glazing was significantly decreased. For the case of the embedded micro-mirrors in the whole glazing, illuminance increased beyond 1.7 m deep; illuminances were above 100 lux up to 6.5 m deep, whereas for the case with low-e double glazing illuminances fell below 100 lux beyond 4.5 m. 100 lux was considered as the lower threshold for computer-based work and in bedrooms in terms of daylight autonomy. The average relative increase in the rear of the room (region from

4 m deep to 8 m deep) with micro-mirrors in the whole glazing was approximately 55% with respect to the case with low-e glazing. The average relative improvement in illuminance increased with the higher ratio of micro-mirrors in the glazing. Under an intermediate sky, the trends of the work-plane illuminance with the use of micro-mirrors were similar to the cases under an overcast sky. Due to higher external horizontal illuminance, the illuminances were above 200 lux for the whole room with the use of micro-mirrors in the whole glazing; the average relative increase in the rear of room was around 55%. Under a clear sky with sun, the effect of micro-mirrors was obvious. With the use of micro-mirrors in the whole glazing, the average reduction of work-plane illuminance with respect to the case with low-e double glazing was about 15000 lux for the region within 1-m depth. It was noticed that, for the cases with micro-mirrors in the upper third and the upper two-thirds glazing, higher illuminances could be observed in the region next to the glazing; for the places where the illuminances were higher, the direct transmitted sunlight was dominant, and meanwhile the redirected sunlight by micro-mirrors contributed to the illuminance on the working plane. For example, at a depth of 0.18 m, the illuminance from direct transmitted sunlight was around 30000 lux, which was the same with the case of low-e double glazing. However, due to the illuminance contributed by micro-mirrors, the total work-plane illuminance at the depth of 0.18 m was approximately 33000 lux. At around 1.5 m deep, a sharp drop of illuminance appeared for the case with low-e double glazing, whereas the variation of illuminance for the case with micro-mirrors in the whole glazing was much smoother. Significant increase of illuminance for the case with micro-mirrors in the whole glazing could be seen beyond 2.5 m from the window. The work-plane illuminance at a depth of 8 m was around 1200 lux while for the case with low-e double glazing it was only around 300 lux. The average relative increase in the rear of the room for the case with micro-mirrors in the whole glazing reached 400%.



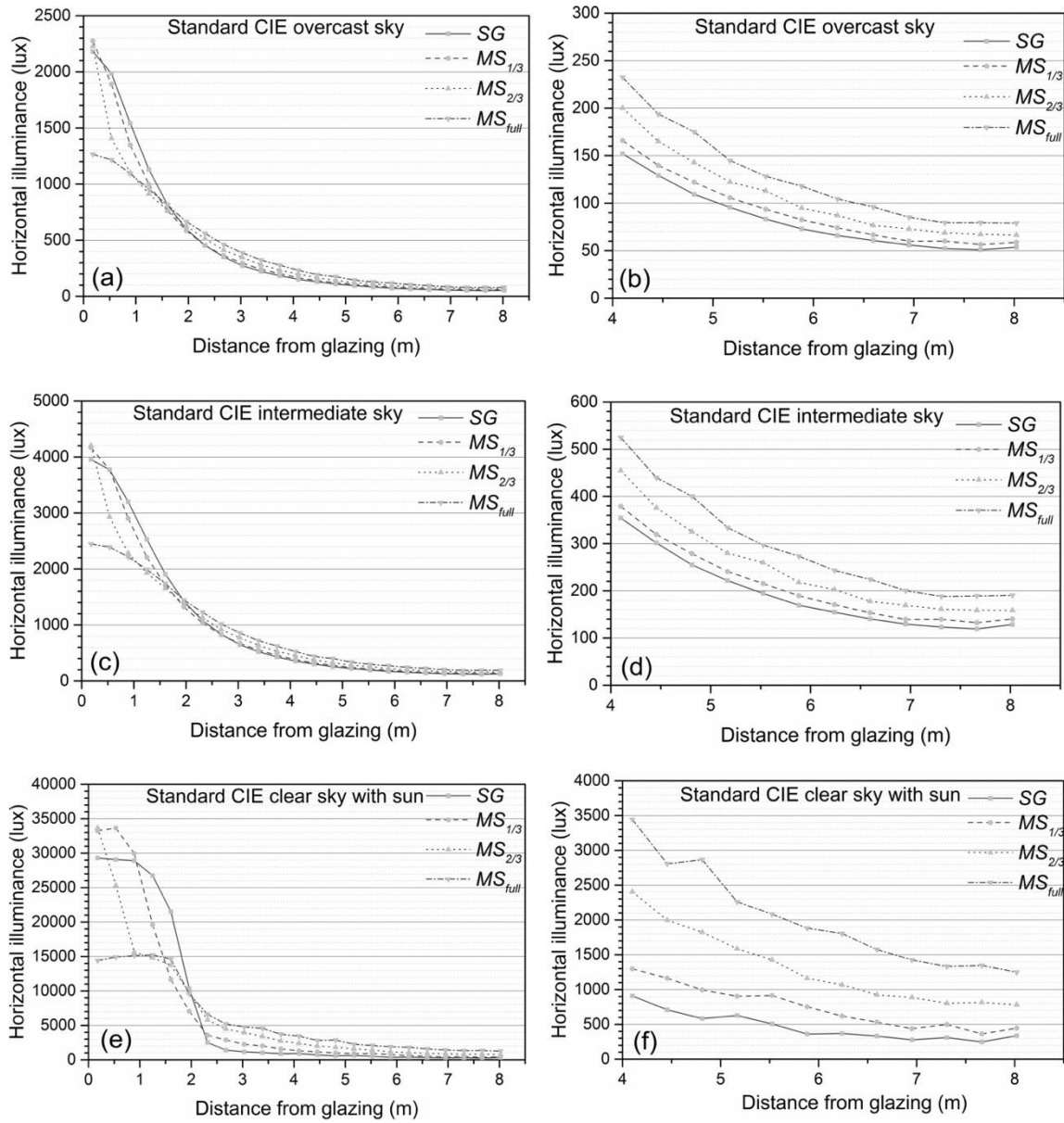


Figure 6-16. Illuminance on the working plane for (a) standard CIE overcast sky, (c) standard CIE intermediate sky and (e) standard CIE clear sky with Sun at spring equinox solstice noon. (b), (d) and (f) show the corresponding illuminance for the region from 4 m deep to 8 m deep.



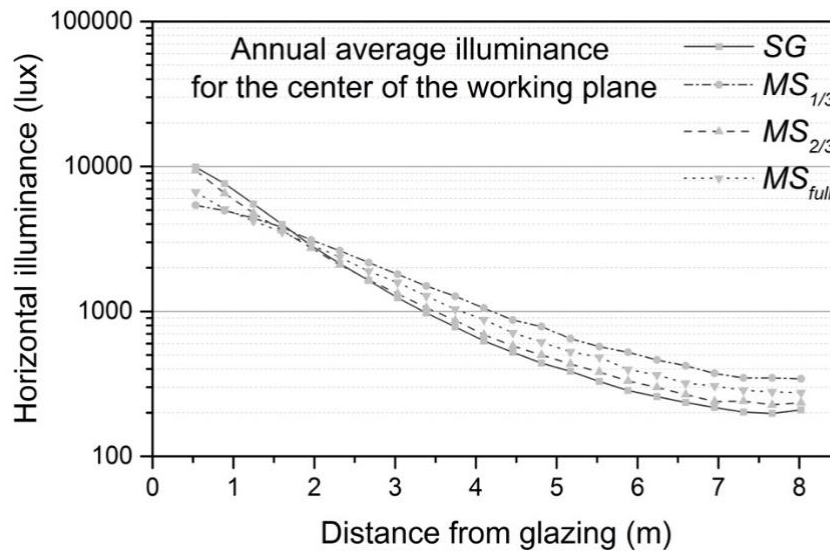


Figure 6-17. Annual average illuminance for working hours (8:00 – 18:00) for the center of the working plane along the depth of room.

Calculation of the annual average illuminance level during working hours (defined as 8:00 – 18:00) was conducted for the center of the work plane along the depth of room, as shown in Figure 6-17. For the case with micro-mirrors in the whole glazing, the work-plane illuminance at a 0.5-m depth was reduced from approximately 10500 to 5500 lux; the relative reduction was 50%. The illuminance was increased beyond 2 m with the use of micro-mirrors in the whole glazing; especially, for the region from 4 m to 8 m deep, the average relative increase of illuminance was approximately 74% with respect to the case with low-e double glazing.

UDI was calculated for the rear of the office, i.e., from 4 m deep to 8 m deep. For the case where micro-mirrors were in the whole glazing, the illuminances in the useful range were around 50%, while for the case with conventional low-e double glazing it was only 35%. For the case where micro-mirrors were in the upper two-thirds of the glazing, the illuminance of falling short was reduced by 10%, and for the case where micro-mirrors were in the upper third of the glazing, the corresponding value was 5%. The increase of UDI with micro-mirrors was not as significant as that of the results of the illuminance along the depth of room: it was due to the presence of the thresholds. As shown in Figure 6-16, under an overcast sky, the illuminance beyond 4 m deep was increased by micro-mirrors but was under the threshold of 300 lux; under a clear sky with sun, even though the illuminance in the rear of the room was much lower than that of the case with micro-mirrors in the whole glazing, it was still above 300 lux. It should be noted that, UDI alone might not be sufficient for the estimation of the energy saving potential in lighting. On one hand, for humans there is no strict threshold to decide whether the daylight is enough for switching the light on or off. On the other hand, energy saving potential with the increased illuminance level due

to micro-mirrors may be seen if daylight-responsive lighting control, (e.g., a dimming control system), is considered. Excellent energy savings with dimming control system has been experimentally demonstrated (Li and Lam, 2003). It was reported that energy savings in electric lighting was about 70% using dimming control systems for a northwest-facing daylit corridor of the City University of Hongkong.

### 6.3.2 Luminance ratio

The illuminance maps for all configurations in Figure 6-18 give a qualitative view regarding the daylighting distribution. A high contrast of illuminance appeared on the top of the table for the case with conventional double low-e glazing, leading to visual discomfort. The ratio of the maximum illuminance value to the minimum could be more than 8. Concerning the case where the micro-mirrors were in the upper third of the glazing, a part of the table was exposed to the direct solar radiation by the low-e double glazing. For the case where the micro-mirrors were in the upper two-thirds glazing, the ratio of maximum illuminance value to the minimum one was approximately 2.2, and for the case with micro-mirrors in the whole glazing was around 1.7, suggesting a significant improvement of the uniformity of the daylighting distribution.

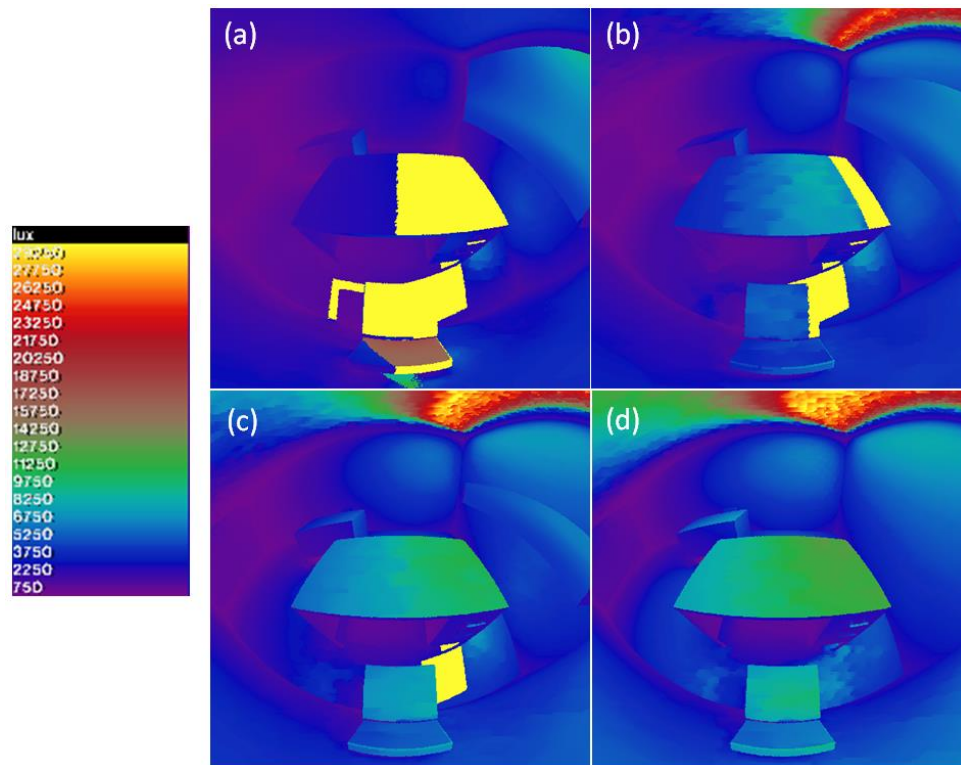


Figure 6-18. The illuminance maps on April 7th at 12:00 (GMT+2) in Lausanne: (a) the case with conventional low-e double glazing, (b) the case of micro-mirrors in the upper third of the glazing, (c) the case of micro-mirrors in the upper two-thirds of the glazing and (d) the case of micro-mirrors in the whole glazing.

The luminance ratios falling in the acceptable range for the case with low-e double glazing were 50%. The luminance ratios in the acceptable range were improved by approximately 20% for the cases with micro-mirrors in the upper third glazing. The luminance ratios in the acceptable range remained constant with the increased portion of micro-mirrors in glazing. No luminance ratios fall in the exceeding range with micro-mirrors. The luminance ratios of falling short for the cases with micro-mirrors were mainly due to the low luminance values of the shadows created by the table in the field of view.

### 6.3.3 Daylight Glare Index

Glare is an important factor affecting visual comfort. The third simulation looks at the Daylight Glare Index (DGI) from 8:00 to 17:00 on the spring equinox, the summer solstice and the winter solstice. Two view points were chosen: the view point from which the view line pointed towards the window (employee's position) and the one from which the view line was parallel to the window (guest's position). Figure 6-19 shows the DGI sorted in three ranges: acceptable, unacceptable and intolerable. From the employee's position, the reference room suffered from glare for 40% of daytime on the spring equinox, among which 20% fell in the uncomfortable range and 20% fell in the intolerable range. The cases for which the micro-mirrors were in the upper third and the upper two-thirds glazing had the same distribution in the three ranges, and for 80% of daytime, the DGI values fell in the acceptable range. On the summer solstice, glare was not an issue due to the high elevation angles. On the winter solstice, the percentage in the acceptable range for the case of micro-mirrors in the upper two-thirds of the glazing was improved to 70%, and meanwhile the percentage in the intolerable range was reduced to 20%, while the distribution of DGI values for other cases remained similar.

For the guest position, under the condition of micro-mirrors in the whole glazing, glare exceeded the acceptable range on spring equinox for 50% of daytime, whereas the DGI values of other cases remained within the acceptable range. The redirected light rays by micro-mirrors integrated to the part which was below the view line might lead to a high risk of glare. The distinguished distribution of DGI values concerning the case of micro-mirrors in the whole glazing implied that the installation of micro-mirrors should take the average height of view line into account. On summer solstice, the percentage of DGI values of all the cases integrated with micro-mirrors was in the acceptable range and slightly increased from 90% to 100%.

Figure 6-20 shows the plots of hourly DGI values on the spring equinox and the winter solstice for the employee's position. From 9:00 to 12:00 on the winter solstice, the case with conventional low-e double glazing and the case of micro-mirrors in the upper third of the glazing, suffered serious glare problems due to the low elevation angles of the sun, while for the case with micro-mirrors in the upper two thirds of the double glazing, there was an average reduction of 20.96% in

DGI values at 11:00 and 12:00 compared to the reference room, and the subjective perception level was improved by 5 levels, i.e., from ‘intolerable’ to ‘just perceptible’. On the winter solstice, the evolution of DGI values for all cases remained similar, as the micro-mirrors were not sensitive to the solar rays of low elevation angles.

Likewise, the hourly DGI values on the spring equinox and the winter solstice at guest position were plotted in Figure 6-21. In spring in the reference room and the room using micro-mirrors in the upper one-third and two-thirds of the glazing, the subjective appreciation of glare stayed in the imperceptible range for most of daytime. However, as mentioned before, applying micro-mirrors to the whole glazing suffered from a high risk of unacceptable glare in spring, due to the upwards light redirected by the micro-mirrors located lower than that of the head of occupants. On the winter solstice, it was unavoidable to suffer serious glare for all cases, due to the low elevation angle coupled with the eye line towards the glazing.

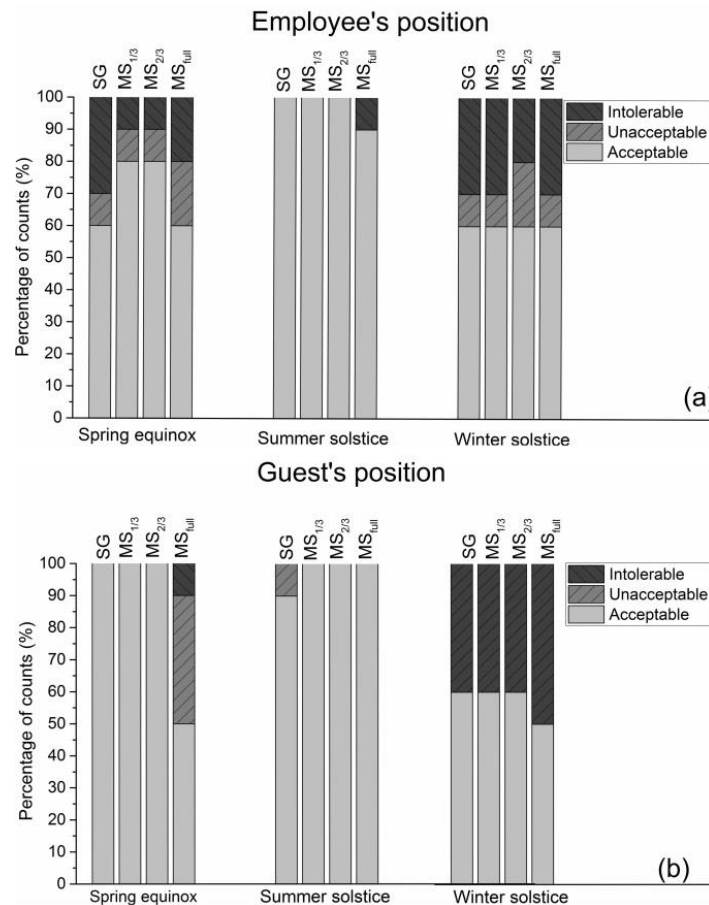


Figure 6-19. Daylight Glare Index sorted in three ranges: acceptable, unacceptable and intolerable.

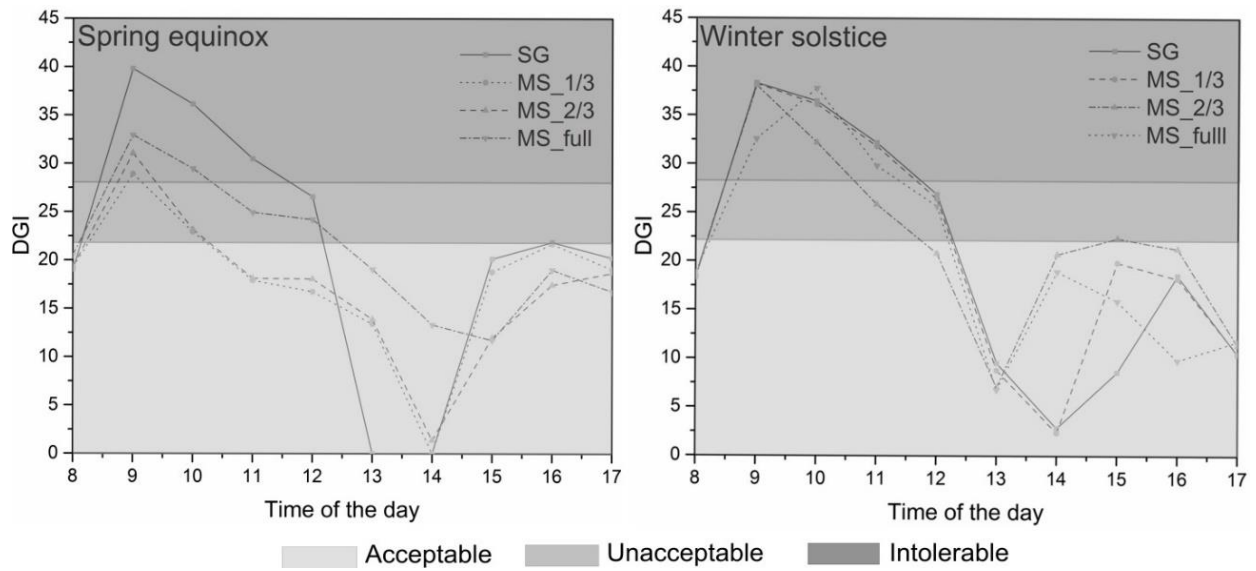


Figure 6-20. The plots of hourly Daylight Glare Index (DGI) values: a) on the spring equinox, and b) on the winter solstice at the employee's position.

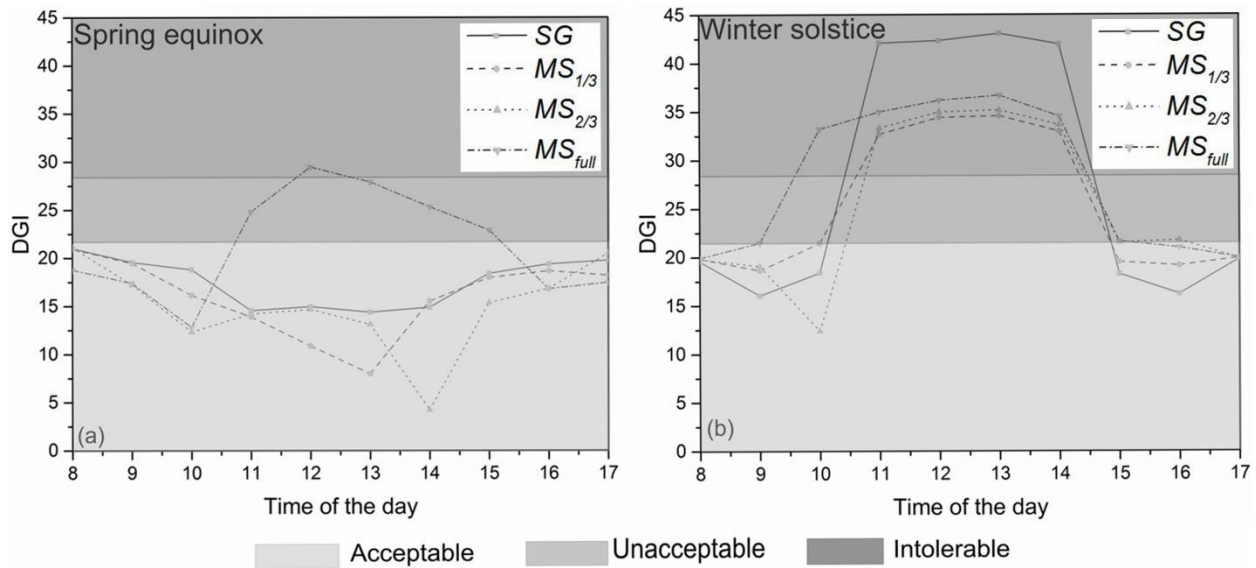


Figure 6-21. The plots of hourly Daylight Glare Index (DGI) values: a) on the spring equinox, and b) on the winter solstice at the guest's position.

### 6.3.4 Vector-to-scalar illuminance ratio ( $E_V/E_S$ )

In order to explore the intrinsic three-dimensional nature of daylight, evaluation of directivity based on the vector-to-scalar illuminance ratios ( $E_V/E_S$ ) on the sunny spring equinox was conducted. Figure 6-22 shows the  $E_V/E_S$  ratios for the reference case and the cases with micro-mirrors along the depth of the room for different times on the spring equinox in Lausanne. Solar noon was at around 12:40. In the early morning before 9:00 am, strong directivity ( $E_V/E_S \geq 2.5$ ) is dominant in the room. The trends of the vector-to-scalar ratios for all the four cases were similar, as only a small portion of solar radiation was directed by the micro-mirrors when the elevation angle was low. For the case where the whole glazing was integrated with micro-mirrors, less than 20% of the direct solar rays were redirected by the micro-mirrors when the elevation angle was lower than  $20^\circ$ .

From 11:00 to 15:00, the vector-to-scalar ratios showed noticeable differences. The  $E_V/E_S$  ratios were reduced to the acceptable range, for the case of micro-mirrors in the upper two-thirds and in the whole glazing for different distance from the glazing, whereas for the case with the micro-mirrors in the upper third of the glazing as well as the reference with conventional low-e coating, the  $E_V/E_S$  ratios were in the harsh range which indicated a strong directivity. The most significant reduction appeared in the region near the window. After 16:00, the directivity for all cases stayed similar, due to the low elevation angle.

Figure 6-23 shows the relative fraction of  $E_V/E_S$  ratios falling into the preferred range, acceptable or harsh range at noon on the spring equinox in Lausanne. It is shown that, at 12:00, for the case of micro-mirrors in the upper two-thirds and in the whole glazing, the percentage falling in the preferred range was 40%, which was 4 times that of the room with conventional low-e glazing; additionally, no counts were outside of the acceptable range. At 13:00, the percentage falling in the preferred range in the case of micro-mirrors in the whole glazing was up to 70%, whereas for the reference case, this number was only 10 %. At 14:00, the relative fraction falling in the preferred range was slightly reduced for the case of micro-mirrors in the whole glazing, as the elevation decreased; nevertheless, it was still up to 60 %, which was 6 times more than that of the reference room.

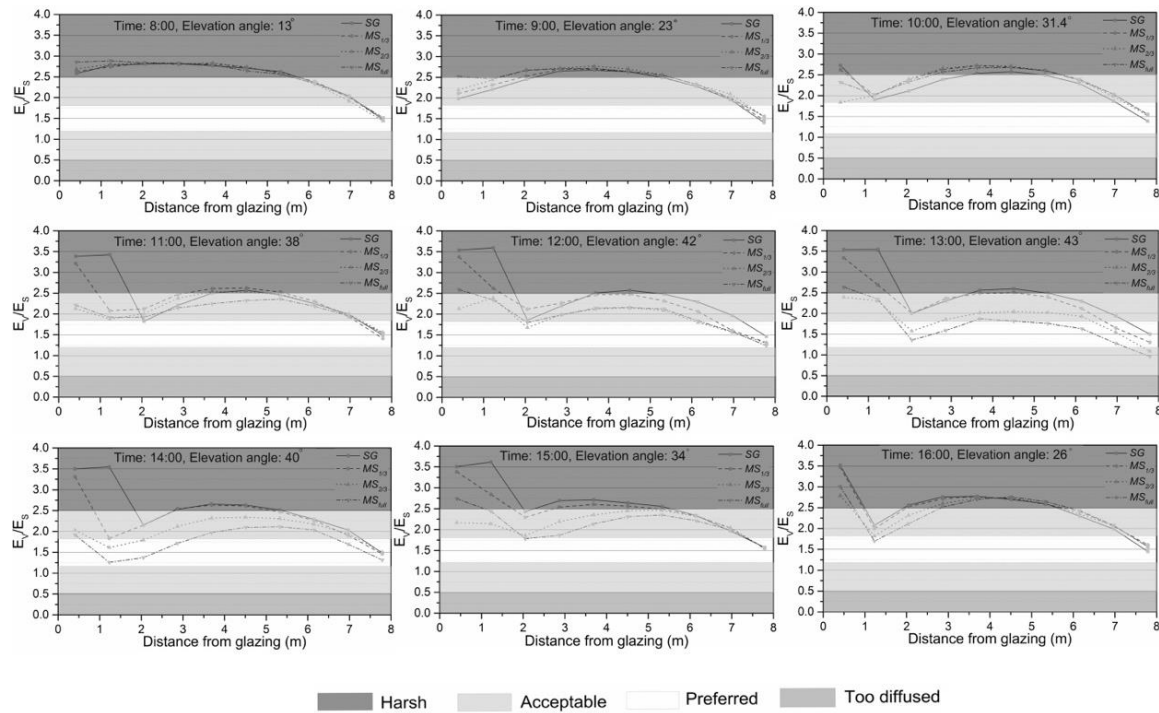


Figure 6-22. The vector-to-scalar illuminance ratios ( $E_v/E_s$ ) along the depth of the room for different working hours on the spring equinox in Lausanne.

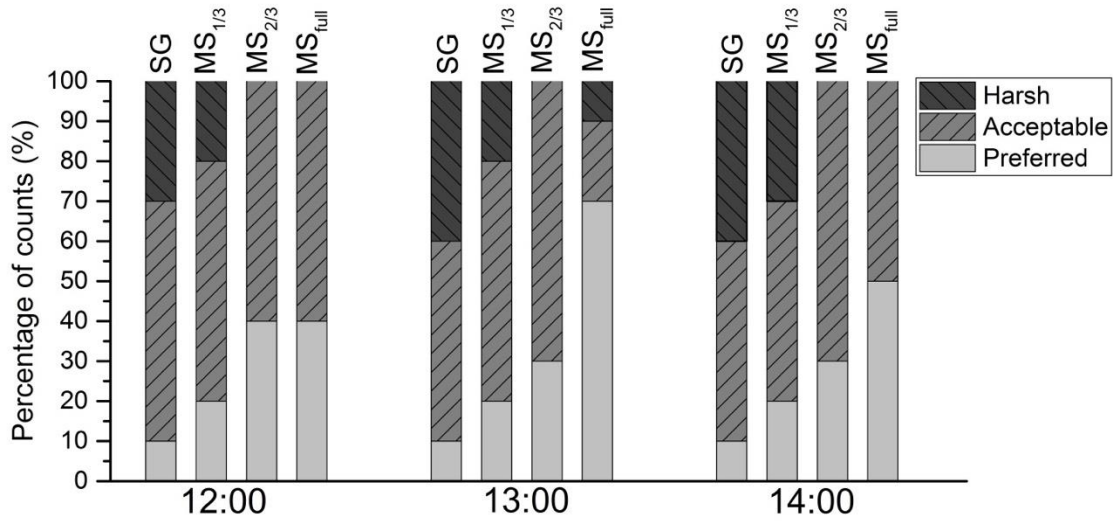


Figure 6-23. Percentage of the vector-to-scalar illuminance ratios ( $E_v/E_s$ ) falls in the preferred range, acceptable or harsh range for different time on the spring equinox in Lausanne.



### 6.3.5 Discussion

For convenience, the abbreviation of  $SG$ ,  $MS_{1/3}$ ,  $MS_{2/3}$  and  $MS_{full}$  were used to identify: (i) the case with conventional low-e double glazing, (ii) the case of the micro-mirrors in the upper third of the glazing, (iii) the case of the micro-mirrors in the upper two-thirds of the glazing, and (iv) the case of micro-mirrors in the whole glazing, respectively.

Glazing with micro-mirrors required the fabrication of microstructures on which selective facets were coated with highly reflective materials; several steps of replications using polymers were necessary. The microstructures for the sample in the present manuscript were produced by laser ablation. Laser ablation could help to fabricate a mold of the area 1.8 m x 1 m for glazing with micro-mirrors in several hours. The molds could be considered as permanent assets. Replication of the molds could be conducted by roll-to-roll process. The alignment between the parabolic reflective surfaces and the secondary reflective surfaces might not be trivial, but it could be solved if the two arrays of reflective surfaces were made from one microstructure. In terms of cost effectiveness, compared with the low-e glazing and electrochromic glazing which required expensive chemical elements for coating, the initial cost of glazing with micro-mirrors (for investment of machines) might be comparable but the running cost (from consumable materials) was relatively low.

For the case of  $MS_{full}$ , the average annual work-plane illuminance for the rear of the office (the region from 4 m deep to 8 m deep) was approximately 550 lux. Such illuminance value was equivalent to approximately 450 kWh/year of electrical consumption for the office during the working hours, if fluorescent luminaires of luminous efficacy of 60 lm/W were considered. Assuming that in a ten storey commercial building there are 100 offices which are identical to the one used in the simulation, the illuminance of 550 lux is equivalent to 45000 kWh of electricity consumption and approximately 900 Swiss Francs saving in electricity bills per year in Switzerland. Compared to the office with low-e glazing, the average increase of the annual average illuminance of  $MS_{full}$  for the rear of the office is approximately 250 lux. Such increase is equivalent to approximately 200 kWh of electricity consumption of working hours per year for the room. For the case of  $MS_{full}$ , at spring equinox noon the illuminances are higher than 1000 lux under a clear sunny sky, and the illuminances are generally higher than 100 lux under an overcast sky. A study (Galasiu and Veitch, 2006) showed that, the preferred illuminance levels lied between 100–300 lux for people working on computers. Therefore, the electric load in lighting for the case of  $MS_{full}$  may be significantly reduced in a computer-oriented office.

The psychological benefits due to the increase of the illuminance by micro-mirrors might not be negligible. Daylight is considered to be the best source of light for good color rendering; it is a light source that most closely matches human visual response. Increased daylight illuminance may



result in the improvement of personal satisfaction and productivity (Li and Lam, 2003; Shin, 2007). It was shown that the lower limit of the illuminance level on the working plane which could give pleasing impression was around 50 lux (Navvab, Siminovitch and Love, 1997). It should be noted that, with the use of micro-mirrors, large amount of daylight could be redirected on the ceiling. The illuminance of the ceiling in the rear of the room might be higher than 2000 lux. The brighter ceiling might result in a pleasing environment for office work.

The bright spots in the rendering in Figure 6-15 were due to the resolution of the full Klems basis for the calculation of bidirectional transmittance distribution function (BTDF). A BTDF is essentially a table of reflectance and transmittance coefficients for incident and outgoing directions. The full Klems basis (Klems, 1994) divides an hemisphere into 145 patches, i.e., 145 incoming and 145 outgoing directions. However, the Klems angle basis was developed for thermal simulations. It may be too low of a resolution for some types of daylighting systems (Reinhart and Breton, 2009). Considering the full Klems angle basis as a reference, two higher resolution angle bases are created by subdividing the full Klems angle basis leading to a 2 x Klems angle basis 580 divisions and 4 x Klems angle basis 2320 divisions. A study by A. McNeil (McNeil, 2011) showed that high resolution bases were appropriate for specific types of complex fenestration systems and performance metrics. The resolution may lead to the overestimate of discomfort glare. To minimize the problem, 2 x Klems and 4 x Klems may be used for daylighting simulation.

In terms of the UDIs, three potential sources of errors (Laouadi, Reinhart and Bourgeois, 2008) in the input that can lead to the inaccurate results: i) the BTDF inappropriately or incorrectly characterizes the scattering distribution of the system; ii) inadequate resolution of the BTDF data results in incorrect spatial distributions of flux within the interior space, and peak intensities of illuminance for sunlight-redirecting systems can be averaged over a single or multiple patches; and iii) the Perez sky may not be able to accurately reproduce luminance distribution. It is reported that, by applying a calibration factor on the sky matrix, the root mean squared errors of the simulated results with respect to the measured results can be less than 23%, which is acceptable (Reinhart and Breton, 2009). However, without experimental measurement, an appropriate calibration factor is almost impossible to define. Therefore, the present authors are dedicated to develop window-size prototype with micro-mirrors. It should be reminded that there are two limitations of using UDI for the interpretation of energy potential. On one hand, UDI is defined by a lower threshold and an upper threshold of certain levels of illuminance, but for individuals there is no strict and identical threshold; on the other hand, UDI does not consider the potential benefit of increased illuminances which do not reach the lower threshold.

The geometry of the micro-mirrors was chosen so that all redirected solar radiation was going upwards. However, a small fraction of the redirected rays was in the range of 0°-5° elevation angle with respect to the horizon, leading to the undesired glare if the micro-mirrors were integrated

below the height of an occupant's head. In the present work, the Daylight Glare Index (DGI) was calculated for the working positions of a sitting occupant in an office. In this case,  $MS_{2/3}$  (micro-mirrors were integrated at 1.5 m from the floor) showed a large reduction of the risk of glare. However, for the working place where employees stand for most of their working time,  $MS_{1/3}$ , (micro-mirrors are integrated at approximately 2.1 m from the floor) might be preferred. Therefore the integration of the micro-mirrors should take into account the working position of occupants (standing or sitting), and the height of a window.

In terms of daylighting performance in a south-oriented office where occupants were assumed to sit down for most of their working time,  $MS_{2/3}$  was considerable for every aspect. Compared with  $MS_{1/3}$ ,  $MS_{2/3}$  brought more daylight to the rear of room, improving the uniformity of the daylighting distribution, reducing the directivity of daylight to the preferred level. Meanwhile, on spring equinox the DGI values of  $MS_{2/3}$  stayed in the imperceptible range from 10:00 to 15:00, whereas  $MS_{full}$  suffered from intolerable glare.

It is suggested to divide the window area into two parts: the daylighting section at the top and the view section below (in the present work it is approximately from 0.7 m to 2 m) (Tzempelikos and Athienitis, 2003; Tzempelikos, 2005). The case of  $MS_{2/3}$ , where part of the view section was integrated with micro-mirrors and the other part of the view section is a plain double glazing, may create an unpleasant view through the window because of the bifurcation of the appearances of objects; taking into account the bifurcation of the appearances of objects,  $MS_{1/3}$  where the micro-mirrors were integrated in the daylighting section (Bastien and Athienitis, 2015) might be preferred by occupants and architects.

The illuminance and the directivity of  $MS_{1/3}$  were similar to that of  $SG$ . However, its advantages could not be neglected: it could improve the uniformity of distribution for the area located at less than 2 m away from the window; the risk of glare was reduced on the spring equinox with the view line parallel to the glazing.

# Chapter 7 Experimental results and discussion

The results for the following fabrication steps are presented: master mold fabrication using both laser ablation and mechanical scanning engraving, replications of PDMS, shape fidelity stability analysis of UV imprinting, thin film deposition and roll-to-roll extrusion. The results of optical characterization were used to evaluate the optical performance of the produced sample with embedded optical microstructures.

## 7.1 Laser ablation

Three types of microstructure were fabricated by nanosecond excimer scanning laser ablation on polycarbonate (PC) substrates. Based on the resulted microstructure on the polycarbonate substrate, they were sorted into three categories: curve sidewall grooves for micro compound parabolic concentrators (CPCs), sharp edges for micro CPCs and high aspect-ratio triangular grooves for the retro-reflective microstructure. In this section, the optimized fabrication parameters are presented. The morphology of the resulted microstructures and the shape fidelity were analyzed. The related effects during ablation were interpreted.

### 7.1.1 Curve sidewall grooves for micro CPCs

#### 7.1.1.1 Curve side wall grooves at different scales for CPC(30, 30)

*The text and images in this section were reproduced from Gong, J., Violakis, G., Infante, D., Hoffmann, P., Kostro, A., & Schöler, A. (2018, February). Microfabrication of curved sidewall grooves using scanning nanosecond excimer laser ablation. In Laser-based Micro-and Nanoprocessing XII (Vol. 10520, p. 105200Z). International Society for Optics and Photonics.*

For the production of micro CPCs, curved sidewall grooves with a controlled optical surface and an aspect ratio of about 2.3 were fabricated. The mask was designed based on the micro CPCs with the half acceptance angle of  $30^\circ$ . In order to study the feasibility of the laser ablation for microstructures at different scales, three values of the opening of the groove were chosen:  $22\mu\text{m}$  (marked as A),  $37\mu\text{m}$  (B), and  $50\mu\text{m}$  (C).

#### *Static ablation*

The length of a unit opening on the mask for the three structures were  $1300\mu\text{m}$ ,  $1825\mu\text{m}$ , and  $2500\mu\text{m}$ , respectively. The smallest openings on the mask were  $10.5\mu\text{m}$ ,  $17\mu\text{m}$  and  $2.5\mu\text{m}$ , respectively. Prior to the scanning ablation, static ablation were conducted to identify ablation rates,

imaging resolution and produced surface. Lower rows of the Fig. 3 show the top surface microscope images of three different elongated triangular mask openings for CPCs on a PC substrate. The blowing gas direction was responsible for the weakly attached debris that was visible as nonsymmetric dark features above the triangles in Figure 7-1. The bases of the triangles were about 20  $\mu\text{m}$ , 35  $\mu\text{m}$ , and 50  $\mu\text{m}$ ; with the lengths of the triangles of 260  $\mu\text{m}$ , 365  $\mu\text{m}$ , and 470  $\mu\text{m}$ , respectively. The contour graphs in the top row of Figure 7-1, and the depth profiles along the lengths of the ablated triangles were presented after 20 pulses at 50 Hz static ablation. For the structure A and B, when the width of the projected triangular mask opening being less than 6  $\mu\text{m}$ , deeper ablation was observed that could be explained either by optical spatial interference effects and /or less plume shielding in tiny ablation regions. The ablation rate for the region of the width larger than 6  $\mu\text{m}$  was about 0.25  $\mu\text{m}/\text{pulse}$  while for the region where the width was about 6  $\mu\text{m}$  the ablation rate was almost twice, which was about 0.5  $\mu\text{m}/\text{pulse}$ . This high ablation rate was kept until the visibly well-defined end of the triangle tip. This indicated that the mask opening at the end of the triangle was larger than the optical diffraction limit of the optical system that was about 2  $\mu\text{m}$ . For the structure C, first the interference effects resulted in a maximum ablation depth of 0.5  $\mu\text{m}/\text{pulse}$  at a width of around 6  $\mu\text{m}$ . Then with decreasing width of the opening the ablated depth decreased due to the possible spatial destructive interference and the resolution limit of the projection system. Therefore, the tip of the structure faded out and the resulting length was less than the theoretical calculation of using the length on the mask divided by the demagnification factor.

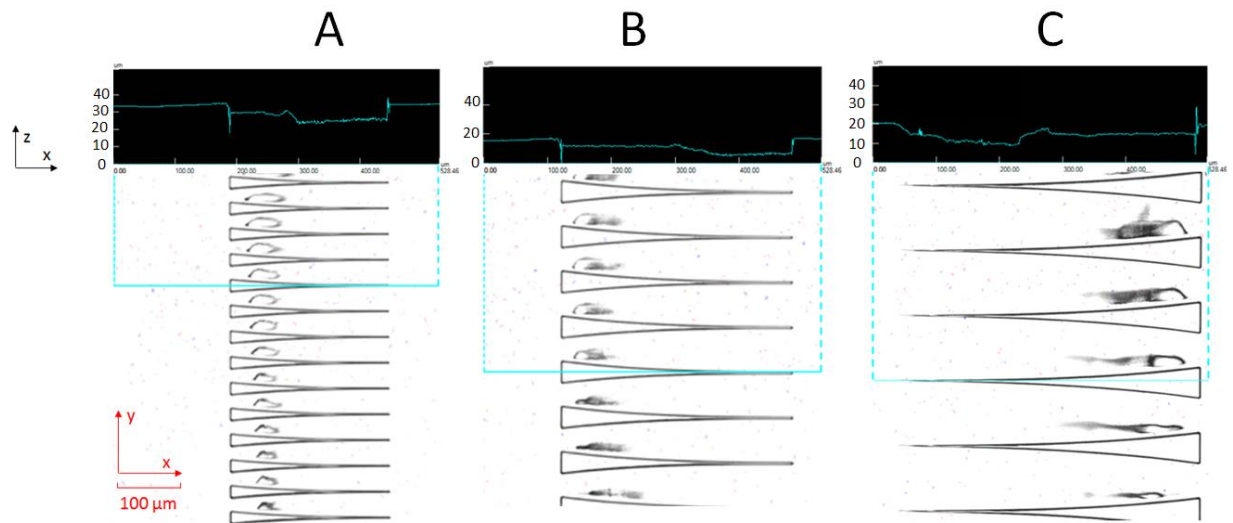
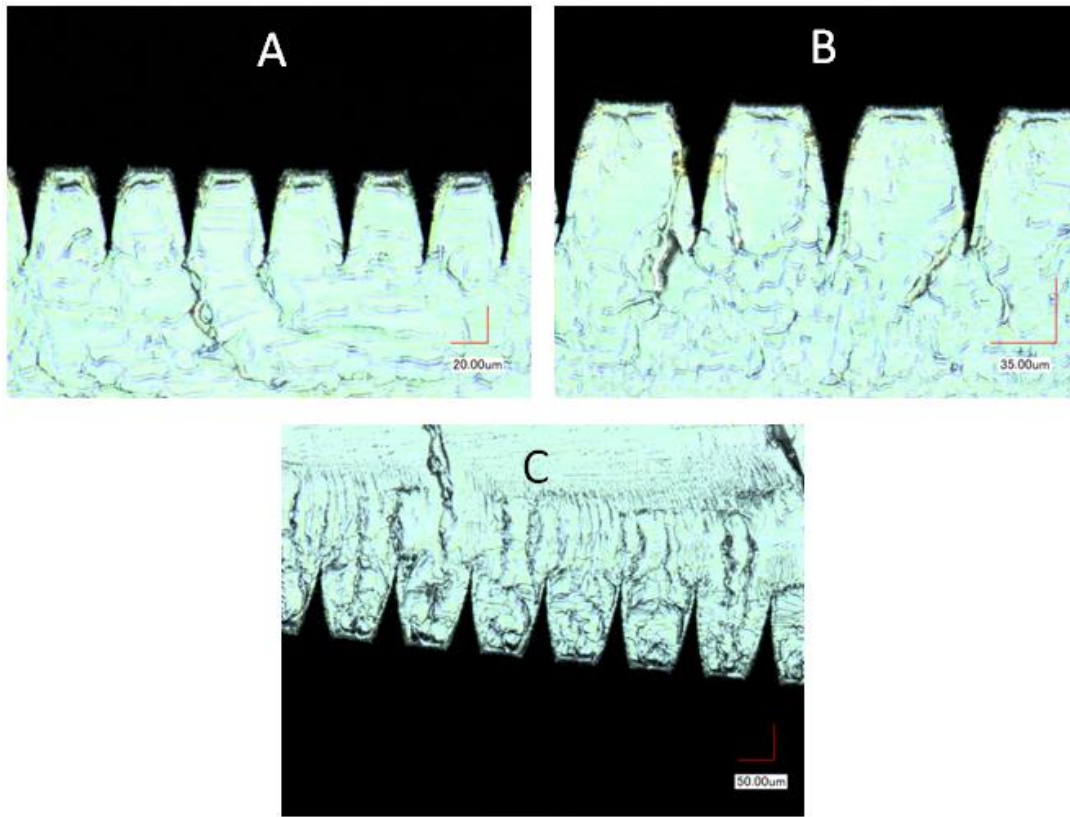


Figure 7-1. The top-view microscope images of the three elongated triangular mask openings for the CPCs on a PC substrate.

### *Scanning ablation*



*Figure 7-2. The cross-sections of the CPCs for A, B, and C on PC substrates.*

Scanning ablation by moving the substrate below the mask, as schematically presented in Fig. 5-4 appears to be a simple geometrical task in order to obtain wanted geometries of the side walls. Unfortunately, there were several phenomena that increased the complexity of the estimation of the final shape of the ablation resulting topography. The ablation depth per pulse as most important parameter is actually influenced by several cross correlated parameters such as the already ablated depth, the ramp angle under which ablation takes place (Braun, 2002), the mask geometry (see for instance the depth profile of static ablated mask C in Fig. Figure 7-1 C), and potentially other parameters that we are not aware yet. In this study no systematic modification of the mask geometry was performed in order to get the obtained results. Implementation of the above-mentioned parameters into the scanning mask design is currently progressing. The obtained structures were of surprising good quality, probably due to balancing counteraction of the above-mentioned parameters. Figure 7-2 shows the cross-sections of the CPCs for A, B, and C on PC substrates. The curved shape of the sidewall was fabricated. The aspect ratio for the three structures was about 2.3. The depth of the curved sidewall grooves ranges from 48 µm to 113 µm, and the scanning ablation rate for the micro grooves A, B, C are 0.15 µm/pulse, 0.14µm/pulse, 0.11µm/pulse. With increasing depth, the loss of energy by heat conduction increased and thereby

decreased the laser-induced temperature rise. Moreover, the transport of ablated species became less efficient and favored material re-condensation within the groove. For deep holes/grooves the attenuation of the incident light by scattering and secondary excitation of product species was important and became more efficient with increasing depth.

### ***Quality analysis of the observed cross-sections***

In order to analyze the shape fidelity from the mask to a PC substrate, for each structure the profile of a unit groove was extracted from the microscope image of the cross-section, and it was compared with the theoretical profile, as shown in Figure 7-3. The resulting curve sidewalls were not perfectly symmetric potentially due to the blowing direction of the plume. Starting from about 1/9 of the total ablated depth, the width of the fabricated groove tended to be larger than the theoretical design at the same depth. The relative average expansion of the width with respect to the maximum groove opening for structure A, B, C were approximately 4%, 2.4%, and 2.8%, respectively. Overall, the shape fidelity was considered to be good. Compared with structure A and B, it was observed that the curvature of the structure C was slightly better than those of structure A and B, due to the lower average ablation rate.

The ablation of structure B was taken as example to explain the mechanism of achieving the correct shapes. Going from the static ablation to the scanning ablation, the speed of sample displacement and the repetition rate of the laser together with the fixed fluence on the mask determined the depth of the groove after one full length of the triangle was scanned through. The ablation rate decreased with increasing depth of the structure. Observed from the top-view microscope images of the elongated triangular mask opening, 2/3 of ablation pulses came with half of the ablation rate, then about 1/3 of the ablation pulses resulted in the twice the ablation rate per pulse. The two counteracting effects resulted in the correct ablation of the shapes.

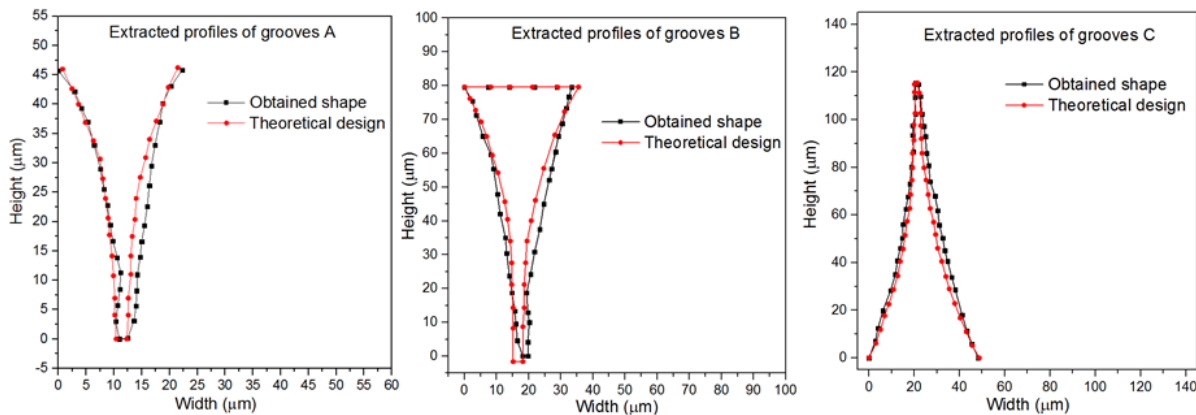


Figure 7-3. The profiles of the fabricated grooves extracted from the microscope images and the theoretical design.

The possible optical properties of the CPC based on structure B on a PC substrate was investigated using ray-tracing simulation. The morphology of the cross-sections of both the blades and the polymer microstructures were extracted for building the computer model. In the computer model, the curve sidewalls were coated with highly reflective material (reflectance 0.9), as shown in Figure 7-4 (a). The theoretical design was of the half opening angle of  $30^\circ$ . The transmittance of the visible light as the function of elevation angles at the azimuth angle of  $0^\circ$  was calculated. The good agreement between the observed final shapes in cross-sections and the design of the mask, resulted in the highly similar angular-selective transmittance profiles predicted from ray-tracing simulations. The transmittance remained at about 0.95 in the angular range between  $-30^\circ$  and  $30^\circ$ , as the theoretical design was of half acceptance angle of  $30^\circ$ . Starting from  $30^\circ$ , partial incident light was redirected by two or more times and then leave the system through the input aperture. Therefore, the transmittance significantly reduced beyond  $30^\circ$ . The application of such angular feature can be used in the place where the winter is mild and summer is hot, or the elevation angle of the winter sun for the working hours are lower than  $30^\circ$ .

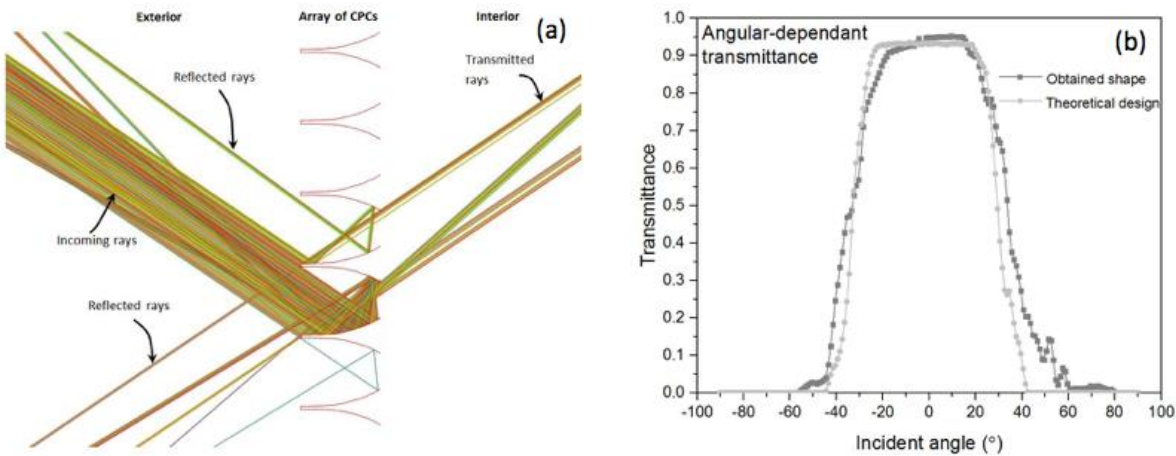


Figure 7-4. Computer model with extracted profile of the theoretical design for ray-tracing simulation; (b) calculated angular-dependent transmittance at the azimuth angle of  $0^\circ$ .

#### 7.1.1.2 Curve sidewall grooves for CPC(40, 40)

Curved sidewall grooves for micro CPCs with the half acceptance angle of  $40^\circ$  were fabricated. The aspect ratio (the height to the the maximum width) of the curved sidewall grooves was about 2.6.

Lower rows of the Figure 7-5 (a) shows the top-view microscope images of the elongated triangular-like mask openings for the CPC(40, 40) on a PC substrate, coupling with the profile (upper part of Figure 7-5(a)) of the ablated depth along the length of the projected mask opening, under static ablation with 10 pulses. The maximum opening was about  $27\ \mu\text{m}$  and the elongated length is  $300\ \mu\text{m}$ . Unlike CPC(30, 30), for the structure 40-40, the ablation depth was first constant



and then decreases with decreasing width of opening due to the destruction of interference and the resolution limit of the projection system. No increased ablation depth due to interference was observed, and it might be due to insufficient focusing. More experimental data are needed in order to explain why there was no constructive interference. The average static ablation rate was  $0.25 \mu\text{m}/\text{pulse}$ . However, the average scanning ablation rate was only  $0.068 \mu\text{m}/\text{pulse}$ .

The cross-sectional view of the resulted microstructure in Figure 7-5 (b). It was seen that the ablated parabolic curve was smooth and continuous. The ablated depth was up to  $68 \mu\text{m}$ . The comparison of the extracted contours of theoretical design and the microstructures on the PC substrate in Figure 7-6. Despite the non-appearance of the interference effect mentioned above, the shape fidelity was good. As the depth increased, the ablated volume was significantly reduced, resulting in less absorption of laser energy by plume. This effect offset the loss of laser energy due to defocus as the ablated depth exceeded the focus depth.

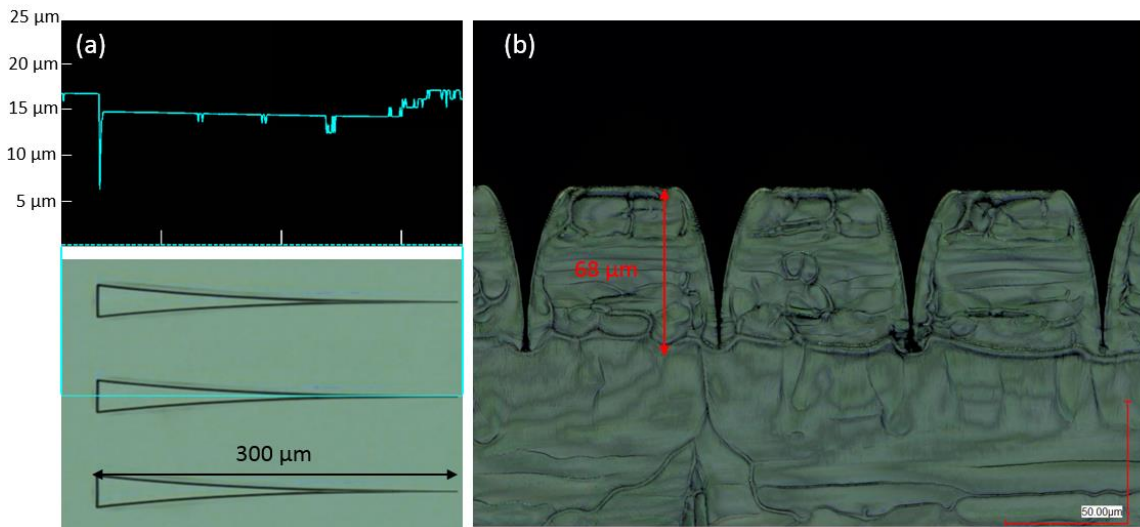


Figure 7-5. (a) the top-view microscope images of the elongated triangular-like mask openings for the CPC(40, 40) on a PC substrate, coupling with the profile (upper part of Figure 6-5 (a)) of the ablated depth along the length of the projected mask opening, under static ablation; (b) the cross-section of CPC(40, 40) under scanning ablation.



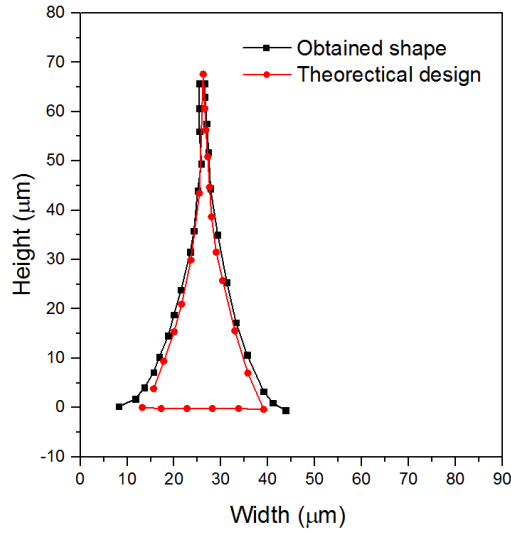


Figure 7-6. The comparison of the extracted contours of theoretical design and the obtained microstructures on the PC substrate

Based on the results for both CPC(30, 30) and CPC(40, 40), it can be concluded that laser ablation is appropriate for the fabrication of the micro-grooves with parabolic curve sidewall, the case where the ablated volume significantly reduces as the ablated depth increase.

## 7.1.2 Sharp edges for micro CPCs

The resulted microstructures on PC substrates should favor the following procedures in the lab: replication of PDMS, UV-imprinting and thin film coating. In the present work, thin film coating based on self-shadowing effect was adopted and developed, and for this aspect, microstructure with sharp edges for micro CPCs on PC substrate was preferred. However, due to the ablation of large mass and significant absorption by plumes and debris, the fabrication of microstructure with sharp edges was very challenging.

### 7.1.2.1 Dependence on repetition rate

Figure 7-7 shows the elongated mask opening (the darker part) projected on the PC substrate under static ablation for 2 pulses. The maximum mask opening was 100  $\mu\text{m}$  and the elongated length was 1200  $\mu\text{m}$ . The average ablation rate over 20 pulses under static ablation was about 0.25  $\mu\text{m}$ /pulse. Under scanning ablation, the ablated cross-sectional area was more than twice the area of the microstructured pattern on PC substrate which were high aspect-ratio sharp edges.

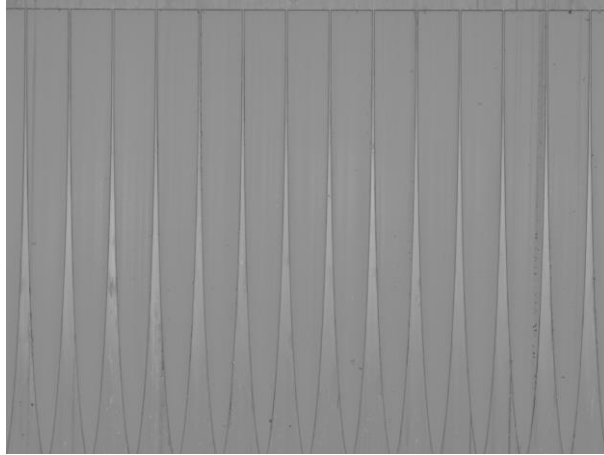


*Figure 7-7. The elongated mask opening (the darker part) projected on the PC substrate under static ablation for 2 pulses.*

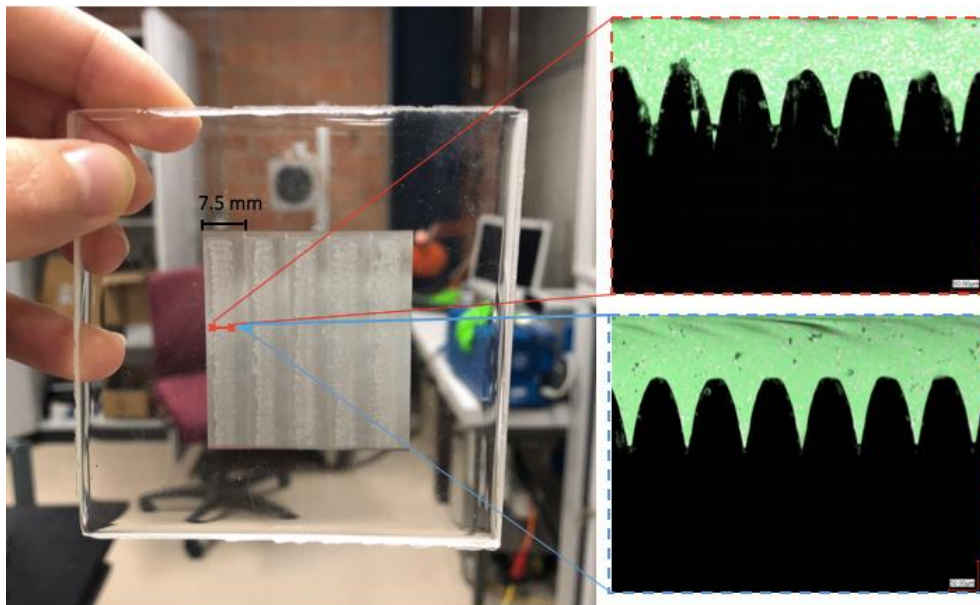


*Figure 7-8. The PDMS microstructures replicated from the microstructure on PC substrate under 50 Hz repetition rate, and the cross-sections of the UV-cured polymer microstructures imprinted by the PDMS microstructures at two different regions.*

On the left-hand side of Figure 7-8 is the PDMS microstructures replicated from the microstructure on PC substrate under 50 Hz repetition rate. The total pulse number of going through the full length of the mask opening was 1150 pulses. The width for each scanning on the PC substrate was 7.5 mm. It was observed that, for each scanning, the optical properties appeared different between the microstructure in the mid region and the microstructure next to the edge. Compared with the semi-transparent appearance in the region next to the edge, the white appearance of the microstructure in the mid region suggested that, more light was scattered due to irregular microstructure. The upper right of Figure 7-8 shows the cross-section of the UV-cured

polymer microstructures imprinted by the PDMS microstructures along the mid region. It is shown that along the mid region, the microstructures are of irregular shape and inconstant height. In contrast, the microstructures at the edge shows the regular shape and constant height, as shown in the lower right of Figure 7-8. In the region next to the edge, the plumes were mainly surrounded by atmosphere, and therefore, it was easier for plumes to expand due to the lower side pressure. However, in the mid region, the expansion of plumes was less effective due to the higher pressure at the inner cloud of plumes, and therefore, the density of plumes was higher. Moreover, as mentioned in chapter 4, part of the plumes can redeposit on the substrate, and then interact with the laser pulses. The strong interaction of a laser pulse with plumes and debris in the mid region of a scan results in the loss of laser energy and inhomogeneity of fluence. The results showed the complication of the redistribution of the plumes as well as debris, and their effect on the absorption of laser beam, in the multi-channels/grooves scanning ablation.

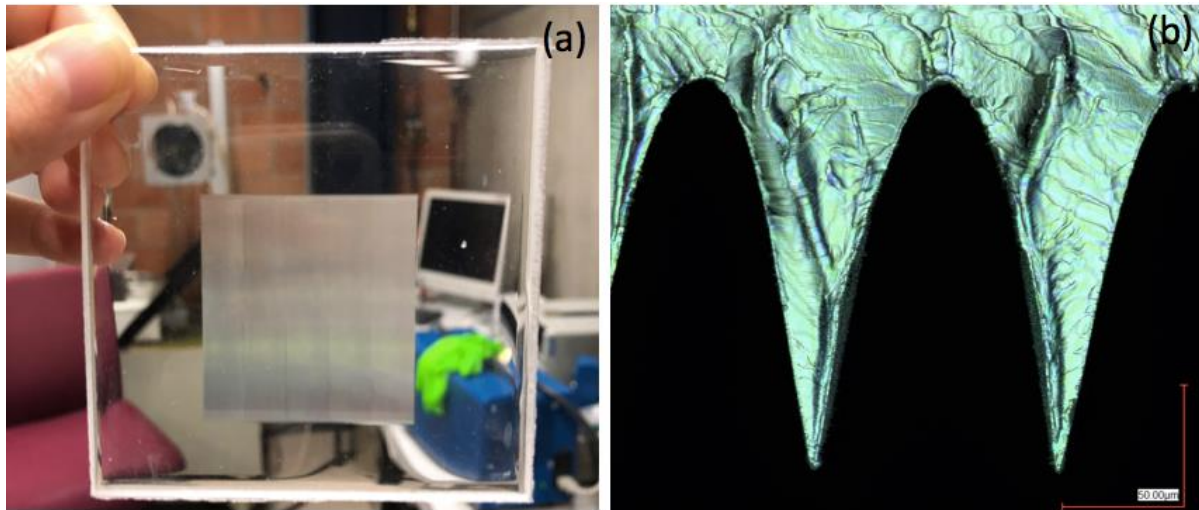


*Figure 7-9. (a) The PDMS mold replicated from the microstructure on PC substrate, and (b) the cross-section on PC substrate under the scanning ablation with 20 Hz repetition rate.*

Figure 7-9 shows (a) the PDMS mold replicated from the microstructure on PC substrate and (b) the cross-section on PC substrate under the scanning ablation with 20 Hz repetition rate. For both the cases with 20 Hz and 50 Hz, the total pulse number of going through the full length of the mask opening and the ramp angle were identical. However, different to the case with 50 Hz, it was observed that, at the repetition rate of 20 Hz, the appearance looked homogenous throughout a scan. The cross-sectional image of the microstructure shows that the height, the periodicity and the shape are constant. The results proved that at the repetition rate of 20 Hz, the spatial distribution of the fluence remained rather constant from one groove to another groove.

The difference between the case of 20 Hz and the case of 50 Hz, suggested the significant effect of repetition rate on the properties of debris. At higher repetition rate, the stacking of debris was faster, i.e., the debris from one pulse would have less time for relaxation and/or being oxidized

before the debris from next pulse arrives. The adherence of the debris layers/particles was stronger to each other and to the substrate. Therefore, at higher repetition rate, due to the stronger interaction between debris layers and therefore larger plume particle size and content interaction with the laser light in the following laser pulses, the microstructures became irregular.

### 7.1.2.2 Quality analysis of the observed cross-sections

Figure 7-10 presents the profiles of the fabricated grooves extracted from the microscope images for the case of 20 Hz and 50 Hz, and the theoretical design. As mentioned before, the total pulse number of going through the full length of the mask opening was identical. However, the depth of the groove for the case with 20 Hz was about 20  $\mu\text{m}$  higher than the case with 50 Hz repetition rate, due to the less absorption of laser energy by the debris and plumes. The depth of the microstructure at the repetition rate of 20 Hz could be matched with the depth of theoretical design by reducing the pulse numbers for scanning the full length of mask opening.

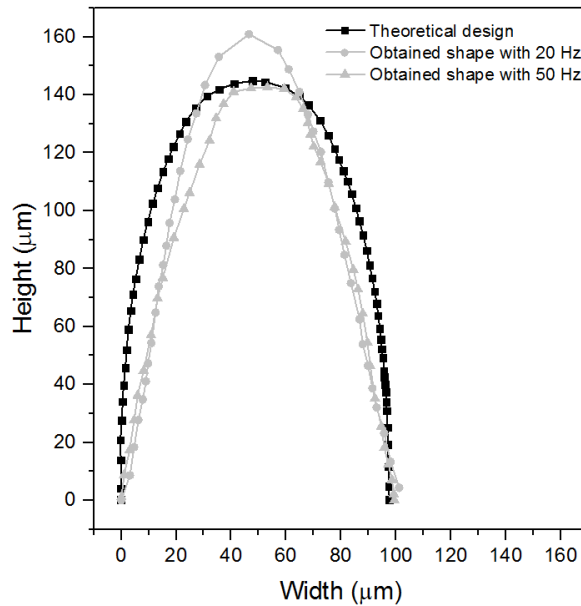


Figure 7-10. The profiles of the fabricated grooves extracted from the microscope images for the case of 20 Hz and 50 Hz, and the theoretical design.

The obtained grooves were narrower than that of theoretical design. On one hand, it was due to the present (false) scanning direction. The present direction is shown on the left-hand side of Figure 7-11. The dash contours represent the projected mask opening from next pulse. It was assumed that the step size of the two pulses were identical. Compared with the preferred (correct) direction, the area marked with dotted gray line in the case of false direction was not covered by the next pulse, resulting in the narrower opening of the micro grooves. In fact, it is observed from Figure 7-10 that, the geometry of the difference between the cross-section of the obtained grooves and the theoretical design is similar to the arear marked with gray dot lines.

On the other hand, the defocus of the laser when the ablated depth was beyond 25  $\mu\text{m}$  could also contribute to the discrepancy of the cross-section.

Despite of the use of the false scanning direction, the obtained shape in Figure 7-9 (b) and the shape comparison in Figure 7-10 show the potential of the production of sharp edges. The corresponding mask opening allows much more photons arrives on the substrate, and therefore offset the huge absorption by plume, compared with the fabrication for curve sidewall grooves.

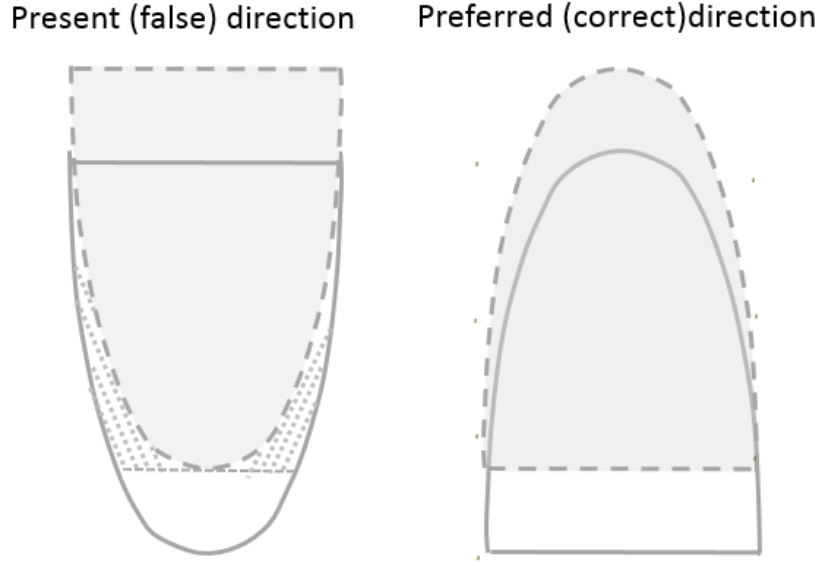


Figure 7-11. The sketch of the two scanning direction: the present (false) direction and the preferred (correct) direction. The dash contours represent the projected mask opening from next pulse.

### 7.1.3 High aspect-ratio triangular grooves for the retro-reflective microstructure

For the retro-reflective microstructure, elongated triangular mask opening was used, leading to high aspect-ratio triangular grooves on the PC substrate.

#### 7.1.3.1 Static ablation with various ablation rates

Figure 7-12 shows the top-view microscope images of the elongated triangular mask openings for the L-shape microstructure on a PC substrate under static ablation with the repetition rate of 50 Hz for 20 pulses. The length and the maximum width of the opening were 90  $\mu\text{m}$  and 12  $\mu\text{m}$ , respectively. Unlike the mask contour for the CPC microstructure of which the width decreased exponentially with the increased of the ablated depth, for the mask contour of the “L”-shape microstructure, the width decreased linearly with the increase of the ablated depth.

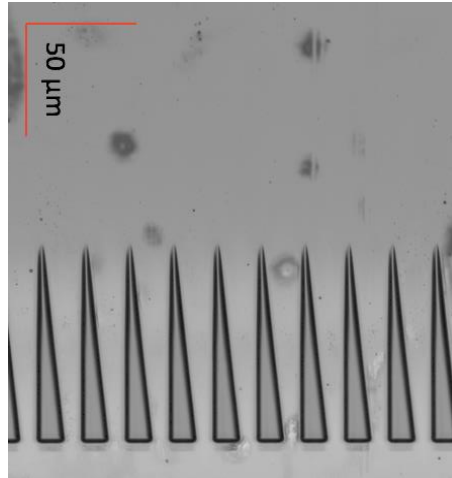


Figure 7-12. The top-view microscope images of the elongated triangular mask openings for the “L”-shape microstructure on a PC substrate.

Table 7-1. Average ablation rate as function of repetition rate under static ablation with 20 pulses.

Repetition rate	50	100	150	200
Ablation rate (nm/pulse)	232	223	216	207

In the previous section, the effect of the repetition rate on the quality of microstructured surface and the geometrical parameters were presented and analyzed. In order to understand more about the effect of repetition rate, average ablation rate under static ablation for various repetition from 50 Hz to 200 Hz was conducted, and the results were summarized in Table 6-1. The ablation rate is the total ablation depth over 20 pulses. It was observed that, the ablation rates slightly and gradually reduced when the repetition rate increased from 50 Hz and 200 Hz, and the average reduction rate per frequency change was rather constant: 8 nm per 50 Hz. The present ablation output energy was set at a constant energy mode at 350 mJ, and at the repetition rate of 50 Hz, this energy output corresponded to 19-20 kV voltage of the gas discharge. For higher repetition rate, higher voltage for discharging the gas was needed to maintain the constant energy output. However, the upper limit of the voltage is in the order of 20 kV (Li and Ananthasuresh, 2001). Therefore, the voltage cannot be further increased with the increase of the repetition rate to maintain the constant energy output. Therefore, the incident fluence reaching the substrate decreased and the ablation rate decreased.

#### 7.1.3.2 Scanning laser ablation under various repetition rate

Figure 7-13 shows the cross-sections of the microstructures fabricated under scanning laser ablation with 50 Hz repetition rate and 20 Hz repetition rate, respectively. The total pulse number



of going through the full length of the mask opening, and the fluence were identical. It was observed that, the difference due to the change of repetition rate was pronounced for high aspect ratio under scanning ablation. The micro grooves under scanning ablation with 50 Hz repetition rate tended to be U-shape, while the shape of micro grooves under scanning ablation with 200 Hz repetition rate was similar to the curve side wall micro grooves for CPC microstructure, and the height was less than the height of the microstructure fabricated with 50 Hz repetition rate. The morphology difference was due to the significant decrease of ablation rate under scanning ablation.

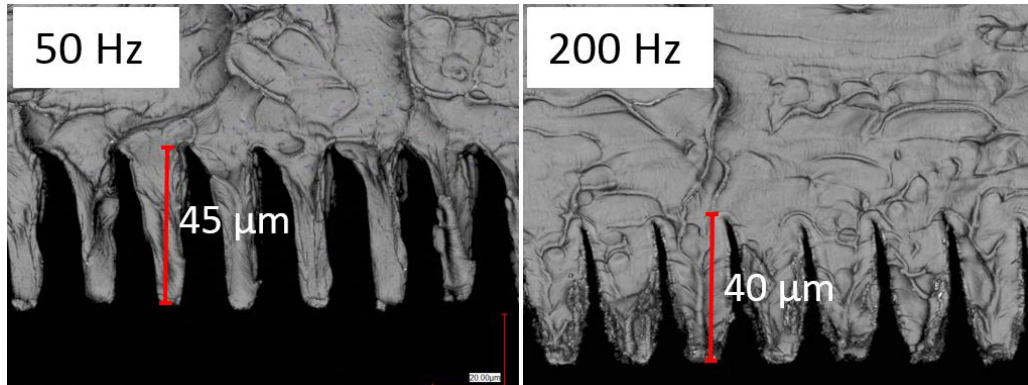


Figure 7-13. The cross-sections of the resulted microstructure on the PC substrates under scanning laser ablation with the two repetition rates: (a) 50 Hz, and (b) 200 Hz.

#### 7.1.4 Feasibility of laser ablation

In summary, scanning laser ablation has been tried on three types of the microstructures: i) curve sidewall grooves for micro CPCs, ii) sharp edges for micro CPCs, and iii) high aspect-ratio triangular / rectangular grooves for the retro-reflective microstructure. The feasibility and the key impact factors of the fabrication for the three types of microstructures using laser ablation are summarized in Table 7-2. For the fabrication of curve sidewall grooves for micro CPCs, as the ablated depth increases, the ablated volume and therefore plume is reduced significantly; moreover, the amplified fluence because of interference effect also contribute to the deep-groove ablation. The second type of the microstructure is the counterpart to the triangle-like parabolic sidewall grooves, the ablated volume is very large. However, the mask opening is also very large which allows more photons for ablation, and the aspect ratio is relative low; therefore, for such kind of microstructure, it is rather difficult to fabricate but it is possible with lower repetition rate, for example, 20 Hz. The third one is the structure which is somewhere in between the other two structures in terms of the ablated volume, for example, the rectangle-like microstructures. For such kind of microstructures, it is large volume ablation; the mask opening in the present work does not allow enough photos; moreover, the aspect ratio of this type of microstructure is difficult for the plume to expand and favors the re-deposition of debris. Therefore, it is very difficult to fabricate such kind of microstructure using laser ablation.

*Table 7-2. The feasibility and the key impact factors of the fabrication for the three types of microstructures using laser ablation.*

	<b>Curve sidewall grooves for micro CPCs</b>	<b>Sharp edges for micro CPCs</b>	<b>High aspect-ratio triangular / rectangular grooves for the retro-reflective microstructure</b>
<b>Feasibility</b>	Easy	Difficult but possible	Very difficult
<b>Reasons</b>	a). Significantly decreased ablation volume with the increase of ablated depth b). Amplified ablation rate by interference effect	a). Large mass ablation b). The amount of photons also large c). Low aspect-ratio	a). Large mass ablation b). High aspect-ratio



## 7.2 Scanning mechanical engraving

A novel mechanical engraving method using blades with microstructure of desired patterns on soft substrates was developed. Such blades could be obtained in a large variety of shapes using UV-LIGA technology which combined photolithography and electroforming. The usage of the blade enabled the combination of high aspect ratio with almost any closed profile. In the present work, the feasibility of high aspect-ratio rectangle-like microstructure with parabolic side wall and microstructure with overhang was proven. Master molds were prepared and the following steps of micro UV-imprinting from the master molds were also introduced. Shape fidelity in terms of pattern transfer for this method was analyzed and presented. The roughness of the engraved microstructure was investigated. The resulted microstructures on wax cylinder roll which gave the potential of upscaling were fabricated.

### 7.2.1 High aspect-ratio rectangle-like microstructure with parabolic side wall

*The text and images in this section are reproduced from: Gong, J., Delaunay, A., Kostro, A., & Schüller, A. (2018). Development of a novel mechanical micro-engraving method for the high-aspect-ratio microstructures of an advanced window system. Microelectronic Engineering, 191, 48-53.*

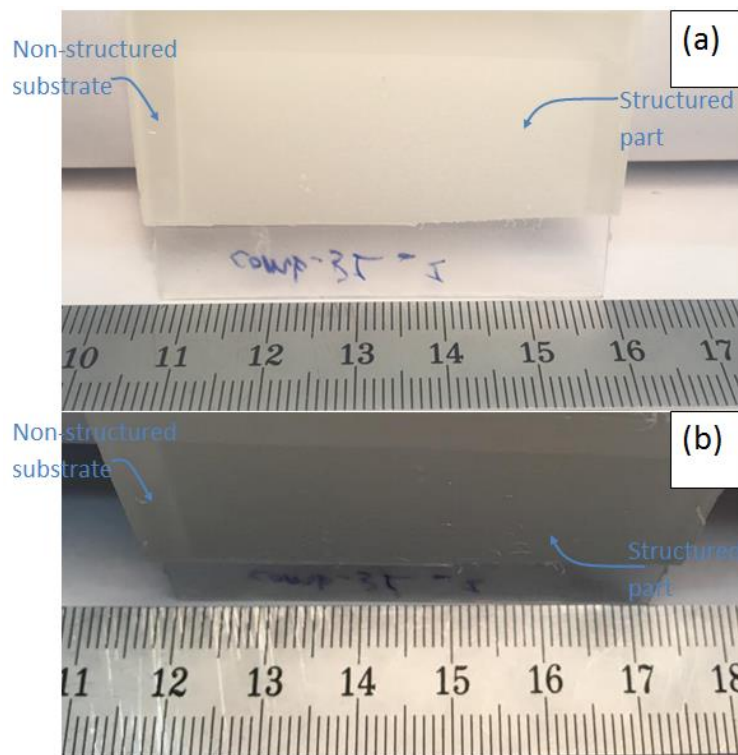


Figure 7-14. A sample with microstructures of aspect ratio of 3.8 on the paraffin-based substrate. The sample is observed lower than (a) 25° and higher than (b) 60° with respect to the normal to the surface.

Figure 7-14 shows a sample with microstructures of aspect ratio of 3.8 on the paraffin-based substrate. The sample was observed to be lower than  $25^\circ$  (Figure 7-14 (a)) and above  $60^\circ$  (Figure 7-14 (b)) in diffused daylight. Light of incident angle lower  $25^\circ$  was partially redirected to eyes. Therefore, the microstructured part appeared brighter than the non-structured part. In contrast, light of incident angle higher than  $60^\circ$  was redirected to the blocking surface and then reflected back to the coming side, as shown in the sketch of Figure 3-1. Thus, the microstructured part looked darker than the non-structured part. The redirection effect and the blocking effect due to the optimized geometry were preliminarily confirmed. The microstructured area was about 45 mm x 25 mm, corresponding to one linear scan of the 25-mm wide blade along the substrate for 45 mm. The speed of the scanning was 150 mm/min. Therefore, a 45-mm scan took 20 seconds.

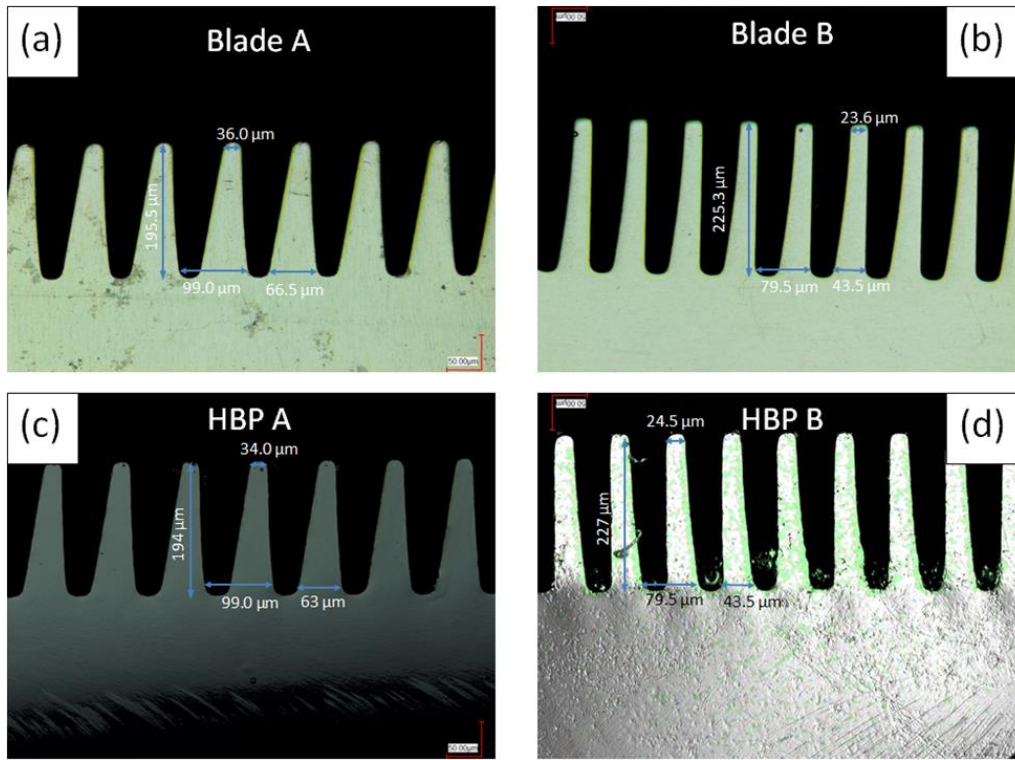


Figure 7-15. The cross-sections of the microstructures on the blade A and B and their corresponding HBP microstructures.

Figure 7-15 shows the cross-sections of the blade A and B and their corresponding HBP microstructures. For the blade A, the average depth of the micro teeth was  $195.5 \pm 0.5 \mu\text{m}$ , and the width of the two ends of a teeth were  $36 \pm 0.3 \mu\text{m}$  and  $66.5 \pm 0.5 \mu\text{m}$ , respectively. The corresponding dimensions of the polymer microstructures HBP A were  $194 \pm 0.5 \mu\text{m}$ ,  $34 \pm 0.3 \mu\text{m}$  and  $66.5 \mu\text{m}$ . It was likely due to the shrinkage of polymerization (Gong *et al.*, 2017), the dimensions of microstructures HBP A were slightly reduced. Nonetheless, the relative reduction was below 5%. For the blade B, the average depth of the micro teeth was  $225.3 \pm 0.5 \mu\text{m}$ , and the width of the two ends were  $23.6 \pm 0.3 \mu\text{m}$  and  $43.5 \pm 0.5 \mu\text{m}$ , respectively. Correspondingly, the

dimensions of the polymer microstructure HBP B were  $227 \pm 3 \mu\text{m}$ ,  $24.5 \pm 0.5 \mu\text{m}$  and  $43.5 \pm 0.5 \mu\text{m}$ , respectively. It is shown that the dimensions of the polymer microstructures HBP B are slightly increased by maximum 3.8% can be due to the swelling (Miller-Chou and Koenig, 2003; Nandi and Winter, 2005) of polymer during cleaning in the dissolve solvent. Nonetheless, the swelling could be suppressed by the reduction of cleaning time with the improvement of the cleaning procedures. Overall, the observation of the cross-sections showed the good control of shape by the method.

In order to study the shape fidelity, the morphology of the cross-sections of both the blades and the polymer microstructures were extracted for ray-tracing simulation to calculate the angular dependent transmittance. A reference case was taken with the conventional double glazing. In the computer models, micro-mirrors were coated on selected facets and embedded in a polymer layer. Then the polymer was attached to the second surface of the outer glass pane of a double glazing. Figure 7-16 shows the simulated angular-dependent transmittance: transmittance in the visible range for different incident angles at the azimuth of  $0^\circ$ . For the case A and case B, there was a decrease of the transmittance from  $0^\circ$  to  $20^\circ$ . It was mainly because that in this angular range, a fraction of incoming light directly went to the blocking mirror without being redirected by the parabolic mirrors and then was reflected to exterior. The application of such angular feature can be used in the place where the winter is mild or the elevation angle of the winter sun for the working hours are higher than  $20^\circ$ . For the blade A and the polymer microstructure HBP A, the simulated transmittances were highly similar, confirming the good shape preservation and surfaces with similar roughness. The profiles of the angular-dependent transmittances were identical to the case of the conventional double glazing in the angular range from about  $20^\circ$  to  $55^\circ$ , and then the transmittance moderately reduced from  $55^\circ$  to  $75^\circ$ . Such designs would be used mainly for light redirection and glare protection, as they do not offer a strong angular dependence. For blade B and the polymer microstructure HBP B, the trends of the profiles were similar but the deviation was observed. The transmittance drop was shifted by about  $7^\circ$  toward the normal incidence. The shift was likely due to two reasons: designs with higher aspect ratio were more sensitive to variation in the curvature of the mirrors and the variation in shape during engraving and replication also tended to increase. Nonetheless, a strong angular dependence of the transmittance was achieved. When the target is to moderate solar gains in summer but maximize them in winter, such a design is desired. Compared with blade A, the strong angular dependence of blade B was due to its higher aspect ratio and curvature, which led more direct incident light redirected by the parabolic mirrors to the blocking mirrors

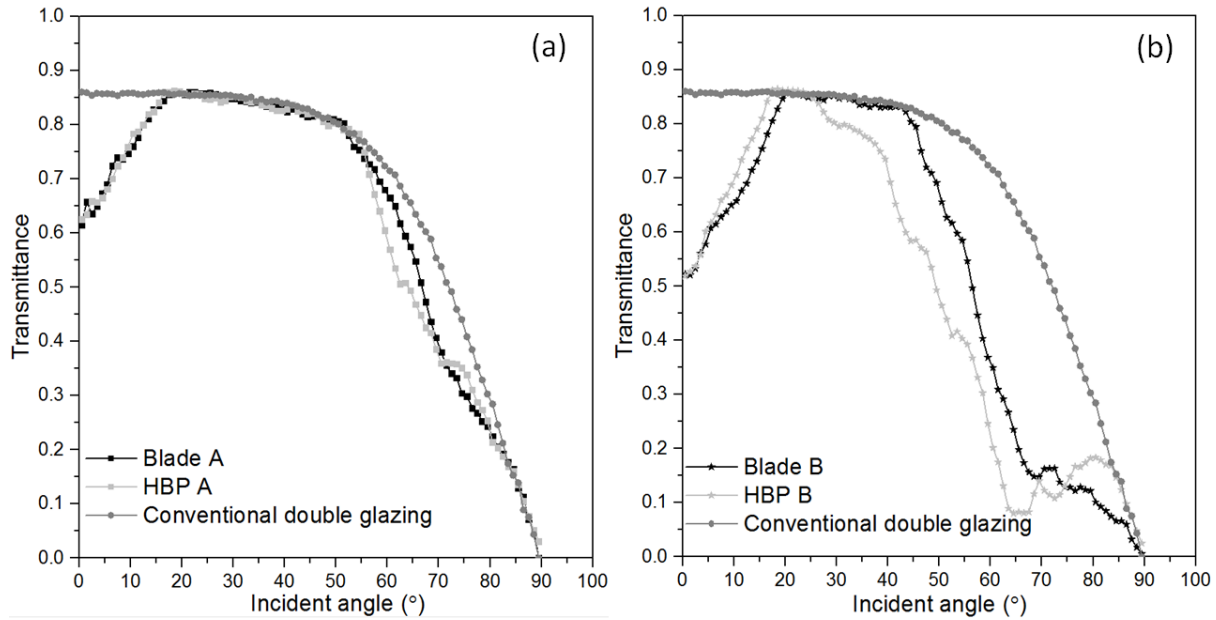


Figure 7-16. The simulated angular-dependent transmittance for blade A and B and their corresponding HBP microstructures.

### 7.2.2 Microstructures with overhang

Figure 7-17 shows a UV-cured polymer microstructure with overhang replicated from the engraved wax substrate. The microstructured area was 4 cm<sup>2</sup>. After the replication, the wax was molten by heat and the residual UV-cured polymer microstructure washed in organic solvent for half an hour. It was observed that there were no residual wax flakes on the surface, proving the effectiveness of the cleaning procedure. The periodic linear lines suggest a good replication and effective pattern transfer from the blade to the wax substrate.

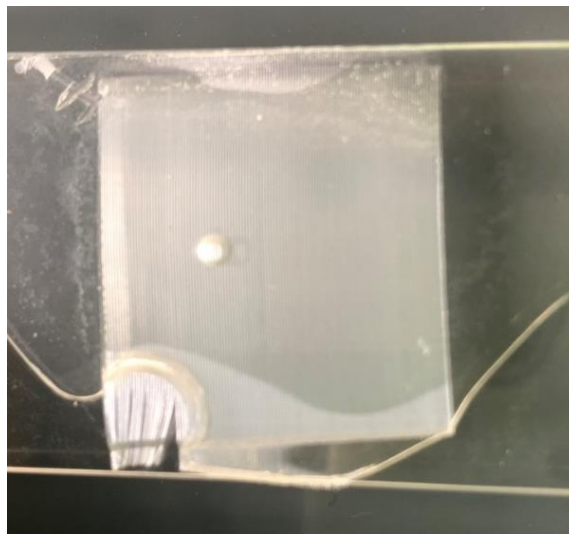


Figure 7-17. An UV-cured polymer microstructure with overhang replicated from the engraved wax substrate.

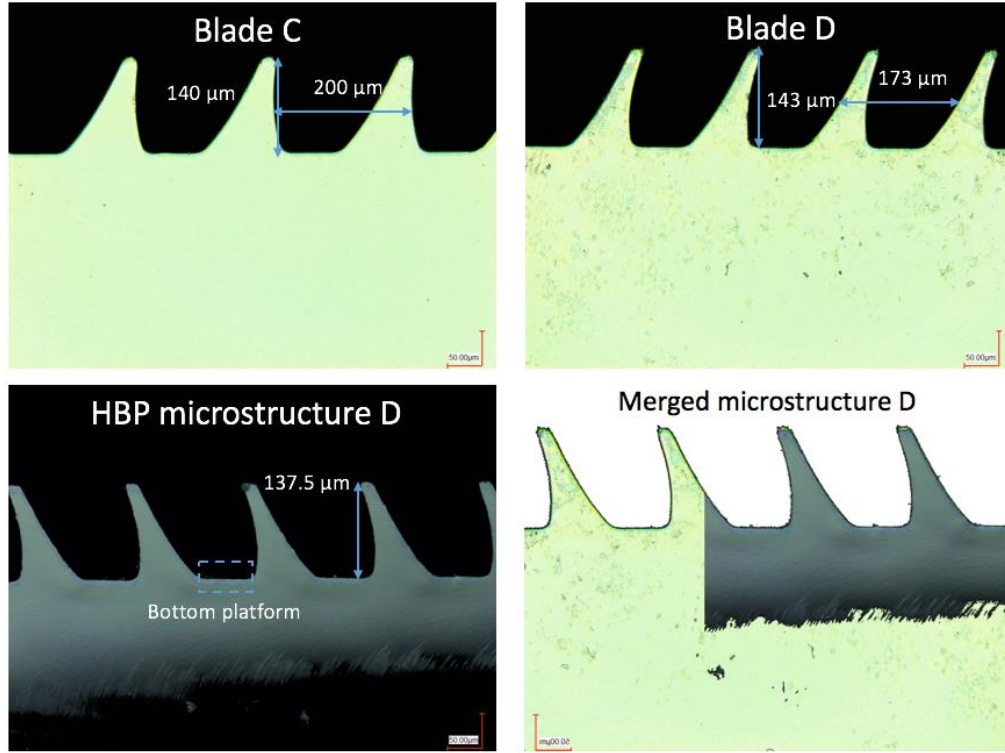


Figure 7-18. The cross-sections of the the microstructure on blade C and D and the corresponding HBP microstructure D.

Figure 7-18 shows the cross-sections of the blade C and D and the corresponding HBP microstructure D. For the blade C, the average depth of the microstructure was  $140 \pm 0.5 \mu\text{m}$ , and the periodicity was  $200 \pm 0.5 \mu\text{m}$ , respectively. Slight overhang exist on the microstructure on the blade C. For the blade D, the average height of the microstructure was  $143 \pm 0.5 \mu\text{m}$ , and the periodicity was  $173 \pm 0.5 \mu\text{m}$ , respectively. Because of the shrinkage of polymerization, the height of microstructures HBP D was slightly reduced by about 3.8%. The contours of the microstructure on blade D (the bright part) and the HBP microstructure D (the dark part) are extracted and overlapped, marked as merged microstructure D in Figure 7-18. It is shown that the two contours are perfectly matched except for that the microstructure on the blade is slightly higher.

By observing the macroscopic clean appearance and good shape fidelity of the engraved microstructures, it can be concluded that mechanical engraving is appropriate for the fabrication of the linearly microstructures with overhang.

#### 7.2.2.1 Roughness

In order to estimate the roughness of the engraved surface, the surface topology of the bottom platform (as marked in Figure 7-18) of the HBP microstructure D replicated from wax substrate with 5% beeswax and 20% beeswax was investigated using laser confocal microscope. The laser scans (marked with dash lines) to obtain the average height as the indication of the surface



roughness are along the dash lines, as shown in Figure 7-19. For each case, the upper graph shows the top view of the bottom channel, and the lower graph shows the height along the scan. The average height of the surface roughness was about  $0.33\text{ }\mu\text{m}$  for the substrate with 5% beeswax, while for the substrate with 20% beeswax the roughness was about  $1.17\text{ }\mu\text{m}$ . In fact, one can see stripes along the scanning direction for the HBP microstructure replicated from the substrate with 20% beeswax. There are two main reasons for the higher roughness with 20% beeswax: on one hand, more beeswax makes the removal materials more adhesive on the blade; on the other hand, more beeswax makes the substrate more ductile, leading to higher roughness when the blade breaks the substrate material. Therefore, substrate with less beeswax leads to smoother surface.

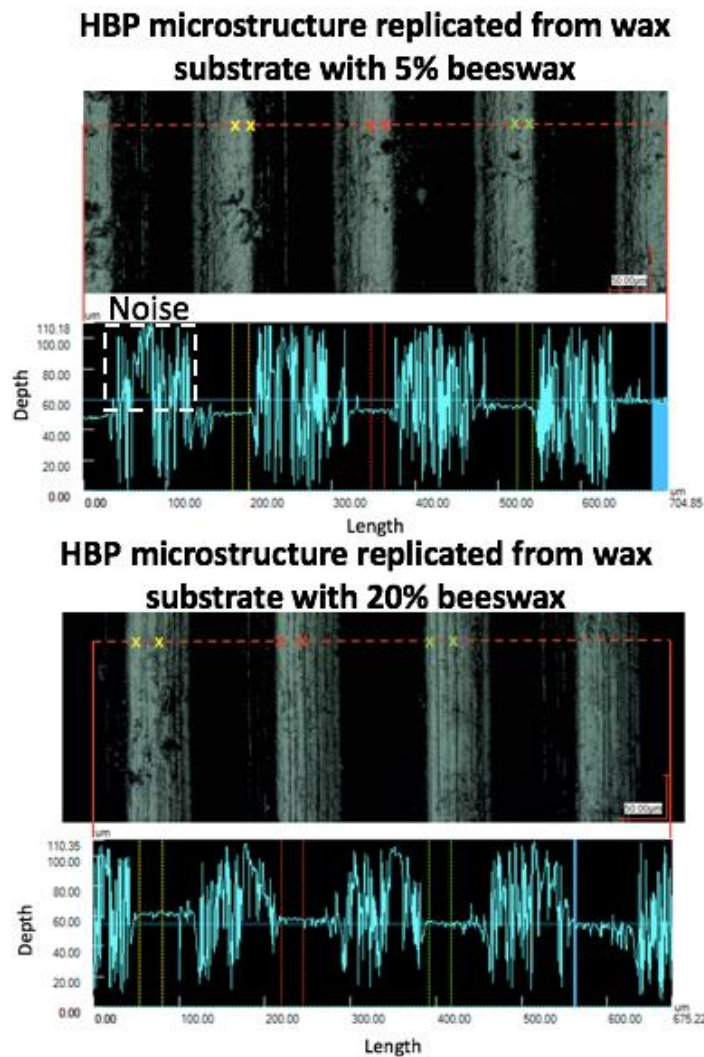


*Figure 7-19. Roughness profile of the bottom platform (as marked in Figure 7-18) of the HBP microstructure D replicated from wax substrate with 5% beeswax and 20% beeswax. For each case, the upper graph shows the top view of the bottom channel, and the lower graph shows the roughness profile along the scan. The roughness profile is taken using a confocal microscope.*

### 7.2.3 Engraving on wax cylinder roll

Prior to engraving on a wax cylinder roll, about 2-mm surface of the wax cylinder roll was peeled off to have smooth surface. Figure 7-20 shows the swarf due to the peeled-off surface from the wax cylinder roll with 5% beeswax. The morphology of the swarf looks like that of stainless steel with good ductility, confirming the similarity of the two materials (Enamul Hossain, Ketata and Rafiqul Islam, 2009).

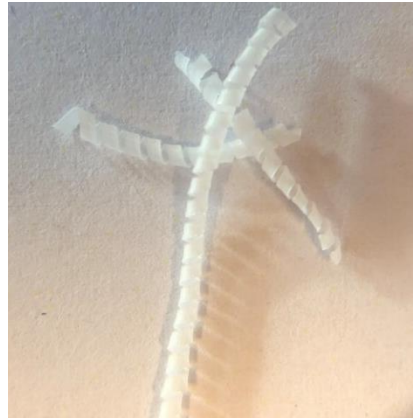


*Figure 7-20. The swarf from the peel-off surface of the wax substrate with 5% beeswax*

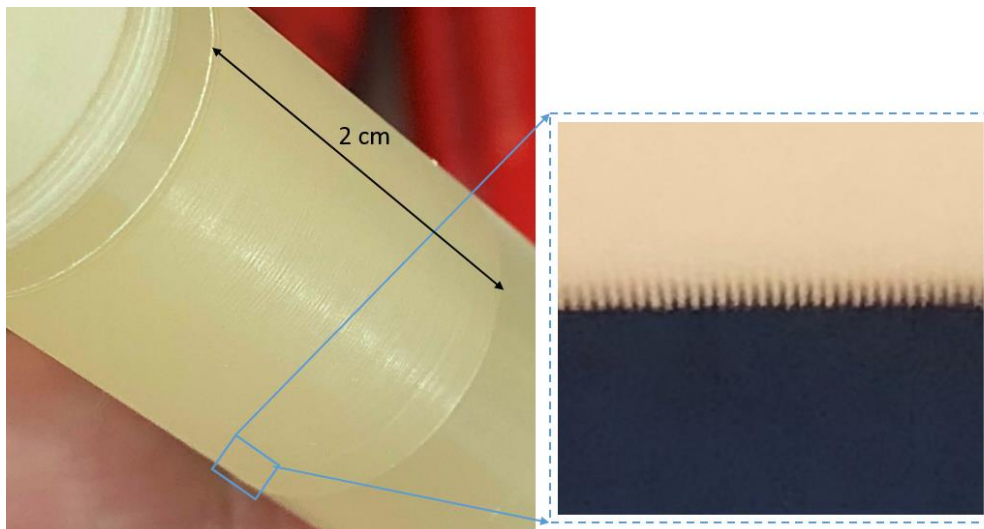


*Figure 7-21. A sample engraved with blade A on wax cylinder roll with 5% beeswax.*

Figure 7-21 shows a sample engraved with blade A on wax cylinder roll with 5% beeswax. The engraved surface was homogenous, and no residual wax flakes appeared. The wax microstructure was periodic and the high aspect ratio was retained.



*Figure 7-22. A sample engraved with blade A on wax cylinder roll with 20% beeswax.*

Figure 7-22 shows a sample engraved with blade A on wax cylinder roll with 20% beeswax. The roll rotated for about 30s due to the multiple rotations of roll and therefore several scanning on the same area, the negative effect of the adhesive wax on the blade became pronounced. Therefore, the microstructures were breaking and irregular.

#### **7.2.4 Summary of the engraving results**

A novel mechanical engraving method using blades with micro-teeth of desired patterns for the preparation of master molds was developed. The following steps of UV-microimprinting from the master molds were also developed. The fabrication for rectangle-like microstructures with parabolic-side-wall and aspect ratio of 3.8 as well as 6.7 was achieved. The method is also appropriate for microstructure with overhang. The pattern transfer showed good controlled shape fidelity. The desired angular-dependent optical properties were obtained. With a scanning speed of 15 cm/min, the method has the potential to be efficient and appropriate for large-area microstructured fabrication.

#### **7.2.5 Comparison between laser ablation and mechanical engraving**

In the present section, comparison has been made in terms of scanning speed (operation speed), roughness, resolution and fabricated shape between laser ablation and mechanical engraving, in order to choose the appropriate master mold fabrication technique for different microstructures.

- Scanning speed (operation speed)

For the microstructures in the present thesis, the scanning speed of laser ablation varies from 1.5 mm/min to 3mm/min, depending on the ablated depth. The used scanning speed for mechanical engraving on flat soft substrates is 150 mm/min. However, for mechanical engraving, after each scan, the blade needs to be taken off from the CNC machine for cleaning and then installed back; if 15 minutes is considered as the time for the uninstalling, cleaning and installing procedures, the



actual speed (operation speed) for one scan is in the order of 10 mm/ min. For a microstructured area of 150 mm × 150 mm, assuming the same scanning width of 10 mm, the mechanical engraving takes 210 minutes whereas laser ablation can take up to 24 hours. However, the speed might not be a critical problem for master mold fabrication with laser ablation, especially for the sample at the lab scale; during ablation, labor force is not necessary, and the machine can be left for running overnight.

- Roughness

Based on the result of (Naessens, Kris, et al.), rms surface roughness is less than 1.3% of the ablated depth for static ablation ablated after 20 pulses of 47 mJ/cm<sup>2</sup> with an ArF laser on polycarbonate; for scanning ablation, the roughness along the scanning direction can be in the order of several hundred nanometers due to the discrete pulses. For mechanical engraving, the roughness depends on the roughness of the microstructures on the blade, the materials, and the use of vibration-damping device. In the present work, the blade is with the roughness of several-tens nanometers, and no vibration-damping device is used. The roughness of about 300 nm has been observed for the microstructures fabricated using mechanical engraving on wax substrate with 5% beeswax and 95% paraffin, and the roughness can be further reduced by post-polishing or using vibration-damping machine during engraving. Overall, the roughness is not a decisive factor to choose the either of the two techniques.

- Feature size

The feature size of the scanning laser ablation can be less than 1 μm in diameter whereas the feature size of the microstructure on the blade is about 20 μm in diameter. It means that, the edge fabricated by mechanical engraving cannot be as sharp as the one fabricated by laser ablation. The feature size has considerable impact on the optical properties on the embedded microstructures. For example, for micro CPCs, which require sharp edges, the feature size 20 μm in diameter will result in the sacrifice of the transparency at normal incidence.

- Scale of microstructures.

Due to the feature size of mechanical engraving, for micro CPCs, in order to maintain good transparency of the sample, generally speaking, the base width for the sharp edge is recommended to be greater than 50 μm, and correspondingly, the height of the microstructure will be larger than 100 μm; this scale may be difficult for the following processing procedures, which will be introduced next sections. In contrast, there is no strict limitation of the width of the base or the periodicity, the height of the microstructures can vary from 40 μm to 160 μm, based on the present experimental results.

- Shape

Due to the mechanism of laser ablation, it is difficult to have controlled shape of microstructures with overhang. Moreover, it is also very difficult to fabricate high aspect-ratio rectangle-like microstructures using laser ablation, as analyzed in the section 7.1.4. With mechanical engraving, the feasibility of the fabrication of the two types of difficult microstructures have been proven by the experimental results.

In summary, for samples at the lab scale, to decide either of the two fabrication technique for master mold, the important factors to consider are the feature size, the scale and the shape of the microstructures. For micro CPCs based on the microstructures with sharp edges/grooves, laser ablation is preferred. For microstructures with overhang or high aspect-ratio, mechanical engraving should be considered first.

For industrial upscaling, it is easier to achieve seamless mold for roll-to-roll process with mechanical engraving. The running cost should also be compared thoroughly.

## 7.3 Replication of PDMS

By inducing solutions with HPMC diluted in water, the processes for PDMS casting from PDMS, and PDMS casting from a wax mold, have been developed, respectively. The microscopic wetting behavior of PDMS was investigated. The feasibility of the replication processes with different concentration of HPMC solution was studied. The feasibility study was also conducted for different types of the microstructures.

### 7.3.1 PDMS replicated from PDMS

In order to understand more the wetting behavior of HPMC solution on PDMS mold. Figure 7-23 shows the three status of the PDMS mold: (a) before immersing in liquid, (b) during the pouring of 0.5% HPMC solution, (c) 30 seconds after being immersed under the 0.5 wt% HPMC solution. It can be seen that, the solution surrounds the microstructured area and forms a “ring”. The microstructured surface is hydrophobic. The 0.5 wt% HPMC solution is poured until the PDMS mold is fully immersed in the liquid for 30 seconds, and then the PDMS mold is taken out of the liquid. It is observed that, during the 30 seconds, very few parts of the PDMS start to be wetted by the solution. These wetted parts distribute randomly.

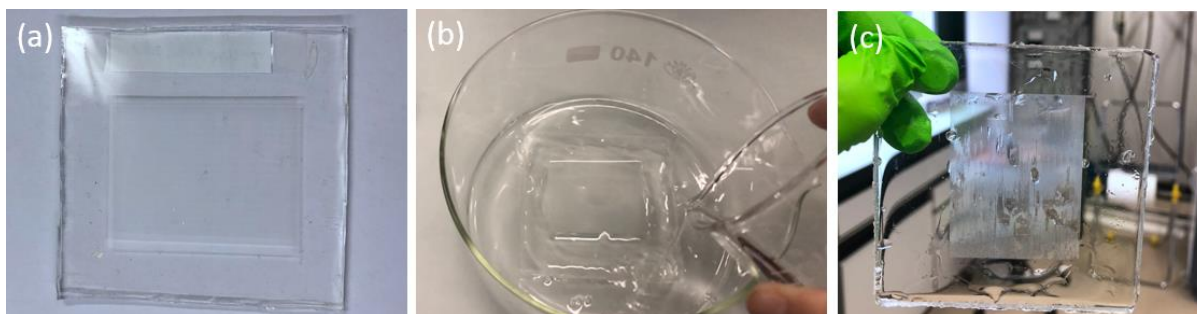


Figure 7-23. The three status of the PDMS mold: (a) before immerse liquid with the sketch of the cross-section, (b) during the pouring of 0.5% HPMC solution, (c) 30 S after being immersed under the 0.5% HPMC solution.

Lower concentration may result in thinner film cover the microstructure, leading to better preservation of the dimensions of the 1<sup>st</sup> (original) PDMS mold. Moreover, lower concentration of HPMC was with lower viscosity, which was more favorable for wetting a surface. However, if the concentration of HPMC were too low, there was insufficient mass to form an effective coating. in contrast, HPMC of higher concentration may contribute to the formation of a denser and a continuous coating due to the increase of mass per unit area. However, the higher viscosity reduced the wettability of the solution. Therefore, solution with HPMC of different concentration should be applied and the good concentration should be optimized. Figure 7-24 shows the example of the appearance of the 1<sup>st</sup> CPC(30, 30) PDMS microstructures coated with HPMC of the three concentrations, and the resulted 2<sup>nd</sup> PMDS. For all the concentrations, the resulted 2<sup>nd</sup> PDMS showed homogenous appearance which was similar to the 1<sup>st</sup> PDMS coated with HPMC,

suggesting a good replication. The appearance of the 1<sup>st</sup> CPC(40, 40) PDMS microstructures coated with HPMC of the three concentrations, and the resulted 2<sup>nd</sup> PMDS is shown in Figure 7-25. For CPC(40, 40), the appearance of the 2<sup>nd</sup> PDMS looked homogenous but slightly less homogenous compared with the case for CPC(30, 30). For CPC(40, 40), the aspect ratio of the micro grooves was higher compared with that of 1<sup>st</sup> CPC(30, 30), resulting in worse wetting of HPMC.

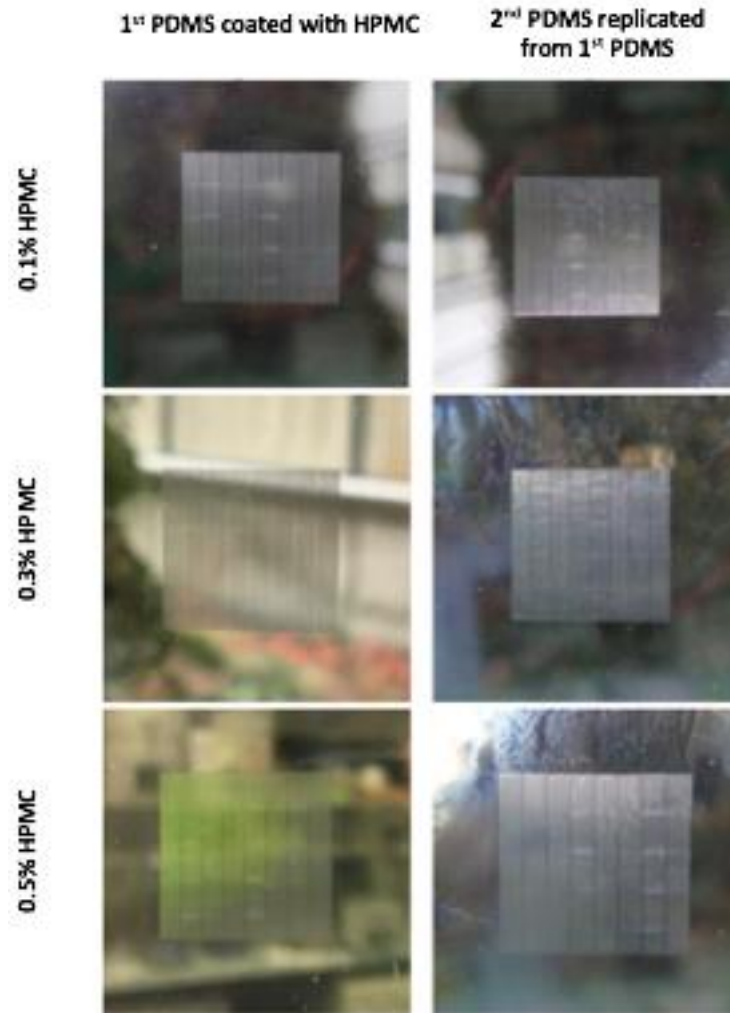


Figure 7-24. The appearance of the 1<sup>st</sup> CPC(30, 30) PDMS microstructures coated with HPMC of the three concentrations, and the resulted 2<sup>nd</sup> PMDS.

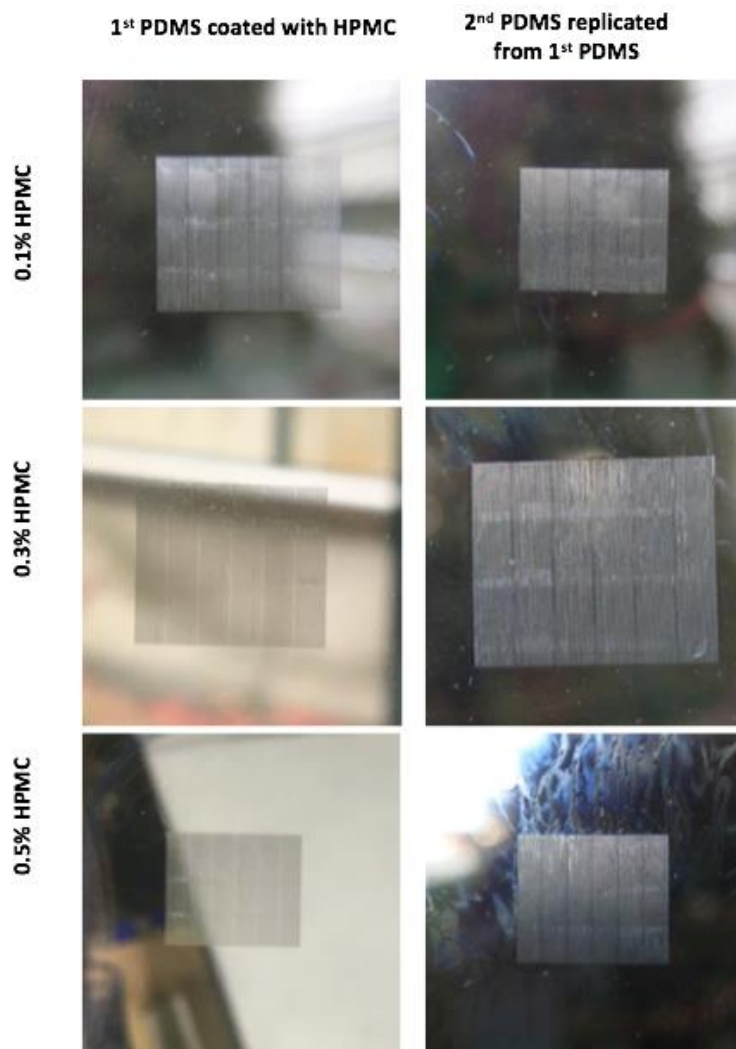


Figure 7-25. The appearance of the 1<sup>st</sup> CPC(40, 40) PDMS microstructures coated with HPMC of the three concentrations, and the resulted 2<sup>nd</sup> PMDS.

## 7.3.2 PDMS replicated from wax

### 7.3.2.1 Flat wax substrates

Replication of PDMS was first conducted from wax substrate with different beeswax concentration but no engraved microstructures, for various HPMC concentrations for 24 h. Table 7-3 summarize the ease of demolding and curing level for each case. According to table 9, we saw the best results were given by the substrate with 5%wt beeswax and 0.5wt% HPMC. The worst result was given by the 20% beeswax substrate with the interlayer of 0.1wt% HPMC. Beeswax was more hydrophobic than paraffin so it needed a higher concentration of HPMC to get a thicker interlayer.

Table 7-3. The ease of demolding and curing level for the replication of PDMS from wax substrates with different beeswax concentration but no engraved microstructures, for various HPMC concentrations.

Beeswax concentration	Comments	HPMC concentration (wt%)		
		0.1	0.3	0.5
5 wt%	Demolding	OK	easy	Very easy
	Curing	Not fully cured	Fully cured	Fully cured
10 wt%	Demolding	Ok	easy	very easy
	Curing	Not fully curd	Not fully cured	Not fully cured
20 wt%	Demolding	Difficult	OK	Easy
	Curing	Not fully cured	Not fully cured	Not fully cured

### 7.3.2.2 Wax substrates with asymmetric CPCs

PDMS replicated on the wax substrate (5 wt% beeswax) with asymmetric CPCs was carried out. The used HPMC concentration was 0.5% and the immersion time for the wax microstructure was 24 h. The appearance of the PDMS microstructure is shown in Figure 7-26. The majority of the microstructured area had white appearance, while in some region, the appearance was more transparent. The white region was most likely because of the cover of the residual wax, while in the transparent region there was no residual wax. The residual wax, links to the diffusion of wax into PDMS (Ren *et al.*, 2006). The top view optical microscope image is shown in the dashed frame. The dark part corresponds to the white-appearance region at macroscopic scale. The bright part corresponds to the transparent region. In the optical microscope image, the dark part seems to be at the same plane as the bright part, as at the same focused point for the optical microscope image, the small features for both dark and bright part are rather sharp and clear, suggesting that the absorbed wax does not have significant impact on the height of the microstructures.

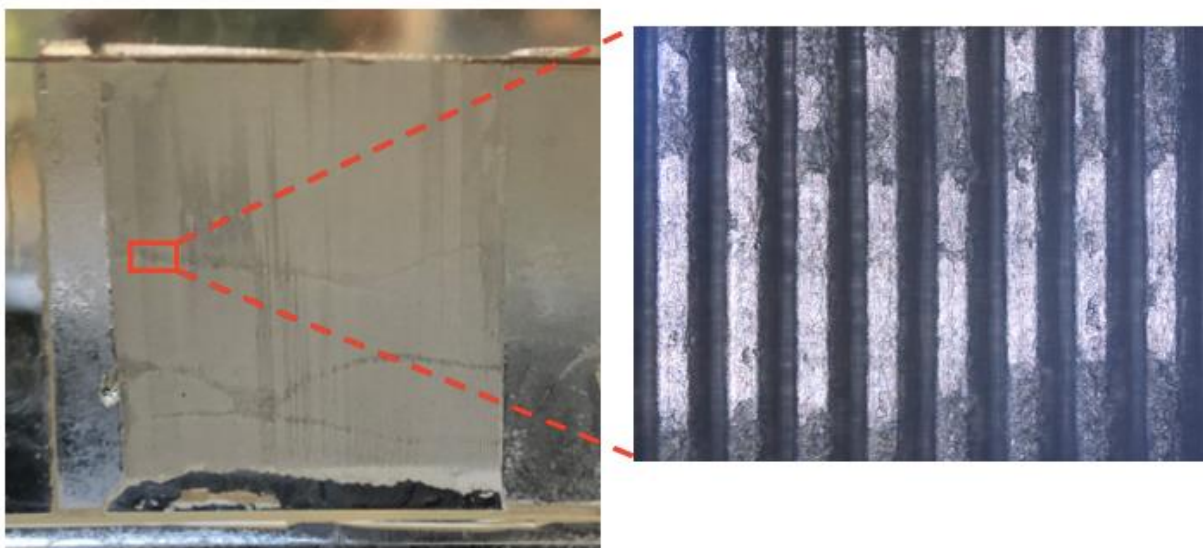


Figure 7-26. The top view of the macroscopic appearance of the PDMS mold and the zoom-in image from the optical microscope.

In order to understand more the impact of the absorption of on the cross-sectional morphology, the cross-sectional images have been taken with confocal microscope for the transparent region and the white region in the macroscopic appearance of PDMS, corresponding to the region without wax and the region with wax, respectively. It was observed that the height of the microstructure remained the same. There was no perceptible morphological difference between the HBP microstructures replicated from the PDMS mold with and without wax residual.

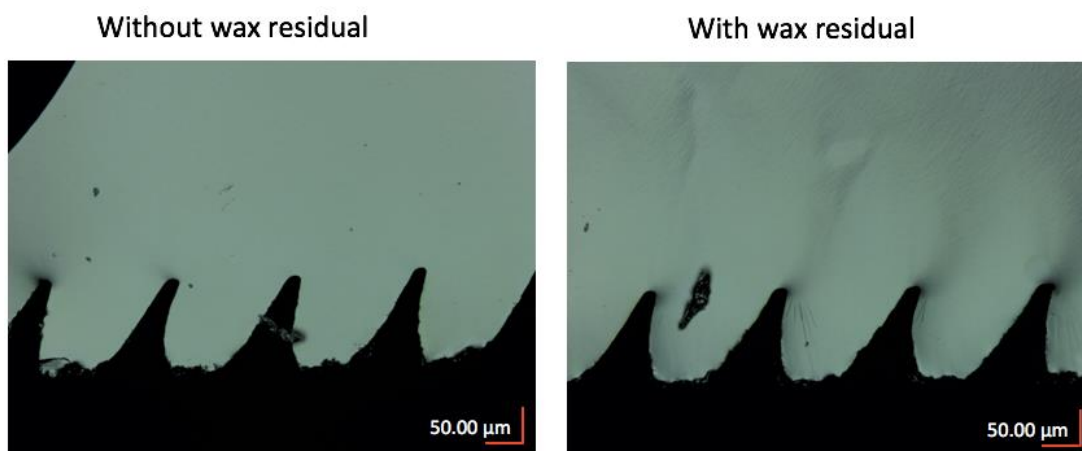


Figure 7-27. The HBP microstructures replicated from the PDMS mold with and without wax residual. The cross-sectional images are taken using the confocal microscope.

### 7.3.2.3 Wax substrates with retro-reflective microstructures

Replication of PDMS from wax substrate with the retro-reflective microstructure whose aspect ratio is 3.8 was investigated. The wax substrate was immersed in the 0.5% HBP solution for 24 h



and then air-dried for another 24h. The resulted PDMS mold after washing in the organic solvent in the ultrasonic bath for 1h is shown in Figure 7-28. The crack along the diagonal was due to the relaxation of deformation of the swollen PDMS after absorbing the solvent. The optical properties did not appear constant. In some regions, straight and clean lines were observed, suggesting a regular morphology, while in some regions, the wave-like structures appeared, suggesting an irregular morphology.



*Figure 7-28. The top view of the macroscopic appearance of the PDMS mold.*

The cross-sectional optical microscope images of the corresponding HBP (6% TPO) microstructures for the two regions mentioned are shown in Figure 7-29. The preparation of the HBP microstructure is described in 5.4.4. For the region where straight and regular lines appeared when observed from the top, the microstructure was periodic and the periodicity was about  $99\text{ }\mu\text{m}$ . The height of the microstructure was  $190\text{ }\mu\text{m}$ . Compared with the microstructures on the blade A for engraving (Figure 7-15), the periodicity of the PDMS microstructure kept identical, and the relative reduction of the height was only 2.6%. The width of the base was slightly increased with 2.2%. Therefore, it could be concluded that in the region where the shape fidelity of the microstructure transferred from the blade to the wax substrate and then to the PDMS was good.

For the region where the wave-like appearance was observed, there was no constant distance between two rectangle-like tips and the microstructures were not periodic. In these regions, the HBP solution did not fully wet the wax microstructure surface, and the PDMS were contaminated with the wax during curing. The induced wax resulted in not-fully-cured PDMS. The non-fully-cured structures were deformed due to the relaxation of internal force after demolding and/or washing, leading to the non-periodic microstructures. However, the height of the microstructure was identical to the region where the replication was good. Based on the equation (5-6), wetting



transition to Wenzel (in which the microstructure was fully wetted) states occurred when liquid pressure exceeded certain value. Therefore, the wetting and replication quality may be improved by increasing the immersion depth of the wax substrate under HBP solution, as well as increasing the immersion time to ensure that it was longer than the life span of the metastable states.

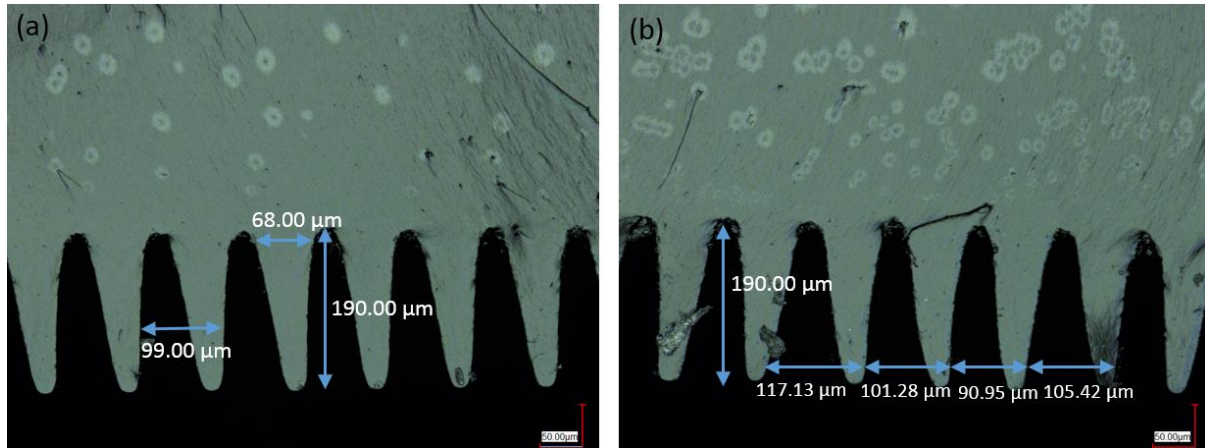


*Figure 7-29. The cross-sectional morphology of (a) microstructures in the region where straight and regular lines appear when observed from the top; and (b) microstructures in the region where the wave-like appearance is observed.*

## 7.4 Shape fidelity analysis during UV-imprinting

In the present section, the results of dimensional changes for two different UV-imprinted microstructures are presented and discussed: a) light-redirecting HBP microstructures with sharp edges, and trapezoid-like HBP microstructures. The dimensional changes due to the concentration of photoinitiator, internal stress, thermal aging were investigated and analyzed.

### 7.4.1 Light-redirecting HBP microstructures with sharp edges

*The text and images in this section are reproduced from: Gong, J., Meyer, F., Leterrier, Y., Kostro, A., & Schüller, A. (2017). Dimensional stability analysis of a UV printed polymer microstructure for a novel glazing system. Energy Procedia, 122, 763-768.*

Dimensional stability for the light-redirecting HBP microstructures with sharp edge was studied. The cross-sectional morphology of such microstructure is shown in Figure 7-30. The preparation of the HBP microstructure is described in the section 5.4.4. The height (H), periodicity (P), the width and width at mid-height ( $W_{1/2}$ ) of the microstructure were measured with 1  $\mu\text{m}$  accuracy. The parabolic surface where a highly reflective material (a mirror) was deposited was indicated with a red curve and the height of the mirror was the full height H minus 5  $\mu\text{m}$  (H-5).

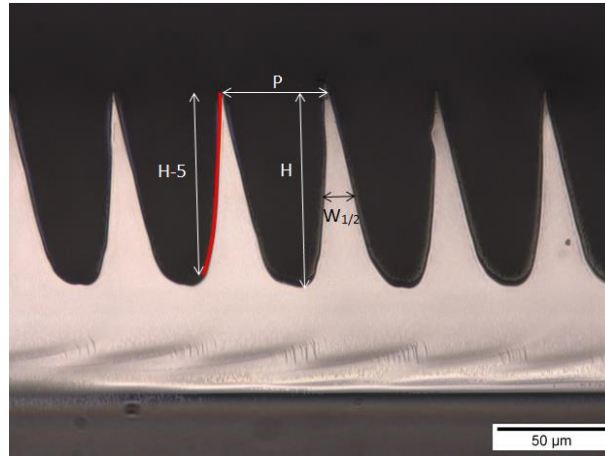


Figure 7-30. An example of the light-redirecting HBP microstructures with sharp edges and the measured parameters.

#### 7.4.1.1 Impact of photoinitiator concentration

Figure 7-31 shows the dimensional changes of the UV printed HBP microstructure. The data represent the normalized shrinkage in absolute values,  $\Delta x/x_0$ , where  $\Delta x = |x - x_0|$  and  $x$  and  $x_0$  were one of the dimensions (P, H and  $W_{1/2}$ ) of the molded HBP and the reference PDMS, respectively. The periodicity P was found to slightly contract and remained within 1.5 % equal to that of the PDMS template. This result was consistent with the fact that in-plane shrinkage was restricted in

the periodic microstructure due to lateral confinement during UV polymerization, and the resulting tensile stress only partly relaxed upon demolding in the solid state. The shrinkage of the height  $H$  was about 11% on average for the case with 1.5% PI. It decreased to 3% for 3% PI, and increased to 5% for 6% PI. The trend for  $W_{1/2}$  was the opposite, going through a maximum shrinkage close to 10% at 3% PI, so that the product of shrinkage along the height and width was independent of PI concentration within experimental scatter. This result indicates that the Poisson effect indeed contributed to the anisotropy in dimensional changes. Such rather complex behavior reveal the intricate interplay between polymerization shrinkage and associated stress build up, and viscoelastic relaxation processes as already reported for UV printed polymer gratings (Geiser *et al.*, 2010).

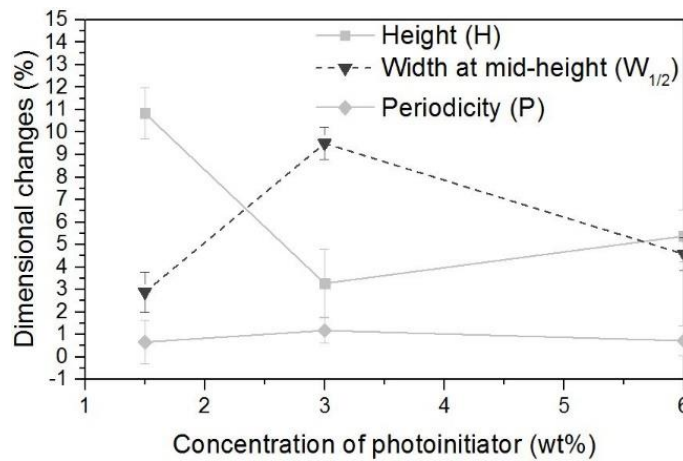


Figure 7-31. Dimensional changes with the variation of the concentration of the photoinitiator.

#### 7.4.1.2 Impact of thermal aging

Figure 7-32 shows the dimensional changes measured at ambient temperature as a function of exposure time under accelerated aging at 80°C for a printed HBP microstructure with a concentration of 6% of PI. The periodicity  $P$  progressively decreased with time (i.e. shrinkage increased). In this case the microstructure was not confined in plane, in contrast with the process-induced shrinkage shown in Figure 7-31. The observed evolution might be due to both chemical aging and physical aging. The photo-induced conversion of the acrylated HBP may indeed proceed as a thermally activated rate process, leading to additional shrinkage. Further thermally activated processes such as thermo-oxidative and hydrolytic degradation could not be excluded, but should be marginal at the investigated temperature. One may also invoke physical aging, which occurs when a polymer is cooled below its glass transition temperature  $T_g$ , and evolves toward thermodynamic equilibrium. This evolution is characterized by the slow decrease of the free volume and enthalpy of the polymer. The dimension  $W_{1/2}$  also increased with aging time, up to 14.5%, and, again, followed an opposite trend to the change of height  $H$ . It should be noted that

the microstructure would be constrained when encapsulated with another polymer counterpart in the glazing system, i.e., the dimensional changes should be less severe under aging.

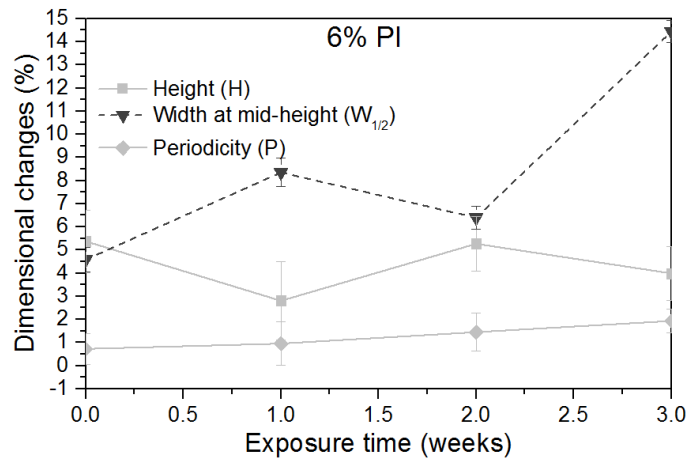


Figure 7-32. Dimensional changes as functions of exposure time under accelerated aging at 80 °C.

#### 7.4.1.3 Impact on the redirection of daylight

Four edges for each concentration of PI were selected, and their contours were extracted using the software WebPlotDigitizer with step size around 2.5  $\mu\text{m}$ . The contour of the negative PDMS microstructure was also determined as reference. The parabolic edge of individual edges was fitted with second order polynomial functions. The relative changes of dimensions of H, P, and  $W_{1/2}$  with respect to the PDMS reference were calculated. The extracted parabolic edges were used for ray-tracing simulation with CFSpro and their angular dependent transmittances at normal incidence were calculated, in order to analyze the impacts of the dimensional changes on the redirection of daylight.

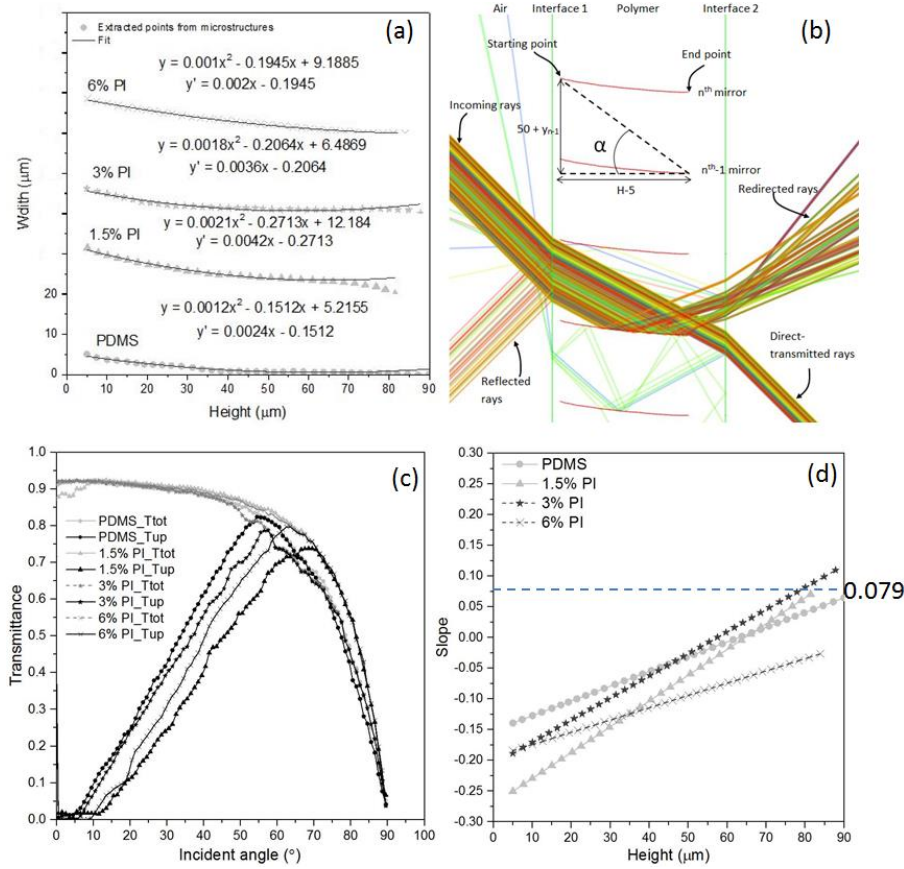


Figure 7-33. (a) extracted micro-mirrors profiles (points) and corresponding quadratic fits; (b) ray-tracing analysis of model parabolic micro-mirrors embedded in a polymer layer with refractive index of 1.495 showing direct-transmitted rays and reflected rays; (c) total transmittance ( $T_{\text{tot}}$ ) and transmittance of redirection ( $T_{\text{up}}$ ) as a function of incident angle at normal incidence; (d) derivatives of the polynomial fits as functions of the height of parabolic surfaces.

The impacts of these dimensional changes on the redirection of daylight are presented in Figure 7-33 for the three investigated concentrations of PI. Figure 7-33 (a) shows the actual shapes of the micro-mirrors and corresponding quadratic fits. Figure 7-33 (b) shows an example of modeling for ray-tracing simulations. The refractive indexes of glass and the used polymer were the same (refractive index  $n = 1.5$ ), and therefore, the glass pane where the polymer layer was attached, was not modeled in the present simulation for the convenience of viewing. Plots of the total transmittance and transmittance of redirected rays are presented in Figure 7-33 (c). The total transmittance (namely  $T_{\text{tot}}$ ) is the sum of redirected rays ( $T_{\text{up}}$ ) and direct-transmitted rays. The transmittance of redirected rays reaches a maximum value when it becomes equal to the total transmittance, i.e., when redirection for all rays at a given angle occurs on the micro-mirrors. The corresponding incident angle  $\alpha$  defined in Figure 7-33 (b) is:

$$\alpha = \tan^{-1}((y_{n-1} + 50)/(H - 5)) \quad (7-1)$$

where  $y_{n-1}$  is the value of  $y$  as a function of a secondary polynomial fit for the  $n-1$  mirror (Figure 7-33 (a)), and the unit for the variables and the constants is  $\mu\text{m}$ . Therefore  $\alpha$  is the angle between the line defined by the starting point of the  $n$ th mirror and the end point of the previous  $((n-1)\text{th})$  mirror, and the horizon through the end point at the  $(n-1)\text{th}$  mirror.

The angles  $\alpha$  calculated were  $33^\circ$  (PDMS),  $39^\circ$  (1.5% PI),  $34^\circ$  (3% PI) and  $37^\circ$  (6% PI), after conversion with respect to the refractive index based on the Snell's law (Harald and Hans, 2009), corresponding to the incoming angles  $55^\circ$ ,  $70^\circ$ ,  $57^\circ$ ,  $63^\circ$  in Figure 7-33 (c). Comparison of the cases for 1.5% PI and 6% PI showed that the change of the incoming angles of maximum redirected transmittance was significantly affected by the dimensional change in  $H$  but not sensitive to the dimensional change in  $W_{1/2}$ . When the incident angle was larger than  $70^\circ$ , for the four cases the transmittance was only contributed from redirected rays. The transmittances for 1.5% PI and 6% PI were approximately identical in the angular range between  $70^\circ$  and  $90^\circ$ , while for the cases of the PDMS and 3% PI case, the transmittances were relatively lower. The difference of the transmittance in the angular range between  $70^\circ$  and  $90^\circ$  results from the different average slopes. Figure 7-33 (d) shows the derivative (e.g. the slope) of the fitted curves as a function of micro-mirror height  $H$  from Figure 7-33 (a). The angle of incoming rays at the interface 2 between the back side of the polymer and air would change after being redirected by the parabolic mirrors. For the incident angle of  $70^\circ$ , the average slopes over the parabolic segment covered by the incoming rays for the four cases were -0.046 (PDMS), -0.09 (1.5% PI), -0.054 (3% PI) and -0.108 (6% PI), respectively. In the present coordinate system, a negative slope implies a decrease of incoming angles for the interface 2 and thus contributes to the increase of transmittance, while a positive slope has the opposite effect. Since reflection on interface 1 increases with the increase of incident angle, it is expected that the maximum redirected transmittance at  $57^\circ$  for the case of 3% PI was larger than that for the case of 6% where maximum redirected transmittance is at  $63^\circ$ ; however, it was the other way around, as slopes which are larger than 0.079 (marked in Figure 7-33 (d)) will result in total reflection on interface 2, and thus considerable reduction of transmittance may occur..

#### 7.4.2 Trapezoid-like HBP microstructures

The dimensional stability for microstructures with the negative counterpart of sharp edge was analyzed, i.e., trapezoid-like HBP microstructures. Trapezoid-like HBP Microstructures of two different aspect-ratios were prepared with different concentration photoinitiator, and the typical dimensions are shown in Figure 7-34. The two types of microstructure were replicated from the microstructure CPC(30, 30) and CPC(40, 40) on the master molds fabricated by laser ablation. The investigated dimensions were periodicity ( $P$ ), the width of the platform ( $W$ ), and the height ( $H$ ).

The aspect ratio (height/width at half height) for CPC(30, 30) was 1.45; while for CPC(40, 40) it was 1.14. For both CPC(30, 30) and CPC(40, 40), the periodicity and the width of the platform were constant with respect to the PDMS mold. For CPC(30, 30), the relative shrinkage for 1.5%, 3%, and 6% photoinitiator were 3%, 5% and 6%, respectively. The shrinkage increased with the increase of photoinitiator which resulted in higher conversion of level for polymerization. For CPC(40, 40) with 6% photoinitiator, the relative shrinkage of the height was 6.2%, in the same order as that for CPC(30, 30) with 6% photoinitiator. Therefore, for the microstructure with the aspect ratio lower than 1.45, the shrinkage was independent of the aspect ratio.

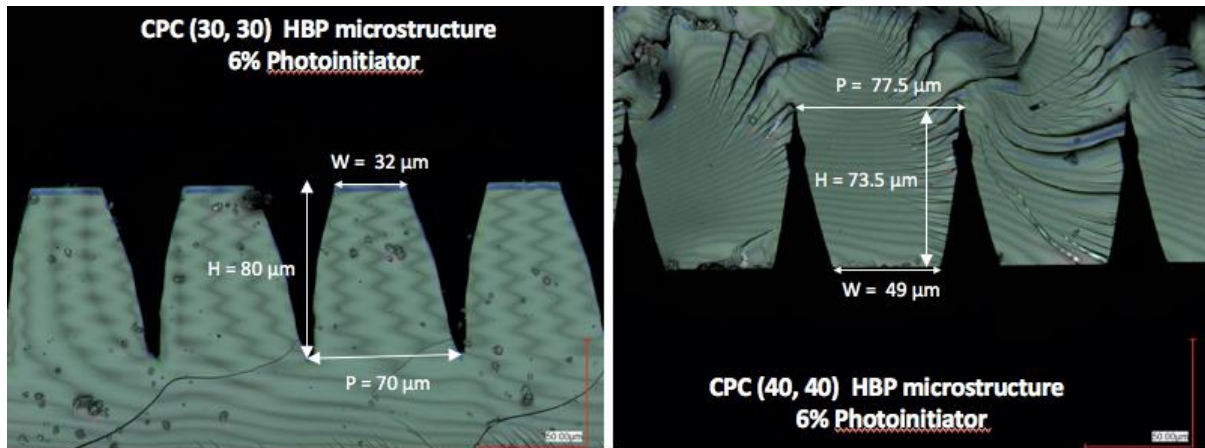


Figure 7-34. Trapezoid-like HBP Microstructures of two different aspect-ratio: CPC (30, 30) and CPC (40, 40). The photoinitiator is 6 wt%.

### 7.4.3 Discussion

Compared with the HBP microstructures with sharp edges, the trapezoid-like microstructures shows more a predictable behavior. The mass in the trapezoid-like HBP microstructures with the aspect ratio less than 1.45 and the height above 70  $\mu\text{m}$  is enough to resist the deformation caused by the relaxation of internal force.

Once the reduced dimensions due to shrinkage is quantified, corresponding enlargement of the dimensions during master can be considered.



## 7.5 Thin film deposition and optical properties

In this section, the result of the structural characterization for an example of embedded optical microstructure is presented. The feasibility of polishing after coating was proven. The symmetric micro CPCs with various optical coatings and the resulting optical properties are introduced. The angular-dependent transmittance of the first asymmetric micro CPCs (optical microstructure with overhang) will be also presented.

### 7.5.1 Facet-selective coating based on self-shadowing effect

#### 7.5.1.1 Results

Figure 7-35 indicates an example for the cross-section of a polymer layer with embedded parabolic micro-mirrors observed by scanning electron microscope. The bright white lines were the opaquely reflective aluminum thin films, which was deposited by facet-selective coating based on the self-shadowing effect of a microstructure. The thickness of the polymer layer was around 0.2 mm. Structural characterization was rather difficult due to the fact that the thickness of the thin films was in the order of several-tens nanometer while the thickness of a polymer layer was in the order of several hundred micrometers. In Figure 7-35, the cross-section is prepared with a diamond knife cutting cross the extruded direction of the aluminum micro-mirrors. Since aluminum was harder than the polymer, the micro-mirrors separated from the microstructure during cutting. The contrast between the micro-mirror was due to their different electric properties and the edge effect. It was observed that, the cross-section of micro-mirrors were smooth and continuous, and the micro-mirrors were only on the selected surface, proving the feasibility of facet-selective coating based on the self-shadowing effect of a microstructure.

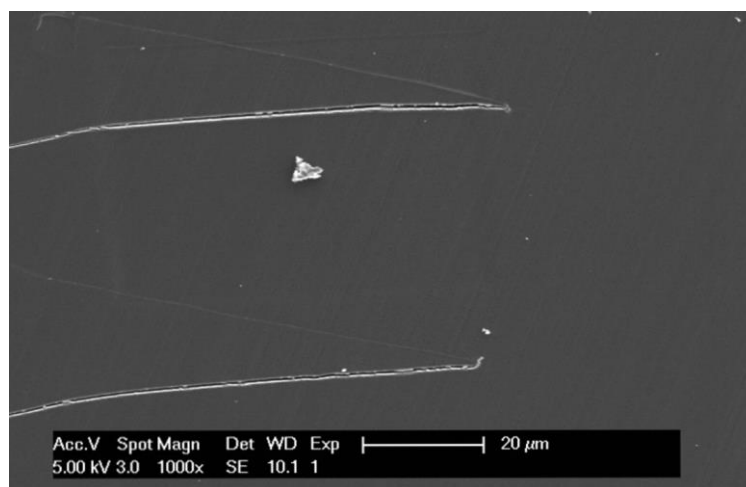


Figure 7-35. An example of a polymer layer with embedded parabolic micro-mirrors observed by scanning electron microscope.



### 7.5.1.2 Discussion

Thanks to the directionality, thermal evaporation is an effective tool for facet-selective coating based on self-shadowing effect of a microstructure; however, the appropriate optimization of the angular opening of the vapors has to be considered, in order to have relatively homogenous optical properties over the microstructured surface.

Figure 7-36 shows the sketch of the key components and dimensions for the facet-selective coating based on self-shadowing effect in the thermal evaporation chamber. In the present thesis, samples with two widths are present: 4 cm and 2 cm. The relative height deviation (namely standard deviation of the height relative to the average height) of 5% has been observed for the HBP microstructures after multi-steps of processing; this results in the angular opening of  $\pm 2^\circ$ . For the sample width of 4 cm for deposition, the angular opening due to the width of 4 cm is  $\pm 3^\circ$ ; this is closed to the angular opening due to the height deviation, and therefore it is not considered critical. For the sample width of 2 cm for deposition, the corresponding angular opening is  $\pm 0.5^\circ$ , which is below the angular opening due to the height deviation and therefore negligible.

For industrialized production, polymer samples are fabricated by roll-to-roll process (see section 5.6) with flexible materials; during deposition, a curve sample holder with the curvature corresponds to the angular distribution of the deposition vapor can be used to enlarge the angular opening. Alternatively, a shield with narrow slit and a automatic sliding device can be applied on a flat substrate; the sliding device is used to move and expose the polymer samples to the deposition vapor through the slit.

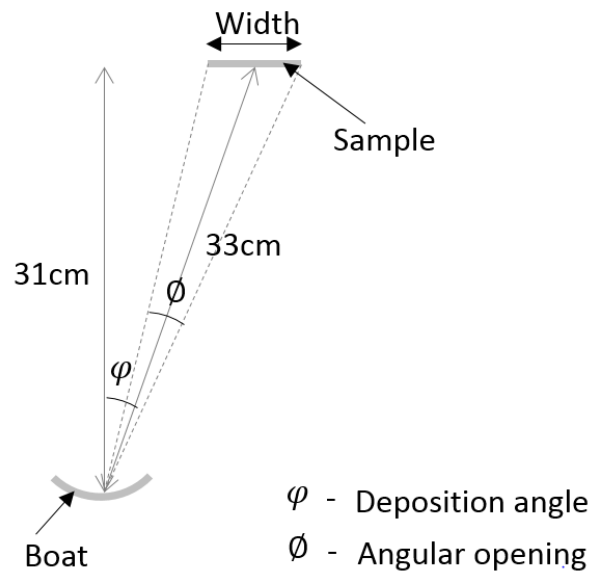


Figure 7-36. Sketch of the key components and dimensions for the facet-selective coating based on self-shadowing effect in the thermal evaporation chamber.

## 7.5.2 Feasibility of polishing after coating

### 7.5.2.1 Results

To explore the possible way for facet-selective coating, during the thermal evaporation deposition process, the coating was all over the surface of the microstructures, but the polishing was applied on the facet where the coating was not required. Figure 7-37 shows the optical microscope image of the cross-section of the HBP microstructure which was used for the polishing test. Based on the surface to be polished, and the geometry of the microstructure, it was known that, if not only the thin film but also the mass of the microstructure was polished away, the height of the HBP microstructure would be reduced, and therefore, the width of the polished stripes increased correspondingly. The evolution of the surface at the beginning, the mid and the finishing status of the polishing is shown in Figure 7-38. The bright stripes were the Aluminum coating. It was observed that, there was only slight increase of the width of the microstructure when the polishing finished with respect to the beginning of the polishing, suggesting that a good control of polished mass during the polishing process with ultra-fine Silicon Carbide grinding paper (Struers, FEPA P4000, and the diameter of the grain size 5  $\mu\text{m}$ ). No rough scratches were observed, suggesting a relatively smooth exposed surface after polishing. It was also observed that the removal rate of the aluminum coating was not homogenous on all the polished surfaces, and the reasons were multiple. First of all, the PDMS for the replication of HBP was flexible and soft, without a support it was easily bent. Secondly, the shrinkage of HBP during polymerization might lead to a concave shape of the polished surface. The two reasons mentioned above led to an imperfectly flat HBP surface. Thirdly, the pressure applied on the polished surface was not homogeneously distributed. Better control of the three factors were needed.

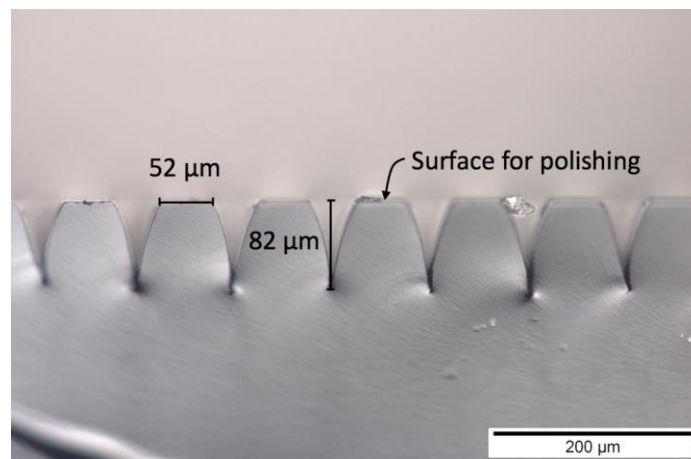


Figure 7-37. Optical microscope image of the cross-section of the HBP microstructure which was used for the polishing test.

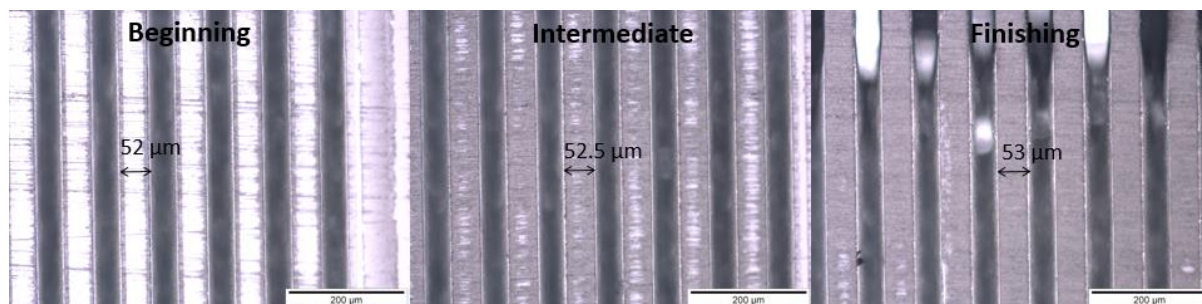


Figure 7-38. Optical microscope images (top view) for the evolution of the microstructures and the coated surface at the beginning, the mid and the finishing status of the polishing.

### 7.5.2.2 Discussion

During the industrial fabrication, the replication of HBP from PDMS and the shrinkage of HBP can be avoided by the alternative fabrication methods and materials. The good control of the homogenous pressure on the polished surface can be achieved by better engineering and tools.

During polishing, the peel-off thin film flakes are generated. Therefore, water-flow or any other possible liquid should be present and post-washing after polishing is preferred.

For achieving facet-selective coating by post polishing, other coating methods, which are less sensitive to directions and do not require the precision control of the tilted angle, can be considered, e.g. spin coating. Spin coating is normally used for uniform coating on a flat surface. During spin coating, fluid material is deposited on the center of a substrate; a spin coater is used and rotates the substrate. Centripetal acceleration makes the fluid materials spread to the edge of the substrate. The desired thickness can be down to several-ten nanometers, depending on the properties of the fluid material, such as viscosity, drying rate and wettability, etc., as well as the machining parameters. Compared with thermal evaporation deposition and sputtering deposition, the cost of the machine is much less expensive. Moreover, the coating process can be more efficient as it does not require time to pump for ultra-high vacuum.

### 7.5.3 Symmetric micro CPCs with various optical coatings

In the present section, aluminum (Al) thin films and silver (Ag) thin films of various thickness deposited on symmetric micro CPCs are introduced. The results of preliminary study on the thermal evaporation for ITO thin films are also presented. The spectral characteristics of the thin films were analyzed. Diffraction, appearance and angular-dependent transmittance of the encapsulated samples were investigated.

### 7.5.3.1 Aluminum coating

Part of the text and images in this section are reproduced from: Gong, J., Kostro, A., Scartezzini, J. L., & Schüler, A. (2018, September). Feasibility study on a novel daylighting system with embedded micro compound parabolic concentrators (CPCs). In *Nonimaging Optics: Efficient Design for Illumination and Solar Concentration XV* (Vol. 10758, p. 1075807). International Society for Optics and Photonics.

Aluminum (Al) thin films of 6 different thicknesses were deposited for three samples with embedded CPC arrays. The operating parameters are summarized in Table 7-4. Based on the thickness of Aluminum thin films for the two reflective parabolas of a CPC, the three samples were named as CPC52-36, CPC50-11, and CPC 15-15, respectively.

Table 7-4. Operating parameters for Aluminum coating with different thickness by physical vapor deposition. The values of the thickness are read from the monitor, i.e., nominal thickness.

Nominal Thickness	Initial pressure (mbar)	Maximum pressure (mbar)	Ave. pressure (mbar)	Maxi. deposition rate (Å/s)	Ave deposition rate (Å/s)
11 nm	$< 1 \times 10^{-6}$	$3.5 \times 10^{-6}$	$3.0 \times 10^{-6}$	2.5	1.85
15.4 nm	$< 1 \times 10^{-6}$	$3.4 \times 10^{-6}$	$2.5 \times 10^{-6}$	3.4	2.6
15.9 nm	$< 1 \times 10^{-6}$	$3.2 \times 10^{-6}$	$2.7 \times 10^{-6}$	2.2	1.6
36 nm	$< 1 \times 10^{-6}$	$1.2 \times 10^{-5}$	/	6	2.5
50 nm	$1.2 \times 10^{-6}$	$5.0 \times 10^{-6}$	$2.4 \times 10^{-6}$	2.2	2.0
52 nm	$1.6 \times 10^{-6}$	$5.7 \times 10^{-6}$	$3.2 \times 10^{-6}$	8.5	6

#### *Spectral direct transmittance of Al thin film*

Figure 7-39 shows the spectral characteristics of direct transmittance of Aluminum thin films with various thicknesses on glass substrates. It was observed that the Aluminum thin films with the thickness of 11 nm showed the phenomenon of weak spectral selectivity, with the average visible transmittance ( $T_{vis, ave}$ ) of 0.24 and the average transmittance of 0.16 in the near infrared range (780 nm – 1800 nm in the present work). Likewise, the two Aluminum thin films of about 15 nm showed weak spectral selectivity. Due to more pores and voids, the transmittance of 15.9 nm thin film was higher than that of 15.4 nm. When the the thickness of an Aluminum thin film increased to 36 nm, the average transmittance for the wavelength range from 380 nm to 1800 nm was almost 0, which was similar to that of the thin film with the thickness more than 50 nm.

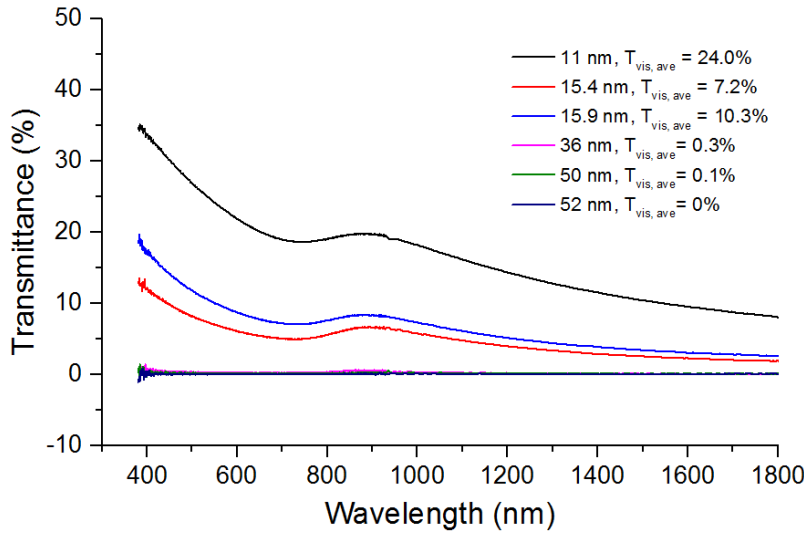


Figure 7-39. Spectral characteristics of direct transmittance of Aluminum thin films with various thicknesses.

### Diffraction

The micro CPCs arrays of micrometric scale can induce diffraction. Figure 7-40 shows the “ghost” images and the “rainbow” phenomenon due to diffraction, when the edge of a computer screen was seen through the sample 52-36. For small periods of microstructures with the redirection of light, the first orders of diffraction were clearly separated from the central peak (zero order). Beside the main image, one will see at least two-colored images (named “ghost” images) close by, which are less intense than the main image. For a “white” light source, the diffraction grating led to several “orders”. Each order contained the complete spectrum of colors. Based on the equation (7-2), diffraction effects depended on the wavelength of the light. Therefore, “rainbow” phenomenon was observed, and the red light at the maxima of each order was further away from the object compared with the blue light.

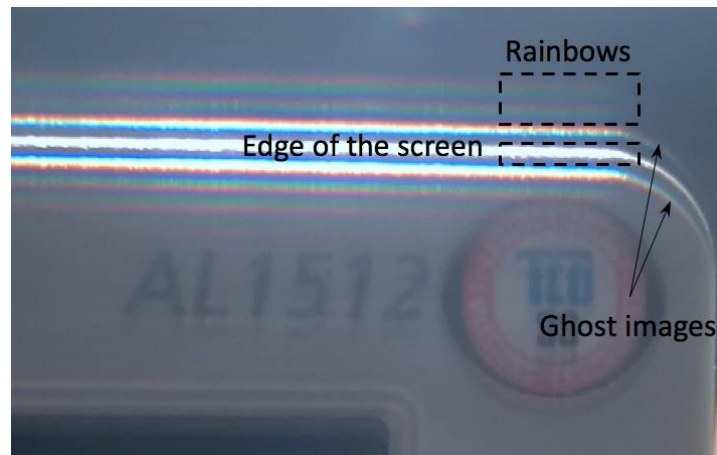


Figure 7-40. Diffraction phenomenon when the edge of a computer screen is seen through sample 52-36. The numbers “52” and “36” stand for the nominal thin film thickness of the two side walls for a micro CPC.

A red laser beam with the wavelength of about 650 nm was used to identify the diffraction effect, as shown in Figure 7-41. Two sets of bright fringes appeared: fringes in far front of the sample (named as front fringes) and fringes on the white board beside the sample (named as side fringes). It is assumed that the micro CPC arrays as multiple slits, separated by a distance  $d$ ; each slit has a width  $a$ . The distance from the plane of the slits to the screen where the fringes are projected as  $L$ . The distance between two fringes  $y$ . The bright fringes due to diffraction is assumed to appear on the white screen at an angle  $\theta$  with respect to the norm of the sample. The relative path difference between each pair of adjacent slits is  $d \sin \theta$ . If this path difference is equal to an integral multiple of wavelengths, the slits will constructively interfere with each other; therefore, bright fringes will appear. Based on the assumption above, the condition for the principal maxima is given by

$$d \sin \theta = m\lambda, m = 0, \pm 1, \pm 2, \pm 3, \dots \quad (7-2)$$

The location of the maxima does not depend on the number of slits,  $N$ . If  $L \gg d$ , and  $d \gg \lambda$ , the angle  $\theta$  is very small. Then,

$$\sin \theta \approx \tan \theta = y/L \quad (7-3)$$

The bright fringes in front of the sample, was due to the multi-slit interference mentioned above. The circular laser beam was of diameter of 3 mm. The zero front fringe was approximately 1.68 m away from the light source. The distance between two front fringes was predicted to be about 1.6 cm. Based on the equation (7-3), the calculated periodicity of the micro CPCs arrays was about 68  $\mu\text{m}$ . The calculated periodicity matched the measured periodicity by optical microscope, suggesting that the front fringes were induced by the interference of direct-transmitted beam. Concerning the side fringes, the redirection of light by a reflective parabolic surface created the difference of light paths and thus caused interference. Similar to Bragg diffraction (Egami and Billinge, 2012), the position of the side fringes depended on the distance between two points where redirection occurred, and the angle of scattering. For a parabola, the curvature was not constant. The distance between two redirecting point and the angle of scattering could be any value, as long as the path length difference was equal to an integer number of wavelengths. As a result, unlike the front fringes which depended on the fixed periodicity, the distance between two fringes was not constant, as shown in Figure 7-42. Figure 7-42 shows the side fringes due to the interference of the redirected light by parabolic reflective surface with 50-nm Al thin film and 11-nm Al thin film. It was observed that, the brightness of the side fringes for the 11-nm Al thin film was much weaker than that of the 50-nm Al thin film.

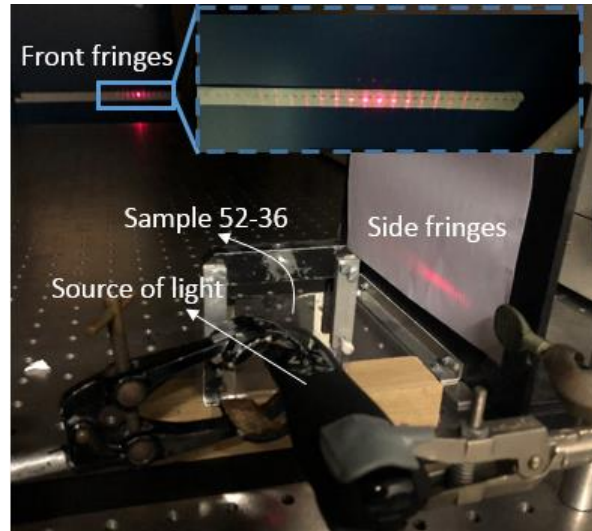


Figure 7-41. Diffraction effect identified by a red laser beam. The numbers “52” and “36” stand for the nominal thin film thickness of the two side walls for a micro CPC.

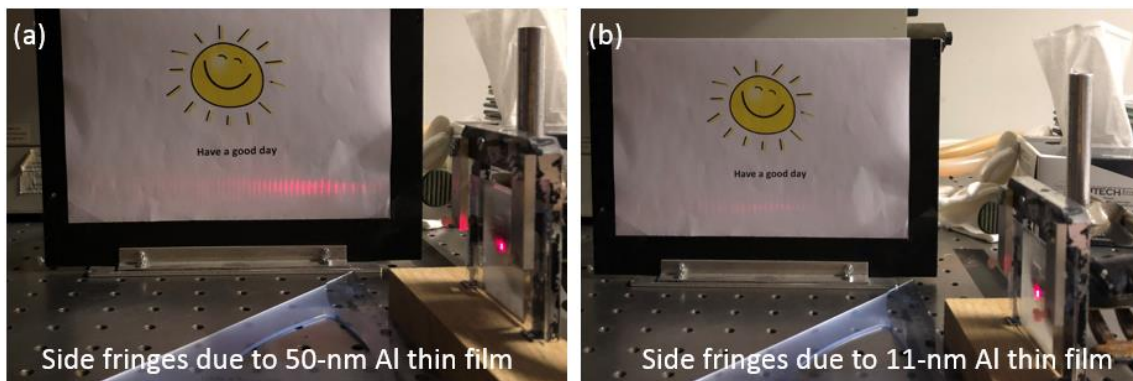


Figure 7-42. Side fringes due to the interference of the redirected light by parabolic reflective surface with (a) 50-nm Aluminum thin film and (b) 11-nm Al thin film.

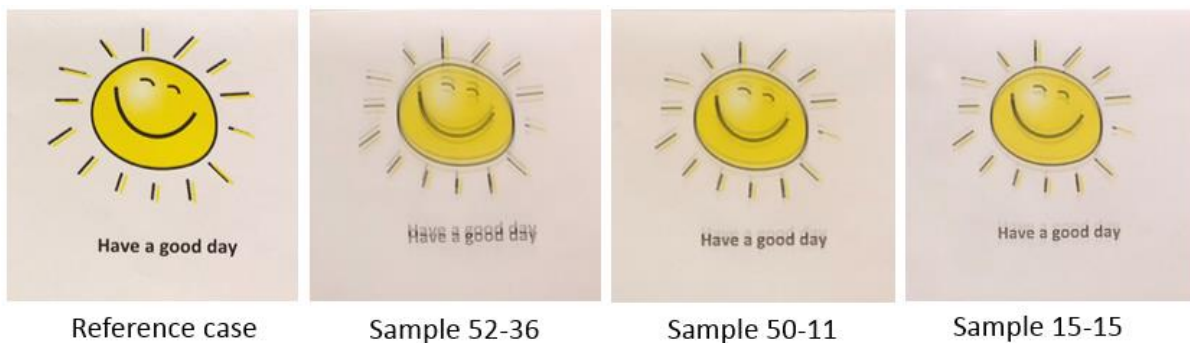
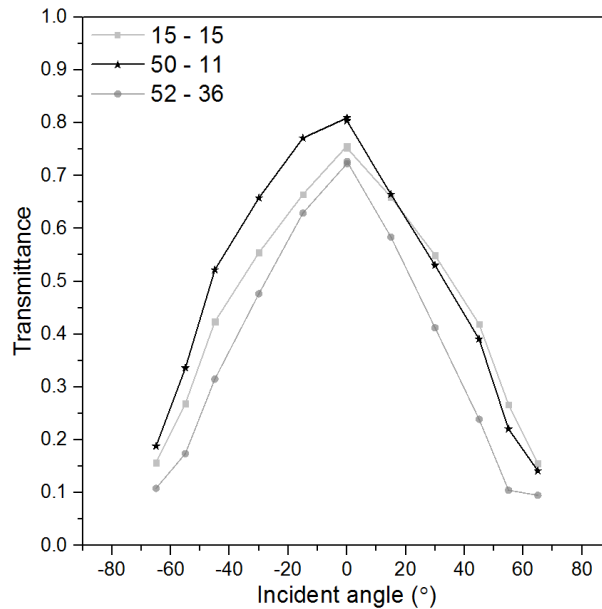


Figure 7-43. Views seen through the samples with various thicknesses of the Aluminum thin films. The numbers in the name of a sample, stand for the thickness of the nominal thin film thickness of the two side walls for a micro CPC.



Views seen through the samples with various thicknesses of the Aluminum thin films are shown in Figure 7-43. For sample 52-36, the diffraction was very strong and the letters were difficult to read. For sample 50-11, the diffraction along one direction was stronger than the other direction. However, the view was quite clear and the features of objects were sharp enough to be distinguished. The visible transmittance of Aluminum thin film with about 15 nm was about 0.1. For sample 15-15, only subtle diffraction was observed and the view was clear, suggesting that diffraction effect due to redirected interference played an important role. Once there was slight increase of the visible transmittance, the diffraction effect wouldl significantly fade out.

#### ***Angular-dependent transmittance***



*Figure 7-44. Angular-dependent total transmittance with respect to various incident angles for samples with aluminum coating. The measurement is conducted by minigonio-photometer, and the measuring procedure is described in the section 5.7.2.2.*

For all the cases, strong angular-dependent transmittance was observed. The highest transmittance with the value of 0.8 occurred at the normal incidence. The lowest transmittance shown in the graph was at the incident angle of  $\pm 65^\circ$  is less than 0.2. Due to the analogous average visible transmittance on the both parabolas, for both sample 15-15 and sample 52-36, the profile of angular-dependent transmittance was rather axisymmetric. However, because of the thinner coating, the transmittance at the same incident angle for sample 15-15 was higher than that of the sample 52-36. For sample 50-11, due to the difference of the average visible transmittance between the two parabolas, the profile of the angular dependent transmittance was asymmetric. At the range from  $0^\circ$  to  $-65^\circ$ , where the first redirection of the incident light occurred on the parabola with 11 nm-thin film, the angular-dependent transmittance was higher compared with its counterpart, due



to the direct-transmitted light through the 11-nm thin film. From  $0^\circ$  to  $65^\circ$ , where the first redirection of the incident light occurred on the parabola with 50 nm-thin film; then part of the light was redirected to the 11-nm thick parabola, part of the light was reflected through the incoming aperture, part of the light transmitted through the 11-nm thick parabola. For angular-dependent behavior of light through the sample 50-11 is further explained in the following section.

### ***Light redirection ability***

Figure 7-45 shows the distribution of the transmitted light at the normal incidence for the three samples coated with Al. The peak at the outgoing angle of  $0^\circ$  was due to the direct-transmitted light. The evident redirection was observed for outgoing angles between  $(-) 20^\circ$  and  $(-) 70^\circ$ . For the case CPC 15-15, the intensity distribution of the redirected light was rather symmetric. Whereas for the case CPC 50-11 and CPC 52-36, the intensity for was nonsymmetrical due to the different thickness of Al coating on the two parabolic surfaces which make a unit of a CPC. The redirection ability reduced as the thickness decreased, as observed for the outgoing angle range from  $-40^\circ$  to  $-60^\circ$ .

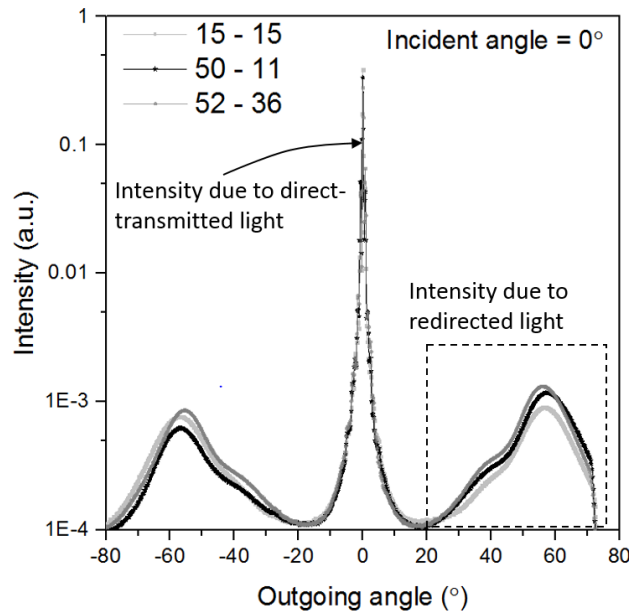


*Figure 7-45. Normalized intensity distribution of the transmitted light for the three samples with Al thin films encapsulated. The incident angle is at the normal incidence.*

Figure 7-46 presents the distribution of the transmitted light at the incident angle of  $55^\circ$  for the sample CPC (50, 11). The red curve represents the case where the incident light first meets the 11-nm thick Al coating. Figure 7-47 shows the example paths along which the light goes through the polymer layer with embedded CPC. As shown in Figure 7-47 (a), the light can transmit through the 11-nm thick Al coating, then redirecting by the 50-nm thick Al coating, and transmitting. The purple curve represents the case where the incident light is first redirected by the 50-nm thick Al

coating. As observed in Figure 7-47 (b), the light is redirected by the 50-nm thick Al coating, transmitting through the 11-nm thick coating. After that, total reflection occurs, which induce the light to be reflected to the external side after several more redirections. It can be concluded that, due to the complicated behavior of the light in the system, the redirectability for the case where the incident light first meets the 11-nm thick Al coating is higher than that for the case where the incident light is first redirected by the 50-nm Al coating. The choice of the orientation of the embedded CPCs with coating of two different thickness have important impact on the optical properties of the system.

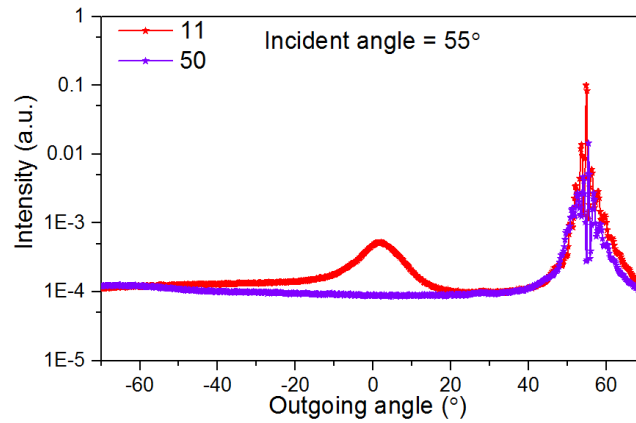


Figure 7-46. Distribution of the transmitted light at the incident angle of  $55^\circ$  for the sample CPC (50, 11).

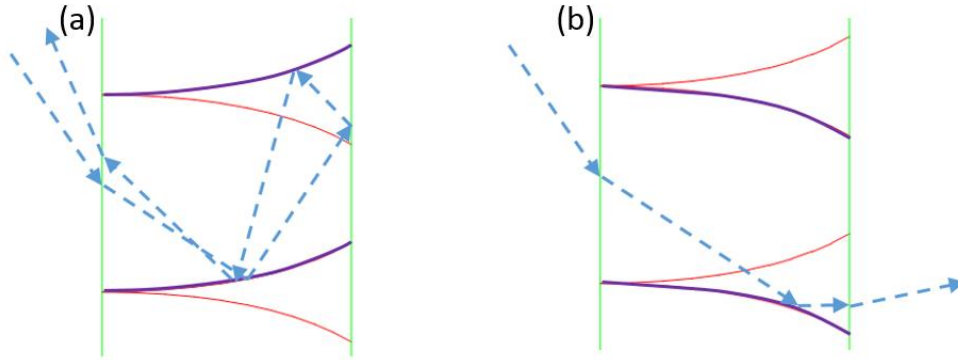


Figure 7-47. Example paths along which the light goes through the polymer layer with embedded CPC for (a) the case where the incident light is first redirected by the 11-nm thick Al coating (represented by the red curves), and (b) by the 50-nm Al coating (represented by the purple curves). The example paths are indicated by blue dash lines.

### 7.5.3.2 Silver coating

Silver thin films of 6 different thicknesses were deposited for three samples with embedded CPC arrays. The operating parameters are summarized in Table 7-5. Based on the thickness of silver thin films for the two parabolas of a CPC, the three samples were named as CPC 10-10, CPC16-16, and CPC 25-25, respectively.

Table 7-5. Operating parameters for six silver thin films of different thickness for three samples with embedded CPC arrays. The values of the thickness are read from the monitor.

Thickness	Initial pressure (mbar)	Maximum pressure (mbar)	Ave. pressure (mbar)	Maximum deposition rate ( $\text{\AA}/\text{s}$ )	Ave deposition rate ( $\text{\AA}/\text{s}$ )
10.7 nm	$< 1 \times 10^{-6}$	$1.8 \times 10^{-6}$	$1.6 \times 10^{-6}$	3.4	1.8
10.4 nm	$1.3 \times 10^{-6}$	$3.9 \times 10^{-6}$	/	2.7	2.2
16.4 nm	$< 1 \times 10^{-6}$	$2.0 \times 10^{-6}$	$2.0 \times 10^{-6}$	3.8	3
16.8 nm	$1.2 \times 10^{-6}$	$2.6 \times 10^{-6}$	$2.4 \times 10^{-6}$	3.5	2.7
25.6 nm	$< 1 \times 10^{-6}$	$1.9 \times 10^{-6}$	$1.6 \times 10^{-6}$	3.1	2.6
25.9 nm	$< 1 \times 10^{-6}$	$2.7 \times 10^{-6}$	$2.2 \times 10^{-6}$	3.9	3.0

### *Spectral properties of Ag thin films*

Figure 7-48 shows the spectral characteristics of silver thin films with various thicknesses. The trend of the evolution of the transmittance for Ag thin films along the wavelength was the opposite to the reflectance. For the dip of the spectral transmittance of 10.7 nm thin film at the wavelength of 570 nm, it was most probably due to the plasmonic resonance (Weimer and Dyer, 2001). It had been shown that most metal films grew from initially isolated metallic islands to a connecting network and finally to complete coverage of the whole area (Smith and Srolovitz, 1996; Fan *et al.*, 2005; Sun *et al.*, 2007). The conduction electrons were trapped in individual islands. Therefore, they could not move freely like in a continuous film. The electromagnetic field of an incoming light wave can excite surface plasmons (Charton and Fahland, 2003)..

For the film thickness of 16.8 nm and 25.6 nm, considerable selectivity was observed. The average visible total transmittance over 400 nm to 800 nm were 41% and 32.5%, respectively. Concerning the average transmittance in the near-infrared spectrum, the values were 25% and 7%, respectively.

Considering the absorbance,  $A=1-R-T$ , the average absorbance over the wavelength from 500 nm to 1800 nm were 36%, 20% and 4%, for the film thickness of 10.7 nm, 16.8 nm and 25.6 nm,

respectively. With increasing thickness, isolated islands were connected and electrons could move freely. This reduced the probability of the surface plasmon excitation and thus the absorption.

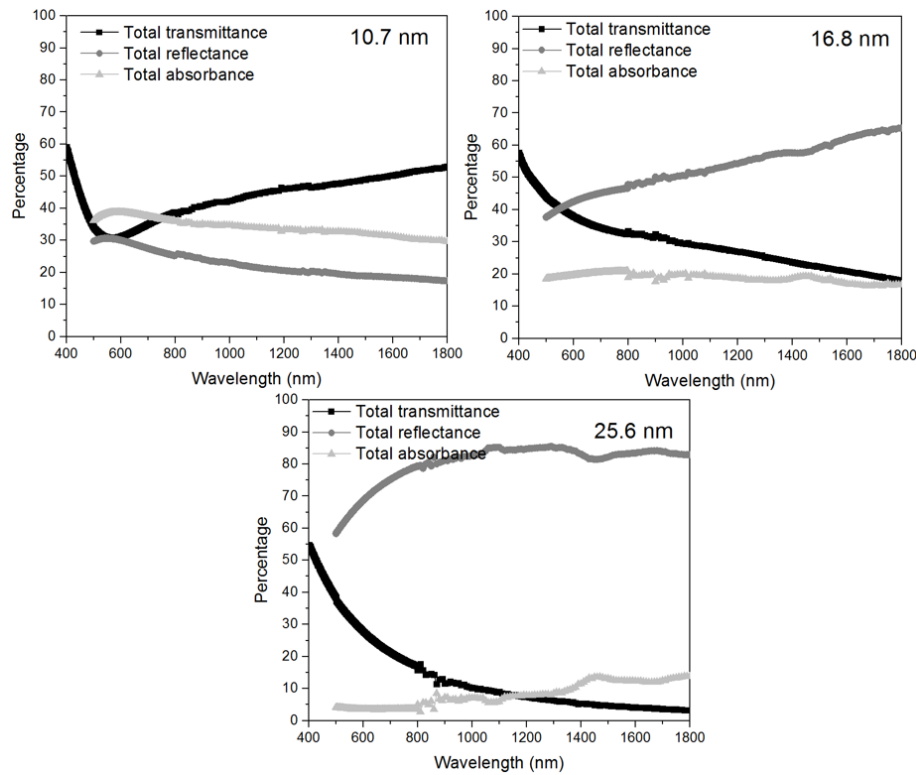


Figure 7-48. Spectral characteristics of Silver thin films with various thicknesses measured by spectrometer with integrated sphere.

### ***Appearance and diffraction of encapsulated samples***

The appearance of the samples at the normal incidence is shown in Figure 7-49. The sample 10-10 appeared to be highly transparent and spectrally neutral. However, with the increase of the thickness of the thin film to 16 nm, yellowness in the microstructured area appeared. Two colors on the samples were observed: blue color on the non-microstructured part coated with Ag, light yellow color in the microstructured area; these were especially obvious for the sample 16-16. The blue color, was due to the spectral-selective transmission. From Figure 7-48, it is seen that the transmittance of the Ag thin films for the wavelength from 400 nm to 500 nm is higher than that of the wavelength from 500 nm to 800 nm. The yellowness, was due to reflected-transmitted incoming light by micro CPCs, as shown in the sketch in Figure 7-50 (a). The spectral-selective reflection resulted in the yellow color.

When the sample 16-16 was viewed at higher incident angle, especially at the incident angle larger than that of the acceptance angle, the light arriving at observer's eyes was the light which

transmitted through the parabolic thin films, as shown in the sketch in Figure 7-50 (b). Therefore, in this case, the sample appeared to be blue, as presented in Figure 7-51.

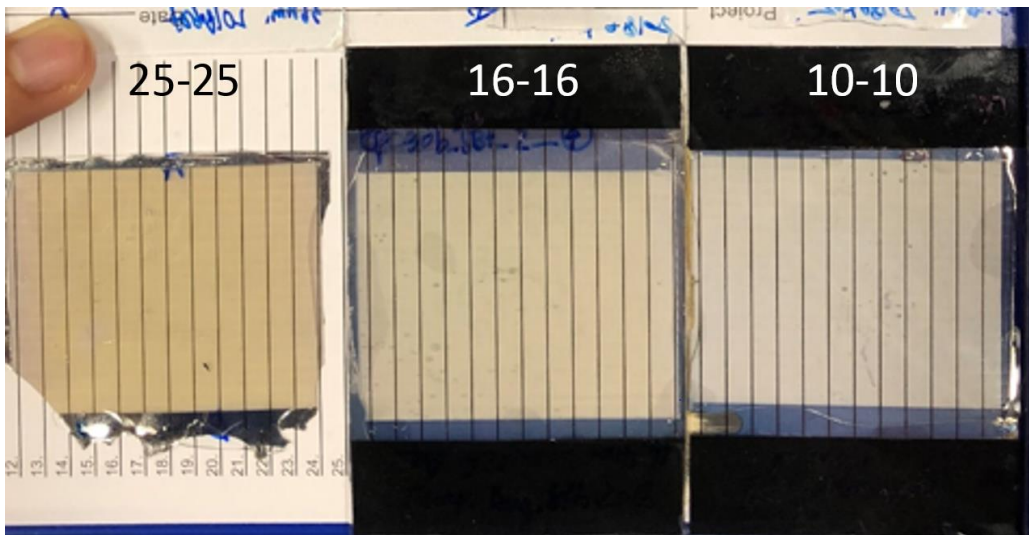


Figure 7-49. The appearance of the encapsulated samples.

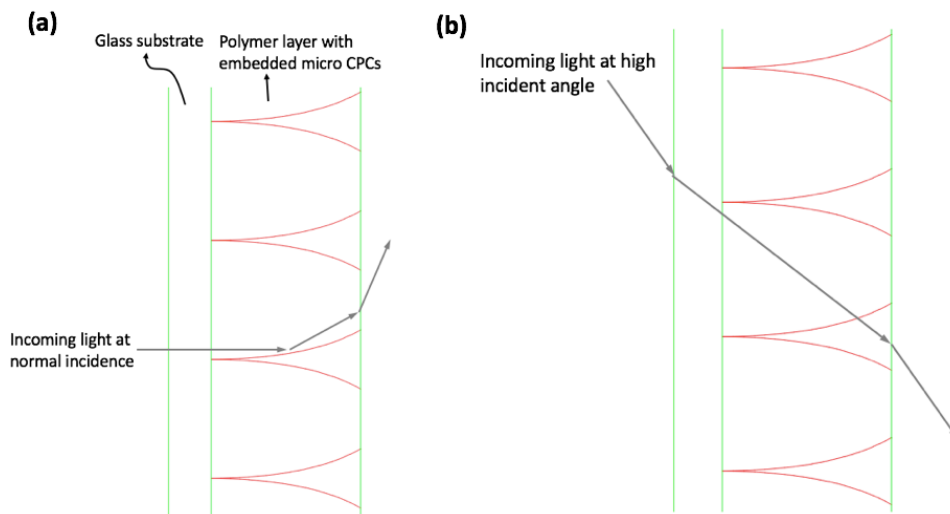


Figure 7-50. The sketch of the light path (indicated by gray arrows) coming to observer's eyes for a) incoming light at normal incidence, and b) incoming light at high incident angle.



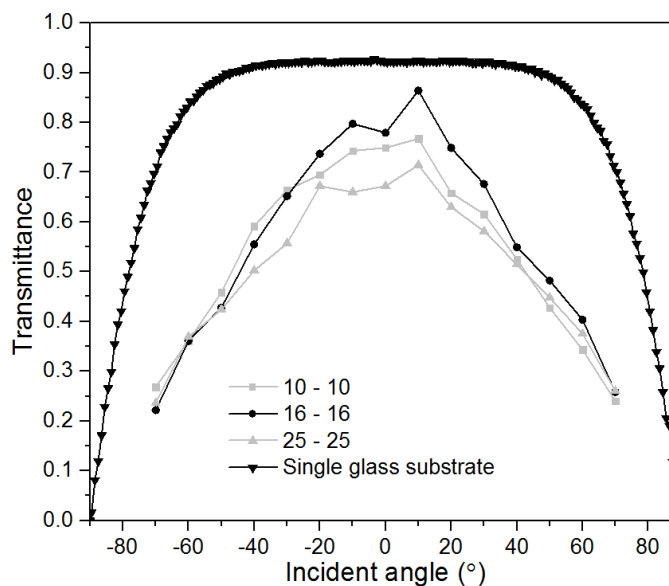
Figure 7-51. The blue appearance of the sample 10-10 when it is viewed at higher incident angle.



Figure 7-52. View see through the samples. In the reference case, the view is directly seen through a conventional double glazing without a sample.

Figure 7-52 shows the view seen through the samples. Two reference cases (shown in the upper two graphs) were used. One was the view seen through a conventional double glazing without a sample, representing the clear view. The other one was the view seen through the sample with embedded opaque reflective Al thin films, representing the extreme case of diffraction for the geometry of CPC(30, 30). In the extreme case of diffraction, one would see at least two-colored images (named “ghost” images) beside the main image. In particular, for the small and dense objects, e.g., the colorful leaves on the left-hand side, the side images (“ghost” images) overlapped and thus the edges of the leaves were very blurred and difficult to distinguish. For the larger objects, such as the buildings and the cars, blurring effect was weaker despite of the “ghost” images. For the three samples with Ag thin films, the clearness was increased as the film thickness decreased. For the sample 16-16 and 10-10, the difference was not perceptible in terms of transparency and diffraction, and they gave very similar view to the reference case without the sample. For the sample 25-25, the diffraction effect was subtle for the present view, however, the yellowness on the view was observed.

#### ***Angular-dependent transmittance of encapsulated samples***



*Figure 7-53. Angular dependent transmittance with respect to various incident angles for samples with silver coating). The measurement is conducted using the mini-goniophotometer.*

At the lower incident angle (incident angle between  $\pm 20^\circ$ ), for the sample 10-10 and 16-16, their transmittance was at the same order. This is because of the similar visible transmittance confirmed by the spectral measurement mentioned before. Likewise, the transmittance for the sample 25-25 at the identical angle range was lower than the other two samples. As the incident angle was beyond  $\pm 20^\circ$  and increased, the transmittance difference decreased. When the incident angle was beyond  $60^\circ$ , the difference of transmittance for the three type of samples was subtle.



This was because when the incident angle increased, the effective thickness of the thin film for the incident light increased. The effective thickness was calculated by considering that Ag was deposited on a flat surface. For the light with the incident angle of  $60^\circ$  coming to the polymer layer (refractive index is 1.5), the incident angle on the thin film was about  $35^\circ$ . Thus, the effective thickness was 18nm, 28nm and 44 nm, respectively.

Concerning the present samples for measurements, the polymer layers consist of embedded micro CPCs were laminated with glass substrates. Compared with the reference case with single glass substrate, the angular-dependent sample showed high transmittance at low incident angle (i.e., in the angular range between  $\pm 20^\circ$ ), while significant reduction when the at high incident angle (e.g., at  $60^\circ$ ), suggesting the potential of strong seasonal thermal dynamics with applying micro CPCs.

### ***Discussion***

The indoor light color is a factor, which influence the visual comfort. The yellowish color through sample 25-25 due to the different transmitted spectra from the sunlight spectra is not necessarily a problem. First, based on some study, the yellowish can contribute beneficial psychological effects (Noguchi and Sakaguchi, 1999; Chain, Dumortier and Fontoynt, 2001). Second, the color of the indoor illuminance is not only affected by the color of glazing itself, but also the area and the position of the glazing. The acceptance of the yellowish color for sample 25-25 needs to be evaluated with correlated color temperature (CCT) and color rendering index (CRI).

#### ***7.5.3.3 Indium tin oxide coating***

Figure 7-54 shows the as-deposited ITO thin film on a glass substrate and ITO thin film after annealing at  $490^\circ\text{C}$  for 1h. Due to the lack of oxygen for the process of thermal evaporation, the as-deposited thin film appeared to be dark-brown. After annealing, the film became highly transparent. However, both films were not conductive due to their actual stoichiometry. Deposition of ITO thin films with oxygen admitted into chamber during thermal evaporation may help obtain the stoichiometry for good conductance. It is reminded that the nominal ratio of  $\text{SnO}_2$  to  $\text{In}_2\text{O}_3$  is 10 wt% to 90 wt%. However, during the thermal evaporation, the tin oxide with lower melting point tended to melt and evaporated faster, leading to a gradient of the ration in the thin film. At the beginning of the deposition, the actual ratio of  $\text{SnO}_2$  to  $\text{In}_2\text{O}_3$  was higher than the nominal ratio; at certain thickness, the actual ratio equal to the nominal ratio; afterward, the actual ratio decreased as the thin film thickness increased. In order to solve the problem, the gradient as function of the film thickness should be studied; a shutter could be used to control the start and the end of the deposition based on the gradient-thickness function, to get a plain thin film where the actual ratio equal to the nominal ratio.



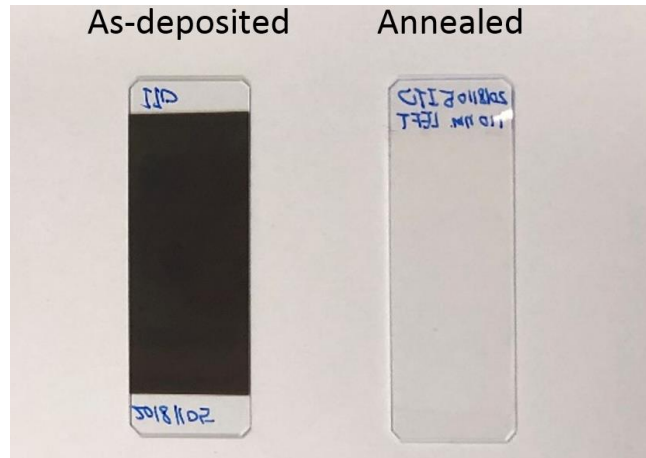


Figure 7-54. The as-deposited ITO thin film on a glass substrate and ITO thin film after annealing at 490°C for 1h.

Figure 7-55 shows the direction transmittance as function of wavelength for the as-deposited and annealed ITO thin film on glass substrates. For the as-deposited sample, the transmittance was approximate to linearly increased from 4% to about 30% for the wavelength range from 500 nm to 800 nm. Therefore, the appearance of the as-deposited thin film appeared to be brown. The transmittance increased from about 40% to 52% when the wavelength increased from 1000 nm to 2000 nm (near infrared light).

For the annealed thin film, the transmittance was significantly improved. For the wavelength from 400 nm to 550 nm, the transmittance linearly increased from 52% to 82%. For the wavelength range between 650 nm to 800nm, the transmittance was rather constant and in the order of 90%. When the wavelength was above 800 but below 2000nm, the transmittance slightly decreased and then remained constant at 85%.

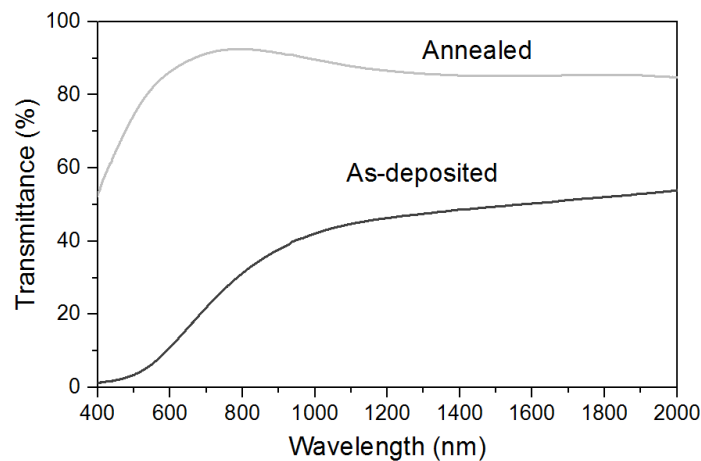


Figure 7-55. Direct transmittance as function of wavelength for the as-deposited and annealed ITO thin film on glass substrates.

## 7.6 Roll-to-roll extrusion for upscaling

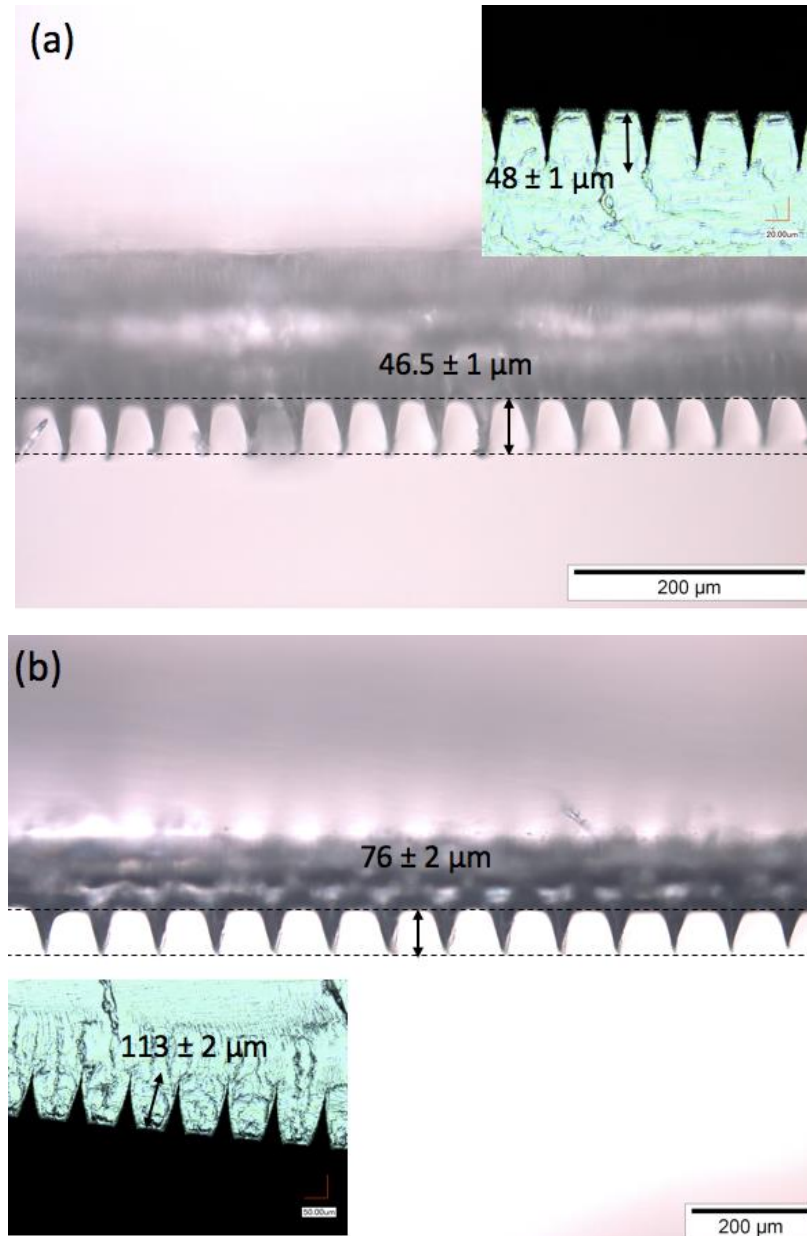


Figure 7-56. The cross-sectional optical microscope images of the two microstructures fabricated by roll-to-roll extrusion. The embedded small images are the cross-sections of the microstructures on the master molds fabricated by laser ablation.

Figure 7-56 shows the cross-sectional optical microscope images of the two microstructures fabricated by roll-to-roll (R2R) extrusion on polypropylene (PP). The embedded small images were the cross-sections of the microstructures on the master molds fabricated by laser ablation. The microstructures had the same shape but their dimensions were at different scale. Both microstructures appeared to be periodic and homogenous in dimensions. For the microstructure

shown in Figure 7-56 (a), with only 4% reduction, the height was reserved during multiple replications from the master mold to the product from the R2R extrusion. For the microstructure shown in Figure 7-56 (b), the height was reduced by 33%, due to the method limitation with the present fabrication parameters. However, the considerable reduction could be avoided. On one hand, further parameter optimization in terms of the extrusion pressure, the temperature of the roll with the shim which carries the negative microstructure with respect to the microstructure on PP, and the speed for extrusion will be conducted. On the other hand, even though that microstructure of larger scale has less diffraction, microstructure of the same shape with smaller scale of dimensions can be considered. For example, the microstructure, which was used for Al and Ag coating and the optical properties presented in section 7.5.3, had the same shape as that of the microstructure in Figure 7-56 (b), but its height was only about 80  $\mu\text{m}$  and the diffraction effect was reduced by increasing the visible transmittance of the coating at the normal incidence..

# Chapter 8 Conclusions and outlook

In this chapter, a summary of the key achievements is outlined followed by the conclusion of the results and finally, the outlook regarding the future investigation and development.

## 8.1 Summary of the key achievements

The key achievements of the present thesis are summarized as follows:

- Glazing with embedded “L” shape retro-reflective optical microstructures, and glazing with embedded micro compound parabolic concentrators (symmetric and asymmetric), were originally proposed and developed in this thesis.

The suggested applications, the advantages and the disadvantages of the proposed glazing are summarized in the tables below.

Table 8-1. The suggested applications and the corresponding configurations of the proposed glazing.

<b>Glazing section</b> <b>Façade orientation</b>	<b>Vision section</b>	<b>Daylighting section</b>
<b>South</b>	“L”- shape + selective coating	“L”- shape + opaque coating
<b>West, east</b>	CPC + selective coating	CPC + opaque coating
<b>Tilted roof, skylight</b>	CPC + selective coating, if vision needed	CPC + opaque coating

Table 8-2. The advantages and disadvantages of the proposed glazing

	<b>“L”-shape retro-reflective microstructure</b>	<b>Embedded micro CPCs (symmetric and asymmetric)</b>
<b>Advantages</b>	<ul style="list-style-type: none"> <li>• Very good daylighting performance</li> <li>• Efficient Glare protection</li> <li>• Improving thermal comfort</li> <li>• Retro-reflectivity: avoiding overheating and glare on streets</li> <li>• No need of alignment during fabrication</li> </ul>	<ul style="list-style-type: none"> <li>• Potential daylighting performance</li> <li>• Strong seasonal thermal dynamics</li> <li>• Applicable to various façade orientations</li> <li>• No need of alignment during fabrication</li> </ul>
<b>Disadvantages</b>	<ul style="list-style-type: none"> <li>• Limited to vertical and south-oriented façade</li> <li>• High aspect ratio</li> <li>• Sensitive to roughness</li> </ul>	<ul style="list-style-type: none"> <li>• Risk of glare at certain situations</li> <li>• Microstructure with overhang needed for asymmetric micro CPCs</li> </ul>

- Samples with embedded optical microstructures have been prepared in the lab. All the microstructures proposed in the present thesis have been obtained. For the fabrication, the following had been achieved:
  - 1) The curve-side wall grooves for micro CPCs (symmetric) had been fabricated using laser ablation.
  - 2) A novel mechanical scanning engraving method was developed for the fabrication of high-aspect ratio rectangle-like microstructures which were later used for the preparation of the “L”-shape retro-reflective optical microstructure, and the fabrication of micro CPCs (asymmetric) with overhangs.
  - 3) The replication of PDMS from PDMS, and the replication of PDMS from wax, with the interlayer of HPMC, had been proven to be feasible.
  - 4) The shape fidelity of UV-imprinted microstructures during UV-imprinting had been investigated.
- The combination of microstructures and coatings of various materials were investigated. Samples of high transparency at the normal incidence with the minimized diffraction effect. Meanwhile, the interesting angular-dependent transmittance for seasonal thermal dynamics had been achieved.
- In order to adapt the lab fabrication to the process for industrial upscaling, mechanical engraving on a wax cylinder had been conducted and proven to be promising for industrial upscaling. The roll-to-roll extrusion was also executed and it was proven to be feasible for the fabrication micro CPCs (symmetric)

## 8.2 Conclusions

The conclusions is sorted into three categories: simulation to estimate the potential benefits of the proposed glazing, fabrication of samples, and optical characterization.

### 8.2.1 Simulation

The calculation of the angular-dependent transmittance based on the computer modeling of conventional double glazing with optical microstructures helped estimate the potential of seasonal thermal dynamics. The parameter study showed that, for the “L”-shape microstructures, the change of angular-dependent transmittance and the retro-reflectivity were not sensitive to the reduction of the microstructured height with the relative reduction below 26%, whereas for micro CPCs, the tolerance of the microstructured height could be up to 28.5% or even higher, depending on the locations and the climates.

In order to further evaluate the potential seasonal thermal dynamics, annual dynamic solar gains conventional double glazing with the “L”-shape retro-reflective microstructure was calculated for

Lausanne and Athens. A significant average reduction of the transmitted-directed radiation by 60% over the mid of April to the mid of September was found in Lausanne. For Athens, the significant reduction by 76% of transmitted-direct radiation was seen from the mid of April to the mid of September. The potential benefit of glazing with micro CPCs in terms of seasonal thermal control was estimated by the calculation of direct transmittance as function of working hours, and two cases in Athens were used. Micro CPCs were found to be appropriate for tilted glazing (or horizontal skylight).

The potential advantages of a multifunctional complex fenestration system with embedded micro-mirrors for daylighting was evaluated for a south-facing façade in Lausanne. Three configurations according to the position of the embedded micro-mirrors in the glazing were investigated. It was shown that the embedded micro-mirrors could reduce the unnecessary illuminance peak closed to the window and increased the brightness in the rear of a room. Under a clear sky with sun, the average illuminance on the working plane with the use of micro-mirrors may be four times higher than that of the case with low-e glazing, for the region beyond 4 m deep into the room. The luminance ratio in the acceptable range could be improved by 20 %. The risk of glare in spring at working positions could be significantly reduced by placing embedded micro-mirrors at the position which was higher than a sitting occupant's eyes. In terms of directivity of daylight, for the cases of micro-mirrors in the upper two-thirds and the whole glazing, the vector-to-scalar illuminance ratios along the depth of the room were reduced from the harsh range to the acceptable range at noon in spring, and the ratios in the preferred range were significantly improved, suggesting a comfortable visual situation. The evaluation of the daylighting performance contributed to optimize the geometrical parameters of micro-mirrors for a specific location, provided a reference for further developing novel micro-mirrors, and determined the reasonable configuration of installation.

## 8.2.2 Fabrications

The fabrication flow and the optimized processing steps for samples in the lab are presented in Figure 8-1.

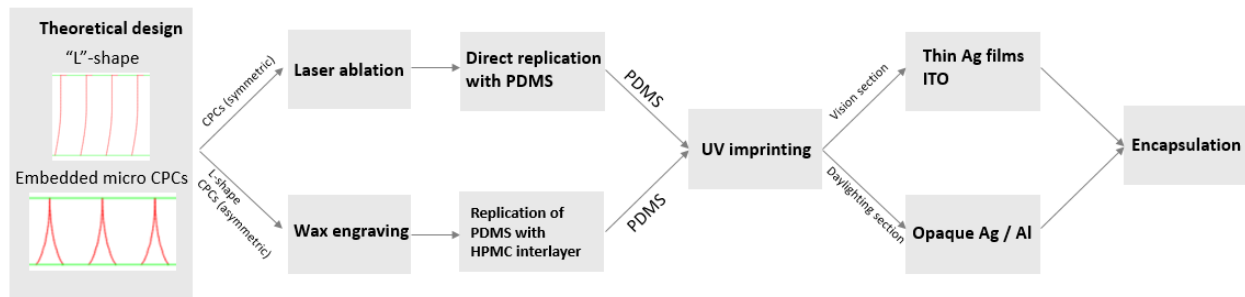


Figure 8-1. Fabrication flow of samples in the lab.

#### **8.2.2.1 Laser ablation**

For the production of micro CPCs (symmetric), curved sidewall grooves with a controlled optical surface were fabricated on polycarbonate substrates by scanning nanosecond 248-nm excimer laser ablation. The shapes of the obtained grooves were in good agreement with the design of the mask. Scanning nanosecond excimer laser ablation is therefore a promising approach for the realization of high-quality micro CPCs. With the repetition rate at 20 Hz or below, excimer laser ablation with scanning width of 7.5 mm may also be used for the fabrication of the microstructures for which large volume of mass (i.e., the ablated cross-sectional area is more than twice the area of the microstructured pattern) is ablated.

#### **8.2.2.2 Engraving**

A novel mechanical engraving method using blades with micro-teeth of desired patterns for the preparation of master molds was developed as alternative for the fabrication of the microstructures proposed in the present thesis. The following steps of UV-imprinting from the master molds were also developed. In order to obtain the “L”-shape optical microstructure, the rectangle-like microstructures of aspect ratio of 3.8 and 6.7 with parabolic sidewall and good controlled shapes were fabricated. The microstructures for asymmetric micro CPCs with overhang were also obtained. With a scanning speed of 15 cm/min, the method has the potential to be efficient and appropriate for large-area microstructure fabrication.

#### **8.2.2.3 Replications**

The replication of PDMS from PDMS, and the replication of PDMS from wax, with the interlayer of HPMC, had proven to be feasible. The microstructures on the replicas showed good shape fidelity. The study in this section provided an alternative for the processing of microstructures.

#### **8.2.2.4 UV-imprinting**

The shape fidelity of a UV printed periodic polymer microstructure for a novel glazing system, produced with different concentrations of photoinitiator (PI) and under thermal aging was investigated. For the microstructure with sharp edge, the period was found to be stable, with shrinkage below 1.5% after printing, independent of PI concentration, and which remained rather constant upon thermal exposure. In contrast, dimension  $W1/2$  decreased by up to 14.5% with time at 80°C, presumably due to additional chemical conversion and physical aging processes. A change of height also occurred, but it was partly compensated by the change of  $W1/2$  as a result of Poisson's effects and a complex distribution of internal stress. The impact of dimensional changes on the redirection of daylight were also investigated. The dominant reason accounting for the change of the angular dependence and intensity of the maximum transmittance of redirected rays was the

shrinkage of the micro-mirrors along their height  $H$  and resulting change of their local curvature. For the trapezoid-like HBP microstructures, the period and the width ( $W$ ) of the top surface were stable and independent of the PI concentration. The relative shrinkages of the height increased with the increase of the PI concentration. Nonetheless, when the PI concentration was 6%, the relative shrinkage of the height did not exceed 6%.

### **8.2.3 Optical characterization**

The feasibility of facet-selective coating based on self-shadowing effect or polishing after coating was proven. Aluminum (Al) thin films and silver (Ag) thin films of various thickness were deposited on symmetric micro CPC(30, 30) with the periodicity of 68  $\mu\text{m}$ . It was found that improving the visible transmittance of the thin films at normal incidence could significantly reduce the diffraction. Due to the spectral selectivity, sample with embedded optical microstructures had high transparency at normal incidence. Compared with the reference case of a clean glass substrate, the optical measurement of angular-dependent transmittance showed more than 60% relative reduction of transmittance at high elevation angle ( $> 50^\circ$ ), suggesting the potential for seasonal thermal dynamics. The study of the optical properties as function of thin film thickness provided guideline for the optimization of the spectrum to balance diffraction, transparency, color of the appearance and angular-dependent transmittance.

## **8.3 Research outlook**

In the future, the relative energy saving due to the reduction of thermal loads by using the optical microstructures, can be investigated by simulation. Novel microstructures with optimized selective thin films will be further studied. Industrial roll-to-roll process for commercial production will be developed. Field study with window-sized prototype and users will be considered.



# Appendix A: Mask openings for laser ablation

In the appendix A, the representative mask openings (the confined contours) for the three types of the types of the microstructures (mentioned in section 5.1.7) on polycarbonate substrates.

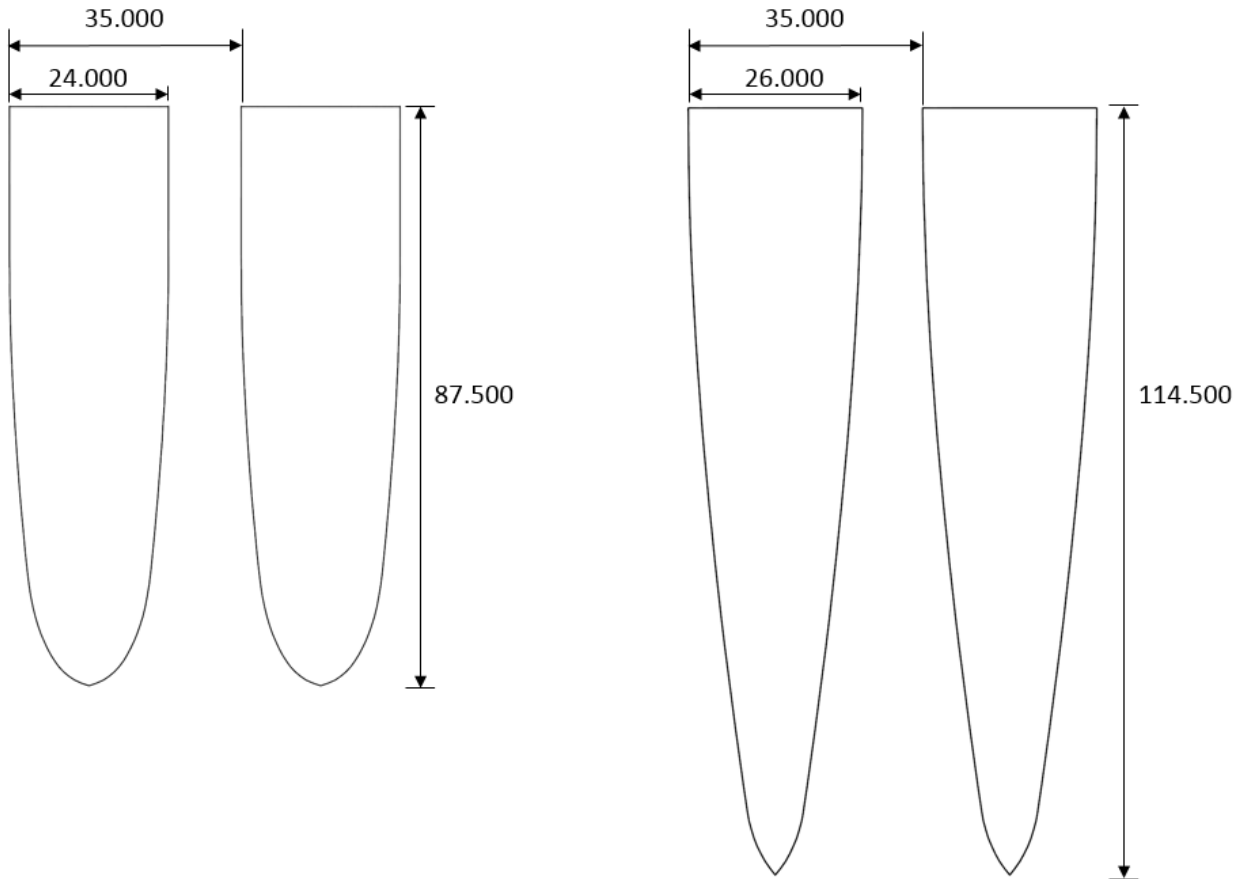


*Figure A-1. The mask opening of the rectangle-like microstructures for “L”-shape optical microstructures at different aspect ratio. The periodicity for such mask openings are 35  $\mu\text{m}$ , 50  $\mu\text{m}$  and 75  $\mu\text{m}$ . Unit for the numbers in the graph:  $\mu\text{m}$ .*

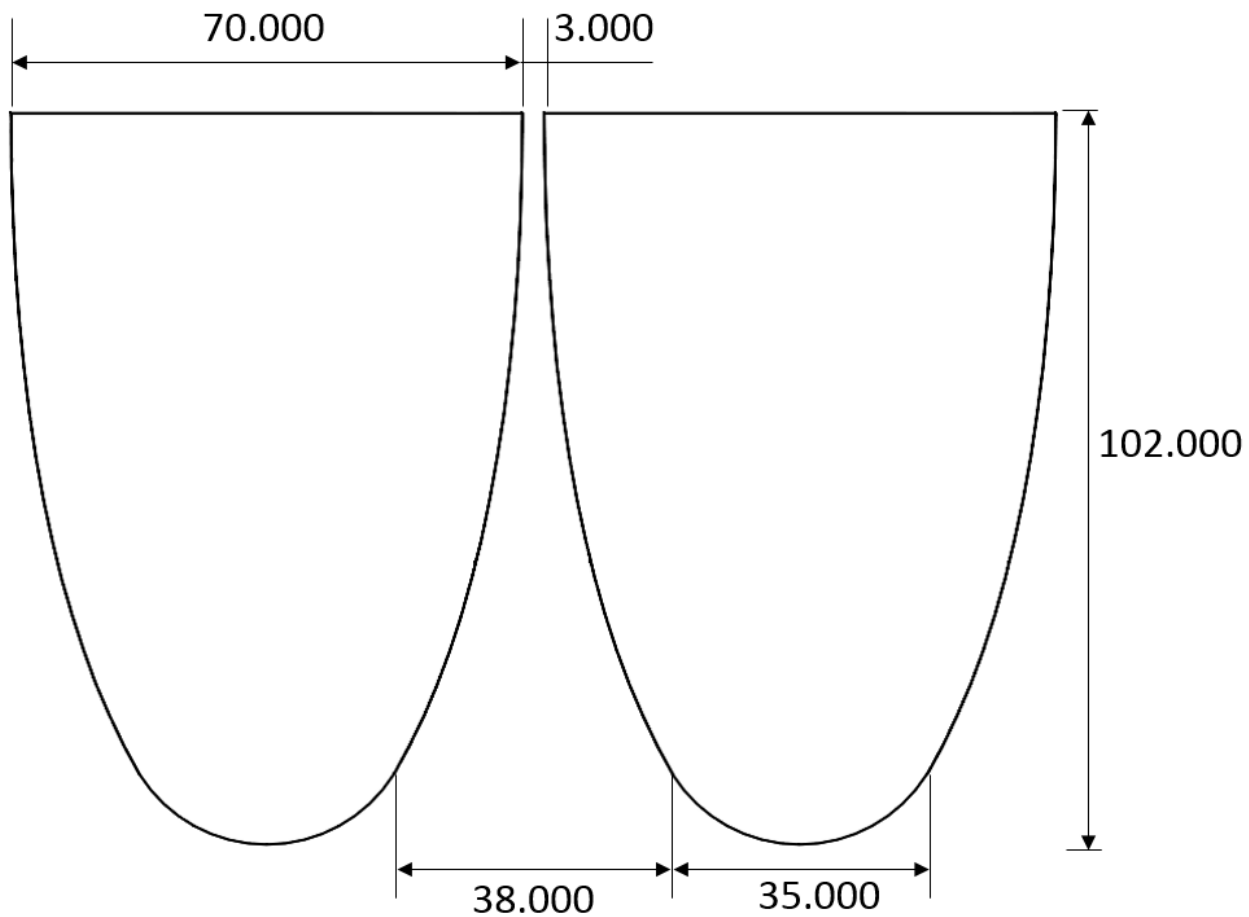
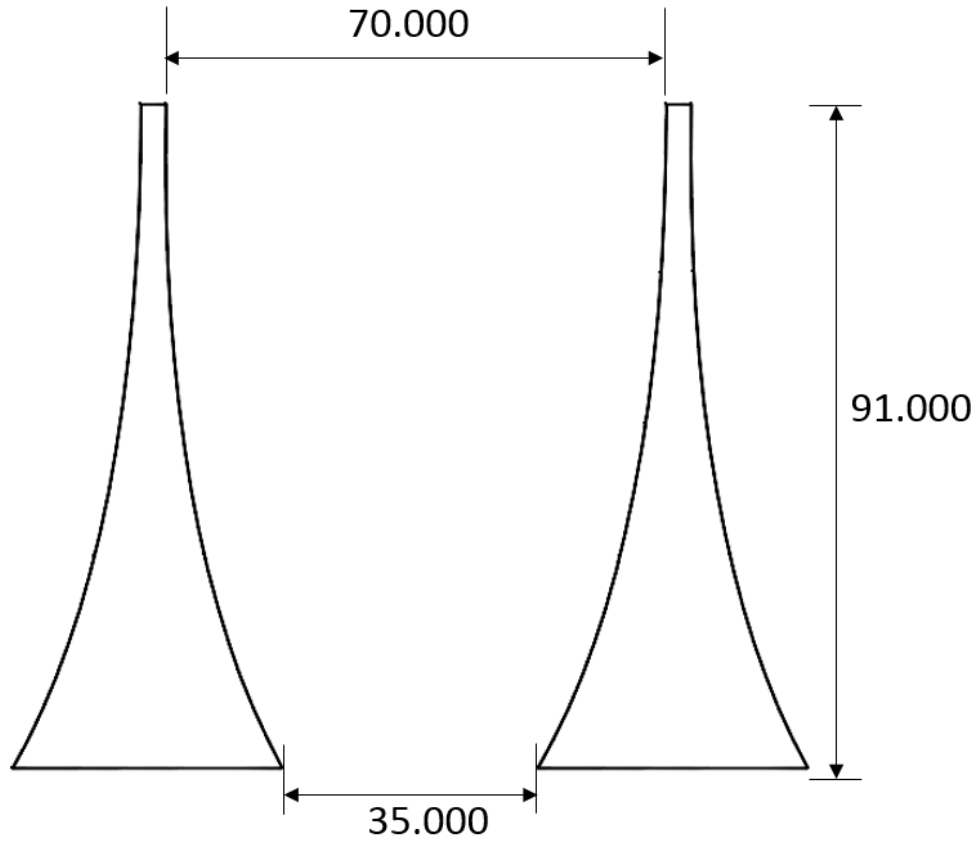


Figure A-2. The mask opening of the sharp edges for micro CPC(30, 30). On the mask there are also mask opening of the same shape with the periodicity of 50. Mask opening for sharp edges for micro CPC(40, 40) is also on the mask, and the critical geometrical parameter is presented in Table 4-2. Unit for the numbers in the graph:  $\mu\text{m}$ .



*Figure A-3. Mask openings for curve-sidewall grooves for micro CPC(30, 30). On the mask there are also mask opening of the same shape with the periodicity of 50. Mask opening for curve-sidewall grooves for CPC(40, 40) is also on the mask, and the critical geometrical parameter is presented in Table 4-2.*

# Appendix B: Blades with micro asymmetric CPCs for engraving

In the appendix B, the computer design for the blades with micro asymmetric CPCs for engraving are presented.

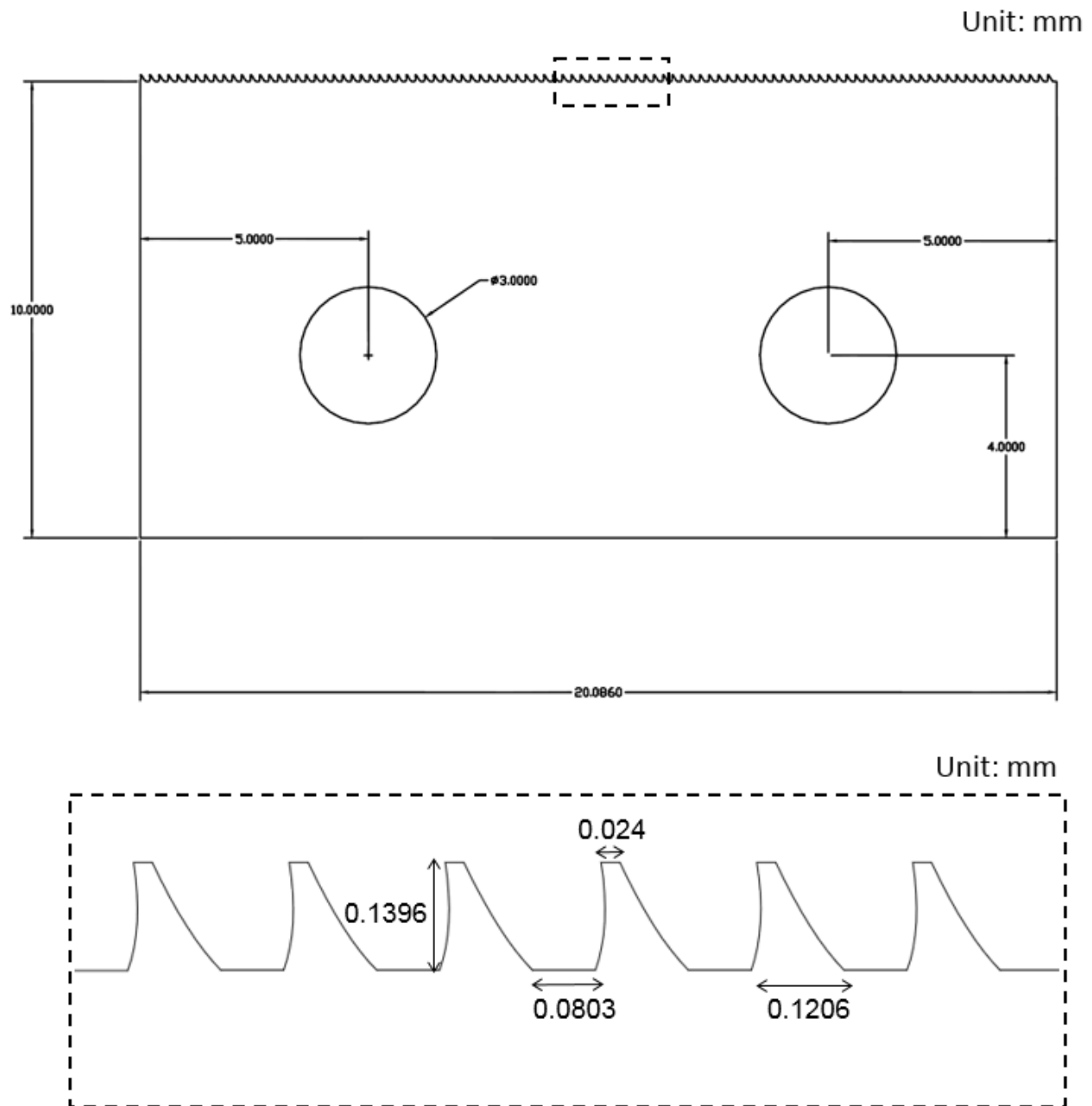


Figure B-1. Blade with micro asymmetric CPC(50, 0).

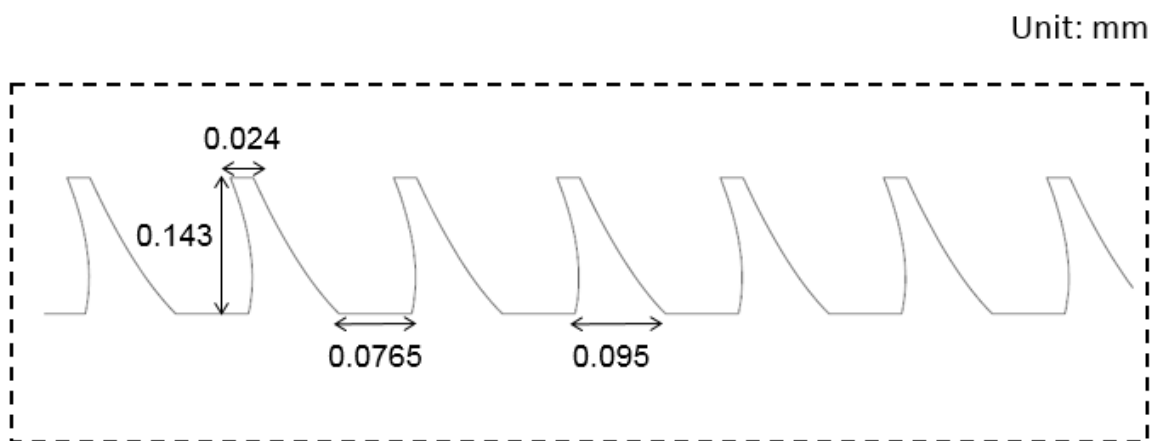
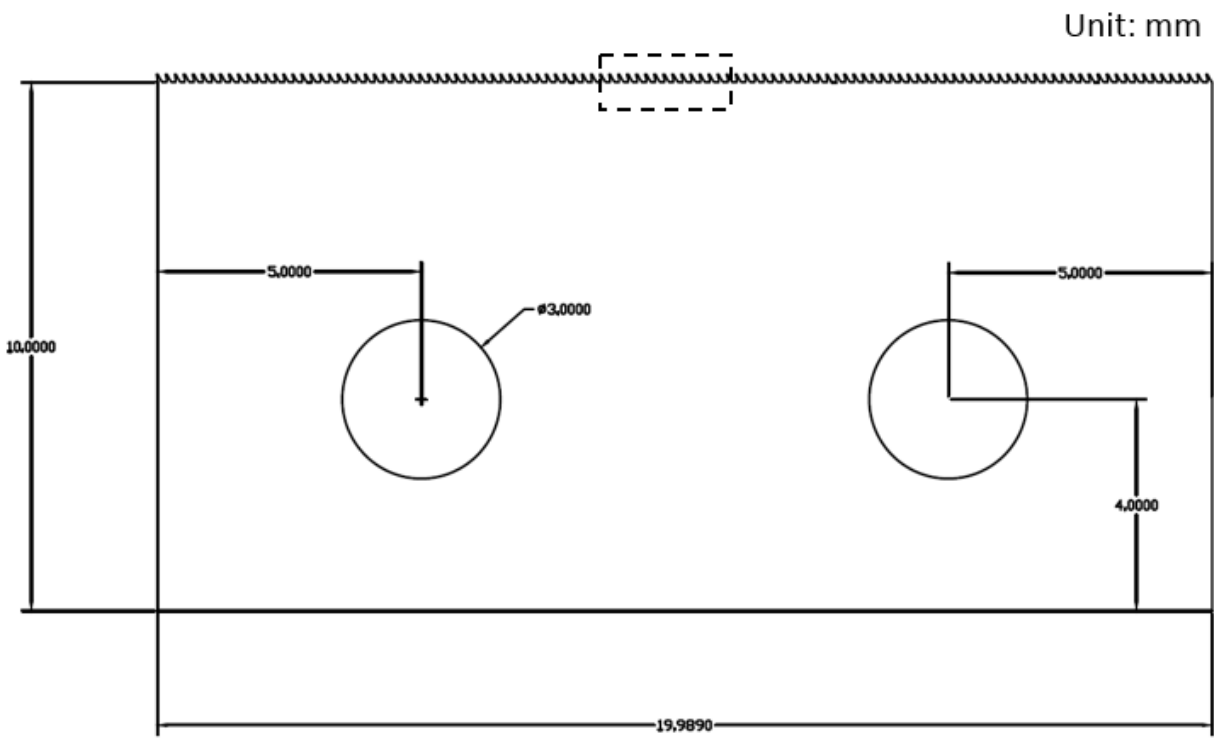


Figure B-2. Blade with micro asymmetric CPC(65, 0).

# Bibliography

- Abramczyk, H. (2005) *Introduction to Laser Spectroscopy*. Elsevier.
- Allen, K. and Wu, Y. (2015) 'Smart Window - a Window for Dynamic Control of Building Energy Performance', 139, pp. 65–70.
- Alonso, R. C. B. *et al.* (2014) 'Photoinitiator concentration and modulated photoactivation: influence on polymerization characteristics of experimental composites', *Applied Adhesion Science*, 2(1), pp. 1–11. doi: 10.1186/2196-4351-2-10.
- Andersen, M. (2002) 'Light distribution through advanced fenestration systems', *Building Research and Information*, 30(4), pp. 264–281. doi: 10.1080/09613210210132937.
- Andrzejewska, E. (2001) 'Photopolymerization kinetics of multifunctional monomers', *Progress in Polymer Science (Oxford)*, 26(4), pp. 605–665. doi: 10.1016/S0079-6700(01)00004-1.
- Baetens, R., Jelle, B. P. and Gustavsen, A. (2010) 'Properties, requirements and possibilities of smart windows for dynamic daylight and solar energy control in buildings: A state-of-the-art review', *Solar Energy Materials and Solar Cells*. Elsevier, 94(2), pp. 87–105. doi: 10.1016/j.solmat.2009.08.021.
- Barrios Ricardo; Sanchez-Pena, Jose M.; Granqvist, Claes G.; Niklasson, Gunnar A., D. V. (2013) 'Toward a quantitative model for suspended particle devices: Optical scattering and absorption coefficients', *Solar Energy Materials and Solar Cells*, 111(0), pp. 115–122. doi: <http://dx.doi.org/10.1016/j.solmat.2012.12.012>.
- Bastien, D. and Athienitis, A. K. (2015) 'Methodology for selecting fenestration systems in heating dominated climates', *Applied Energy*. Elsevier Ltd, 154, pp. 1004–1019. doi: 10.1016/j.apenergy.2015.05.083.
- Bäuerle, D. (2011) *Laser Processing and Chemistry*. Springer Science & Business Media.
- Boogh, L., Pettersson, B. and Månson, J. A. E. (1999) 'Dendritic hyperbranched polymers as tougheners for epoxy resins', *Polymer*, 40(9), pp. 2249–2261. doi: 10.1016/S0032-3861(98)00464-9.
- Brandt, W. C. *et al.* (2010) 'Effect of different photo-initiators and light curing units on degree of conversion of composites.', *Brazilian oral research*, 24(3), pp. 263–270. doi: 10.1590/S1806-83242010000300002.
- Bratton, D. *et al.* (2006) 'Recent progress in high resolution lithography', *Polymers for Advanced Technologies*, 17(2), pp. 94–103. doi: 10.1002/pat.662.
- Braun, A. (2002) *Oberflächenformgebung von synthetischen Polymeren mittels UV-Laserablation unter Verwendung abbildender Maskentechniken*. Universität Leipzig.
- Brilliant Universal Limited (2012) *UV curing Technology*, Brilliant Universal Limited.
- Bundesamt für Energie Bern (2016) *Analyse des schweizerischen Energieverbrauchs 2000 - 2014 nach Verwendungszwecken*.
- Buratti, C. and Moretti, E. (2012) 'Glazing systems with silica aerogel for energy savings in

buildings', *Applied Energy*, pp. 396–403. doi: 10.1016/j.apenergy.2012.03.062.

Bystritskaya, E. V., Pomerantsev, A. L. and Rodionova, O. Y. (1999) 'Prediction of the aging of polymer materials', *Chemometrics and Intelligent Laboratory Systems*, 47(2), pp. 175–178. doi: 10.1016/S0169-7439(98)00205-6.

C.M.Kuo, A. (1999) 'Poly(dimethylsiloxane)', *Polymer Data Handbook*, pp. 411–435. doi: 10.1021/ja907879q.

Cantin, F. and Dubois, M. C. (2011) 'Daylighting metrics based on illuminance, distribution, glare and directivity', *Lighting Research and Technology*, 43(3), pp. 291–307. doi: 10.1177/1477153510393319.

Carlucci, S. *et al.* (2015) 'A review of indices for assessing visual comfort with a view to their use in optimization processes to support building integrated design', *Renewable and Sustainable Energy Reviews*. Elsevier, 47(7491), pp. 1016–1033. doi: 10.1016/j.rser.2015.03.062.

Chain, C., Dumortier, D. and Fontoynt, M. (2001) 'Consideration of daylight's colour', *Energy and Buildings*, 33(3), pp. 193–198. doi: 10.1016/S0378-7788(00)00081-5.

Chang, C. Y. and Chen, P. K. (2005) 'Human response to window views and indoor plants in the workplace', *HortScience*, 40(5), pp. 1354–1359.

Charton, C. and Fahland, M. (2003) 'Optical properties of thin Ag films deposited by magnetron sputtering', *Surface and Coatings Technology*, 174, pp. 181–186. doi: 10.1016/S0257-8972.

Chayen, N. E. and Saridakis, E. (2008) 'Protein crystallization: From purified protein to diffraction-quality crystal', *Nature Methods*, 5(2), pp. 147–153. doi: 10.1038/nmeth.f.203.

Chow, T. T. and Li, C. (2013) 'Liquid-filled solar glazing design for buoyant water-flow', *Building and Environment*, 60, pp. 45–55. doi: 10.1016/j.buildenv.2012.11.010.

Chow, T. T., Li, C. and Lin, Z. (2011) 'Thermal characteristics of water-flow double-pane window', *International Journal of Thermal Sciences*. Elsevier Masson SAS, 50(2), pp. 140–148. doi: 10.1016/j.ijthermalsci.2010.10.006.

Citherlet, S., Di Guglielmo, F. and Gay, J. B. (2000) 'Window and advanced glazing systems life cycle assessment', *Energy and Buildings*, 32(3), pp. 225–234. doi: 10.1016/S0378-7788(98)00073-5.

Compagnon, R. (2001) 'Radiance a simulation tool for daylighting systems', p. 39.

Costanzo, V., Evola, G. and Marletta, L. (2016) 'Thermal and visual performance of real and theoretical thermochromic glazing solutions for office buildings', *Solar Energy Materials and Solar Cells*. Elsevier, 149, pp. 110–120. doi: 10.1016/j.solmat.2016.01.008.

Cox, R. A., Drews, M., Rode, C., & Nielsen, S. B. (2015) 'Simple future weather files for estimating heating and cooling demand', *Building and Environment*, 83, 104–114.

Cuttle, C. (1997) 'Cubic illumination.pdf', *Lighting Research and Technology*, 29(1), pp. 1–14.

Cuttle, C. (2014) 'Research Note: A practical approach to cubic illuminance measurement', *Lighting Research and Technology*, 46(1), pp. 31–34. doi: 10.1177/1477153513498251.

Dallies, G., Berger, P. and Huge, H. (1995) 'Time-resolved observation of gas-dynamic discontinuities arising during excimer laser ablation and their interpretation', *Journal of Physics*

*D: Applied Physics*, 28(4), pp. 794–806. doi: 10.1088/0022-3727/28/4/026.

Demir, A. and Necdet Konan, A. (2013) ‘Impact of daylight on student and teacher performance’, *Journal of Educational and Instructional Studies*, 3(1), pp. 1–7.

Despont, M. (1997) ‘High-Aspect-Ratio, ultrathick, negative-tone near-UV photoresist for MEMS application’, *Ieee*.

Egami, T. and Billinge, S. (2012) *Underneath the Bragg Peaks: Structural Analysis of Complex Materials focuses*. 2nd edn. Elsevier.

EIA-U.S. Energy Information Administration (2018) *Energy use in homes*.

Enamul Hossain, M., Ketata, C. and Rafiqul Islam, M. (2009) ‘Experimental Study of Physical and Mechanical Properties of Natural and Synthetic Waxes Using Uniaxial Compressive Strength Test’, pp. 1–5.

Fan, P. *et al.* (2005) ‘The characteristic criterion of the growth of metallic films from discontinuous to continuous’, *Proceedings of SPIE - The International Society for Optical Engineering*, 5774(December 2004), pp. 8–12. doi: 10.1117/12.607271.

Ferracane, J. L. *et al.* (1997) ‘Wear and marginal breakdown of composites with various degrees of cure’, *Journal of Dental Research*, 76(8), pp. 1508–1516. doi: 10.1177/00220345970760081401.

Fratini, F. *et al.* (2016) ‘Beeswax: A minireview of its antimicrobial activity and its application in medicine’, *Asian Pacific Journal of Tropical Medicine*. Elsevier B.V., 9(9), pp. 839–843. doi: 10.1016/j.apjtm.2016.07.003.

Freewan, A. A. (2010) ‘Maximizing the lightshelf performance by interaction between lightshelf geometries and a curved ceiling’, *Energy Conversion and Management*. Elsevier Ltd, 51(8), pp. 1600–1604. doi: 10.1016/j.enconman.2009.09.037.

Freewan, A. A., Shao, L. and Riffat, S. (2008) ‘Optimizing performance of the lightshelf by modifying ceiling geometry in highly luminous climates’, *Solar Energy*, 82(4), pp. 343–353. doi: 10.1016/j.solener.2007.08.003.

Gago, E. J. *et al.* (2015) ‘Natural light controls and guides in buildings. Energy saving for electrical lighting, reduction of cooling load’, *Renewable and Sustainable Energy Reviews*. Elsevier, 41, pp. 1–13. doi: 10.1016/j.rser.2014.08.002.

Galasiu, A. D. and Veitch, J. A. (2006) ‘Occupant preferences and satisfaction with the luminous environment and control systems in daylit offices: a literature review’, *Energy and Buildings*, 38(7), pp. 728–742. doi: 10.1016/j.enbuild.2006.03.001.

Gao, C. and Yan, D. (2004) ‘Hyperbranched polymers: From synthesis to applications’, *Progress in Polymer Science (Oxford)*, 29(3), pp. 183–275. doi: 10.1016/j.progpolymsci.2003.12.002.

Geiser, V. *et al.* (2010) ‘Nanoimprint lithography with UV-curable hyperbranched polymer nanocomposites’, *Macromolecular Symposia*, 296(1), pp. 144–153. doi: 10.1002/masy.201051022.

Genolet, G. and Lorenz, H. (2014) ‘UV-LIGA: From development to commercialization’, *Micromachines*, 5(3), pp. 486–495. doi: 10.3390/mi5030486.



Ghantasala, M. K. *et al.* (2001) 'Patterning, electroplating and removal of SU-8 moulds by excimer laser micromachining', *Journal of Micromechanics and Microengineering*, 11(2), pp. 133–139. doi: 10.1088/0960-1317/11/2/308.

Ghosh, A. and Norton, B. (2017) 'Interior colour rendering of daylight transmitted through a suspended particle device switchable glazing', *Solar Energy Materials and Solar Cells*. Elsevier, 163(October 2016), pp. 218–223. doi: 10.1016/j.solmat.2017.01.041.

Ghosh, A., Norton, B. and Duffy, A. (2016a) 'Behaviour of a SPD switchable glazing in an outdoor test cell with heat removal under varying weather conditions', *Applied Energy*. Elsevier Ltd, 180, pp. 695–706. doi: 10.1016/j.apenergy.2016.08.029.

Ghosh, A., Norton, B. and Duffy, A. (2016b) 'ScienceDirect Daylighting performance and glare calculation of a suspended particle device switchable glazing', *Solar Energy*. Elsevier Ltd, 132, pp. 114–128. doi: 10.1016/j.solener.2016.02.051.

Gil-Lopez, T. and Gimenez-Molina, C. (2013) 'Influence of double glazing with a circulating water chamber on the thermal energy savings in buildings', *Energy and Buildings*. Elsevier B.V., 56, pp. 56–65. doi: 10.1016/j.enbuild.2012.10.008.

Gitlin, L., Schulze, P. and Belder, D. (2009) 'Rapid replication of master structures by double casting with PDMS', *Lab on a Chip*, 9(20), pp. 3000–3002. doi: 10.1039/b904684d.

Glass education center (2018) *What is Low-E Glass?*

Glassner, A. S. (1989) *An introduction to ray tracing*. Elsevier.

Gombert, a. *et al.* (2003) 'Replicated microstructures with optical functions in solar and display applications', *Physics, Theory, and Applications of Periodic Structures in Optics II*, 5184(December 2003), pp. 60–73. doi: 10.1117/12.504588.

Gong, J., Kostro, A., Scartezzini, J. L., & Schüler, A. (2018, September) 'Feasibility study on a novel daylighting system with embedded micro compound parabolic concentrators (CPCs)', In *Nonimaging Optics: Efficient Design for Illumination and Solar Concentration XV* (Vol. 10758, p. 1075807). International Society for Optics and Photonics.

Gong, J., Delaunay, A., Kostro, A., & Schüler, A. (2018) 'Development of a novel mechanical micro-engraving method for the high-aspect-ratio microstructures of an advanced window system', *Microelectronic Engineering*, 191, 48-53.

Gong, J., Violakis, G., Infante, D., Hoffmann, P., Kostro, A., & Schüler, A. (2018, February) 'Microfabrication of curved sidewall grooves using scanning nanosecond excimer laser ablation', In *Laser-based Micro-and Nanoprocessing XII* (Vol. 10520, p. 105200Z). International Society for Optics and Photonics.

Gong, J. *et al.* (2017) 'Dimensional stability analysis of a UV printed polymer microstructure for a novel glazing system', *Energy Procedia*, pp. 763–768. doi: 10.1016/j.egypro.2017.07.393.

Gong, J., Kostro, A., Motamed, A., & Schueler, A. (2016) 'Potential advantages of a multifunctional complex fenestration system with embedded micro-mirrors in daylighting', *Solar Energy*, 139, 412-425.

Gonzales Lazo, M. A. (2015) 'Light trapping polymer-based coatings for cost effective flexible thin film photovoltaics. TH 6537', 6537.

Hansen, S. G. (1989) 'Velocity profiles of species ejected in ultraviolet laser ablation of several polymers examined by time-of-flight mass spectroscopy', *Journal of Applied Physics*, 66(7), pp. 3329–3336. doi: 10.1063/1.344129.

Harald, I. and Hans, L. (2009) *Solid-State Physics, An Introduction to Principles of Materials Science*. 4th edn. Springer Science & Business Media.

Hee, W. J. *et al.* (2015) 'The role of window glazing on daylighting and energy saving in buildings', *Renewable and Sustainable Energy Reviews*. doi: 10.1016/j.rser.2014.09.020.

Hemmerich, K. J. (1998) 'General aging theory and simplified protocol for accelerated aging of medical devices', *Medical Plastic and Biomaterials*, 5, pp. 16–23.

Hielscher, T. (2005) 'Ultrasonic Production of Nano-Size Dispersions and Emulsions', *Ens*, (December), pp. 14–16. doi: arXiv:0708.1831v1 [cond-mat.mtrl-sci].

Ho, K. H. and Newman, S. T. (2003) 'State of the art electrical discharge machining (EDM)', *International Journal of Machine Tools and Manufacture*, 43(13), pp. 1287–1300. doi: 10.1016/S0890-6955(03)00162-7.

Hossain, M. E. *et al.* (2009) 'SEM-based structural and chemical analysis of paraffin wax and beeswax for petroleum applications', *Journal of characterization and Development of Novel Materials*, 1(1), pp. 21–38.

Hossain, M. E. (2015) 'Comparative pathway analysis of paraffin wax and beeswax for industrial applications', (September).

Huang, Y., Niu, J. lei and Chung, T. ming (2014) 'Comprehensive analysis on thermal and daylighting performance of glazing and shading designs on office building envelope in cooling-dominant climates', *Applied Energy*. Elsevier Ltd, 134, pp. 215–228. doi: 10.1016/j.apenergy.2014.07.100.

Hukins, D. W. L., Mahomed, A. and Kukureka, S. N. (2008) 'Accelerated aging for testing polymeric biomaterials and medical devices', *Medical Engineering and Physics*, 30(10), pp. 1270–1274. doi: 10.1016/j.medengphy.2008.06.001.

Imazato, S. *et al.* (1995) 'Relationship between the degree of conversion and internal discoloration of light-activated composite.', *Dental materials journal*, 14(1), pp. 23–30. doi: 10.4012/dmj.14.23.

Inanici, M. (2007) 'Computational Approach for Determining the Directionality of Light: Directional-To-Diffuse Ratio', *Proceedings: Building Simulation*, pp. 1182–1188.

Ize, T., Wald, I. and Parker, S. G. (2008) 'Ray tracing with the BSP tree', *RT'08 - IEEE/EG Symposium on Interactive Ray Tracing 2008, Proceedings*, pp. 159–166. doi: 10.1109/RT.2008.4634637.

Jańczuk, B. and Białopiotrowicz, T. (1990) 'The total surface free energy and the contact angle in the case of low energetic solids', *Journal of Colloid And Interface Science*, 140(2), pp. 362–372. doi: 10.1016/0021-9797(90)90356-S.

Jerod, A. (2018) *The Role of Adaptive Facades*.

Joye, C. D. *et al.* (2010) 'Microfabrication of a 220 GHz grating for sheet beam amplifiers', in *In Vacuum Electronics Conference (IVEC), 2010 IEEE International*. IEEE, pp. 187–188.

- KD Solution.Co., L. (2018) *EDM tips*.
- Khurshheed, A. (2011) *Scanning electron microscope optics and spectrometers*. Singapore : World Scientific.
- Kim, J. and Xu, X. (2003) ‘Excimer laser fabrication of polymer microfluidic devices’, *Journal of Laser Applications*, 15(4), pp. 255–260. doi: 10.2351/1.1585085.
- Kim, S. M., Lee, S. H. and Suh, K. Y. (2008) ‘Cell research with physically modified microfluidic channels: A review’, *Lab on a Chip*, 8(7), pp. 1015–1023. doi: 10.1039/b800835c.
- Klammt, S., Neyer, A. and Müller, H. (2012) ‘Microoptics for efficient redirection of sunlight.’, *Applied optics*, 51(12), pp. 2051–6. doi: 10.1364/AO.51.002051.
- Klems, J. H. (1994) ‘New method for predicting the solar heat gain of complex fenestration systems- 2. Detailed description of the matrix layer calculation’, *ASHRAE Transactions*, 100.
- Kong, L. B. *et al.* (2013) ‘Modeling and characterization of generation of 3D micro-structured surfaces with self-cleaning and optical functions’, *Optik*, 124(17), pp. 2848–2853. doi: 10.1016/j.ijleo.2012.08.061.
- Kopitkovas, G. *et al.* (2004) ‘Fabrication of beam homogenizers in quartz by laser micromachining’, *Journal of Photochemistry and Photobiology A: Chemistry*, 166(1–3), pp. 135–140. doi: 10.1016/j.jphotochem.2004.05.001.
- Kostro, A., Gonzalez, L. M. A., Leterrier, Y., Siringil, E., Hoffmann, P., & Schueler, A. (2015). ‘Laser ablation and nanoimprint lithography for the fabrication of embedded light redirecting micromirrors’, In Proceedings of International Conference CISBAT 2015 Future Buildings and Districts Sustainability from Nano to Urban Scale; EPFL-CONF-213287; (pp. 15-20).
- Kostro, A. (2015) *Microstructured glazing for daylighting , glare protection , seasonal thermal control and clear view*. École polytechnique fédérale de Lausanne.
- Kostro, A. *et al.* (2016) ‘CFSpro: ray tracing for design and optimization of complex fenestration systems using mixed dimensionality approach’, *Appl. Opt.*, 55(19), pp. 5127–5134. doi: 10.1364/AO.55.005127.
- Kozowyk, P. R. B., Langejans, G. H. J. and Poulis, J. A. (2016) ‘Lap Shear and Impact Testing of Ochre and Beeswax in Experimental Middle Stone Age Compound Adhesives’, *PloS one*, 11(3), p. e0150436. doi: 10.1371/journal.pone.0150436.
- Küper, S. and Brannon, J. (1991) ‘Ambient gas effects on debris formed during KrF laser ablation of polyimide’, in *MRS Online Proceedings*.
- Kurdikar, D. L. and Peppas, N. A. (1994) ‘A Kinetic Model for Diffusion-Controlled Bulk Cross-Linking Photopolymerizations’, *Macromolecules*, 27(15), pp. 4084–4092. doi: 10.1021/ma00093a009.
- Labib, R. (2013) ‘Improving daylighting in existing classrooms using laser cut panels’, *Lighting Research and Technology*, 45(5), pp. 585–598. doi: 10.1177/1477153512471366.
- Lafuma, A. and Quéré, D. (2003) ‘Superhydrophobic states’, *Nature materials*, 2(7), pp. 457–460.
- Lampert, C. M. (2003) ‘Large-area smart glass and integrated photovoltaics’, *Solar Energy*

*Materials and Solar Cells*, 76(4), pp. 489–499. doi: 10.1016/S0927-0248(02)00259-3.

Lampert, C. M. (2004) ‘Chromogenic smart materials’, *Materials Today*, 7(3), pp. 28–35. doi: 10.1016/S1369-7021(04)00123-3.

Lange, D. A. and Jennings, H. M. (1992) ‘Relationship between Fracture Surface Roughness and Fracture Behavior of Cement Paste and Mortar’.

Laouadi, A., Reinhart, C. F. and Bourgeois, D. (2008) ‘Efficient calculation of daylight coefficients for rooms with dissimilar complex fenestration systems’, *Journal of Building Performance Simulation*, 1(1), pp. 3–15. doi: 10.1080/19401490701868299.

Larson, G. and Shakespeare, R. (2003) *Rendering with Radiance: the art and science of lighting visualization*. Space & Light.

Lei, J., Yang, J. and Yang, E. H. (2016) ‘Energy performance of building envelopes integrated with phase change materials for cooling load reduction in tropical Singapore’, *Applied Energy*. Elsevier Ltd, 162, pp. 207–217. doi: 10.1016/j.apenergy.2015.10.031.

Li, D. H. W. and Lam, J. C. (2003) ‘An investigation of daylighting performance and energy saving in a daylight corridor’, *Energy and Buildings*, 35(4), pp. 365–373. doi: 10.1016/S0378-7788(02)00107-X.

Li, J. and Ananthasuresh, G. K. (2001) ‘Quality study on the excimer laser micromachining of electro-thermal-compliant micro devices’, *Journal of Micromechanics and Microengineering*, 11(1), pp. 38–47. doi: 10.1088/0960-1317/11/1/307.

Lippert, T. *et al.* (1999) ‘Imaging-XPS/Raman investigation on the carbonization of polyimide after irradiation at 308 nm’, *Applied Physics A: Materials Science and Processing*, 69(7), pp. 651–654. doi: 10.1007/s003390051497.

Luciani, A. *et al.* (2004) ‘Rheological and Physical Properties of Aliphatic Hyperbranched Polyesters’, *Journal of Polymer Science, Part B: Polymer Physics*, 42(7), pp. 1218–1225. doi: 10.1002/polb.10671.

Macarie, L. and Ilia, G. (2005) ‘The influence of temperature and photoinitiator concentration on photoinitiated polymerization of diacrylate monomer’, *Central European Journal of Chemistry*, 3(4), pp. 721–730. doi: 10.2478/BF02475199.

Mardaljevic, J., Andersen, M. (2012) ‘Mardaljevic, J., Andersen, M., Roy, N., & Christoffersen, J. (2012, September). Daylighting metrics: is there a relation between useful daylight illuminance and daylight glare probability. In Proceedings of the building simulation and optimization confere’, in. In Proceedings of the building simulation and optimization conference (BSO12).

McNeil, A. (2011) *On the sensitivity of daylight simulations to the resolution of the hemispherical basis used to define bidirectional scattering distribution functions*.

McNeil, A. (2014) ‘The Three Phase Method for Simulating Complex Fenestration with Rdiance’, (October 2010), p. 35.

McNeil, A. and Lee, E. S. (2012) ‘A validation of the Radiance three-phase simulation method for modelling annual daylight performance of optically complex fenestration systems’, *Journal of Building Performance Simulation*, 6(1), pp. 24–37. doi: 10.1080/19401493.2012.671852.

Meteonorm (2018) *Meteonorm: intro*.

Miller-Chou, B. A. and Koenig, J. L. (2003) 'A review of polymer dissolution', *Progress in Polymer Science (Oxford)*, 28(8), pp. 1223–1270. doi: 10.1016/j.ejps.2016.08.019.

Murthy, S. *et al.* (2016) 'Replication of nanopits and nanopillars by roll-to-roll extrusion coating using a structured cooling roll', *Journal of Vacuum Science & Technology B, Nanotechnology and Microelectronics: Materials, Processing, Measurement, and Phenomena*, 34(6), p. 06KM02. doi: 10.1116/1.4967217.

Nabil, A. and Mardaljevic, J. (2006) 'Useful daylight illuminances: A replacement for daylight factors', *Energy and Buildings*, 38(7), pp. 905–913. doi: 10.1016/j.enbuild.2006.03.013.

Naessens, K., Ottevaere, H., Baets, R., Van Daele, P., & Thienpont, H. (2003) 'Direct writing of microlenses in polycarbonate with excimer laser ablation'. *Applied optics*, 42(31), 6349–6359.

Nandi, S. and Winter, H. H. (2005) 'Swelling behavior of partially cross-linked polymers: A ternary system', *Macromolecules*, 38(10), pp. 4447–4455. doi: 10.1021/ma048335e.

Navvab, M., Siminovitch, M. and Love, J. (1997) 'Variability of daylight in luminous environments', *Journal of the Illuminating Engineering Society*, 26(1), pp. 101–114. doi: 10.1080/00994480.1997.10748171.

Noguchi, H. and Sakaguchi, T. (1999) 'Effect of illuminance and color temperature on lowering of physiological activity', *Applied human science journal of physiological anthropology*, 18(4), p. 117–23 ST–Effect of illuminance and color tempe. doi: 10.2114/jpa.18.117.

Nomura, Y. *et al.* (2006) 'Genotoxicity of dental resin polymerization initiators in vitro', *Journal of Materials Science: Materials in Medicine*, 17(1), pp. 29–32. doi: 10.1007/s10856-006-6326-2.

Ochoa, C. E. and Capeluto, I. G. (2006) 'Evaluating visual comfort and performance of three natural lighting systems for deep office buildings in highly luminous climates', *Building and Environment*, 41(8), pp. 1128–1135. doi: 10.1016/j.buildenv.2005.05.001.

Ohmori, H. *et al.* (2001) 'Ultraprecision micro-grinding of germanium immersion grating element for mid-infrared super dispersion spectrograph', *CIRP Annals - Manufacturing Technology*, 50(1), pp. 221–224. doi: 10.1016/S0007-8506(07)62109-X.

Okulova, N. *et al.* (2017) 'Replication of micro-sized pillars in polypropylene using the extrusion coating process', *Microelectronic Engineering*, 176, pp. 54–57. doi: 10.1016/j.mee.2017.01.027.

Paone, A. (2012) 'Advanced switchable selective absorber coatings for overheating protection of solar thermal collectors', 5878, pp. 0–12. doi: 10.5075/epfl-thesis-5878.

Park, S. and Hong, J. W. (2009) 'Polymer dispersed liquid crystal film for variable-transparency glazing', *Thin Solid Films*. Elsevier B.V., 517(10), pp. 3183–3186. doi: 10.1016/j.tsf.2008.11.115.

Patel, S., Nelson, D. R. and Gibbs, A. G. (2001) 'Chemical and physical analyses of wax ester properties', *Journal of Insect Science*, pp. 1–7. doi: 10.1093/jis/1.1.4.

Pedder, J. E. A. and Holmes, A. S. (2006) 'A Study of Angular Dependence in the Ablation Rate of Polymers by Nanosecond Pulses', *Photon Processing in Microelectronics and Photonics V*, 6106, pp. 286–294. doi: 10.1117/12.659793.

Phadtare, D., Phadtare, G. and Asawat, M. (2014) 'Hypromellose : A Choice of Polymer in

Extended Release Tablet Formulation', *World Journal of Pharmacy and Pharmaceutical Sciences*, 3(9), pp. 551–566.

Priyadarshi, A. *et al.* (2006) 'Fiber misalignment in silicon V-groove based optical modules', *Optical Fiber Technology*, 12(2), pp. 170–184. doi: 10.1016/j.yofte.2005.07.003.

Qu, W. *et al.* (1998) 'UV-LIGA: a promising and low-cost variant for microsystem technology', in *1998 Conference on Optoelectronic and Microelectronic Materials and Devices*. Perth, WA, Australia, Australia: IEEE, pp. 380–383.

Rabl, A. (1976) 'Comparison of solar concentrators', *Solar Energy*, 18(2), pp. 93–111. doi: 10.1016/0038-092X(76)90043-8.

Radhi, H. (2009) 'Evaluating the potential impact of global warming on the UAE residential buildings - A contribution to reduce the CO<sub>2</sub> emissions', *Building and Environment*, pp. 2451–2462. doi: 10.1016/j.buildenv.2009.04.006.

Rea, M. S. (1984) 'Window blind occlusion: a pilot study', *Building and Environment*, 19(2), pp. 133–137. doi: 10.1016/0360-1323(84)90038-6.

Reinhart, C. and Breton, P. (2009) 'EXPERIMENTAL VALIDATION OF 3DS MAX ® DESIGN 2009 AND DAYSIM 3.0 Ottawa, Canada (2001–2008) Harvard University, Graduate School of Design Cambridge, MA, USA (2008 - ) Autodesk Canada, Media & Entertainment, Montreal, Canada', pp. 1514–1521.

Reinhart, C. F., Jakubiec, J. A. and Ibarra, D. (2013) 'Definition Of A Reference Office For Standardized Evaluations Of Dynamic Façade And Lighting Technologies', *13th Conference of International Building Performance Simulation Association*, pp. 3645–3652.

Ren, K. *et al.* (2006) 'Convenient Method for Modifying Poly(dimethylsiloxane) To Be Airtight and Resistive against Absorption of Small Molecules', *Abate, A. R.; Anal. Chem*, 442(1), p. 12. doi: 10.1021/ac100830t.

Sarmah, N., Richards, B. S. and Mallick, T. K. (2011) 'Evaluation and optimization of the optical performance of low-concentrating dielectric compound parabolic concentrator using ray-tracing methods.', *Applied optics*, 50(19), pp. 3303–10. doi: 10.1364/AO.50.003303.

Scartezzini, J. L. and Courret, G. (2002) 'Anidolic daylighting systems', *Solar Energy*, 73(2), pp. 123–135. doi: 10.1016/S0038-092X(02)00040-3.

Schmidt, L. E., Leterrier, Y., Schmäh, D., Månson, J. A. E., James, D. (2007) 'Conversion analysis of acrylated hyperbranched polymers UV-cured below their ultimate glass transition temperature', *Journal of Applied Polymer Science*, 104(4), pp. 2366–2376.

Shin, W. S. (2007) 'The influence of forest view through a window on job satisfaction and job stress', *Scandinavian Journal of Forest Research*, 22(3), pp. 248–253. doi: 10.1080/02827580701262733.

Singleton, D. L., Paraskevopoulos, G. and Irwin, R. S. (1989) 'XeCl laser ablation of polyimide: Influence of ambient atmosphere on particulate and gaseous products', *Journal of Applied Physics*, 66(7), pp. 3324–3328. doi: 10.1063/1.344128.

Smith, R. W. and Srolovitz, D. J. (1996) 'Void formation during film growth: A molecular dynamics simulation study', *Journal of Applied Physics*, 79(3), pp. 1448–1457. doi:

10.1063/1.360983.

SOLARTRAN (2018) *LASER CUT PANEL*.

Van Steenberge, G. *et al.* (2006) ‘Laser ablation of parallel optical interconnect waveguides’, *IEEE Photonics Technology Letters*, 18(9), pp. 1106–1108. doi: 10.1109/LPT.2006.873357.

Stine, W. B. and Geyer, M. (2018) *Power From The Sun*.

Sun, X. *et al.* (2007) ‘Thickness dependence of structure and optical properties of silver films deposited by magnetron sputtering’, *Thin Solid Films*, 515(17), pp. 6962–6966. doi: 10.1016/j.tsf.2007.02.017.

Thuot, K. W. and Andersen, M. (2011) ‘A Novel Louver System for Increasing Daylight Usage in Buildings’, *PLEA 2011 - Architecture and Sustainable Development, July 13-15, 2011*, pp. 1–6. doi: 10.1016/B978-0-08-006370-6.50005-4.

Thuot, K. W. and Andersen, M. (2013) ‘PASSIVELOUVER-BASEDDAYLIGHTING SYSTEM’. doi: 10.1371/journal.pone.A61P.

Tien, C. H. *et al.* (2003) ‘Microlens array fabricated by excimer laser micromachining with gray-tone photolithography’, *Japanese Journal of Applied Physics, Part 1: Regular Papers and Short Notes and Review Papers*, 42(3), pp. 1280–1283. doi: 10.1143/JJAP.42.1280.

Tseng, A. A. *et al.* (2007) ‘Recent developments on microablation of glass materials using excimer lasers’, *Optics and Lasers in Engineering*, 45(10), pp. 975–992. doi: 10.1016/j.optlaseng.2007.04.003.

Tulloch, A. P. (1970) ‘The composition of beeswax and other waxes secreted by insects’, *Lipids*, 5(2), pp. 247–258. doi: 10.1007/BF02532476.

Tzempelikos, A. (2005) *A methodology for integrated daylighting and thermal analysis of buildings*. Concordia University.

Tzempelikos, A. and Athienitis, A. K. (2003) ‘SIMULATION FOR FAÇADE OPTIONS AND IMPACT ON HVAC SYSTEM DESIGN’, in *Proceedings of IBPSA*, pp. 1301–1308.

Varnik, F. *et al.* (2011) ‘Stability and dynamics of droplets on patterned substrates: Insights from experiments and lattice Boltzmann simulations’, *Journal of Physics Condensed Matter*, 23(18). doi: 10.1088/0953-8984/23/18/184112.

Walze, G. *et al.* (2005) ‘Combination of microstructures and optically functional coatings for solar control glazing’, *Solar Energy Materials and Solar Cells*, 89(2–3), pp. 233–248. doi: 10.1016/j.solmat.2004.11.016.

Waqas, A. and Ud Din, Z. (2013) ‘Phase change material (PCM) storage for free cooling of buildings - A review’, *Renewable and Sustainable Energy Reviews*, 18, pp. 607–625. doi: 10.1016/j.rser.2012.10.034.

Ward, G., Mistrick, R., Lee, E. S., *et al.* (2011) ‘Simulating the {Daylight} {Performance} of {Complex} {Fenestration} {Systems} {Using} {Bidirectional} {Scattering} {Distribution} {Functions} within {Radiance}’, *Leukos*, 7(4), pp. 241–261. doi: 10.1080/15502724.2011.10732150.

Ward, G., Mistrick, R., Ph, D., *et al.* (2011) ‘Simulating the Daylight Performance of Complex

Fenestration Systems Using within Radiance’, pp. 241–261.

Weimer, W. A. and Dyer, M. J. (2001) ‘Tunable surface plasmon resonance silver films’, *Applied Physics Letters*, 79(19), pp. 3164–3166. doi: 10.1063/1.1416473.

Welford, W. T. and Winston, R. (1978) *Optics of nonimaging concentrators. Light and solar energy*. New York: United States: Academic Press Incorporated.

Wittkopf, S. K. (2007) ‘Daylight performance of anidolic ceiling under different sky conditions’, *Solar Energy*, 81(2), pp. 151–161. doi: 10.1016/j.solener.2006.04.002.

Wittkopf, S. K., Yuniarti, E. and Soon, L. K. (2006) ‘Prediction of energy savings with anidolic integrated ceiling across different daylight climates’, *Energy and Buildings*, 38(9), pp. 1120–1129. doi: 10.1016/j.enbuild.2006.01.005.

Xue, Y. *et al.* (2016) ‘Underwater Superhydrophobicity: Stability, Design and Regulation, and Applications’, *Applied Mechanics Reviews*, 68(3), p. 030803. doi: 10.1115/1.4033706.

Zhang, J., Sugioka, K. and Midorikawa, K. (1998) ‘Direct fabrication of microgratings in fused quartz by laser-induced plasma-assisted ablation with a KrF excimer laser’, *Optics Letters*, 23(18), pp. 1486–1488. doi: 10.1364/OL.23.001486.



# Curriculum Vitae

## Jing GONG

### Basic information

**Nationality:** Chinese

**Tel.:** +41-(0)789667236

**Email:** gongjinghit@126.com

### Languages

**Chinese:** Native

**English:** Advanced

**French:** Intermediate

**German:** Intermediate

### Skills

#### Microsoft Office:

- Word, Excel, PowerPoint

#### Graphical design:

- Photoshop, AutoCAD, SolidWork, Inventor

#### Programming:

- C++, Java, Matlab

#### Materials characterization:

- Structural and compositional characterization using optical microscopy, SEM, TEM, various X-ray techniques, and neutron techniques
- Optical measurements using spectra meter and goniophotometers

### About me

I am passionate about science, engineering, badminton and fashion. I have been and enjoy hardworking in an international environment. With high resilience, focused mindset and problem-solving-oriented attitude, I can deal with various challenges under high pressure. I am able to work independently but I am teamwork-oriented.

### Key achievements

- PhD project was presented in the annual report 2016 of EPFL, on the homepage of EPFL and other media, various publications on prestigious scientific journals and a granted patent
- The Best Paper Award in non-imaging optics at the SPIE Optical Engineering & Applications Conference of 19-20 August 2018, in San Diego, CA, USA
- Qualification of International Welding Engineer (IWE)
- President of the student association – the Consulting Society EPFL (11.2017-07.2018)
- Third place for mixed double (3/72) at the Swiss Badminton Tournament Morges, November 2017

### Academic backgrounds

Nano/micro-fabrication, Thin film deposition, Materials processing, Mechanical engineering, Operations and supply chain management

### Educations

02/2015-2019	Doctoral program in Energy École polytechnique fédérale de Lausanne (EPFL), <b>Switzerland</b>
09/2012-10/2014	Master in Material Science Technical University of Munich, <b>Germany</b>
09/2013-02/2014	Master in Material Science University Rennes 1, <b>France (exchange)</b>
08/2008-07/2012	Bachelor of Engineering in Welding Science Harbin Institute of Technology, China

## Granted patent

Patent No. CN102581415 B: A fluxless soldering method with self-mechanical abrasion for joining aluminum foams and aluminum panels.

## Publications and conferences

1. Embedded optical microstructures with thin metallic coatings for energy regulation in buildings. In preparation.
2. Development of glazing with novel embedded optical microstructures: simulation, fabrication and characterization, manuscript in preparation
3. Engraving and replicating optical microstructures with high aspect ratio and overhang, manuscript in preparation.
4. **Gong J.**, Kostro A., Scartezzini J-L., et al. (Aug. 2018), Towards the optical properties of a novel daylighting system with embedded micro compound parabolic concentrators (CPCs). In the proceeding of **SPIE Optical Engineering + Applications 2018**, oral presentation, **San Diego**, United States.
5. **Gong J.**, Violakis G., Infante D., et al. (Feb. 2018), Microfabrication of curved sidewall grooves using scanning nanosecond excimer laser ablation. In Proceedings of the conference **SPIE Photonics West - LASE 2018**, oral presentation, **San Francisco**, United States.
6. **Gong J.**, Delaunay A., Kostro A., et al. (2018), Development of a novel mechanical micro-engraving method for the high-aspect-ratio microstructures of an advanced window system, **Microelectronic Engineering**, Volume 191: 48-53. Associated with the conference Micro/Nano Engineering (MNE) 2017, **Braga, Portugal**.
7. **Gong J.**, Kostro A., & Schüler, A. (2017). Towards novel glazing with seasonal dynamics based on micro compound parabolic concentrators. In Proceedings of the ISES **Solar World Congress 2017** (No. EPFL-CONF-232573, oral presentation, **Abu Dhabi**, The United Arab Emirates.
8. **Gong J.**, Meyer F., Leterrier Y., et al. (2017), Dimensional stability analysis of a UV printed polymer microstructure for a novel glazing system. **Energy Procedia**, 122:763-768.
9. **Gong J.**, Kostro A., Motamed A., et al. (2016), Potential advantages of a multifunctional complex fenestration system with embedded micro-mirrors in daylighting. **Solar Energy**, 139:412-425.
10. **Gong J.**, Paul N., Nagy B., et al. (2017), Nano-metric self-diffusion of Fe: effect of grain size. **Rsc Advances**, 7(16):9573.
11. **Gong J.**, Paul N., Nagy B., et al. (2016), Morphology of Fe nanolayers with Pt overlayers on low-temperature annealing. **Journal of Applied Crystallography**, 2016, 49(5):1682–1692.
12. Huang Y., **Gong J.**, Lv S., et al. (2012), Fluxless soldering with surface abrasion for joining metal foams. **Materials Science & Engineering A**, 552(5):283-287.

## Experience

2015 - 2019

**Doctoral program in Energy**, Laboratory of Solar Energy and Building Physics, École polytechnique fédérale de Lausanne, Switzerland.

**Project** : Novel daylighting system based on advanced embedded optical microstructures for various facade orientation and climates

- Ray-tracing simulation to optimize the geometries of the periodic micro-

	<p>optics and their alignments</p> <ul style="list-style-type: none"> <li>• Daylighting simulation using RADIANCE to estimate the daylighting potential and visual comfort</li> <li>• Nano/micro-fabrication by laser ablation and mechanical engraving</li> <li>• Shape fidelity analysis of UV-printed polymer microstructures</li> <li>• Facet-selective thin film coating with by physical vapor deposition</li> <li>• Structural and optical characterization for microstructures and optical thin films</li> </ul>
02/2014-10/2014	<p><b>Research Assistant (for master thesis)</b>, Physical Department E21, Technische Universität München, Germany.</p> <p><b>Project:</b> Study of self-diffusion and exchange spring effect in <math>^{56}\text{Fe}/^{57}\text{Fe}/\text{Pt}</math> multilayers</p> <ul style="list-style-type: none"> <li>• Preparation of the nano-meter thin film multilayers using molecular beam epitaxy method (<a href="#">MBE</a>)</li> <li>• Characterization of <math>^{56}\text{Fe}/^{57}\text{Fe}/\text{Pt}</math> multilayers by x-ray reflectometry (<a href="#">XRR</a>), x-ray diffuse scattering (<a href="#">XDS</a>), x-ray diffraction (<a href="#">XRD</a>) and grazing-incidence small-angle scattering (<a href="#">GISAXS</a>)</li> <li>• Study on magnetic properties by superconducting quantum interference device (<a href="#">SQUID</a>)</li> <li>• Investigation of Fe self-diffusion by <a href="#">neutron scattering technique</a></li> </ul>
08/2011-07/2012	<p><b>International Welding Engineer trainee</b> at International Institute of Welding (Chinese branch)</p> <ul style="list-style-type: none"> <li>• Theoretical training on welding operations: <ul style="list-style-type: none"> <li>➤ Welding Process and Equipment</li> <li>➤ Materials and Their Behavior During Welding</li> <li>➤ Construction and Design of Joints</li> </ul> </li> <li>• Study of quality control based on the standards and specifications of <a href="#">ISO</a>, <a href="#">EN</a>, <a href="#">DIN</a></li> <li>• Hands-on practice in <a href="#">China Aerospace and Technology Corporation</a>, <a href="#">China State Shipbuilding Corporation</a>, and <a href="#">FAW-Volkswagen Automobile Co. Ltd China</a>, subsequently</li> <li>• Monitored and optimized the efficiency of welding process with good quality control</li> </ul>
06/2011-08/2012	<p><b>Research Assistant (for Bachelor thesis)</b>, State Key Laboratory of Advanced Joining and Welding, China</p> <p><b>Project:</b> Fluxless soldering with surface abrasion for joining metal foams</p> <ul style="list-style-type: none"> <li>• Investigation of the mechanical properties of the joints by <a href="#">tension and three-point bending tests</a>.</li> <li>• Analysis of the microstructure and chemical composition of the joints using</li> </ul>

the scanning electron microscope (SEM) equipped with an energy dispersive spectrometer (EDS).

- Simulation of the strain field by finite element method (FEM)



